UNIVERSITY OF
OXFORD

Thesis

Homogeneous Dose Delivery for Very High Energy Electron Beams

Cameron Robertson

Oriel College

University of Oxford

A thesis presented for the degree of

Doctor of Philosophy

Trinity Term 2024

Acknowledgements

I would like to start by thanking my three incredible supervisors who have guided me through the work for this thesis: Andrea Latina, for his invaluable expertise in beam dynamics, minimisation based optics designed and constant support in the use of RF-Track; Alex Gerbershagen for his encyclopedic knowledge of accelerator and beam physics especially applied to treatment delivery, as well as his work in motivating the directions of my research during my DPhil; and Manjit Dosanjh, who has served as a real inspiration and guiding light throughout, through both her academic expertise in collaborative work on RT, as well as her invaluable guidance on communication and development as a researcher. I couldn't have asked for a better supervising team.

I am also extremely appreciative of the support of the continued work on e-GaToroid from Luca Bottura; it has been a privilege to contribute to this concept and its applicability to VHEE FLASH. I must also thank the entire CLEAR operation team led by Roberto Corsini, who have all contributed heavily to this work through extensive discussions and advice, as well as operation of the machine during the many experiments carried out for this thesis. I haven't the space here to individually list the contributions from every member, but I will always value my time spent as part of the CLEAR team and the impact each member has had on this work. I would like to single out the efforts of Wilfrid Farabolini. He is most responsible for the success of the experimental portion of this thesis, having aided in the continued development and led the manufacture and installation of the finalised experiments.

No less important has been the continued support of my family and friends throughout. To anyone who's proofread my work, helped with preparations, or even just joined me in R1 or the Lamb and Flag; I'll be forever grateful. I will highlight in particular the valued encouragement from Emily Archer and Vilde Rieker during the many challenges over these years. Of course, I must also mention the one and only Joe Bateman, who has been a constant companion and friend throughout this DPhil. The only thing I've valued more than Joe's extensive knowledge and expertise of the clinical aspects of our work has been the immeasurable motivation, empathy and inspiration he's provided every step of the way.

And finally, I couldn't have achieved any of this work without the continued love of my fiancée, Eda, who has been so supportive through the most challenging times.

Abstract

Very High Energy Electrons (VHEE) are a promising modality for the treatment of deep seated tumours. Advances in accelerator technologies for the Compact Linear Collider have made the production of VHEE beams with a compact machine suitable in a clinical setting feasible. There is interest in using VHEE for dose delivery to deep-seated tumours, as well as inducing the FLASH effect - a phenomenon which selectively spares healthy tissues at ultra-high dose rates. Shaping of the beam to the tumour for conformal treatment is essential. The tumour may be eventually be treated with a single large beam, which would ideally be homogeneous to minimise dose to surrounding healthy tissues. This thesis is concerned with the delivery of such uniform VHEE beams.

Magnification of an initially uniform beam to the size of a large tumour using linear optics was demonstrated for e-GaToroid: a novel gantry concept to allow irradiation from multiple angles within a FLASH timescale. This solution required quadrupoles of modest strength and provided high transmission. The TOPAS Monte-Carlo code was used to investigate scattering foils as an alternative method for uniform beam production. Dual-scattering foil design and operation at 200 MeV was studied with a range of setups. Bremsstrahlung emission in the foils required extended beamlines to prevent the loss of uniformity through a water phantom when producing a beam with a homogeneous radius of 75 mm. An automated method for foil design was developed and validated through successive experiments at the CERN Linear Electron Accelerator for Research. This allowed the first measurements of enlarged and flattened VHEE beams to take place. Scattering systems installed in the beamline allowed the evolution of uniform VHEE beams in a phantom to be measured, comparing well with combined RF-Track and TOPAS simulations. The scattering setup is now a permanent upgrade to the user facility.

Contents

1 Introduction **1**

1.1 Global Perspective of Cancer . . . 1

1.2 History of RT . . . 3

1.3 Modern Developments in Conventional Radiotherapy . . . 5

1.4 Hadron Therapy . . . 8

1.5 The FLASH Effect . . . 9

1.6 Very High Energy Electrons . . . 12

1.7 Homogeneous Dose Delivery for VHEE Beams . . . 14

1.7.1 Purpose . . . 14

1.7.2 Thesis Structure . . . 15

2 Accelerator Physics and Interactions **16**

2.1 Transverse Motion of Charged Particles . . . 16

2.1.1 Single Particle Dynamics . . . 16

2.1.2 Twiss Parameters . . . 19

2.1.3 Particle Ensembles . . . 21

2.2 Practical Considerations for Operation . . . 22

2.2.1 Quadrupole Scans . . . 22

2.2.2 Dispersion . . . 23

2.3 High Gradient Acceleration and Uniform Beam Generation . . . 24

2.4 Multiple Coulomb Scattering . . . 27

2.4.1 Moliere's Fundamental Equations . . . 27

2.4.2 Moliere's Transformed Equation . . . 28

2.4.3 Moliere's Functions . . . 30

2.5 VHEE Particle Production . . . 33

2.6 Functions for Uniform Beam Optimisation . . . 34

2.7 Summary . . . 39

3 Optics Studies for a Novel VHEE Gantry **41**

3.1 Introduction . . . 41
3.1.1 The GaToroid Concept . . . 41
3.1.2 VHEE GaToroid and Aim . . . 42
3.2 Preservation of Uniform Beam Profiles . . . 44
3.2.1 Beam Magnification in a Riesenrad Gantry . . . 44
3.2.2 Tracking and Benchmarking . . . 47
3.3 Merit Based e-GaToroid Optimisation . . . 49
3.3.1 System Geometry and Initial Beam . . . 49
3.3.2 Isocentre Beam Requirements and Constraints . . . 51
3.3.3 Initial Merit Function . . . 52
3.3.4 Optimisation Summary . . . 53
3.3.5 Results . . . 55
3.4 Sensitivity Analysis of Lattice Design . . . 57
3.4.1 Individual Scans . . . 57
3.4.2 Sensitivity Study Summary . . . 65
3.5 Discussion, Current Status and Future of VHEE GaToroid . . . 67
3.6 Summary . . . 68

4 Scattered Beams in the VHEE Regime **70**
4.1 Introduction . . . 70
4.1.1 Motivation . . . 70
4.1.2 Aim . . . 72
4.2 Methodology of Monte-Carlo Simulations . . . 72
4.3 Single Scattering . . . 74
4.4 Analytical Design of Dual-Scattering Foils . . . 80
4.5 Characteristics and Practical Considerations of Large, Flattened Beams from Dual-scattering Foils . . . 85
4.6 Collimation and Neutron Production from VHEE Beams . . . 93
4.7 Optimisation of Dual-scattering Systems with TOPAS . . . 97
4.8 Future and Ongoing Work . . . 100
4.8.1 Rapid Design of Dual-scattering Foils in RF-Track . . . 100
4.8.2 Bremsstrahlung Reduction or Production? . . . 101
4.8.3 Outlook of Dual-Scattering Foil use for VHEE . . . 102
4.9 Summary . . . 103

5 Uniform Beams at CLEAR **105**

5.1 Introduction . . . 105

5.1.1 Aim . . . 105

5.1.2 The CLEAR User Facility . . . 105

5.2 Dosimetry at CLEAR . . . 109

5.3 Single Scattering Experiments . . . 111

5.4 Uniform Intensity Profiles at In-air Test Stand . . . 118

5.5 Uniform Dose Profiles at In-air Test Stand . . . 122

5.6 CLEAR Vacuum Dual-Scattering System I . . . 125

5.6.1 Positioning, Design and Installation . . . 125

5.6.2 Profile Measurement . . . 128

5.6.3 Removal of V1 . . . 133

5.7 CLEAR Vacuum Dual-Scattering System II . . . 134

5.7.1 Design Overview . . . 134

5.7.2 Initial Characterisation and Beam Evolution . . . 135

5.7.3 Optimisation and Robustness of Charge-Dose Relationship . . . 139

5.7.4 X-ray Production from V2 . . . 145

5.8 Recent Developments and Future Outlook . . . 147

5.8.1 Performance of Scattering Foils for Sample Irradiations . . . 147

5.8.2 Proposed Experiments and Extensions of Dual-scattering Systems at CLEAR 148

5.9 Summary . . . 150

6 Conclusions **152**

6.1 Summary . . . 152

6.2 Final Remarks . . . 157

Appendix A Surplus PLA/Al Scattering Results **179**

Appendix B Availability of Data **180**

List of Figures

1.1 Number of projected worldwide cases against year for most common cancers, from [18].Reproduced with permission from Springer Nature . . . 2

1.2 Diagram of typical conventional linac (left), and flattening filter principle for X-rays (right). Images adapted from [80, 81]. . . . 5

1.3 Relative dose deposition against depth in water, for 16 MV X-ray and 200 MeV proton beams, with demonstration of Spread-Out-Bragg-Peak. Image from [83][01]. SSD refers to distance between source and water entrance. . . . 6

1.4 Tumour response and normal tissue toxicity against delivered radiation dose, with therapeutic window (index) concept indicated. Image from [86]. . . . 7

1.5 Ion gantry at Heidelberg Ion Therapy Centre. Image from [122]. . . . 9

1.6 Total irradiation time for set dose delivery against instantaneous dose rate per train from pre-clinical in-vivo studies. UHDR healthy tissue sparing qualities indicated from markers, described as FLASH effect in caption. Dose delivery structures indicated with coloured circles. Figure from [141]. . . . 10

1.7 Normalised longitudinal dose against depth in water for 200 MeV electrons, 2 MeV X-rays, 200 MeV protons and 6 MeV electrons. Generated from Monte-Carlo dose simulations. . . . 12

1.8 Percentage dose against depth in water-equivalent tissue demonstrating impact of focusing on VHEE beam, with unfocused, symmetrically and asymmetrically focused distributions indicated. Image from [162]. . . . 13

2.1 Charged particle moving in a magnetic field, with coordinates x, y, s and z displayed. Image from [178]. . . . 17

2.2 x-x' transverse trace space ellipse with invariant area and relationship to Twiss parameters indicated. ϵ equivalent to J_x in Equation 2.21. Image from [179]. . . . 20

2.3 Diagram of elements required for quadrupole scan technique, for the case of a focusing quadrupole. Screen and reconstruction point indicated. Labels as used for calculation in Equation 2.29 also shown. . . . 22

2.4 Schematic of key components of CLIC, showing drive beam and main beam complexes. Image from [180]. . . . 25
2.5 Photograph of test 100 MeV m^{-1} CLIC cavity. Image from [181]. . . . 25
2.6 Histograms of beam intensity in transverse position (left) and divergence (right) from simulated uniform beam generated from a photocathode. Figure from [187]. . . . 27
2.7 $f^{(2)}$ value from Equation 2.57 derived from replacement of integral with Equation 2.58, as function of summing index n in this equation. Shown for different values of $x \equiv \vartheta^2$ with coloured lines. . . . 32
2.8 Bremsstrahlung photon production cross section in lead against fractional photon energy for different beam energies across VHEE regime, indicated by colour. Generated from Equation 2.61. . . . 34
2.9 Theoretical interaction cross sections for photons against energy in carbon (left) and lead (right), with experimental data indicated as circular data markers. Contributions from relevant processes highlighted. κ_{nuc} and κ_e refer to nuclear and electron pair-production, respectively. Giant dipole resonance highlighted in right-hand diagram. Figure adapted from [195]. . . . 35
2.10 Value of normalised shaped and super-Gaussian function of Equation 2.67 in 2D (left) and 1D against x (middle) and y (right). Power term of 1 (top), 2 (middle) and 5 (bottom). . . . 37
2.11 Value of normalised super-Gaussian function of Equation 2.74 in 2D (left) and 1D against x (middle) and y (right). Different P, $k_{x,y}$ and $h_{x,y}$ parameters indicated for top, middle and bottom rows. . . . 39

3.1 Original hadron GaToroid concept, showing initial kicker magnet and bending toroid with patient at system isocentre. Image from [200] . . . 41
3.2 Conceptual visualisation of e-GaToroid, demonstrating toroidal lattice elements, patient location at isocentre, and beam travelling through one of 7 defined paths. Image from [205]. . . . 43
3.3 Riesenrad gantry concept, with beam entering through left, travelling through single bending dipole and entering patient on dynamic rotating couch. Arbitrary magnet lattice shown. Image from [206]. . . . 44
3.4 Layout of Riesenrad magnification design from MAD-X with displacement s through beamline. Positioning designated by Table 3.1 with beam entering from left and element labels shown. . . . 46

3.5 Transfer matrix ($re \equiv R$) element values against displacement through designed Riesenrad beamline. Relevant matrix elements for transverse quantities in x (left) and y (right) shown. Magnification through beamline demonstrated by enlargement of absolute values of $re11$ and $re33$ terms, with all other relevant elements matched to approximately 0. Lattice element positioning overlaid. 46
3.6 Transverse beam density histogram at isocentre from beam tracked through Riesenrad lattice with PTC (left) and RF-Track (right). 48
3.7 Single particle discrepancies between PTC and RF-Track against displacement along Riesenrad beamline, in position (left) and divergence (right), in both transverse axes. MAD-X lattice overlaid on both sub-figures. 48
3.8 Generic 1D representation of e-GaToroid system showing main components, with conceptual e-GaToroid side-profile courtesy of T. Lehtinen overlaid. Beam entering from left. 50
3.9 Intensity distributions of initial beam used for e-GaToroid design. 2D density histograms in $x - y$ (left) and $p_x - p_y$ (middle), and 1D beam density histogram of particle energy (right). 52
3.10 Transverse beam intensity histogram at e-GaToroid isocentre from initial kurtosis based RF-Track optimisation, with 75 mm radius virtual collimator region highlighted. 1D distributions in respective axes also shown. 54
3.11 1D e-GaToroid design geometry and required magnetic strengths for reference magnet values, with quadrupole gradients shown where necessary. Beam entering from left, with vector magnet not shown. 56
3.12 Histograms of beam intensity against x (left) and y (right) across slices of beam profile at e-GaToroid reference design isocentre, with super-Gaussian fits indicated. Extracted from simulation in RF-Track. 56
3.13 Beam envelope function and dispersion in bending axis against displacement through reference e-GaToroid beamline, with element geometry displayed above. 57
3.14 Fitted uniform ellipse parameters x_{90} and y_{90} at e-GaToroid isocentre against quadrupole strength for each relevant element in beamline, for scan taken around reference k_1 values. Linear fits and coefficient of determination R^2 indicated for correlations between deviations and fitted parameters. 59

3.15 Fitted mean transverse beam position $\mu_{x,y}$ at e-GaToroid isocentre against translation offsets in x (top) and y (bottom) for each element in beamline, as indicated above each column. Linear fits and coefficient of determination R^2 indicated for correlations between deviations and fitted parameters. 61

3.16 Fitted mean transverse beam position $\mu_{x,y}$ at e-GaToroid isocentre against offsets in angular pitch for each element in beamline, as indicated above each figure. Linear fits and coefficient of determination R^2 indicated for correlations between deviations and fitted parameters. 62

3.17 Fitted mean transverse beam position $\mu_{x,y}$ (top) and uniform ellipse parameters x_{90} and y_{90} (bottom) at e-GaToroid isocentre against offsets in angular yaw for each element in beamline, as indicated above each column. Linear and parabolic fits and coefficient of determination R^2 for the former indicated for correlations between deviations and fitted parameters. 63

3.18 Fitted mean transverse beam position $\mu_{x,y}$ (top) and uniform ellipse parameters x_{90} and y_{90} (bottom) at e-GaToroid isocentre against mean energy (left) and absolute energy spread (right). 65

4.1 Illustration of dual-scattering foil principle with initial beam of arbitrary intensity profile entering system from left-hand side. 70

4.2 Reference setup in TOPAS, with beam in red entering from left-hand side, being scattered by S1 and entering green water phantom on right-hand side. 75

4.3 2D transverse primary beam intensity histogram (left), beam intensity against x (middle) and y (right) from indicated slices across distribution, with (super) Gaussian fits shown. Extracted from TOPAS simulation of arbitrary single-scattered beam. 75

4.4 Beam-size from Gaussian fits with prediction from Equation 2.59 indicated (upper-left) and photon production (lower left), against thickness in tantalum S1. Beam energy at surface of water phantom against tantalum S1 thickness (right). Scattering angles also indicated. Extracted from TOPAS simulations with single-scattering reference setup. 76

4.5 2D transverse secondary photon beam intensity histogram (left), beam intensity against x (middle) and y (right) from indicated slices across distribution. Extracted from TOPAS simulation with reference single-scattering setup, at water phantom surface. 77

4.6 Photon yield per primary electron against initial beam energy measured at water phantom surface from S1 producing constant 30 mrad scattering angle according to Equation 2.59 (0.9 mm Ta at 200 MeV). Results from three scattering materials for S1 shown, produced from TOPAS simulation with single-scattering reference setup. 77

4.7 Normalised dose scored in water phantom against depth in water, from TOPAS simulations of reference setup. Components from total, primary and secondary (generated in S1) beams indicated. Shown for 0.12 mm (left), and 0.9 mm (right) tantalum foil thicknesses (10 and 30 mrad scattering angles respectively). Dose integrated across 6 mm (top), 30 mm (middle) and total (bottom) transverse radii. 78

4.8 2D transverse dose histograms (left), dose against x (middle) and y (right) from indicated slices across distributions. Primary beam dose component (top) and secondary beam dose component (bottom) shown. Extracted from TOPAS simulations with reference single-scattering setup and 0.9 mm Ta S1 (30 mrad scattering angle). Measurement taken at peak of on-axis total dose, 80 mm depth in water phantom. 1 nC accumulated charge in simulation. 79

4.9 Relevant scattering parameters for analytical design method. Image from [220][02]. . 80

4.10 Predicted optimised fluence against radial displacement from 10 mm uniform radius design with analytical formalism of [213] (left), beam loss index (middle) and uniformity across 10 mm radius (right) against iteration number during optimisation. 82

4.11 2D transverse primary beam intensity histogram (left), beam intensity against x (middle) and y (right) from indicated slices across distribution, with super-Gaussian fits shown. Extracted from TOPAS simulation of beam after passage through dual-scattering system with geometry described by Row 1 of Table 4.1. Measurement taken at water phantom surface in reference setup. 83

4.12 Schematic showing locations of S1 in the three scattering setups relative to water phantom as described in Table 4.2 used in TOPAS simulations. S2 placed 100 mm downstream of S1 for each setup. 86

4.13 Geometrical visualisation (longitudinal positioning vs radial extent of slice) of scattering systems for production of 75 mm dual-scattering profile with 30 mrad (left), 20 mrad (middle) and 10 mrad (right) divergence angles, described quantitatively in Table 4.2. Systems are composed of tantalum S1 and aluminium S2. 86

4.14 2D transverse total dose histograms (left), total dose against x (middle) and y (right) from indicated slices across distributions, with super-Gaussian fits shown. Extracted from TOPAS simulations with 30 mrad dual-scattering setup. Profiles shown at entrance (a), middle (b) and exit (c) of 30 cm depth water phantom, with measurement positions indicated. Sharp central peak visible at depth from photon contributions generated in dual-scattering system. 87

4.15 r_{90} (top), and peak-to-valley uniformity within r_{90} (bottom) against depth in water phantom, calculated from shaped super-Gaussian fitting of **primary** transverse dose components. Extracted from TOPAS simulation with 30 mrad setup in TOPAS. Errors propagated from covariance matrix of fitting results and statistical uncertainty derived from multiple simulation runs (errors dominated by the former). 88

4.16 r_{90} (top), and peak-to-valley uniformity within r_{90} (bottom) against depth in water phantom, calculated from shaped super-Gaussian fitting of **total** transverse dose. Extracted from TOPAS simulation with 10 mrad (left) and 20 mrad (right) setups in TOPAS. Errors propagated from covariance matrix of fitting results and statistical uncertainty derived from multiple simulation runs (errors dominated by the former). 90

4.17 2D visualisations of physical 20 mrad S2 geometry (longitudinal coordinate against radial coordinate for circularly symmetrical systems) as composed by 25, 10 and 5 slices, from left to right. 91

4.18 Transverse density histogram of primary electron beam generated from dual-scattering system with 5 step S2. Extracted from TOPAS simulation with 20 mrad setup, measured at water phantom surface. Density rings from multiple steps clearly visible. . 91

4.19 k_x parameter from fit of Equation 2.74 to transverse intensity distribution at water phantom surface against S2 misalignment in x. 2D density histograms and 1D slices with fits in x at extrema of misalignment scan shown in insets. Results from TOPAS simulations with 20 mrad setup. Errors from covariance matrix of fits and statistical fluctuations calculated from multiple scanning runs. 92

4.20 2D transverse primary beam intensity histogram (left), beam intensity against x (middle) and y (right) from indicated slices across distribution, with super-Gaussian fits shown. Extracted from TOPAS simulations with 20 mrad setup at water phantom surface, after correction from 300 mrad tilt in S2 alignment. Correction algorithm based upon minimising skew $k_{x,y}$ parameter of fits from Equation 2.74. 93

4.21 Integrated dose deposition in water phantom against collimator slab thickness, from simulations in TOPAS with 20 mrad setup. Normalised to total absorbed dose in phantom without collimation. 94
4.22 Lateral beam dose penumbra against depth in water for dual-scattered beam in 20 mrad setup with collimator inserted and extracted (a), 2D transverse primary beam intensity histogram (left), beam intensity against x (middle) and y (right) from indicated slices across distribution, with super-Gaussian fits shown (b,c). Dose profiles in water at phantom exit for collimator inserted (b) and extracted (c). Extracted from TOPAS dose simulations. 96
4.23 Normalised relative neutron contributions to dose from external sources against depth in water phantom, from TOPAS simulations with 20 mrad setup and extended water phantom. 97
4.24 Summary of MC based dual-scattering foil optimisation process. 98
4.25 Transverse slice of arbitrary S2 (longitudinal positioning vs radial extent) with consistent σ_{S2} and H generated from differing warp factors. 0.5 (left), 1 (middle) and 1.5 (right). 99
4.26 Scattering angles (top) and photon yield (bottom) generated from 200 MeV primary electron beam against tantalum S1 thickness. Results from TOPAS simulations with single-scattering reference setup. 101
4.27 Integrated dose against depth in 30 cm water phantom, data generated from TOPAS simulation of a 200 MeV beam scattering from 12 mm tantalum target 10 cm upstream of phantom. Total, primary and secondary contributions to dose indicated. . 102

5.1 Schematic of CTF3 layout, taken from [230]. 106
5.2 The CLEAR User Facility, photograph inside bunker (top), schematic of accelerator (middle) and schematic of experimental beamline (bottom). Images from [235]. . . 107
5.3 Transmitted charge against time demonstrating length and spacing of trains (top) and bunches (bottom) at CLEAR. Image from [242]. 109
5.4 C-Robot (left) and holder held by C-Robot and used for diagnostic YAG beam imaging in the in-air test stand during operation (right). Images from [241]. 110
5.5 Schematic of pre-scattering experiment in CLEAR in-air test stand. 112

5.6 Sample of single scattering experimental data. YAG screen images of scattered beam showing transverse intensity profile (left), 2D Gaussian fit to YAG data (middle), and fitting residuals (right), for 10 mm S1 inserted (top) and 30 mm S1 inserted (bottom). 113

5.7 Beamsize from Gaussian fits in x (top) and y (bottom) against S1 thickness for single scattering experiment. Experimental data measured with in-air test stand YAG screen, and comparative TOPAS simulations indicated. S1 placed 250 mm upstream of YAG for measurement. Beam energy of 200 MeV (left) and 150 MeV (right). Experimental errors from deviations of ten measurements (trains). 114

5.8 Photograph of setup for more precise single-scattering experiment, beamline entering from right with PMMA holder and materials in centre. Water phantom hidden by enclosed fibre experiment on left. 115

5.9 Measured beamsize against current of relevant quadrupole magnet shown along with fits for derivation of Twiss parameters in x (left) and y (right). Parabolic fits indicated. Quadrupole scan results measured with 7XX triplet at CLEAR, lower (blue values) taken for input to TOPAS simulations for comparison with scattering experiment, at 200 MeV. Twiss parameters extrapolated back to 3XX triplet shown (black values). Also carried out for operation at 180 MeV and 160 MeV. 116

5.10 Beam σ from Gaussian fitting of transverse intensity profiles against energy for each material under investigation, indicated above each figure. Experimental C-Robot YAG screen results and those from comparative TOPAS simulations indicated. Vertical error bars for experimental data represent standard deviation of 25 train measurements. Simulated data errors dominated by material thickness uncertainty. . . . 117

5.11 PLA S2 visualised in CAD (left) and photograph of 3D printed system set in C-Robot holder (right). 119

5.12 Schematic showing layout of dual-scattered profile experiment on CLEAR in-air test stand. 119

5.13 2D transverse beam intensity histograms (left), beam intensities against x (middle) and y (right) from indicated slices across distributions, with super-Gaussian fits shown. Results from TOPAS simulation (top) and in-air test stand YAG screen at CLEAR (bottom), with PLA dual-scattering system inserted. 30 mm S1 and S2 placed 335 mm downstream of S1 (corresponding to Row 4 of Table 5.3). 120

5.14 2D transverse beam intensity histogram (left), beam intensities against x (middle) and y (right) from indicated slices across distributions, with super-Gaussian fits shown. Results from TOPAS simulation (top) and in-air test stand YAG screen at CLEAR (bottom), with PLA dual-scattering system inserted. 30 mm S1 and S2 placed 381 mm downstream of S1 (corresponding to Row 5 of Table 5.3). 121

5.15 Schematic showing layout of dual-scattering dose experiment on CLEAR in-air test stand. Al 1, Al 2 and Al 3 inserted respectively at positions indicated. Film positions A and B used for measurements also indicated. 122

5.16 2D transverse primary beam intensity histogram (left), primary beam intensities against x (middle) and y (right) from indicated slices across distributions, with super-Gaussian fits shown, from TOPAS simulation (a). 2D transverse beam dose histograms (left), beam doses against x (middle) and y (right) from indicated slices across distributions, with super-Gaussian fits shown, from EBT3 film measurements at CLEAR at 3 nC/train (b) and 25 nC/train (c) intensities. Simulation/experiments carried out with Al 2 inserted and measurements taken at Film Position A. (b) and (c) correspond to Rows 3 and 4 in Table 5.4, with (a) used for comparisons to both. 124

5.17 Schematic showing end segment of CLEAR beamline (enlarged from Figure 5.2) with available options for installation of vacuum chambers indicated. Beam passage from right to left. 125

5.18 Simulated profile generated by PEEK in-vacuum dual-scattering foil from 200 MeV initial beam in TOPAS, using generic positioning of C-Robot YAG screen at CLEAR. Primary beam intensity against x (upper left) and y (upper right) from thin slices across distribution. 2D transverse intensity histogram (bottom left) and intensity against primary particle energy (bottom right). 127

5.19 Schematic of first vacuum dual-scattering system components at CLEAR (left), camera images of S1 (middle) and S2 (right) installed in beampipe vacuum chambers. 128

5.20 2D transverse intensity histogram (left), intensity against x (middle) and y (right) from indicated slices across distribution. Extracted from image of C-Robot YAG screen with V1 system inserted in CLEAR. Beam cut by diagnostic YAG screen 910 in beamipe at top of profile, and edge of beampipe itself. Anomalies visible from edge of screen and holder. 128

5.21 Schematic of in-vacuum experiments, indicating components, relevant regions and code choices used for comparative simulations. Inactive quadrupoles represented by open pink boxes. 129

5.22 Transverse profiles with V1 inserted, measured with C-Robot YAG screen in air (a), 20 mm (b), 60 mm (c) and 100 mm (d) depths in water. 2D transverse intensity histogram (left), intensity against x (right) from indicated x slice with super-Gaussian fit shown in each sub-figure. Clipping from diagnostic YAG screen visible. 130

5.23 x_{90} of transverse beam intensity against depth in water with V1 system inserted. Measured with C-Robot water tank positioned 2245 mm downstream of S1, taken from fits to YAG images with comparative TOPAS simulation results also shown. Beam operated at 1 nC per train. TOPAS error margin taken from simulation resolution, with experimental errors propagated from fitting covariance matrix. 131

5.24 Dose (left) and x_{90} (right) against depth in water for single holder irradiation with V1 dual-scattering system inserted. Measured in test stand water tank with long EBT3 film holders, with dose directly extracted from 5x5 mm^2 large sample region, and x_{90} taken from fits to transverse profiles on films. 104.6 nC accumulated charge, delivered at 1 nC/train intensity. Water tank positioned 2245 mm downstream of S1. 132

5.25 2D transverse intensity histogram (left), intensity against x (middle) and y (right) from indicated slices across distribution, with super-Gaussian fits shown. Measured with C-Robot YAG screen in-air with V1 inserted and aligned with steel collimator to avoid diagnostic YAG screen and beampipe clipping. 133

5.26 Design schematic showing longitudinal coordinate in TOPAS component of design simulations for S1 and S2 against radius of transverse PEEK V2 slices (left) and photograph of manufactured components (right). 134

5.27 2D transverse primary beam intensity histograms (left), intensities against x (middle) and y (right) from indicated slices across distributions, with super-Gaussian fits shown. Extracted from combined RF-Track/TOPAS simulations of CLEAR with V2 inserted with different optics settings. No focusing (top) and with typical quadrupole settings used during operation to reduce jitter (bottom). Quadrupole strengths of QFD760 and QDD765 were 3.44 and −3.94 m^{-2} respectively, for this latter case. Initial beam conditions of Table 5.6 assumed to assess changes from conditions of design simulations (caption of Table 5.5) including steel mounting stem. 135

5.28 2D transverse dose histogram (left), dose against x (middle) and y (right) from indicated slices across distribution, with super-Gaussian fits shown. Sample profile of dual-scattered beam measured with EBT3 film at in-air test stand with V2 system inserted. 2.02 nC accumulated charge measured at THz1, at 200 pC/ train. 136

5.29 Dose measured across 5x5 mm^2 region on dual-scattered EBT3 film profiles in-air at test stand, against accumulated charge measured by THz2 BCM. Beam operated at 200 pC/train. Errors from standard deviation across sample region. Linear fit to data and coefficient of determination R^2 displayed. 137

5.30 Dose measured across 5x5 mm region in centre of uniform profile against depth in water with V2 system inserted. Experimentally measured with long C-Robot EBT3 film holders in water tank, with comparative TOPAS simulations indicated. Four train and single train measurements shown. Errors from standard deviation of dose across measurement region. Approximately 20 nC total charge delivered at THz1 BCM for each set. 5.81 and 4.85 nC transmitted charge measured at THz2 BCM for four shot and single shot measurements, respectively (simulations scaled accordingly). Water tank positioned 2378 mm downstream of S1. 138

5.31 Dose x_{90} (left) and lateral penumbra (right) against depth in test stand water phantom from beam with V2 system inserted. Taken from super-Gaussian fits to transverse dose profiles captured by EBT3 films in long holders, with errors propagated from covariance matrix. Four train and single train measurements indicated. Approximately 20 nC total charge delivered at THz1 for each. Results from comparative RF-Track/TOPAS simulations indicated. Error region defined by simulation resolution. Water tank positioned 2378 mm downstream of S1. 139

5.32 Image of V2 S2 scatterer in beam pipe during operation from digital camera, with steel stem mounting visible. 140

5.33 2D transverse dose histogram (left), dose against x (middle) and y (right) from indicated slices across distribution, with super-Gaussian fits shown. Sample profile of dual-scattered beam measured with EBT3 film at in-air test stand with modified V2 system using 100 µm aluminium S1 inserted. 3.8 nC accumulated charge measured at THz1, delivered in 2x1.9 nC trains. 140

5.34 Fitted x_{90} parameter measured from radiochromic EBT3 and EBT-XD films at in-air test against charge per train measured at THz1 BCM, with modified aluminium-PEEK V2 inserted. Measurements carried out by C-Robot in-air, and at 20 mm, 60 mm, and 100 mm depths in water, as indicated. V2 inserted; positioning in water or in-air measurement indicated. Errors from propagation of covariance matrix output. 142

5.35 2D transverse dose histograms (left), dose against x (middle) and y (right) from indicated slices across distribution, with super-Gaussian fits shown. Measurements with V2 inserted, taken with EBT-XD films in-air, with collimator extracted (top) and inserted (bottom). High-charge 40 nC in single train at THz1 delivered. Significant misalignment in x shown. 143

5.36 Dose across 5x5 mm central region against accumulated charge measured at THz2 at 20 mm (left), 60 mm (middle) and 100 mm (right) depths with EBT3 films in C-Robot water phantom. Error bars represent standard deviation across dose region. High intensity data points from Table 5.7 excluded. Line of best fit indicated in each sub-figure. 144

5.37 Dipole field separating secondary photon beam from electron component after dual-scattering, visualised in TOPAS GUI. Beam entering from right-hand-side. 145

5.38 2D transverse X-ray dose histogram (a, left), X-ray dose against x (a, middle) and y (a, right) from indicated slices across distribution, measured with EBT3 film at 105 mm depth in water and V2 inserted. Dose across 5x5 mm large sample size against depth in water phantom from X-rays (b) displaying experimental EBT3 measurements and comparative RF-Track/TOPAS simulations. Errors from standard deviation across dose measurement region in both cases. 400 nC estimated accumulated charge at THz1. 146

5.39 Schematic of proposed 2nd beamline at CLEAR. Image from [251]. 149

List of Tables

3.1 Quadrupole strengths (k_1), field gradients (G) and longitudinal positions in the beamline (s) for Riesenrad transfer line design carried out with MAD-X. 45

3.2 Geometrical e-GaToroid lattice constants, referring to the labels in Figure 3.8. . . . 50

3.3 Quadrupole strengths in initial (**init**) design and subsequent reference (**ref**) design. Quadrupole positioning visualised in Figure 3.11, with drift tube lengths explicitly quantified in Table 3.4. 55

3.4 Lengths of unconstrained drifts in e-GaToroid system as designated by initial lattice design optimisation results, consistent for both initial and reference design. Drift 5 defined to retain constant Drift 6 length. 55

3.5 Fitting and direct parameters for initial and improved reference design. r_{90} values derived from Equation 2.70 from fits shown in Figure 3.12. Transmission and uniformity directly measured within 75 mm virtual collimator. Errors retrieved from running multiple cycles with 10^7 particles. 57

3.6 Summary table displaying statistically significant correlations between offsets in elements and deviation in mean position, within scanning ranges described in Section 3.4. Highest sensitivities highlighted in **bold**. Uncertainties not displayed here for clarity - typically below 1%. 65

3.7 Statistically significant correlations between offsets in elements and uniform radius, within scanning ranges described in Section 3.4. Yaw row values taken from local gradient at maximal scanning extent. Highest sensitivities highlighted in **bold**. Uncertainties not displayed here for clarity - typically below 1%. 66

4.1 Comparison between analytical ($an.$) predictions and TOPAS results for dual-scattering foil designs for different uniform extents at water phantom surface. TOPAS measurements taken from fits to profiles; within statistical uncertainty of direct measurements. "Uni" refers to full (peak-to-valley) variation of fitted profiles within uniform radius r_{90}. 84

4.2 Scatterer geometries and required phantom positioning for production of 75 mm uniform component for 3 scattering angles. H and σ_{S2} refer to quantities for S2 geometry described in Section 4.4. t_{S1} is the thickness of S1. 85

5.1 CLEAR Beam Parameters in 2023 [241]. 110

5.2 Manufactured materials and uncertainties, and resulted predicted scattering angles (generated from 2D Gaussian fitting to intensity profiles at scoring surface in TOPAS). 115

5.3 Super-Gaussian fitting parameters in experiment and simulations of PLA dual-scattering setup, for results with evidence for uniformity region of 1 cm radius. t_{S1} is the thickness of S1; z_{S2} is the distance from the upstream face of S1 to the downstream face of S2, as shown in Figure 5.12. Line in **bold** is setup from design optimisations. Units of mm unless otherwise specified. Errors from fitting covariance output. . . . 121

5.4 Super-Gaussian fitting parameters from transverse experimental dose profiles and TOPAS simulated intensity profiles for aluminium dual-scattering setup. S2, Loc column refers to the choice of scatterer and positioning of transverse profile measurement, as shown in Figure 5.15. Errors from fitting covariance output. 123

5.5 Initial designs for vacuum systems placed in reference to Figure 5.17. Designs based upon nylon S1 and S2 unless otherwise stated, S2 split into 5 slices. Initial symmetrical beam conditions of $\beta_{x,y}$ =20 m, $\alpha_{x,y}$=0 and **normalised** emittance $\epsilon_{x_n,y_n} = 10\,\mathrm{mm\,mrad}$. t_{S1}, H and σ_{S2} as defined in Chapter 4. Transmission defined within virtual collimator of 15 mm radius. 126

5.6 Quadrupole scan results taken with 7XX triplet and used for input into RF-Track/TOPAS combined model for studies in Section 5.6 and 5.7. 131

5.7 Summary of irradiation conditions for V2 charge-dose study. 141

5.8 Summary table of low charge results from characterisation experiments, from combined data. Showing uniform extent in x (x_{90}) and lateral penumbra in x (LP_x). . . 143

A.1 Super-Gaussian fitting parameters in experiment and simulations of PLA dual-scattering setup, for results with evidence for uniformity region of 1 cm radius. t_{S1} is the thickness of S1; z_{S2} is the distance from the upstream face of S1 to the downstream face of S2, as shown in Figure 5.12. Units of mm unless otherwise specified. Errors from fitting covariance output. 179

A.2 Super-Gaussian fitting parameters from transverse experimental dose profiles and TOPAS simulated intensity profiles for aluminium dual-scattering setup. S2, Loc column refers to the choice of scatterer and positioning of transverse profile measurement, as shown in Figure 5.15. Errors from fitting covariance output. 179

1 Introduction

1.1 Global Perspective of Cancer

In the UK, half of us will develop some form of cancer in our lifetime [1]. It is projected that deaths from cancer will reach half a million per year by 2035, mainly as a consequence of the ageing population [2, 3]. Cases of lung, breast and colorectal cancers are expected to increase significantly as shown in Figure 1.1. Smoking remains a major contributor across the world, as well as other environmental factors such as air pollution [4, 5]. Detection, effective treatment and thus mortality rate are dependent on geographical location and socioeconomic condition even in high-income countries [6] including the UK, as highlighted by the recent report of the All Party Parliamentary Group for Radiotherapy in February 2024 [7, 8]. This may be due to lack of financial means [9, 10], or minimal Radiation Therapy (RT) facilities, state of the art technologies as well as sufficiently trained experts.

Indirectly, lack of access to facilities for treatment and lack of a national screening program is similarly shown to increase mortality [11, 12]. Travel costs or loss of employment may increase financial disparities depending on income and location [13, 14]. With increasing lifespans and quality of living, it is becoming an increasing global challenge, and especially in middle and low-income countries [15, 16] where progress is hampered by lack of access resulting in late detection and lower treatment rates [17]. Cancer is projected to become the leading cause of death in lower-income countries within the next century [19]. In high-income countries, regular screenings (particularly for more common cancers such as those in the breast, colon and prostate) have improved outcomes due to earlier detection, along with vaccination for cases such as cervical cancer [1, 20, 21, 22, 23]. However, many challenges still remain. In the UK, the aforementioned disparities and lack of forward planning as well as the struggling National Health Service have resulted in historically high waiting times and a general slow-down of improvements in cancer outcomes [1, 7, 24].

Cancer treatment is categorised as either “curative” or “palliative” [25]. The objective of curative procedures, generally applied to those with higher life expectancies, is to remove or destroy the tumour and prevent recurrences. Such a removal of the disease and symptoms can be referred to as putting the patient into “remission”. If detected sufficiently early, curative treatment can typically

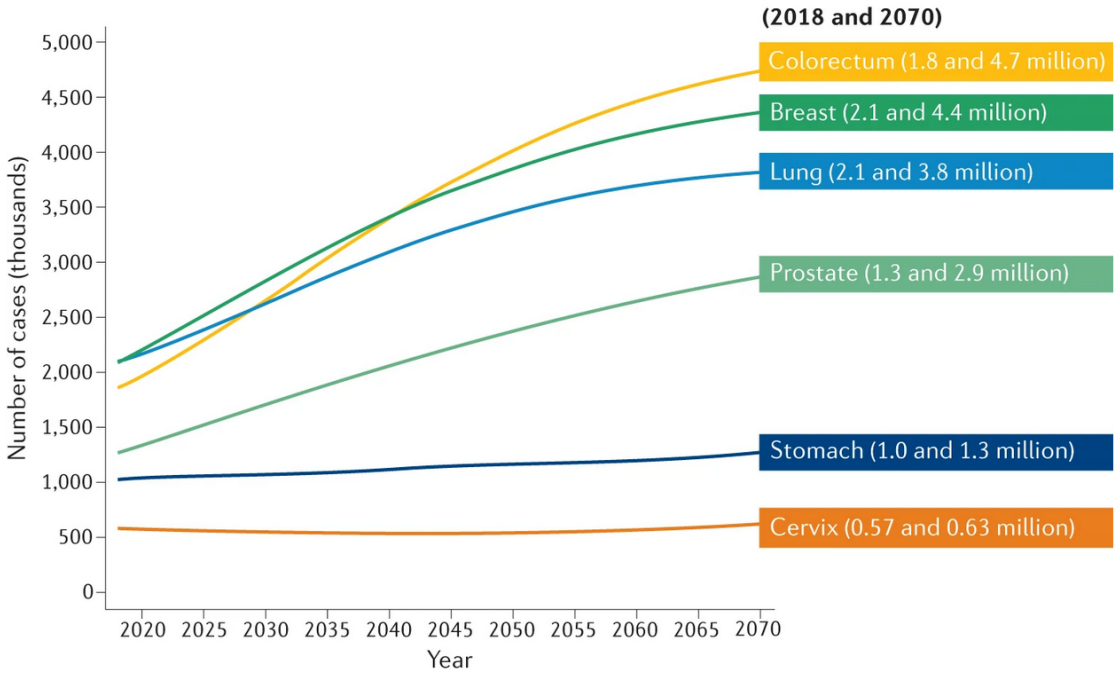

Figure 1.1: Number of projected worldwide cases against year for most common cancers, from [18].Reproduced with permission from Springer Nature

be applied to those cancers with the highest occurrence, such as prostate and breast [26, 27, 28]. If curative treatment is deemed impossible or inappropriate, palliative treatment may be carried out for pain relief and improving quality of life [29]. This treatment direction is frequently chosen with prevalence of an extremely advanced or aggressive form of cancer, or general ill health [30].

Both curative and palliative treatments play a key role in tackling cancer. Due to the range and number of stages the umbrella term "cancer" covers, there is unlikely to be a single cure. Combating cancer requires extensive collaboration, multidisciplinary expertise and resources due to the numerous variants and stages of the disease and necessary treatment modalities. It is a significant burden to the populace of every country in the world both economically and emotionally [31, 32, 33]. For this reason, cancer is an extremely active area of research and investigation [34]. All forms of treatment are a financial burden, be it due to costs of medicine, machinery, or even the salaries of the professionals required to develop and deliver said treatment. This burden may also be due to the loss of the patient's ability to work in many cases [35, 36].

The goal of any cancer treatment is the removal of cancerous tissue whilst minimising damage to the surrounding healthy tissues of the patient and resultant side-effects. Success will be defined by improved quality of life during and after treatment, and lowered probability of tumour resurgence. Surgery, chemotherapy and RT are the most common forms of cancer treatment. Surgery is often chosen to remove a tumour for cases where it has been detected early and is localised, often

followed by RT and/or chemotherapy [37]. Modern techniques have reduced the risks associated with surgery, particularly due to the less severe interventions required [38]. Chemotherapy prevents tumour growth and causes tumour death through the administration of medicinal poisons. These chemotherapeutic agents damage the DNA of all cells, but selectively kill more cancer cells due to their more rapid growth [39]. Despite this differential response, chemotherapy typically causes significant damage to healthy cells and DNA throughout the body [40] - particularly those with rapid proliferation such as blood cells, skin cells, hair follicles and cells in the intestinal lining [41]. This can cause numerous side effects and reduced quality of life for the patient [42, 43]. Tumours may also gain resistance to treatment, further decreasing their response [44]. Thus, techniques for delivery of targeted chemotherapy [45] and triggering of immune response to attack the cancer cells [46] to reduce adverse effects have been developed and are being continuously improved. There is a promising outlook and active research in the fields of surgery, chemotherapy [47] and RT, the treatment method addressed in this thesis.

1.2 History of RT

Around 50% of cancer patients would benefit from some form of RT as part of their treatment [48, 49]. The principle of RT is to utilise ionising radiation to target cancerous cells and tissues. Energy is transferred to the tissue as absorbed *dose*, typically given in units of Gray, where 1 Gy= 1 J kg^{-1}. The delivered dose will cause tumour shrinkage and eventual disappearance of the tumour due to damage caused by ionising energy to cell DNA [48]. The discovery of X-rays by Roentgen in 1895 [50] almost immediately led to the birth of both radiology (imaging with X-rays) and RT. An 1896 issue of the Lyon Medical Record described a patient with gastric carcinoma benefiting from RT delivered in Lyon, France, using X-rays from a kilovoltage vacuum tube [51, 52].

The rapid progression of the field during the early 20th century was propelled by swift technological advances. These included developments in electronics and production of X-rays using hot cathodes, and research on radioactive sources by notable figures such as Marie and Pierre Curie [53]. Clinical outcomes were often poor, due to the lack of methods for dose targeting and measurement. The subdivision of dose delivery through fractionation [54] was observed to spare healthy tissue during treatment. This concept still forms the basis of modern RT. The field of dosimetry did gain significant traction, marked by the definition of the first unit of dosage (the *Roentgen*) in 1928 [53], required due to the advent of measurement with ion-chambers. These could be used to provide real-time dosimetry during RT treatment [55], providing a uniform response to delivered ionising

radiation.

Treatment in this period was carried out only for superficial cancers (for example, near the surface of the skin [53]) due to limitations in the maximal energy of the X-rays. Deep-seated but accessible tumours were typically treated with brachytherapy (RT from an internal radioactive source) [56]. This would remain the case until the introduction of "cobalt bombs", where Cobalt-60 sources were enclosed in lead shielding and a shutter opened to provide X-rays with an energy of 1.2 MeV [57]. The first therapeutic Cobalt-60 source was developed and installed in 1951 [58], enabling RT with photons in the MeV range. Treatment with Co-60 is still common particularly in lower and middle-income countries today [59]. However, there were and are numerous issues associated with Co-60 therapy due to security associated with radioactive sources and their limited energy and intensity, the latter of which also slowly decreases due to the half-life [60]. Treatment times thus increase with the age of the sources, with biological effective dose typically decreasing by a few % annually [61].

The application of resonant cavities to electron acceleration [62] and wartime developments in RF sources [63] resulted in the installation of the first electron linear accelerator (linac) in Stanford [64]. This was powered by a klystron produced by Varian, which remains the dominant company in development of technology for conventional RT [63]. The first clinical linac was installed in Hammersmith Hospital in London in 1953, treating its first patients later that year with an accelerating voltage of 8 MV (the energy of clinical X-rays is typically characterised by accelerating voltage in the linac rather than energy, due to the wide spectrum of the final beam). This was soon followed by the installation of the Stanford Medical Linear Accelerator in the U.S [65, 66], which was used to treat a 2 year old child with an eye tumour in 1956. These advances marked the beginning of the Megavoltage era. Following a short period where X-rays in this energy range were produced from medical betatrons [67], electron linacs became the primary source of X-rays for RT [68].

Numerous additional developments in accelerating technology throughout the latter half of the 20th century were driven by interest in nuclear and particle physics [64]. Much of this technology and expertise was directly applied in RT to provide more effective treatment, as well as enabling the implementation of advances such as hadron therapy [69, 70]. These developments evolved in parallel with advances in treatment planning, imaging, immobilisation and development of operational procedures, as well as improved cellular and molecular understanding of cancer [57, 71, 72, 73, 74].

1.3 Modern Developments in Conventional Radiotherapy

In a standard clinical machine for RT, a compact linac is used to accelerate the electrons to the desired energies. The energy of this primary beam is typically in the range of 10 MeV. The cavities are fed by klystrons, which may be of the standing or travelling wave type, depending on the design of the specific linac. These typically operate at S-Band (3 GHz) frequency [68, 75]. The beam is directed through an achromatic bend to bring it perpendicular to the patient; this is within the circularly symmetrical gantry of the machine to allow treatment from multiple directions [76]. The beam is then sent into a target (usually tungsten), with the electrons converted into X-rays via Bremsstrahlung emission [77]. The X-ray beam will be poly-energetic, with a broad spectrum extending downwards from the accelerated electron beam energy as briefly discussed in Section 1.2 [78]. The generated secondary beam has a non-uniform transverse intensity before passage through a flattening filter system to introduce uniformity through preferential scattering of the beam centre and collimation of remaining tails [79]. A diagram of a typical clinical linac and flattening system is shown in Figure 1.2. An X-ray beam deposits a characteristic longitudinal dose

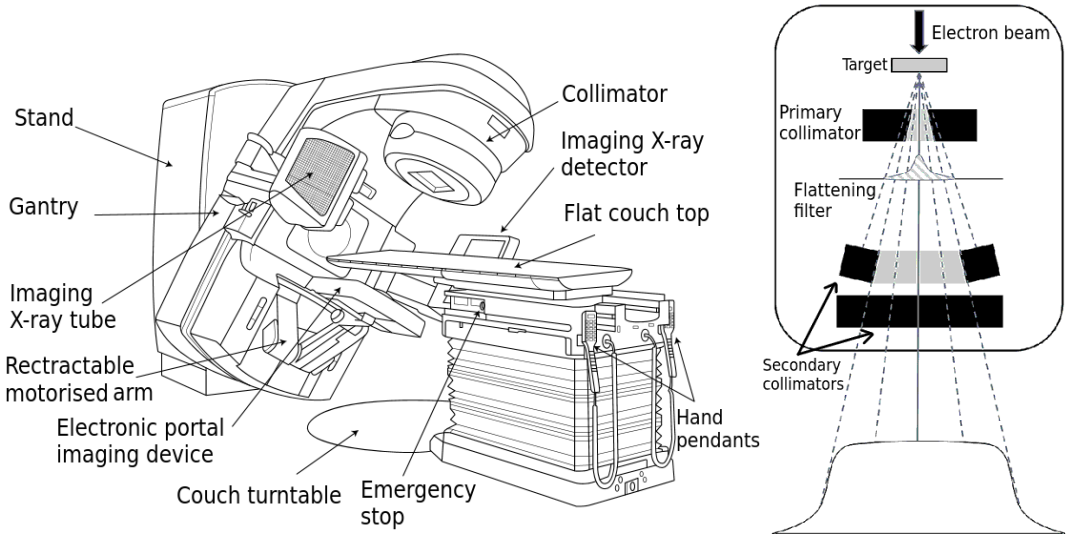

Figure 1.2: Diagram of typical conventional linac (left), and flattening filter principle for X-rays (right). Images adapted from [80, 81].

curve in a patient, as shown in Figure 1.3. There is relatively low deposition in superficial regions, although this rapidly builds up to a peak due to the electromagnetic cascade in the patient. This is known as the "skin-sparing" effect, and is a benefit of the characteristic X-ray dose deposition curve; entry dose in the patient is relatively low [82]. The depth of the peak is dependent on the energy of the electron beam. Beyond this peak, the dose gradually reduces as the beam passes through the patient, resulting in a significant exit dose [82].

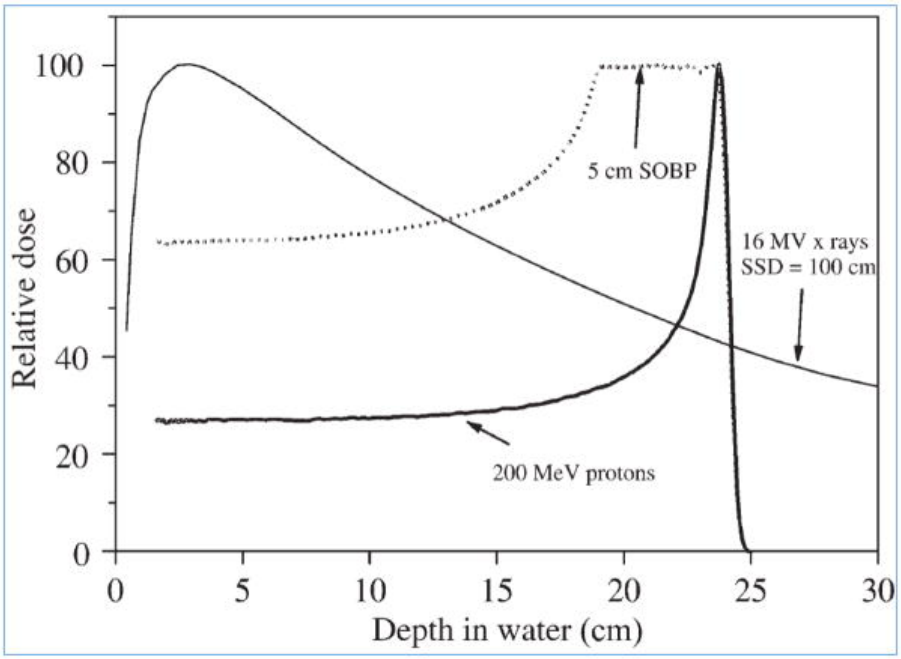

Figure 1.3: Relative dose deposition against depth in water, for 16 MV X-ray and 200 MeV proton beams, with demonstration of Spread-Out-Bragg-Peak. Image from [83][01]. SSD refers to distance between source and water entrance.

There have been notable advances in treatment with conventional radiotherapy in the last few decades. Advanced treatment planning systems working in tandem with diagnostic imaging, positioning and immobilisation systems allow robust plans to be developed [84]. These work in conjunction with the numerous developments in beam delivery to aid in tumour conformality - the targeting and shaping of beam to maximise dose to the tumour whilst minimising dose to surrounding tissues, the key aim of cancer treatment [85]. The effect of conformality can be visualised using the "therapeutic window" as shown in Figure 1.4, designating the separation between dose delivered to the cancerous cells and healthy cells - a parameter which should ideally be kept as large as possible (this is sometimes referred to as *widening* the therapeutic window). This is particularly crucial during the treatment of deep-seated tumours, which may be in the vicinity of Organs At Risk (OAR). These are organs which are particularly sensitive to the damaging effects of radiation, such as the brain, pancreas or spinal cord [87, 88, 89].

Diagnostic Computed Tomography (CT) scanning as part of treatment planning has allowed conformality to be achieved through irradiations with multiple beams in so-called 3D-CRT (3D-Conformal RT) [90]. Multi-directional delivery is now automated for most treatment plans, further assisted by dynamic patient couches to give further flexibility during irradiations. Conformal treatment has been aided by the implementation of Multi-Leaf Collimators (MLCs) - devices with a

[01] Reprinted from Radhe Mohan and David Grosshans: "Proton therapy–present and future". Advanced drug delivery reviews 109, pp. 26–44. Copyright (2017), with permission from Elsevier.

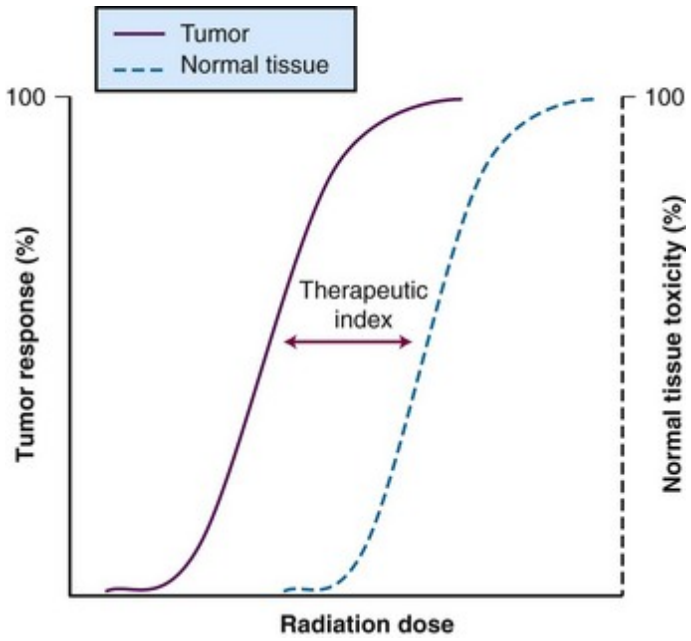

Figure 1.4: Tumour response and normal tissue toxicity against delivered radiation dose, with therapeutic window (index) concept indicated. Image from [86].

series of tungsten leaves to shape the transverse distribution of the beam [91]. MLCs are a crucial component of Intensity Modulated RT (IMRT), a significant advance in the field and a preferred method of RT treatment in many cases [92, 93]. IMRT improves dose conformality by splitting beams into individual beamlets with the MLC and varying the intensity in each of these beamlets. This is assisted by advanced inverse planning systems and may also utilise several angles for irradiation as with 3D-CRT [94, 95]. Current machines are also capable of delivering VoluMetric Arc Therapy (VMAT) which allows dynamic motion of the beam along with the positioning of leaves in the MLC. It has the advantage of being rather faster than equivalent IMRT irradiations [96, 97], whilst still providing superior conformal treatment to 3D-CRT and even IMRT for some cases [98, 99]. VMAT can include many more angles during treatment, thus reducing localised dose in healthy tissues. Detailed and accurate simulations are available to clinicians and medical physicists to allow them to assess and create optimised, predictive plans to deliver the most effective treatment. Monte-Carlo (MC) beam matter interaction codes such as GEANT4 [100] can also be utilised for quality assurance, reference dosimetry and verification of these predictions [101]. There is naturally much interest in the optimisation of the treatment planning process using artificial intelligence, with a promising outlook in the field [102].

Despite the advances outlined above, X-ray treatment will likely always be limited by the shape of the dose deposition curve with high exit dose shown in Figure 1.3. There is currently a great deal of research and treatment being carried out for radiotherapy with particles other than X-rays. Electrons have been used for RT since the 1950s [103], and many machines are capable of deliv-

ering electron therapy by simply removing the Bremsstrahlung target and treating with the primary beam [80]. This is generally done for the treatment of superficial tumours [104, 105], since at clinically available energies, the electrons are only capable of reaching a few cm into the patient [106].

1.4 Hadron Therapy

Despite the first patient being treated with protons in 1954 [107], hadron RT has only become widespread in the last few decades. The first hospital based facilities were Clatterbridge, Liverpool (opened in 1989 for ocular treatments) [108] and a dedicated clinical facility for proton RT for all tumour types (including deep-seated tumours) in 1990 at Loma Linda University Medical Center, California [109]. Conventional RT is still by far the dominant modality, representing over 90% of all treatments carried out worldwide in 2023 [110]. Hadron therapy is only available in high and middle income countries, resulting in limited access [111].

As shown in Figure 1.3, protons exhibit very different dose characteristics in patients compared to X-rays. Dose is low upon entrance to the patient, before peaking very sharply again at a depth dependent on the energy of the proton beam [112]. This is known as the "Bragg Peak", and is a result of the dependence on deposited energy from elastic collisions on the inverse square of the particle velocity for hadrons [113]. Beyond this peak, very little additional dose is absorbed by the patient. The very localised dose deposition allows more precise positioning over the tumour and a reduced exit dose when compared to conventional RT. Typically, multiple beams are delivered with modulated energies to produce a Spread-Out-Bragg-Peak (SOBP) for coverage of the tumour in the longitudinal axis [114], also shown in Figure 1.3. Heavier ions exhibit a similar character to protons, albeit with sharper Bragg Peaks and higher radiobiological effectiveness [115]. With modern treatment planning, hadron therapy has been shown to produce superior outcomes to conventional RT for many cases [116, 117, 118].

The main drawbacks to hadron therapy are the scale and cost of the machines. Protons are typically accelerated to around 200 MeV (400 MeV/c for carbon) [119], to allow treatment of deep-seated tumours [120]. All currently operating hadron therapy centres reach these energies using circular accelerators (cyclotrons or synchrotrons) which are far larger, more expensive in installation and operation, and require more extensive shielding than the linacs for conventional RT [121]. Novel linear proton accelerators for treatment are in development [123], but with available technology these would still be larger than current clinical linacs and require specialist centres for installation. The general issues of size and cost also extend to the beamlines required for multi-directional

Figure 1.5: Ion gantry at Heidelberg Ion Therapy Centre. Image from [122].

treatment. Clinical hadron beams have large bending radii for normal conducting magnets, and thus large mechanical gantries must be installed. For example, the first and only carbon gantry in Europe used at the Heidelberg Ion Therapy Centre [124] as shown in Figure 1.5 has a radius of approximately 15 m and weighs around 600 tonnes [122, 125]. Several facilities have now developed more compact gantries with superconducting bending magnets, but these require specialised cryogenic cooling systems in addition to the magnets themselves [126, 127, 128]. Furthermore, hadron therapy currently requires more expertise in machine operation than conventional facilities [129].

1.5 The FLASH Effect

In 2014, it was discovered that irradiations carried out at Ultra-High-Dose-Rates (UHDRs) above $40\,\mathrm{Gy\,s^{-1}}$ created a differential effect in tumour and healthy tissue response in mice [130] - that is, tumour tissues did not exhibit any signs of sparing when exposed to UHDR, whilst healthy tissues were spared. This defined the so-called FLASH effect, an emerging field of great interest in RT. For reference, X-ray RT is typically carried out at a dose rate of around 1 Gy/min [131]. Evidence for FLASH was also found in cats and mini-pigs [132]. The first patient was treated with UHDR electrons in 2019, with significant tumour response [133]. It is clear that FLASH is a biological effect [134], dependent on dose and dose structure rather than the specific modality of treatment. Thus, the FLASH effect has been observed with not only low energy electrons, but also protons [135], X-rays [136] and carbon ions [137]. The biological origin of the FLASH effect is still unclear [134], although several mechanisms have been proposed and studied, such as the effects of oxygen depletion and immune response [138, 139, 140]. This is an active area of research, as there

are many open questions to be answered before FLASH can be understood and clinically applied.

The dependence of the FLASH effect on dose is also an incomplete picture. Typically, it has been shown that the FLASH effect is induced within irradiation times of less than half a second and doses of more than 10 Gy at UHDRs [131]. Numerous experiments have been carried out to study the parameter space for FLASH, as shown in Figure 1.6. A significant result from these stud-

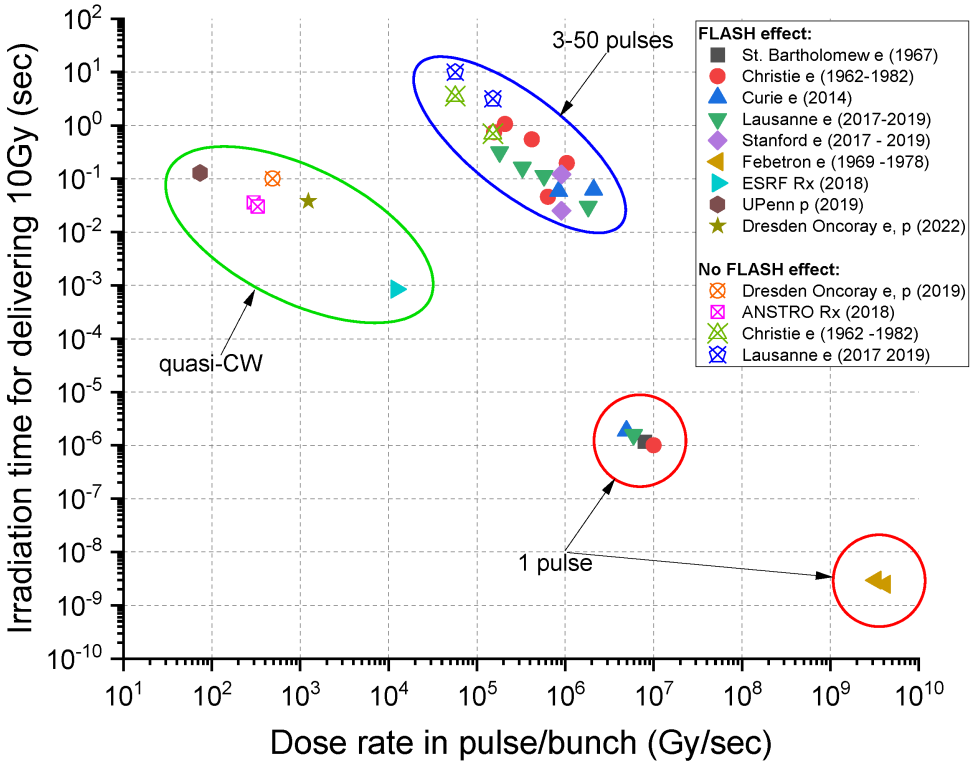

Figure 1.6: Total irradiation time for set dose delivery against instantaneous dose rate per train from pre-clinical in-vivo studies. UHDR healthy tissue sparing qualities indicated from markers, described as FLASH effect in caption. Dose delivery structures indicated with coloured circles. Figure from [141].

ies was the importance of beam parameters and location of dose deposition in animal patients; a failure to provide conformal irradiations was shown to result in disastrous consequences in some cases [142] and emphasised the need for caution for FLASH-RT. Ideally, treatments would be delivered in several fractions and with multiple irradiation angles to increase conformality, as is the case in conventional RT [131]. However, the interaction between the FLASH effect and delivery of multiple doses is also unclear currently [143]. There is evidence for a minimal "trigger dose" for FLASH-RT, which may limit the possible fractionation and number of irradiation angles [144]. Due to the uncertainties outlined above, human patients have only been treated for superficial or extremity based cancers in initial studies [134]. The FLASH effect's healthy tissue sparing properties could be effective for cancer treatment with RT. It could be especially beneficial when treating deep seated tumours near radio-sensitive OARs, where conformal treatment is most crucial to prevent

damage and development of secondary cancers.

Whilst the FLASH effect can be induced by all clinically available RT modalities, there are significant challenges in regards to the beam delivery for each case. FLASH-RT from a conventional linac would require an extremely high-current electron beam to produce a UHDR X-ray beam from the Bremsstrahlung target, due to the reduction in intensity from the electron to X-ray conversion. Furthermore, there would also be limitations in regards to heat buildup from deposition of dose in the target [145]. Dedicated facilities could overcome the dose limitations, but careful design of the target would be needed, with extensive studies of heat buildup and fatigue [146]. Additionally, modern X-ray techniques such as IMRT and VMAT would be challenging to deliver at UHDR, as they would require rapid motion of the beam nozzle and MLC leaves. An alternative to Bremsstrahlung X-ray generation for UHDR treatment could be the use of synchrotron radiation, but this would necessitate extremely large machines and infrastructure [145]. It has been shown through simulation that compact X-ray tubes could be modified to produce UHDR X-rays [147], although their limited energies would only be appropriate for treatment of superficial cancers.

Hadron therapy machines benefit from treating with primary beams, so the required intensity is typically achievable from machines which are already in use - albeit for small tumour volumes [148]. Some scaling up in terms of beam current may be required, although this is realistically achievable with current cyclotron based technology [149]. A concern for the cyclotron based machines is the process of longitudinal positioning and production of the SOBP. As a single machine will be required to produce a beam of an arbitrary energy, most clinical cyclotrons use degraders (typically triangular beam inserts) to reduce the energy from the maximal value to that required for the particular treatment, and a ridge filter to create the SOBP [150]. The insertion particularly of the energy degraders can result in very significant losses in beam intensity [151], and thus cyclotrons may require extremely high beam currents to provide FLASH-RT over the full range of tumour depths [148]. Hadron facilities using synchrotrons face a different set of concerns for FLASH operation. Unlike cyclotrons, the treatment beam can be extracted at an appropriate energy for irradiation without degradation. However, the timescales for ramping and extraction are typically far longer than those required for FLASH [148]. Dedicated machines capable of rapidly extracting beams would be required to overcome this challenge, for example using RF Burst Extraction [152]. All energy layers would need to be extracted within a single cycle [148], however this has already been implemented in some clinical systems and therefore could be feasible [153, 154].

Because of these challenges with SOBP delivery at UHDRs, most [155] research and treatment of patients with hadron FLASH irradiations has been carried out in “shoot-through” mode [156]

where the beam is at its maximum energy with no degrader. Thus, the patient is treated with the flat "plateau" region of the hadron beam. Whilst aiding in robustness [157] one of the main advantages of hadron therapy (the Bragg Peak) is lost in favour of the FLASH effect. The question must then be asked - why use hadrons at all?

1.6 Very High Energy Electrons

As discussed in Section 1.5, low energy electrons have been used to treat patients clinically and in pre-clinical trials with FLASH, but only for superficial cancers due to their limited penetrating power. The range of the beam does however increase with increased beam momentum. Very High Energy Electrons (VHEEs) would be an ideal treatment modality for FLASH-RT. These electron beams with energies above the clinically available range (>50 MeV) could be delivered with cheaper and more compact machines than hadrons with fewer operational concerns than conventional RT at UHDR. Figure 1.7 shows the on-axis distribution for a 200 MeV VHEE beam in comparison with other modalities in a water phantom. VHEE beams do not possess the sharp peaks of low energy

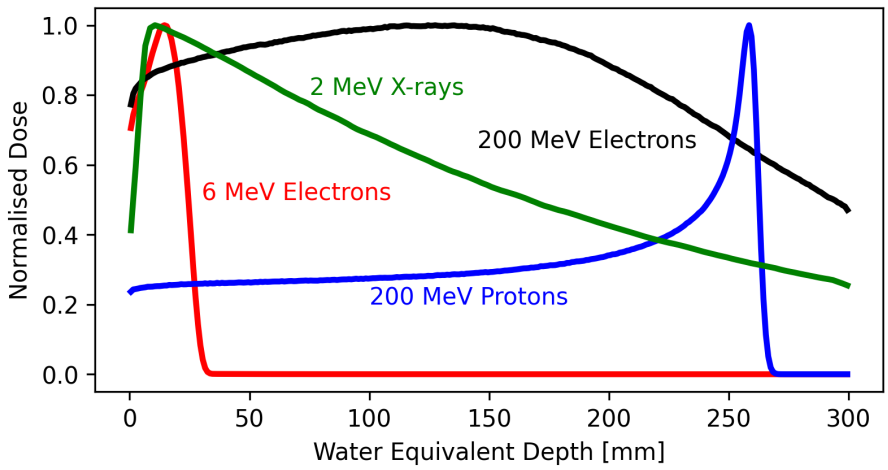

Figure 1.7: Normalised longitudinal dose against depth in water for 200 MeV electrons, 2 MeV X-rays, 200 MeV protons and 6 MeV electrons. Generated from Monte-Carlo dose simulations.

electrons or hadron beams, instead exhibiting a fairly constant longitudinal distribution with a gentle peak and decrease. Crucially, VHEE beams at 200 MeV are capable of reaching deep seated tumours within a patient [158].

There are numerous characteristics of VHEE beams which make them favourable for tumour treatment. VHEE beams have lower lateral penumbrae in water than low energy electrons due to reduced Multiple Coulomb Scattering (MCS). Scattering from air between source and patient would also be significantly reduced [103]. The penumbra is even predicted to compare well to conventional

X-rays up to around 5 cm in a patient depending on the size of the beam [159]. There is simulated and experimental evidence that VHEE beams would be relatively insensitive to inhomogeneities in patient tissues; a key concern for hadron therapy [160]. As lighter charged particles, VHEE beams can be easily magnetically manipulated; they could be scanned to provide tumour coverage, as is carried out for many proton beam therapy treatments, but requiring magnetic elements of lower strength [103]. VHEE beams can also be strong-focused at the tumour. When carried out appropriately, this could be used to produce a localised dose peak on the longitudinal axis as shown in Figure 1.8, which itself may be scanned or shaped [161]. This principle of an "Electron Bragg-Peak" to improve tumour conformality has been demonstrated both by simulation [161, 162] and experiment [163, 164].

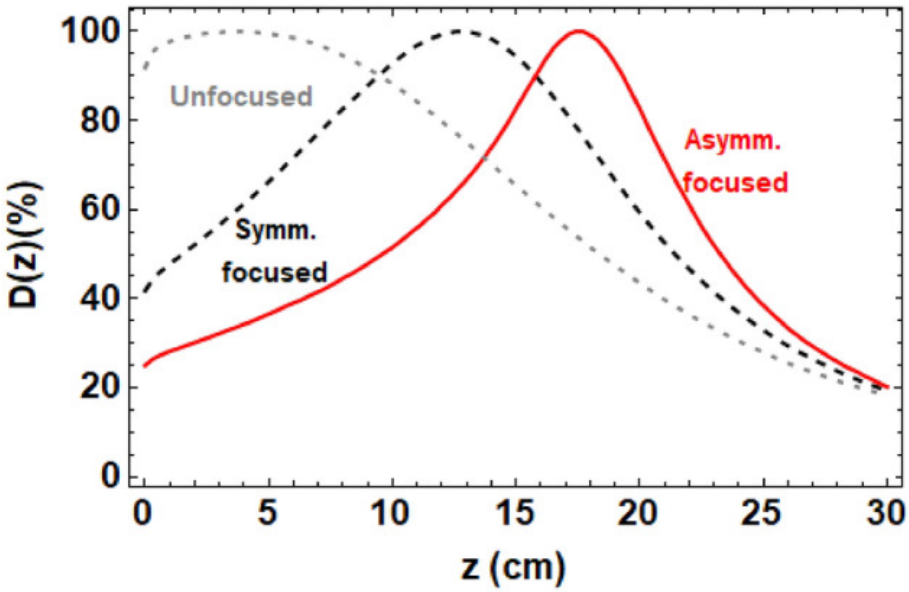

Figure 1.8: Percentage dose against depth in water-equivalent tissue demonstrating impact of focusing on VHEE beam, with unfocused, symmetrically and asymmetrically focused distributions indicated. Image from [162].

Several treatment planning studies have been carried out to compare VHEE with the currently available conventional RT and proton modalities. For some cases when simulating scanned electron beams, VHEE plans can be superior to those achieved with VMAT [165] and at least comparable to those for scanned proton beams [166]. In separate studies, VHEE plans were again found to be superior or comparable to IMRT X-ray treatment plans for glioblastoma and lung cancer [167], and proton plans for inter-cranial lesions [168]. Treatment plans specifically in the context of FLASH have been evaluated to consider required dose rates and tumour volume constraints [169].

Gantries for VHEE beam delivery would require smaller and/or lower strength magnets than those for hadron gantries, due to the significantly reduced magnetic rigidity (see Chapter 2) of VHEE beams compared to hadron beams of even modest energies. Thus, they could be more com-

pact whilst not requiring more expensive super-conducting magnets and the resultant bulky cooling systems. Recent advances in electron acceleration technology for the Compact Linear Collider (CLIC) [170] have also allowed acceleration of VHEE beams to be feasible in a very compact space, as discussed further in Chapter 2. This could allow the installation of a VHEE linac suitable for a clinical/hospital setting.

1.7 Homogeneous Dose Delivery for VHEE Beams

1.7.1 Purpose

VHEE beams present an opportunity to provide UHDR beams for the treatment of deep-seated tumours with more compact machines and delivery systems than similar solutions for hadrons. The use of the primary beams at high energy make them more efficient and less prone to target and dose based limitations for UHDR X-ray RT. Compact electron acceleration and the benefits of VHEE and its feasibility for providing FLASH-RT have been demonstrated with simulation and in experiments. There are however certain questions that surround the delivery of such a beam from the accelerator to the patient, especially when UHDR and FLASH-RT are of concern - specifically, in terms of the off-axis (transverse) distribution. Immediately after acceleration, beams have a typical transverse size of a few mm at most in all modalities, so they must be manipulated in some fashion to provide transverse tumour coverage. As briefly mentioned, state-of-the-art hadron therapy machines typically carry out treatments using a "pencil beam" and scanning across the tumour with dipole magnets in the nozzle. The interaction of such treatment plans with specific dose rate measurement is complex [171, 172, 173, 174] and for such a treatment to be carried out entirely within the FLASH timescale of approximately 100 ms [148], extremely fast, accurate magnets would be required. It is currently unclear if multiple UHDR fields delivered over a longer timescale would be capable of inducing the FLASH effect.

This issue of time dependence could be overcome by irradiating the tumour with a single large field. The initial beam would have to be significantly enlarged to cover a maximal tumour size, in this case. Ideally, the beam would also have a uniform transverse intensity distribution to prevent tails extending into healthy tissue - crucial for the treatment of deep-seated tumours. This would also allow a homogeneous distribution of the dose across the tumour. The purpose of this thesis is to investigate the production of such a beam with a uniform transverse intensity distribution, for the treatment of deep-seated tumours with VHEE FLASH-RT.

1.7.2 Thesis Structure

It has been demonstrated that with appropriate considerations, a beam with a transverse uniform distribution can be generated at the downstream end of a photo-cathode driven electron gun and retained through acceleration up to the VHEE regime [175]. After acceleration, the beam can be magnified whilst retaining the uniform region, using only linear optics. Chapter 3 is based on the development of such an optics design in the context of VHEE GaToroid, a novel gantry concept to allow multi-field VHEE treatment entirely within the FLASH timescale.

The second method of uniform beam production is based upon an established technique used in both conventional and hadron therapy: the dual-scattering system. Unlike the optics based method, this does not require an initially uniform beam and hence could be used to introduce uniformity to an arbitrary transverse intensity distribution, if designed appropriately. Dual-scattering systems are well characterised for hadrons, X-rays and low energy electrons, having been extensively used in each of these treatment modalities; however this is not the case for VHEE beams. The higher energy regime presents a new set of concerns such as reductions in mean energy, particle production, spatial constraints, material choice and robustness. Chapter 4 is based upon the design and characterisation of dual-scattering systems for VHEE beams, and investigating the operation of these systems using the TOPAS MC beam-matter interaction code. Chapter 5 is a demonstration of these design principles and predictions in simulations in an experimental context - specifically, the successive developments, installations and tests of dual-scattering systems and studies on uniform VHEE beam evolution at the CERN Linear Electron Accelerator for Research (CLEAR).

2 Accelerator Physics and Interactions

2.1 Transverse Motion of Charged Particles

2.1.1 Single Particle Dynamics

In this thesis, the particles under study are ultra-relativistic in nature (kinetic energy greatly exceeds rest mass), and thus the total energy is approximately equivalent to kinetic energy of the particles. The accelerator physics theory of this section, along with Sections 2.1.2 and 2.2.2, was taken principally from the presentations and material on transverse beam dynamics given by [176, 177].

A particle with charge q in an electromagnetic field is subject to the Lorentz Force:

$$\vec{F} = q(\vec{E} + \vec{v} \times \vec{B}) \tag{2.1}$$

where $\vec{v}$ is the velocity of the particle, $\vec{E}$ is the electric field and $\vec{B}$ is the magnetic field. Thus, due to coupling with the particle's velocity (very close to the speed of light c), the transverse motion is mainly dependent on the magnetic field. Setting Equation 2.1 equal to the centripetal force for the circular motion of a particle with bending radius ρ, assuming a magnetic field perpendicular to $\vec{v}$ and negligible electric field, its circular motion is described by the product of the magnetic field strength and bending radius:

$$B\rho = \frac{Pc}{q} \tag{2.2}$$

where B=|$\vec{B}$| and P is the total momentum of the particle. Equation 2.2 is known as the magnetic rigidity and characterises the required strength of the magnetic field to bend the particle with a certain radius, with respect to the momentum of the particle. The particle can be defined with respect to a curved, left handed reference system known as the reference orbit. This is shown along with relevant transverse parameters in Figure 2.1. The physical transverse plane is parameterised in the x and y axes, typically given in mm. z is the longitudinal coordinate perpendicular to the transverse plane of motion, with s being the displacement along the reference orbit. The divergence

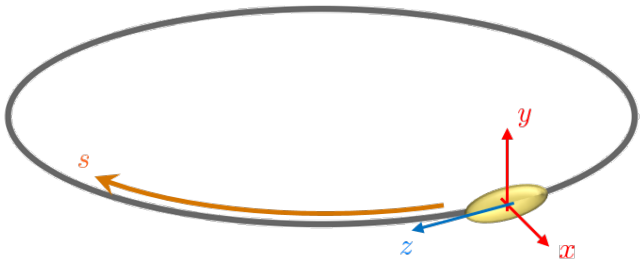

Figure 2.1: Charged particle moving in a magnetic field, with coordinates x, y, s and z displayed. Image from [178].

in the transverse axes is written as

$$x' = \frac{dx}{ds} \qquad\qquad y' = \frac{dy}{ds} \tag{2.3}$$

typically measured in mrad. The parameters p_x and p_y are sometimes used to describe the angular displacement of the particle; these differ subtly from x' and y':

$$p_x = \frac{P_x}{P_0} \qquad\qquad p_y = \frac{P_y}{P_0}. \tag{2.4}$$

where P_x and P_y are the transverse momenta, and P_0 is the reference momentum. (x,x') and (y,y') are generally referred to as the *trace space*, whereas (x,p_x), (y,p_y) are the *phase space* coordinates. The particle's motion in each axis can typically be decoupled into two vectors

$$M_x = \begin{pmatrix} x \\ x' \end{pmatrix} \qquad\qquad M_y = \begin{pmatrix} y \\ y' \end{pmatrix}. \tag{2.5}$$

The equation of motion for a particle in circular motion (for a single transverse coordinate, assumed to be x throughout here) is

$$F = m\left(\frac{d^2\rho}{dt^2} - \rho\left(\frac{d\theta}{dt}\right)^2\right). \tag{2.6}$$

where m is the particle mass. The magnetic field causing this motion B can be described as a Taylor expansion of its components

$$B_y = B_0 + x\frac{\partial B_y}{\partial x}. \tag{2.7}$$

where higher order terms are neglected here to allow the equations of motion to be solved analytically. This is known as the linear approximation. In general, only quadrupole and dipole field components are used in this thesis. The quadrupole strength k_1 is commonly used to give a measurement of the focusing power of a quadrupole field irrespective of the particle energy. It is defined by

$$k_1 = \frac{q}{c}\frac{G}{P} \tag{2.8}$$

for electrons, where G is the quadrupole gradient in $\mathrm{T\,m^{-1}}$. Combining Equations 2.1, 2.6 and 2.7 yields

$$m\frac{d^2}{dt^2}(x+\rho) - \frac{m\dot{x}^2}{x+\rho} = B_y\dot{x}. \tag{2.9}$$

Changing the variable from t to s, rearranging, and using the definition of k_1 from Equation 2.8 the second order differential equation becomes

$$x'' + \left(\frac{1}{\rho^2} + k_1\right)x = (x'' + Kx) = 0 \tag{2.10}$$

where $'$ represents a derivative with respect to the path displacement s. Thus, K in Equation 2.10 is provided by the dipole (weak focusing) and quadrupole (strong focusing) fields, and trivially reduces to k_1 where there is no bend in the relevant axis. Equation 2.10 describes simple harmonic motion with restoring force principally provided through linearly varying quadrupole fields. Imposing appropriate initial conditions, the solution for this in the case where $K > 0$ is

$$x(s) = x_0\cos\left(s\sqrt{K}\right) + x_0'\frac{1}{\sqrt{K}}\sin\left(s\sqrt{K}\right) \tag{2.11}$$

where x_0 and x_0' are the initial values of x and x', respectively. For $K < 0$, the solution is:

$$x(s) = x_0\cosh\left(s\sqrt{|K|}\right) + x_0'\frac{1}{\sqrt{|K|}}\sinh\left(s\sqrt{|K|}\right). \tag{2.12}$$

These solutions represent focusing and defocusing field elements (quadrupoles), respectively. The transformation of the initial beam conditions can be described in matrix form:

$$\begin{aligned} M_{QF} &= \begin{pmatrix} \cos\left(l\sqrt{K}\right) & \frac{1}{l\sqrt{K}}\sin\left(l\sqrt{K}\right) \\ -\sqrt{K}\sin\left(l\sqrt{K}\right) & \cos\left(l\sqrt{K}\right) \end{pmatrix}, \\ M_{QD} &= \begin{pmatrix} \cosh\left(l\sqrt{|K|}\right) & \frac{1}{l\sqrt{|K|}}\sinh\left(l\sqrt{|K|}\right) \\ \sqrt{|K|}\sinh\left(l\sqrt{|K|}\right) & \cosh\left(l\sqrt{|K|}\right) \end{pmatrix} \end{aligned} \tag{2.13}$$

with l referring to to the magnetic length of the element. If the focusing is relatively weak (i.e the focal length is significantly larger than the magnetic length l), the thin lens approximation can be used such that l approaches 0 and

$$M_{QF} \approx \begin{pmatrix} 1 & 0 \\ -Kl & 1 \end{pmatrix} \qquad M_{QD} \approx \begin{pmatrix} 1 & 0 \\ +Kl & 1 \end{pmatrix}. \tag{2.14}$$

A sequence of elements including "drifts" can be described as a single transfer matrix, composed of the multiplication of the matrix describing each element. Thus, the evolution of x and x' through such a sequence in the x axis is written as

$$\begin{pmatrix} x \\ x' \end{pmatrix} = M_{transfer} \begin{pmatrix} x_0 \\ x'_0 \end{pmatrix} \tag{2.15}$$

where $M_{transfer}$ is the 2x2 transfer matrix calculated as described. The evolution of x,x',y,y' can clearly be simply captured together in an appropriate 4x4 matrix since a focusing field in x is a defocusing field in y, and vice versa. In many cases (for example, in MAD-X as discussed in Chapter 3), a 6D phase space representation of the initial particle is used, with each beamline element is represented by a 6x6 transfer matrix. Beyond the 4 transverse coordinates described above, the additional elements typically include terms to account for particles which have deviations in energy or longitudinal position. Thus, each element in the beamline can be represented as full 6x6 transfer matrix and again be multiplied together as before, (starting with the furthest downstream element) to create a total transfer matrix designated by R, as in

$$R = M_n M_{n-1} M_{n-2} ... M_1 \tag{2.16}$$

where M_n is the matrix representing the n$^{\text{th}}$ element.

2.1.2 Twiss Parameters

Equation 2.10 can be altered by changing K to a functional form to represent the periodic oscillation of a particle about the reference orbit. K will depend on the displacement of the beam through the system. Thus, in x,

$$x'' + K(s)x = 0. \tag{2.17}$$

This is Hill's equation, where $K(s)$ is a periodic, restoring force. Hill's equation has a general solution

$$x(s) = \sqrt{\beta_x(s) J_x} \cos(\mu_x(s) + \mu_{x,0}) \tag{2.18}$$

where β_x is the beam envelope function, and μ_x is its phase advance from 0 to s:

$$\mu_x(s) = \int_0^s \frac{ds}{\beta_x(s)} \tag{2.19}$$

and J_x and $\mu_{x,0}$ are constants of integration. β is determined by the lattice properties (dipoles, quadrupoles, drifts and element lengths), with x and y components generally assumed to be uncoupled as before. β is the first of the three Twiss parameters, where the others are defined by

$$\alpha = -\frac{1}{2}\beta'(s) \qquad\qquad \gamma(s) = \frac{1 + \alpha^2(s)}{\beta(s)}. \tag{2.20}$$

Differentiating Equation 2.18 and substituting in the Twiss parameters, the expression:

$$J_x = \gamma_x(s)x^2(s) + 2\alpha_x(s)x(s)x'(s) + \beta_x(s)x'^2(s) \tag{2.21}$$

is found, which is constant in the linear approximation. Multiplying J_x by π gives the invariant area of an ellipse traced out in trace space from motion of a particle through multiple passes of the lattice. This trace space ellipse is shown in Figure 2.2.

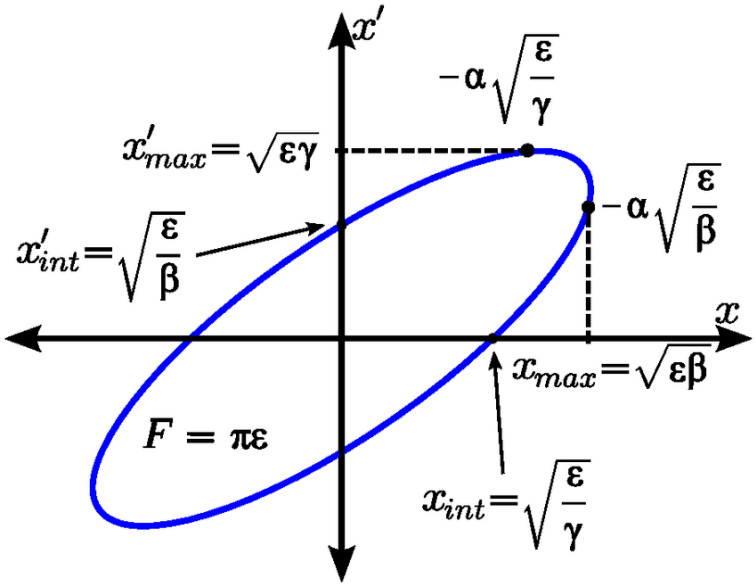

Figure 2.2: x-x' transverse trace space ellipse with invariant area and relationship to Twiss parameters indicated. ϵ equivalent to J_x in Equation 2.21. Image from [179].

2.1.3 Particle Ensembles

The action J is often described as ϵ or the emittance of the beam. The emittance is defined as a statistical property of the ensemble of particles as a whole, rather than a quantity associated with a single particle. The transverse distribution of a beam is often Gaussian, and can be described in this case by the beam matrix:

$$\Sigma = \begin{pmatrix} \sigma_x^2 & \sigma_{xx'} \\ \sigma_{xx'} & \sigma_{x'}^2 \end{pmatrix} = \begin{pmatrix} \langle x^2 \rangle & \langle xx' \rangle \\ \langle xx' \rangle & \langle x'^2 \rangle \end{pmatrix} \tag{2.22}$$

where $\langle\rangle$ designates the variance of the enclosed parameter. The size of a Gaussian beam is often quoted in terms of its standard deviation: σ, given by σ_x in the beam matrix above. The geometrical emittance is the square root of the determinant of the beam matrix Σ, explicitly given by

$$\epsilon_x = \sqrt{\det(\Sigma)} = \sqrt{\langle x^2 \rangle \langle x'^2 \rangle - \langle xx' \rangle^2}. \tag{2.23}$$

The emittance gives a measurement of the characteristic "quality" of the beam, and is invariant barring higher order effects or the actions of non-conservative forces. The beam-size σ in each transverse axis is dependent on the constant emittance and the variable beam envelope β function

$$\sigma_x = \sqrt{\beta_x(s)\epsilon_x}. \tag{2.24}$$

The ensemble of particles will occupy an ellipse in transverse trace space similar to that shown in Figure 2.2 for multiple passes of a single particle, but with the area of the ellipse enclosing exactly 1σ of the particle ensemble. The beam matrix can be represented with Twiss parameters rather than the means and variances of the particles:

$$\Sigma_x = \epsilon_x \begin{pmatrix} \beta_x & -\alpha_x \\ -\alpha_x & \gamma_x \end{pmatrix}. \tag{2.25}$$

If the beam is under acceleration, the emittance ceases to be a constant of the beam profile due to adiabatic damping. For this reason, the normalised emittance

$$\epsilon_{n,x} = \beta_{lorentz}\gamma_{lorentz}\epsilon_x \tag{2.26}$$

may be used where $\gamma_{lorentz}$ and $\beta_{lorentz}$ are the relativistic parameters (not to be confused with the Twiss functions). The normalised emittance is ideally invariant under acceleration, but may change with scattering, collimation or interactions with non-linear magnetic fields as before.

2.2 Practical Considerations for Operation

2.2.1 Quadrupole Scans

An advantage of the use of Twiss parameters to parameterise a certain beam is that they can be experimentally derived at appropriate locations in a beamline. A common method to determine these (and the one which was utilised in the experimental part of this thesis, see Chapter 5) is that of quadrupole scanning. This is also used to measure the emittance. The procedure requires a quadrupole with magnetic length l and strength k_1 as before (focusing or defocusing depending on which transverse coordinate is being studied) and a measurement screen at some distance d from the quadrupole, with which the beam-size σ^{screen} can be measured. As before, it is assumed that the transverse parameters in x are of interest, and as such $k_1 > 0$. The principle is equivalent in y for $k_1 < 0$. The beam matrix evolves with the element transfer matrices described in Section 2.1 as

$$\Sigma_x^{screen} = M\Sigma_x^{init}M^T \tag{2.27}$$

where M is the transfer matrix representing the elements between the reconstruction point and screen, and Σ_x^{screen} and Σ_x^{init} are the beam matrices at the indicated locations in Figure 2.3. For

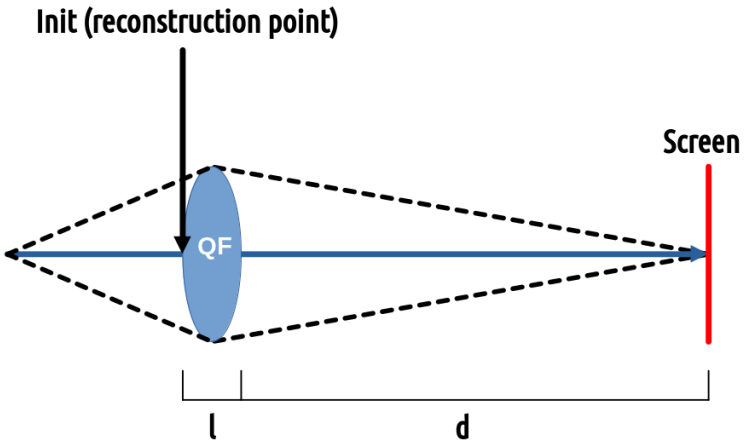

Figure 2.3: Diagram of elements required for quadrupole scan technique, for the case of a focusing quadrupole. Screen and reconstruction point indicated. Labels as used for calculation in Equation 2.29 also shown.

example, in the case shown in Figure 2.3, and using k=k_1 for simplicity, M is given by

$$M = \begin{pmatrix} 1+dkl & d \\ kl & 1 \end{pmatrix} \tag{2.28}$$

when the thin lens approximation is used. During a quad-scan, the strength of the quadrupole is varied such that a beam waist in the appropriate axis is crossed at the screen (α_x=0). Taking just the Σ_{11}=σ_x^2 element from Equation 2.22 for the multiplication in Equation 2.27 and extracting the factors of k, a quadratic equation as a function of the quadrupole strength is found

$$\begin{aligned} \Sigma_{11}^{screen} &= (\Sigma_{11}^{init} d^2 l^2)k^2 + (2dl\Sigma_{11}^{init} + 2d^2\Sigma_{12}^{init})k + \Sigma_{11}^{init} + 2d\Sigma_{12}^{init} + d^2\Sigma_{22}^{screen} \\ &= Ak^2 + Bk + C \end{aligned} . \tag{2.29}$$

Σ_{11}^{screen} can be measured across a range of quadrupole strengths, and a parabola fit through these measurements to determine the parameters A, B and C. The matrix elements of Σ^{init} are then calculated, and the emittance retrieved from Equation 2.23. Twiss parameters can then be derived from comparing the descriptions of the beam matrix in Equations 2.22 and 2.25.

2.2.2 Dispersion

The above relationships hold true and are a good approximation for many applications. Additional effects should however be taken into account - particularly that of the momentum spread of the initial beam. Dispersion is the correlation between momentum spread and transverse position in the beam. Mathematically, Equation 2.2 describing magnetic rigidity can be rewritten as

$$B\rho = B\rho_0\,(1+\delta) = \frac{P_0(1+\delta)}{q} \tag{2.30}$$

where P_0 is the momentum of the reference particles, ρ_0 is bending radius of the reference particle compared to an off-orbit particle with momentum P and bending radius ρ, and $\delta = \frac{P-P_0}{P_0} = \frac{\Delta P}{P_0}$. Taking these considerations into account, the **inhomogeneous** Hill's equation

$$x'' + \left(\frac{1}{\rho^2} + k\right)x = \frac{1}{\rho}\frac{\Delta P}{P_0} \tag{2.31}$$

is derived. The solution to Equation 2.31 is given by a sum of two terms in each axis. Again assuming bending in x, this is

$$x(s) = x_\beta(s) + x_D(s) \tag{2.32}$$

where x_β is the solution to the standard Hill's equation (Equation 2.18) neglecting off-momentum particles, and x_D is an extra deviation term, defined as

$$x_D = D_x(s)\frac{\Delta P}{P_0} \tag{2.33}$$

where $D_x(s)$ is the *dispersion* function in the x axis. Like the Twiss parameters, this dispersion function depends on the structure of the lattice itself rather than the momentum spread, with only the the magnitude of its effect on the beam being dependent on the momentum spread. Dispersion modifies Equation 2.24 to

$$\sigma_x = \sqrt{\epsilon_x\beta_x + D_x^2\frac{\sigma_P^2}{P_0^2}} \tag{2.34}$$

where σ_P is the standard deviation of the beam momentum distribution. Dispersion is often minimised at crucial points in the beamline (for example in particle physics applications, lattices are designed such that it and the beam envelope function are minimised at interaction points). Like the Twiss parameters, it is typically assumed that the dispersion function is decoupled in x and y; thus, Equation 2.34 can be written in the same form for y.

2.3 High Gradient Acceleration and Uniform Beam Generation

As briefly discussed in Chapter 1, much attention at CERN has been based on the development of next-generation colliders. One of those proposed options is a linear lepton collider for increased production and statistics of Higgs bosons. This proposal was named CLIC. CLIC is proposed to be built in three stages, eventually reaching 3 TeV centre-of-mass energy for collisions of positrons and electrons [170].

Reaching these energies in a (relatively) compact space required significant advances in innovations in both acceleration and RF power distribution. CLIC is expected to operate with an RF frequency of 12 GHz (X-band), with structures providing 100 MV m^{-1} accelerating gradient. The required klystrons to provide power to the RF cavities in a typical fashion would be numerous and costly. Thus, the design shown in Figure 2.4 was proposed. This is based upon a novel "drive-beam" system to provide power to the RF-cavities. The drive-beams would be separate, high current accelerators which would accelerate electrons up to 2.4 GeV with RF frequency of 1 GHz, increasing bunch frequency by interleaving bunches through a delay loop and two combiner rings. This beam would then be decelerated to provide power for acceleration of the positrons and electrons in the main CLIC linacs [100].

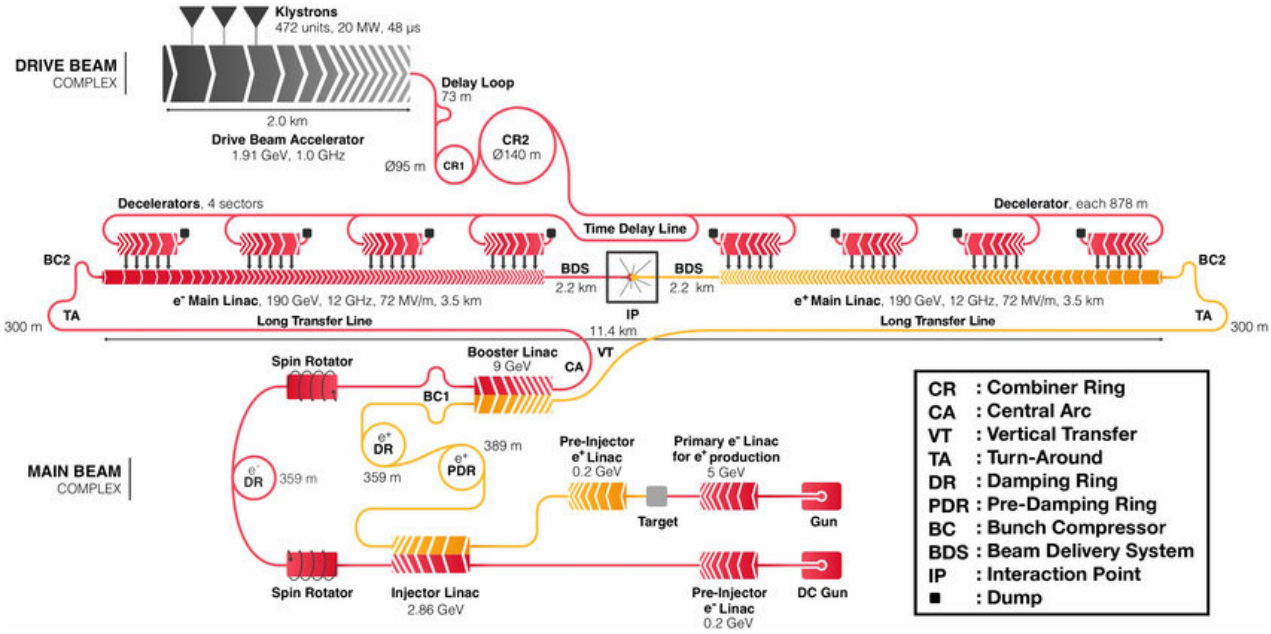

Figure 2.4: Schematic of key components of CLIC, showing drive beam and main beam complexes. Image from [180].

More relevant to the topic of compact acceleration for VHEE therapy are the CLIC X-band accelerating cavities themselves. These are required to sustain the high gradient acceleration of the high current beam, whilst minimising heat buildup and other adverse effects such as surface currents. Thorough optimisations produced solutions of the type shown in Figure 2.4, with a prototype tested to confirm acceleration at a gradient of 100 MeV m^{-1} [181]. The CLIC cavities are normal conducting and composed of copper as shown in Figure 2.5, with the principal design based on a wave-guide damped cell structure to minimise instabilities from transverse wakefields [182]. An alternative to the baseline CLIC cavity is the Damped Detuned Structure, using slot-coupled manifolds to achieve the same [183]. Several considerations are required when translating the advanced,

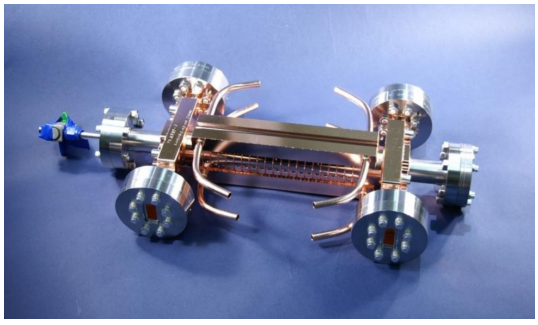

Figure 2.5: Photograph of test 100 MeV m^{-1} CLIC cavity. Image from [181].

high gradient acceleration studied for CLIC techniques to a clinical context. X-band acceleration is favourable due to its high achievable gradients compared to equivalent S or C-band systems. Studies have demonstrated the possibility of developing an X-band linac operational at a high current, capable of delivering UHDR beams (this is often referred to as an Ultra-High Pulse Current

injector (UHPCI)) [184]. There is an ongoing collaboration between CERN, THERYQ and University Hospital of Lausanne (CHUV) in Switzerland to develop a compact accelerator based on this accelerating technology for VHEE FLASH research and treatment [185].

A key assumption made particularly in Chapter 3 of this thesis is that it is feasible for the particle beam before entrance to a transfer line (i.e directly after acceleration) to have a small, **transversely uniform** profile. This would be essential to allow some uniformity to be retained throughout the transfer line without the use of optics of any higher order than quadrupoles. The justification for this is based on recent work on uniform beam generation at a photocathode based electron gun using space-charge forces (caused by the internal interactions of particles inside a bunch) [175]. The initial size and shape of a beam is dependent on its generation in the electron gun, acceleration in RF cavities, and manipulation with optics further downstream. An electron beam in a photo-injector will often have a transversely Gaussian profile, if generated from a Gaussian laser spot. The emittance growth of the beam in the gun originates from 3 principle sources: thermal effects, RF focusing, and space-charge. The space-charge contribution typically dominates, but is compensated for using solenoid magnets [186]. Whilst for most applications the emittance of a particle beam is minimised to preserve beam quality and reduce losses, space-charge forces can alternatively be used to generate uniform beams from a photocathode [187].

When space-charge dominates, the transverse phase-space distribution of the particles will warp in a non-linear fashion, resulting in particles moving outwards from the centre of the beam. This is what would cause the contribution to emittance growth outlined above. An appropriate balancing of the space-charge forces can cause an initially Gaussian beam to transform into a beam with a uniform intensity profile [175]. In a typical photo-injector such as that present at CLEAR, this balance can be achieved by modifying the laser spot size, pulse length, RF gun field strength and laser intensity (charge per bunch). If the space-charge is too high however, the bunch profile may be very diffuse with a sharp peak, or even become “hollow” or double peaked. It has been shown that with an arbitrary setup nevertheless based on generic parameters of the photocathode of an electron gun, a uniform beam profile at the exit of an accelerating structure can be achieved [175]. It was found that the transversely uniform bunches would oscillate through several “uniformity” points, requiring appropriate phase advance to retain uniformity at a defined longitudinal position due to a characteristic “spike” seen in the phase space distributions, shown in Figure 2.6.

This simulated evidence has been strengthened by experiments at CLEAR based upon achieving this uniform beam profile and verifying with intensity measurements on YAG screens [188]. The capability of photocathode based electron accelerators to provide uniform beam profiles has provoked

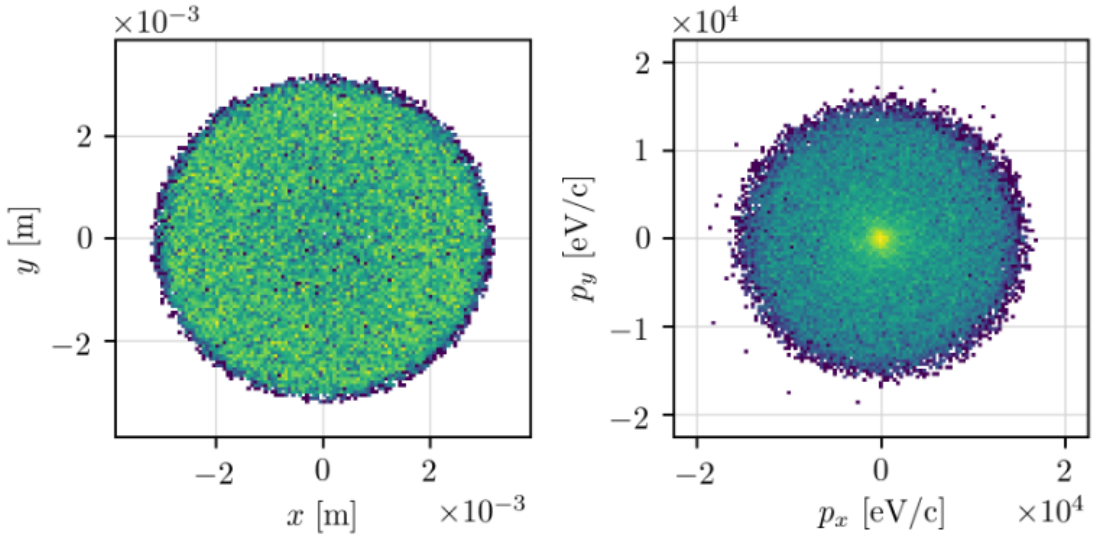

Figure 2.6: Histograms of beam intensity in transverse position (left) and divergence (right) from simulated uniform beam generated from a photocathode. Figure from [187].

a great deal of interest particularly in the VHEE field, as uniform intensity distributions are far preferred for medical applications. Unlike scattering based options, no additional particles would be produced with this method and the uniform profile could be shaped and modified depending on the application or patient. Optimisations and studies of these so-called UHPCIs in the VHEE regime with the capability of providing uniform beam profiles after acceleration are underway at CERN.

2.4 Multiple Coulomb Scattering

2.4.1 Moliere's Fundamental Equations

The second method of uniform beam generation detailed in this thesis is dependent on the scattering of VHEE beams in an appropriately designed system. This section contains a summary of the physical foundation and mathematical model describing Moliere's fundamental theory of multiple Coulomb scattering [189], with derivations as carried out by Bethe [190]. Moliere's theory is based on interactions of a charged particle travelling through a material of arbitrary thickness and density. Bethe begins with the transport equation for $f(\theta, t)$ where $f(\theta, t)\theta d\theta$ are the number of particles within the angular region $d\theta$, after passing through a medium of length t.

$$\partial f(\theta, t)/\partial t = -N f(\theta, t) \int \sigma(\chi)\chi d\chi + N \int \int f(\theta', t)\sigma(\chi) d\zeta. \tag{2.35}$$

$\sigma(\chi)\chi d\chi$ is the differential cross section for scattering into the angular interval χ, N is the number of scattering atoms per cm^3, θ' is the vector representing the direction of the particle before the

previous scatter, and $d\zeta = \chi d\chi d\phi/2\pi$, with ϕ representing the azimuth of vector ζ. Equation 2.35 is equivalent to a transport equation for diffusion [191], and assumes that all angles involved are small such that sin functions can be replaced by their argument. Moliere uses Hankel and Fourier transformations of $f(\theta, t)$ and Equation 2.35 respectively to eventually yield

$$\partial g(\eta, t)/\partial t = -Ng(\eta, t) \int_0^\infty \sigma(\chi)\chi d\chi[1 - J_0(\eta\chi)] \tag{2.36}$$

where $g(\eta, t)$ is the transformed $f(\theta, t)$, J_0 is the Bessel function of the first kind and η is the transformed variable. Carrying out the integration and using

$$\Omega(\eta) = Nt \int_0^\infty \sigma(\chi)\chi d\chi J_0(\eta\chi) \tag{2.37}$$

yields

$$g(\eta, t) = e^{\Omega(\eta)-\Omega_0} \tag{2.38}$$

where Ω_0 is $\Omega(0)$ - the total number of collisions. Finally, this is substituted into the Hankel transform of $f(\theta, t)$:

$$f(\theta, t) = \int_0^\infty \eta d\eta J_0(\eta\theta) e^{-Nt\int_0^\infty \sigma(\chi)\chi d\chi[1-J_0(\eta\chi)]}. \tag{2.39}$$

This equation is valid, irrespective of the specific scattering law or cross-section utilised, assuming that the angles in question are small. The only assumption for σ required until the calculation of the screening angle χ_a is that at large scattering angles, the shape tends towards the Rutherford single scattering cross section: that is, σ is proportional to χ^{-4}.

2.4.2 Moliere's Transformed Equation

Several characteristic angles define the Moliere distribution, dependent on the initial beam and scatterer qualities. Firstly, χ_0 is defined by

$$\chi_0 = \frac{\lambda}{2\pi a} = \frac{\lambda}{5.560 a_0 Z^{-1/3}} \tag{2.40}$$

where a is the Fermi radius, a_0 is the Bohr radius, Z is the atomic number and λ is the de Broglie wavelength of the electron. This represents the maximum limit in angle where the scattering cross section σ can be treated as decreasing simply with χ^{-4}. The second crucial parameter is χ_c, is given by Moliere [189]:

$${\chi_c}^2 = 4\pi N_A t\rho e^4 Z(Z+1)z^2/(Pv)^2 \tag{2.41}$$

where t is the thickness of the material in cm, ρ is the density in g cm^{-3}, N_A is Avogadro's number, a is the molar mass, e is Coulomb's constant, z is particle charge, and P and v are particle momentum and velocity respectively. χ_c is the minimal angle caused by a single scatter in a material (interpreted by Bethe as "The physical meaning of χ_c, is that the total probability of single scattering through an angle greater than χ, is exactly one").

χ_a is the final characteristic parameter. This must be calculated using the chosen cross section σ for the specific application. Here $N = \frac{\rho}{a}N_A$ is used for simplicity. These latter two parameters characterise multiple coulomb scattering. The critical angle χ_c is related to the thickness of the material and defines the minimum angle after a single scatter throughout the medium. The screening angle χ_a defines the angle within which scattering will be reduced to the atomic screening. Moliere's fundamental equation can be recast:

$$Nt\sigma(\chi)\chi d\chi = 2\chi_c^2 \chi d\chi q(\chi)/\chi^4 \tag{2.42}$$

where $q(\chi)$ is the ratio of Rutherford scattering to true scattering. Inserting this into previous equations, the transformed scattering distribution can be expressed as:

$$-\ln(g(\eta,t)) = \Omega_0 - \Omega(\eta) = 2\chi_c^2 \int_0^\infty \chi^{-3} d\chi (1 - J_0(\chi\eta))q(\chi) \tag{2.43}$$

The integral can be solved by separation at some angle k, where

$$\chi_0 << k << 1/\eta \approx \chi_c \tag{2.44}$$

since from k to infinity, $q(\chi) \approx 1$ (this is equivalent to the previous statement that σ must tend to the Rutherford cross section at high angles). For the lower part of the integral, from 0 to k, J_0 is small and thus, a Taylor expansion can be made of $1 - J_0$. χ_a is now defined:

$$-\ln(\chi_a) = \lim_{\chi\to\infty} \int_0^k q(\chi)d\chi/\chi + 0.5 - \ln(k) \tag{2.45}$$

The two integrals are then solved, substituting the results into Equation 2.43 and utilising

$$b = \ln\left(\frac{\chi}{\chi_a}\right)^2 + 1 - 2C \equiv \ln\left(\frac{\chi_c}{\chi_a'}\right)^2 \tag{2.46}$$

where C is Euler's constant, to get

$$\Omega_0 - \Omega(\eta) = 0.25y^2(b - \ln(0.25y^2)). \tag{2.47}$$

where $y = \chi_c\eta$. Finally, using the identity $\theta/\chi_c = \lambda$ and inserting Equation 2.47 into Equation 2.38 and returning to the original Hankel transform of f, Moliere's transformed equation is found:

$$f(\theta)\theta d\theta = \lambda d\lambda \int_0^\infty y dy J_0(\lambda y) exp(0.25y^2(-b + \ln(0.25y^2)) \tag{2.48}$$

2.4.3 Moliere's Functions

For calculation of this integral, b and thus χ'_a, the alternative form of the screening angle χ_a as implicitly defined in Equation 2.46, can now be evaluated. This can be carried out with any chosen potential. Numerically, Moliere calculated this as

$$\chi_a'^2 = 1.167\chi_0^2(1.13 + 3.76\alpha^2). \tag{2.49}$$

where α is the fine-structure constant, using a Thomas-Fermi potential. From the definition of b in Equation 2.46, and folding in the definition of χ_c in Equation 2.41, one obtains

$$b = \ln\left(\frac{\chi}{\chi'_a}\right)^2 = \frac{6680t\rho}{\beta^2_{lorentz}} \frac{(Z+1)Z^{1/3}z^2}{A(1+3.34\alpha^2)}. \tag{2.50}$$

For the final evaluation of the transformed equation

$$B - \ln(B) = b \tag{2.51}$$

is used for compactness, which must be solved numerically. ϑ is then defined:

$$\vartheta = \lambda B^{-1/2} = \frac{\theta}{\chi_c B^{1/2}}. \tag{2.52}$$

Bethe uses a simplified notation to remove repeated powers of ϑ; here, this is not done for the sake of clarity. The equation is expanded in a power series of $1/B$, allowing the final functional form of Moliere's Probability Density Function (PDF) $f(\theta)$ to be given as a sum of terms $f^n B^{-n}$ The first of these is simple, representing a Gaussian contribution:

$$f^{(0)} = 2e^{-\vartheta^2} \tag{2.53}$$

The second, accounting for hard single scatters in the distribution is given by

$$f^{(1)} = 2e^{-\vartheta^2}(\vartheta^2 - 1)(\mathrm{Ei}(\vartheta^2) - \ln\left(\vartheta^2\right) - 2(1 - 2e^{-\vartheta^2})) \tag{2.54}$$

where Ei is the exponential integral, defined as

$$\mathrm{Ei}(x) = \int_{-\infty}^{x} \frac{e^{\tau}}{\tau} d\tau \tag{2.55}$$

where τ is an arbitrary variable. This is available in Python in the Scipy.special library for computation, if desired. The final of the 3 contributions to the PDF described by Bethe is $f^{(2)}$, representing a typically small correction. Bethe gives this in the form

$$\begin{aligned} f^{(2)} = 4e^{-\vartheta^2}([\Psi^2(2) + \Psi'(2)](\vartheta^4 - 4\vartheta^2 + 2)+ \\ \int_0^1 t^{-3}dt[\ln(t/(1-t)) - \Psi(2)][(1-t)^2 e^{\vartheta^2 t})- \\ 1 - (\vartheta^2 - 2)t - (0.5\vartheta^4 - 2\vartheta^2 + 1)t^2] \end{aligned} \tag{2.56}$$

where Ψ and Ψ' are the *digamma* and *trigamma* functions respectively. Moliere [189] gives the same equation as

$$\begin{aligned} f^{(2)} = 2e^{-\vartheta^2}([\Psi^2(2) + \Psi'(2)](\vartheta^4/2 - 2\vartheta^2 + 1)+ \\ 2\int_0^1 t^{-3}dt[\ln(t/(1-t)) - \Psi(2)][(1-t)^2 e^{\vartheta^2 t}- \\ 1 - (\vartheta^2 - 2)t - (0.5\vartheta^4 - 2\vartheta^2 + 1)t^2]) \\ = 4e^{-\vartheta^2}([\Psi^2(2) + \Psi'(2)](\vartheta^4/4 - \vartheta^2 + 0.5)+ \\ \int_0^1 t^{-3}dt[\ln(t/(1-t)) - \Psi(2)][(1-t)^2 e^{\vartheta^2 t}- \\ 1 - (\vartheta^2 - 2)t - (0.5\vartheta^4 - 2\vartheta^2 + 1)t^2]). \end{aligned} \tag{2.57}$$

Equation 2.56 and Equation 2.57 are not equal, with a clear factor of 4 difference in the pre-integral term between both. The tables given by Moliere and improved by Bethe are only retrieved when Moliere's Equation 2.57 is used (Bethe's equation produces entirely different values). Hence, this is taken as the correct one. This discrepancy was also noted in a 1985 review of MCS by Devaney [192]. The *polygamma* functions can also be found in the Scipy library of Python, although one should note that they are defined slightly differently here (in Python, the argument is taken to be n rather than $n + 1$ as in Moliere and Bethe's use of the functions). Thus, the arguments in each polygamma function in the above and following equations should be increased by 1.

Bethe solves the integral in Equation 2.57 using a power series to infinity in ϑ:

$$I = \sum_{0}^{\infty} \frac{1}{n+1}[\Psi(n) + C - \Psi(2)] \left[\frac{x^{n+3}}{(n+3)!} - \frac{2x^{n+2}}{(n+2)!} + \frac{x^{n+1}}{(n+1)!} \right]. \tag{2.58}$$

With the above, values of each function across for a certain angle can thus be found. Many papers simply take the values of these from Bethe's table directly; for some purposes one may wish to evaluate directly for a certain angle however. The sum in Equation 2.58 need not be solved numerically, and indeed converges rather rapidly for most values of ϑ, as shown in Figure 2.7. Alternatively,

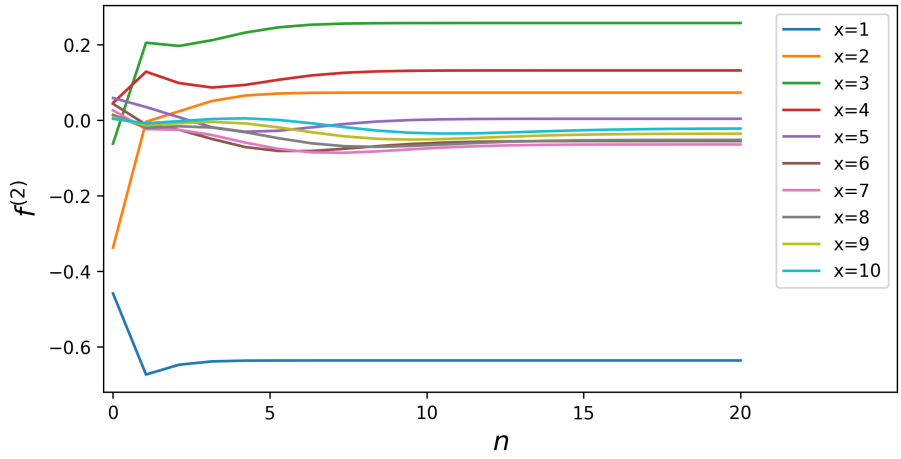

Figure 2.7: $f^{(2)}$ value from Equation 2.57 derived from replacement of integral with Equation 2.58, as function of summing index n in this equation. Shown for different values of $x \equiv \vartheta^2$ with coloured lines.

Equation 2.57 itself can be numerically integrated, but this deviates only very minimally from the power series evaluated up to a reasonable sum n and is computationally more expensive. For most applications, a Gaussian approximation to Moliere's Theory of Multiple scattering is used [193]. This neglects the non-Gaussian tails of the Moliere PDF, but is nevertheless satisfactory for the vast majority of applications. It is more precise to use this rather than just taking the Gaussian contribution ($f^{(0)}$) of the full Moliere function, and is far simpler to implement than the full formalism. It is given by:

$$\theta_{rms} = \frac{13.6\,\text{MeV}}{\beta_{lorentz} cP} z \sqrt{\frac{x}{X_0}} \left(1 + 0.038 \ln \left(\frac{tz^2}{X_0 \beta_{lorentz}^2} \right) \right) \tag{2.59}$$

where z is particle charge (=1 for electrons), t is the longitudinal material thickness, X_0 is the material radiation length, P is the particle momentum and $\beta_{lorentz}$ is the relativistic parameter [193] once again. This equation was taken from a fit to the full Moliere functions described above, with the scattering contribution to divergence added in quadrature to that of the angular distribution before scattering. As it is taken from a fit to the full, physically justified formalism, the dependences on scatterer geometry and initial beam energy are effectively the same for this approximation, but

expressed in different forms. An inverse linear dependence on the energy is evident, with a broadly proportional and inverse proportionality to the square root of material thickness and radiation length of material, respectively.

The logarithmic term in Equation 2.59 is often small and is sometimes neglected in scattering implementations; this has been found to produce anomalies and discrepancies during the work of this thesis however, so it is recommended that this term is not neglected where possible (especially since Equation 2.59 is already an approximation to the more accurate Moliere functions). There is clearly a scenario where the ln term **must** be neglected however. If t is sufficiently small, a negative angle will be produced, which is unphysical. For the case of a highly relativistic beam, this occurs when

$$\frac{t}{X_0} \approx 4 \times 10^{-12} \tag{2.60}$$

at which point the material is so thin that scattering would be minimal, as would the be the loss of accuracy from neglecting the ln term.

2.5 VHEE Particle Production

Section 2.4 describes the principle effects of passing through matter on the particle beam itself, assuming that the MCS is the dominant interaction. It only describes the statistical widening of the particle beam. The Moliere distribution does not describe the resultant energy spread of the beam or handle the deposited energy (dose) in the material. Beams in the VHEE regime undergo numerous inelastic interactions which result in scattering and particle production. These are fully modelled in MC simulations, with these interactions in scattering materials and patient tissues being particularly relevant for the studies of Chapter 4. Bremsstrahlung is the dominant photon emission mechanism in the VHEE regime, although ionisation and collisions with free electrons are also predicted at the lower end of the regime. The Bremsstrahlung cross-section equation for highly relativistic electrons in the VHEE regime is given by:

$$\begin{aligned}\frac{d\sigma}{dk} = \frac{2Z^2 r_0^2}{137}\frac{1}{k}\Bigg(\left(1+\frac{E^2}{E_0^2}-\frac{2E}{3E_0}\right)\left(\ln M(0)+1-\frac{2\arctan(b)}{b}\right)+ \\ \frac{E}{E_0}\left(\frac{2}{b^2}\ln\left(1+b^2\right)+\frac{4(2-b^2)}{3b^3}\arctan(b)-\frac{8}{3b^2}+\frac{2}{9}\right)\Bigg)\end{aligned} \tag{2.61}$$

where E_0 is the beam energy, k is the energy of the radiated photon, and r_0 is the classical electron radius. $b = \frac{2E_0 E Z^{1/3}}{111k}$, $M(0) = (\frac{k}{2E_0E}^2 + \frac{Z^{1/3}}{111}^2)^{-1}$ and $E = E_0 - k$. Equation 2.61 is quoted as being accurate to around 2% for electrons in the VHEE regime [194]. Figure 2.8 displays the

Bremsstrahlung cross section as a function of the fractional photon energy in the VHEE for initial beams between 50 MeV to 250 MeV. The form of this cross section demonstrates that the lower energy photons from the spectrum dominate. The spectrum will span from close to the initial beam energy to zero. Thus, energy losses from the photons across this entire spectrum will also contribute to the dose distribution.

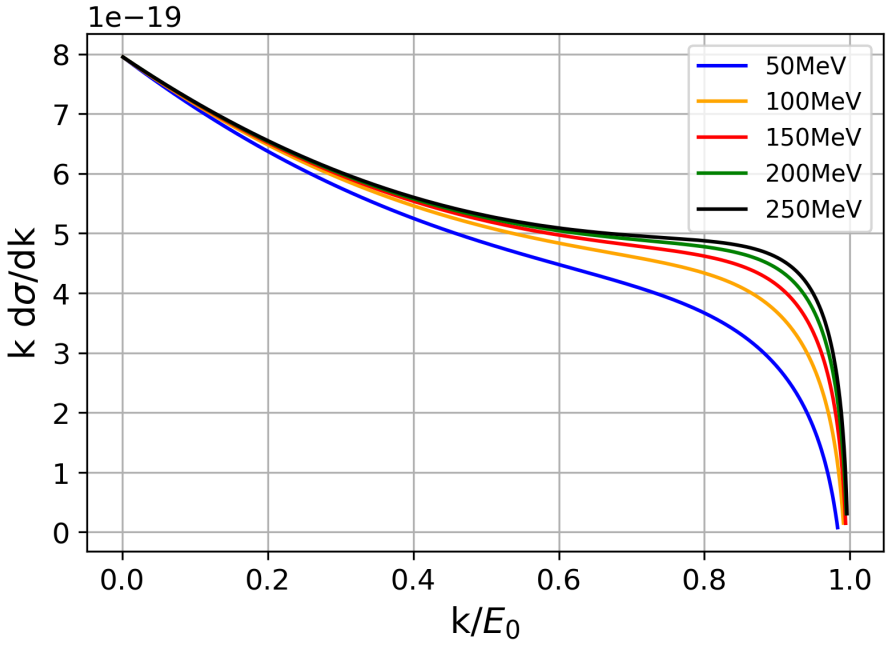

Figure 2.8: Bremsstrahlung photon production cross section in lead against fractional photon energy for different beam energies across VHEE regime, indicated by colour. Generated from Equation 2.61.

The cross sections for several processes of photon energy loss for a 1 MeV beam in water are shown in Figure 2.9. Pair-pair production (shown as κ) is the dominant process for the higher energy photons, with Compton and Rayleigh scattering dominating at lower energies. As such, some dose originating from secondary electrons and positrons is expected from VHEE beams. In the case of passage through high-Z materials such as scattering foils or collimators, it is shown in Figure 2.9 that some of the photons from Bremsstrahlung may fall within the regime of the Giant Dipole resonance [196, 197]. Thus, neutron production in the VHEE regime may be of some concern, and has been studied to some extent in the literature [198].

2.6 Functions for Uniform Beam Optimisation

Throughout this thesis, the common aim is to generate a beam with a transverse uniform component at the position of measurement (patient or tumour location). For the purposes of optimising and designing systems to achieve this aim, flattened transverse beam distributions were quantified, mod-

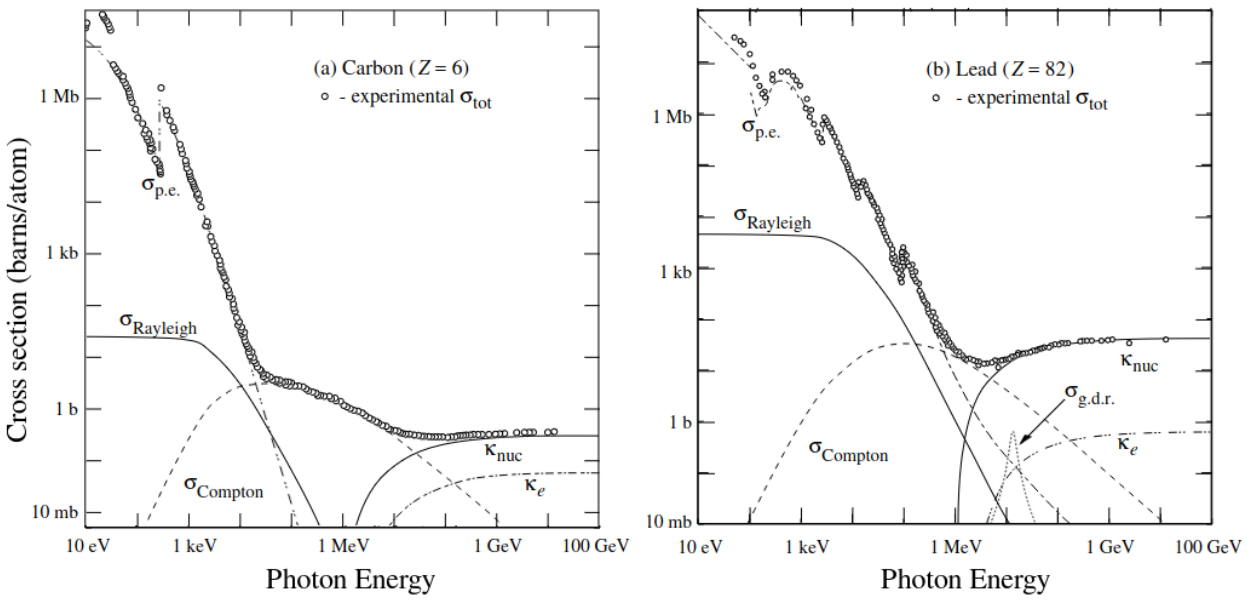

Figure 2.9: Theoretical interaction cross sections for photons against energy in carbon (left) and lead (right), with experimental data indicated as circular data markers. Contributions from relevant processes highlighted. κ_{nuc} and κ_e refer to nuclear and electron pair-production, respectively. Giant dipole resonance highlighted in right-hand diagram. Figure adapted from [195].

elled and fitted for characterisation. This was generally done in preference to direct measurements of beam intensity since these would be more dependent on statistical fluctuations unless extremely large simulations were carried out. One such quantity for measuring the overall uniformity of a distribution is the kurtosis [199]. This is the the fourth central statistical moment, defined for a 1D distribution in x as

$$\text{kurtosis} = \text{E}\left[\frac{(x-\mu)^4}{\sigma^4}\right] \tag{2.62}$$

where E[] designates the expectation value of the enclosed parameter, μ is the mean of the distribution and σ is the standard deviation. For the remainder of this thesis, μ and its orthogonal components $\mu_{x,y}$ are used for the mean of 2D statistical distributions, rather than the earlier definition in Section 2.1 for phase advance. Conversely, σ and its orthogonal components $\sigma_{x,y}$ remain the same as their earlier definitions. Kurtosis describes the "tailedness" of a distribution. A 2D uniform density distribution has a kurtosis of 2, distinct from the 2D Gaussian function (Equation 2.63), which has a kurtosis of 3. It can thus be used to characterise the uniformity of the beam during an optimisation process, and was used as such in Chapter 3. However, kurtosis as a single measurement does not entirely characterise a beam - a ringed distribution with large tails for example may have the same measured kurtosis as a uniform distribution. The quartic dependence of the kurtosis on the transverse positions of the particle ensemble can result in rather high sensitivity to erratic particles extending far from the beam core. Both of these effects were found to significantly hamper

kurtosis-based optimisations, especially during the work for Chapter 4. Thus, fitting based methods of characterising these beams were developed for this purpose and for characterising changes in beams with transversely uniform components.

Gaussian fits regularly utilised for beam characterisation are insufficient to describe uniform beams - the regular Gaussian function can however be generalised to the "super-Gaussian" for this purpose. Care must be taken when comparing the different beam models, particularly in relation to the description of the beam size. The functional form of the 2D Gaussian used to model a typical beam is:

$$f(x,y) = A\exp\left[-\left(\frac{(x-\mu_x)^2}{2\sigma_x^2} + \frac{(y-\mu_y)^2}{2\sigma_y^2}\right)\right] \tag{2.63}$$

where the centre is given by (μ_x, μ_y) and A is the amplitude of the distribution. If a symmetrical beam is assumed, $r^2 = x^2 + y^2$, $\sigma^2 = \sigma_x^2 + \sigma_y^2$ and the PDF is given by

$$p(r) = \frac{1}{2\pi\sigma^2}\exp\left[-\frac{r^2}{2\sigma^2}\right]. \tag{2.64}$$

This can then be integrated between 0 and σ:

$$p(r<\sigma) = \frac{1}{2\pi\sigma^2}\int_0^{2\pi} d\theta \int_0^{\sigma} \exp\left[-\frac{r^2}{2\sigma^2} r dr\right] \tag{2.65}$$

where θ is the angular coordinate, with $d\theta$ integrating to 2π due to symmetry. Integrating the exponential term yields:

$$p(r<\sigma) = \frac{1}{\sigma^2}\sigma^2 - \frac{1}{\sqrt{e}} = 0.393. \tag{2.66}$$

Thus, 1σ encapsulates approximately 39% of the total beam. A Gaussian function can be modified to a super-Gaussian function by including an additional power term P in the standard equation:

$$f(x,y) = A\exp\left[-\left(\frac{(x-\mu_x)^2}{2\sigma_x^2} + \frac{(y-\mu_y)^2}{2\sigma_y^2}\right)^P\right]. \tag{2.67}$$

This super-Gaussian has a uniform component around the mean, with Gaussian tails. The width of the uniform top is dependent on P; at $P = 1$ a regular Gaussian is retrieved, whilst the function becomes uniform when P becomes large. Figure 2.10 displays several examples of super-Gaussian profiles with P=1, 2 and 5. The proportion of particles enclosed within a certain radius e.g σ for a beam modelled by a super-Gaussian function is slightly more complex than the regular Gaussian case, and is dependent on P. Again assuming a symmetrical beam once again and changing

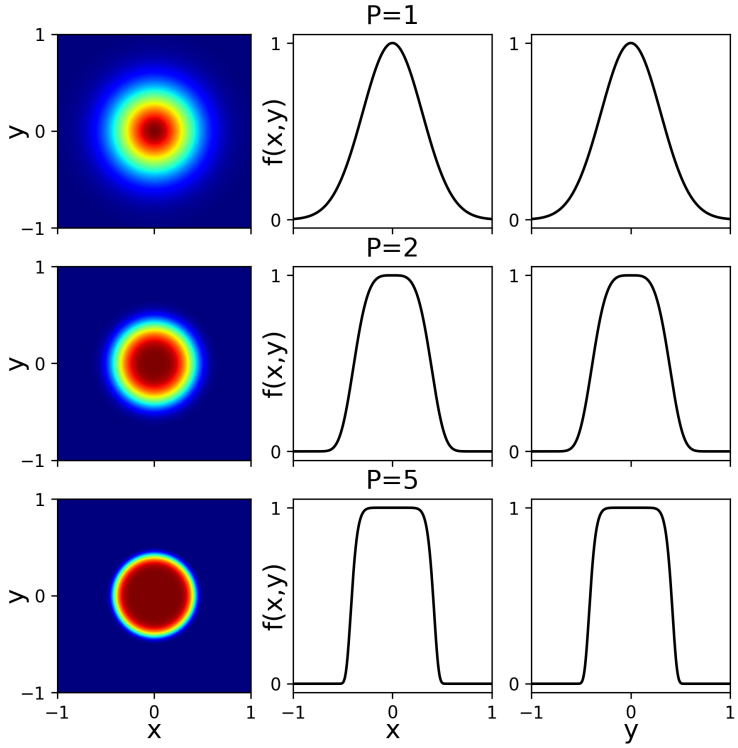

Figure 2.10: Value of normalised shaped and super-Gaussian function of Equation 2.67 in 2D (left) and 1D against x (middle) and y (right). Power term of 1 (top), 2 (middle) and 5 (bottom).

coordinates, the PDF for the super-Gaussian distribution is

$$p(r) = \frac{P}{2\pi\sigma^2\Gamma(P^{-1})} \exp\left[-\frac{r^2}{2\sigma^2}\right] \tag{2.68}$$

where Γ is the Gamma function, the functional form of the factorial operator. Thus, the relationship between σ and the enclosed particles found by taking the integral of Equation 2.68:

$$p(r < \sigma) = \left(1 - \frac{\Gamma_{inc}(P^{-1}, 2^{-P})}{\Gamma(P^{-1})}\right) = C(s, x) \tag{2.69}$$

where Γ_{inc} is the incomplete Gamma function and $C(s, x)$ is the cumulative density function of the gamma distribution with scale 1 and shape s. The proportion of particles within 1σ varies with P; this is no longer a constant parameter. Thus, for this new function, a more useful parameter than σ can be used: the uniform radius. This can be defined for arbitrary uniformity conditions:

$$r_{100F} = \sigma\sqrt{2}\left(-\ln\left(F\right)\right)^{1/2P} \tag{2.70}$$

where r_{100F} is the radius at which point the beam intensity drops below a fraction F of its maximum value. Throughout this thesis, the uniform radius is generally defined as the radius with less than 10% large-scale variation (also described as r_{90}). Thus, the r_{90} can be found for the super-Gaussian

function by simply setting F to 0.9 in Equation 2.70, which yields

$$r_{90} = \sigma\sqrt{2}\left(-\ln 0.90\right)^{1/2P}. \tag{2.71}$$

Ideally, a 2D function would exist which would allow differing powers in each transverse axis to allow asymmetries in uniformity to be modelled. However, no such 2D function could be found for the studies of this thesis. Separating P into x and y components returns a rectangular super-Gaussian function; this may be useful for some other purposes, but not for this work.

Several further generalisations of the super-Gaussian were studied and used for fitting of distributions in subsequent chapters. The super-Gaussian function can be modified with a "tilt" parameter, creating a gradient (linear increase in value across the flat top) across either x or y. This may be a negative or positive gradient depending on its sign. This tilted super-Gaussian function is

$$f(x,y) = A\exp\left[k_x x + k_y y - \left(\frac{(x-\mu_x)^2}{2\sigma_x^2} + \frac{(y-\mu_y)^2}{2\sigma_y^2}\right)^P\right] \tag{2.72}$$

where $k_{x,y}$ are the tilt parameters. The gradient on the slope of the tilted function can be found by Taylor expanding Equation 2.72, and is given by

$$m(x << \sigma_x) = Ak_x \qquad\qquad m(y << \sigma_y) = Ak_y \tag{2.73}$$

in the x and y axes, respectively. A final extension to the super-Gaussian equation here is the addition of a shaping parameter. This introduces either a ring (double peak in 1D) or rounding of the flat top, which were characteristics commonly seen during the dual-scattering studies of Chapters 4 and 5. This most general fitting function including the above is given by

$$f(x,y) = A\exp\left[h_x x^2 + h_y y^2 + k_x x + k_y y - \left(\frac{(x-\mu_x)^2}{2\sigma_x^2} + \frac{(y-\mu_y)^2}{2\sigma_y^2}\right)^P\right] \tag{2.74}$$

where $h_{x,y}$ are the shape parameters, with the effects of these in conjunction with the skew parameters $k_{x,y}$ shown in Figure 2.11. Equation 2.74 can be used to model and describe relevant parameters of beams with various transverse distributions. The large number of variables (10) may cause issues in fitting and optimisation; as such, various constraints may be imposed whilst using the function. For example, assuming a centred and spatially symmetical beam reduces the number of variables to 6. Placing appropriate constraints upon the h and k parameters may also be appropriate, as these can produce extreme functions at high magnitudes. Throughout this thesis, fitting was typically

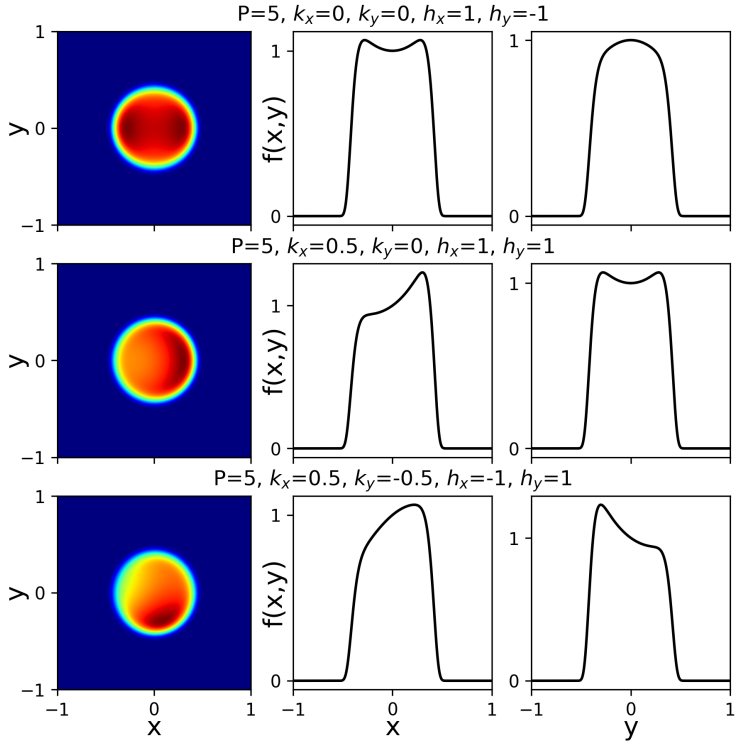

Figure 2.11: Value of normalised super-Gaussian function of Equation 2.74 in 2D (left) and 1D against x (middle) and y (right). Different P, $k_{x,y}$ and $h_{x,y}$ parameters indicated for top, middle and bottom rows.

carried out using the above functions in 1D along thin slices across the transverse beam profiles. This increased the speed and accuracy of the fitting process, since this reduced the number of free variables per fit.

2.7 Summary

Particles in a beamline or accelerator can be focused with a combination of linear elements, and their transverse motion through the system described with harmonic motion. The effect of the elements on the particles in terms of the position and angle of motion can be calculated through successive matrix multiplication of the particle vectors. The transverse axes can typically be considered decoupled, such that motion in x and y can be treated separately. The beam as an ensemble of particles can be described using the Twiss parameters α, β and γ, along with the emittance ϵ, which is a constant assuming only linear magnetic effects and the absence of non-conservative forces (in the case of acceleration, the normalised emittance ϵ_n is constant). Scattering foils or collimation will cause the emittance to increase and decrease, respectively. The ensemble can also be described using the beam matrix Σ, containing the statistical quantities of the particles in phase-space. Off-momentum particles may give rise to so-called "chromatic" effects, which may be characterised by the dispersion

function. The Twiss parameters and emittance of a particle beam can be experimentally measured using the quadrupole scan technique; this is also dependent on the dispersion.

Production of VHEE beams in compact linacs is now feasible due to advances in normal-conducting X-band technology. Recent studies have shown that photocathode based accelerators with appropriate focusing and laser shaping are capable of harnessing space-charge effects to produce beams with transversely uniform beam intensity profiles. So-called UHPCIs may be capable of providing accelerated uniform beams in the VHEE regime at a sufficiently high current for FLASH radiotherapy. The uniformity of such beams can be described using the beam kurtosis, a measurement of the "tailedness" of a distribution. Alternatively, uniform beams or flat-topped beams with Gaussian tails can be modelled using super-Gaussian functions. In this case, it is more useful to describe the beam-size as the uniform portion within a certain limit rather than σ as with typical Gaussian distributions. The super-Gaussian function can be easily extended to model asymmetrical, rounded or ringed distributions, which may be useful for numerous applications.

3 Optics Studies for a Novel VHEE Gantry

3.1 Introduction

3.1.1 The GaToroid Concept

Few treatments in conventional or particle therapy take place without some form of multi-angle delivery. Inducing the FLASH effect from multiple directions could provide improved outcomes from a combination of the differential response as well as tumour conformality. As discussed in Chapter 1, the exact time structure and required dose composition for the triggering of the FLASH effect is unknown. An ideal solution would be to bypass the concerns in time structure by delivering an entire treatment from multiple directions within the FLASH timescale of 0.1 s. This would be impossible for a standard, mechanically rotating gantry, requiring a more novel solution.

Such a solution has been presented: GaToroid [200]. This concept is based on toroidal magnets, exploiting their circular symmetry to provide treatment from multiple angles with an entirely static gantry. The original concept was developed with the purpose of providing proton and heavy ion therapy, and is shown in Figure 3.1. The path of a beam in the GaToroid system is dependent on

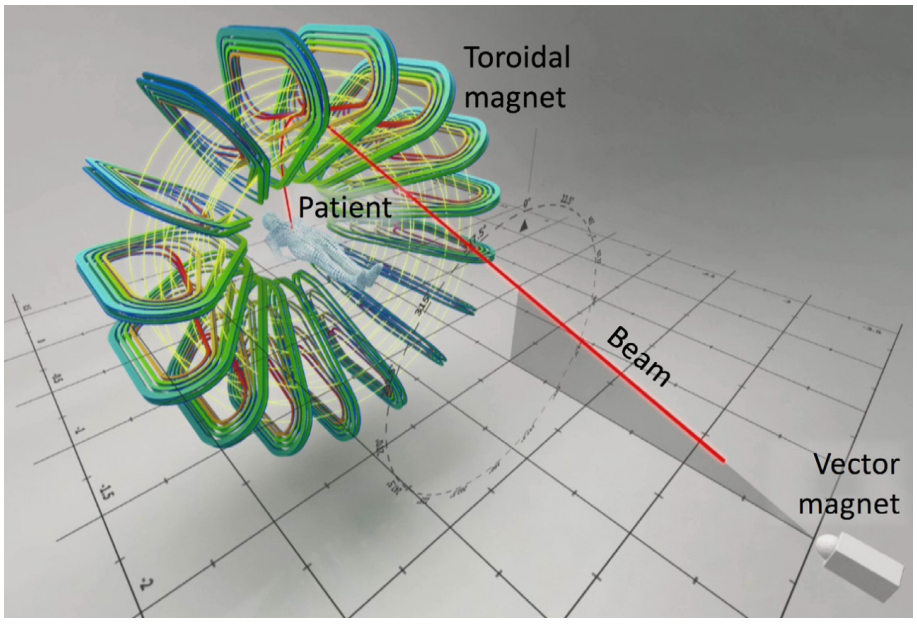

Figure 3.1: Original hadron GaToroid concept, showing initial kicker magnet and bending toroid with patient at system isocentre. Image from [200]

an initial kicker magnet at the entry of the gantry beamline. This would be a "vector" magnet with dipole fields in both x and y to allow a full 2π angular range of kick. This magnet would direct the initial beam along one of several paths towards a large toroidal magnet situated around the *isocentre* (patient position). The toroid would include gaps at each defined angle in which the beams would be bent towards the patient for delivery. The original concept was developed assuming the use of pencil beam scanning with the vector magnet across the tumour. The timescale would only be dependent on the frequency of the oscillating vector magnet, requiring no mechanical moving parts or adjustments during treatment. The research into the specifics of this vector magnet is ongoing.

The GaToroid concept could allow beams to be delivered from multiple angles within a FLASH timescale. Beam tracking studies have been carried out to assess and confirm the required beam parameters and distribution at the patient for the proton GaToroid [201], along with magnetic studies of the toroid itself [202]. Additionally, a small-scale GaToroid demonstrator was designed [203] for experimental testing of the concept, and feasibility studies were carried out for an extension to carbon therapy [204]. Even without the FLASH effect, such a static gantry could be beneficial in reducing beamline misalignment during motion, as well as the costs from operation of a dynamic gantry. The constraints on the vector magnet could be lessened by adding an additional toroidal dipole to "magnify" the initial kick [200], bending the initial beam outwards such that the required strength of the vector magnet to direct the beam would be lessened. The original concept would exploit a large energy acceptance for the positioning and production of the typical SOBPs used in particle therapy [202]. The high rigidity of the hadrons would require superconducting magnets to prevent a gantry with an extremely large radius from being required. Such a system would still be expensive to build and operate, adding to the already considerable cost of hadron acceleration discussed in Chapter 1. This system would also depend heavily on the precision of the vector magnet, due to the reliance upon it for scanning within each delivery direction. The energy modulation would have to be rapid, and the changing rigidity accounted for by the vector magnet.

3.1.2 VHEE GaToroid and Aim

A more cost effective system was proposed: e-GaToroid. This system would be designed for use with 200 MeV VHEE beams rather than hadrons, thus allowing the system to be a similar transverse size to the original concept but using normal conducting magnets due to the reduced magnetic rigidity. This would allow flexibility to include magnetic components for beam manipulation between the vector magnet and toroidal bend. A visualisation of the e-GaToroid concept is shown in Figure 3.2. The first of these is the "magnification" or "septum" toroidal dipole briefly outlined

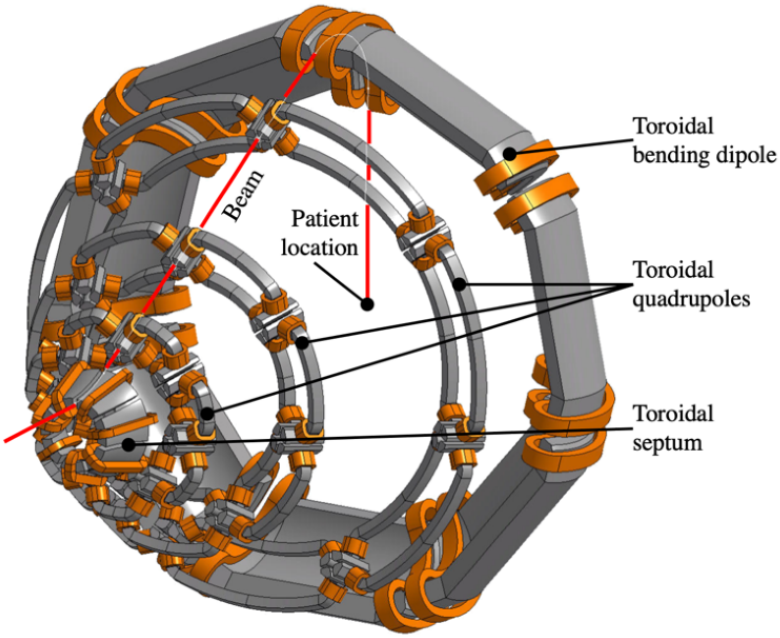

Figure 3.2: Conceptual visualisation of e-GaToroid, demonstrating toroidal lattice elements, patient location at isocentre, and beam travelling through one of 7 defined paths. Image from [205].

in Section 3.1.1, which would increase the distance between the beamline and axis of symmetry after the initial kick. Thus, the requirements on the strength of the vector magnet could be reduced and/or the system as a whole made more longitudinally compact. This would be followed by three novel, circularly symmetric toroidal quadrupoles for beam manipulation. These would be used to produce a large beam at the isocentre rather than relying upon the vector dipole for scanning, again simplifying its requirements for use within the FLASH timescale. e-GaToroid would retain the circularly symmetrical and static characteristics of the hadron GaToroid. Initial studies have assumed a system with seven beamlines to allow sufficient space and margin for error in magnetic designs of the system [205].

Each ideal magnified beam at the isocentre would be uniform. Collimation could be used to retain only a small component of a Gaussian beam (for example, only the central portion with better than 10% uniformity), but this would result in low overall transmission through the system - a particular concern for FLASH. These losses would also require more extensive gantry shielding. A beam with a significant uniform component in both transverse axes could however be collimated to provide a uniform dose across the transverse tumour profile, whilst reducing losses compared to the unflattened case. A UHPCI of the type described in Chapter 2 could be used to provide compact acceleration of the beam for use with e-GaToroid, and designed such that the transverse profile of the beam upon entry to e-GaToroid would be uniform. This could allow a large beam with a significant uniform component to be retained at the isocentre without higher order optics, given an appropriate

lattice design. The magnification optics of this beam through the e-GaToroid lattice should retain as much uniformity as possible to maximise transmission and thus available dose rate from the system. The aim of this chapter is to describe the design techniques for preservation of uniformity, and the results and sensitivity analysis of the resultant e-GaToroid lattice.

3.2 Preservation of Uniform Beam Profiles

3.2.1 Beam Magnification in a Riesenrad Gantry

A simple model was initially used to study uniform beam preservation and compare the tracking codes which would eventually be used for the e-GaToroid design. Geometrically, this toy model consisted of a 1 m horizontal line available for quadrupole insertion if deemed necessary, followed by a single 1.3 m sector-bending dipole bending the beam 90° downwards in the transverse y-axis - a so called "Riesenrad Gantry" layout [206], as shown in Figure 3.3. This dipole length was chosen such that the required field strength would be modest (for the 100 MeV beam described in this section, this would be 0.4 T). This was followed by a further 6 m matching line, the last 1.5 m

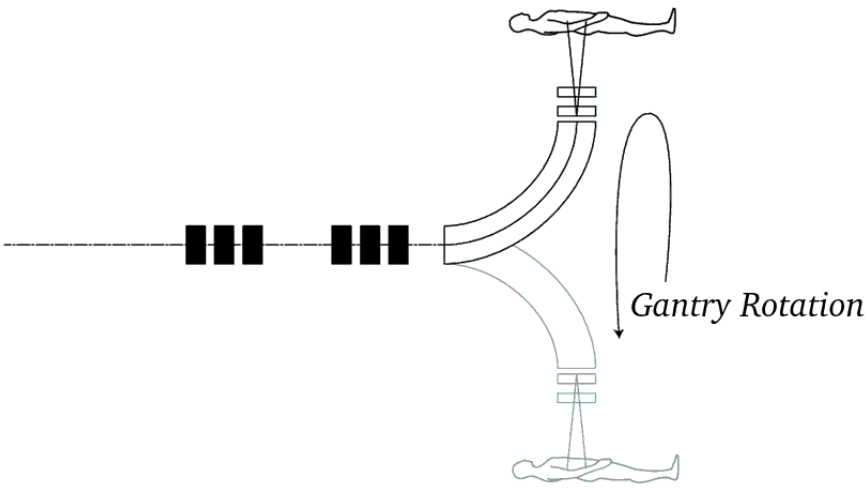

Figure 3.3: Riesenrad gantry concept, with beam entering through left, travelling through single bending dipole and entering patient on dynamic rotating couch. Arbitrary magnet lattice shown. Image from [206].

of which was left empty to allow for diagnostics and collimation systems which would be required for a clinical machine. The layout was constrained by the number of magnets required. MAD-X (Methodical Accelerator Design Version 5.02.08) was used to design the lattice of quadrupoles to be inserted, for matching the beam to the patient. MAD-X is a set of tools for the design and development of particle accelerators [207]. Its MATCH module allows calculation and optimisation

of the beam parameters to be carried out quickly and accurately. This initial design with limited beamline dimensions was carried out using transfer matrix matching.

In MAD-X, particles at any position s in the beamline are represented by the 6 dimensional phase space vectors outlined in Chapter 2. Each element in the beamline was thus represented by a 6x6 transfer matrix, multiplied together to create the total transfer matrix R. The beam was assumed to be 100 MeV for these studies - this was effectively arbitrary since all magnetic elements were defined with quadrupole strength k_1 for quadrupoles, or bending angle for the dipole (the e-GaToroid design described in Section 3.3 and beyond assumed a 200 MeV beam). The beam at entry to the transfer line occupied a 1 mm circle in the $x - y$ plane and 1 mrad in the $p_x - p_y$ divergence plane, with 0 energy spread. These parameters were chosen as a simplification of the possible VHEE phase space distribution from acceleration (a lower emittance variation of that shown in Figure 2.6). The goal of this study was to magnify the beam by a factor of 100, whilst retaining uniformity. For the transfer of the 100 MeV VHEE beam to the patient for this work, 6 constraints on the elements of R were set:

- R_{12}, R_{34} = 0: The beam should be imaged to the isocentre - its angular phase space components in both the x and y axes should have identical structure to the initial beam.
- R_{11}, R_{33} = $\pm$100: The beam should be magnified by a factor of 100 across both transverse axes. The choice of matching to +100 or -100 was arbitrary, assuming that the above imaging condition in both were met.
- R_{36}, R_{46} = 0: Dispersive effects in the vertical (bending) axis should be eliminated or otherwise minimised.

The design process was constrained by the strength of the quadrupole magnets deemed reasonable (this was chosen to be $\pm 75\,\mathrm{m}^{-2}$). The design would preferably utilise as few magnets as possible for the sake of efficiency, cost-effectiveness and ease of operation, whilst still meeting the matrix element matching requirements above.

Table 3.1: Quadrupole strengths (k_1), field gradients (G) and longitudinal positions in the beamline (s) for Riesenrad transfer line design carried out with MAD-X.

Element	k_1 [m^{-2}]	G [T m^{-1}]	s [m]
Quadrupole 0	-15.1255	5.0452	0.5
Quadrupole 1	-8.76986	2.9254	2.9
Quadrupole 2	10.7334	3.5802	3.7
Quadrupole 3	-63.3749	21.139	4.5
Quadrupole 4	-13.9222	4.6439	5.3
Quadrupole 5	-45.6609	15.231	6.7

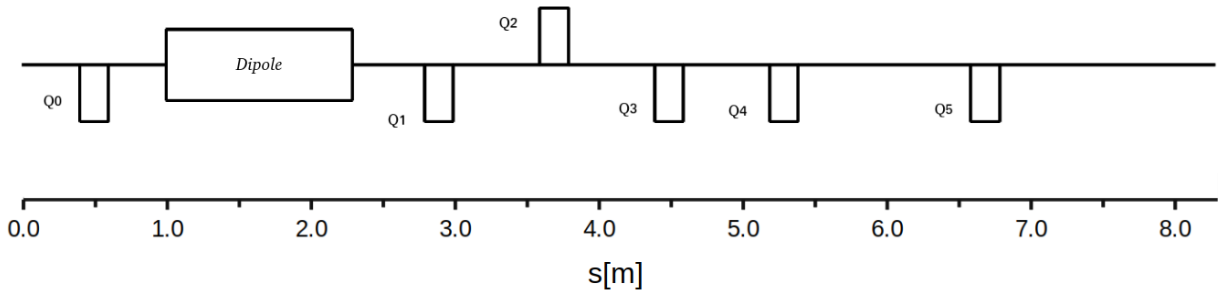

Figure 3.4: Layout of Riesenrad magnification design from MAD-X with displacement s through beamline. Positioning designated by Table 3.1 with beam entering from left and element labels shown.

The lattice design parameters are summarised in Table 3.1, with the layout displayed in Figure 3.4. The 6 parameters were matched with a final penalty function in MAD-X in the order of 10^{-4}, with the most significant (but still very small) errors originating in the values of the y-axis dispersive elements, R_{36} and R_{46}. Whilst the lattice was designed to minimise the number of quadrupoles as previously stated, this did require one quadrupole to be located upstream of the bending magnet in the beamline. With the simpler regime of all 6 quadrupoles being situated after the dipole, y-axis and x-axis matrix elements would oscillate together as the transfer matrix evolved through the beamline. The evolution of the relevant matrix elements through the beamline for the final design is shown in Figure 3.5. The magnitudes of the magnification matrix elements (R_{11} and R_{33}) reached their maxima only very close to the isocentre (termination point of beamline) here, reducing beam losses from collimation in upstream magnetic elements.

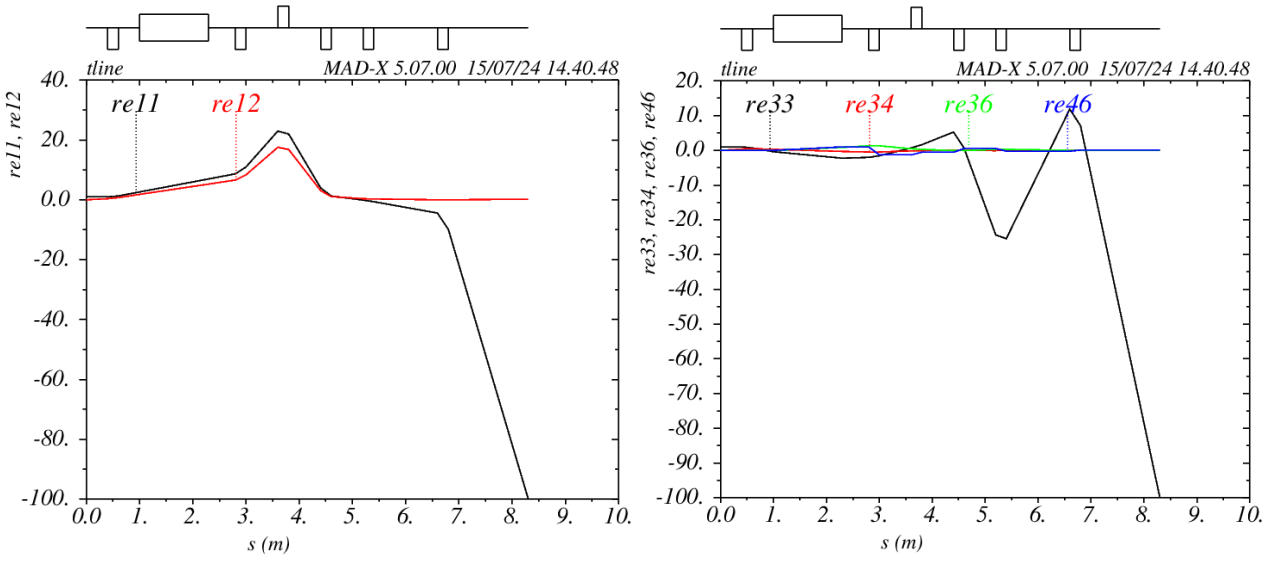

Figure 3.5: Transfer matrix ($re \equiv R$) element values against displacement through designed Riesenrad beamline. Relevant matrix elements for transverse quantities in x (left) and y (right) shown. Magnification through beamline demonstrated by enlargement of absolute values of $re11$ and $re33$ terms, with all other relevant elements matched to approximately 0. Lattice element positioning overlaid.

3.2.2 Tracking and Benchmarking

With the design meeting the 6 matrix element constraints defined in Section 3.1, the next stage of the analysis involved tracking a beam through the lattice. The matching should have resulted in a uniform beam at the isocentre, easily predictable from initial beam parameters and transfer matrix elements. The tracking allowed the comparison of different tracking codes for the VHEE electrons in such a compact beamline. The VHEE regime is at a far lower energy than the typical beams found in high-energy colliders, and thus a benchmark was desirable before progression to the more detailed design studies for e-GaToroid. The two tracking codes compared in this section were the PTC (Polymorphic Tracking Code) module implemented in MAD-X [208], and RF-Track [209]. The PTC module was chosen here rather than the default MAD-X tracking module, as PTC was specifically designed to account for designs of smaller and lower energy systems, with better defined element models [210]. The PTC module can be called directly from a MAD-X script to perform tracking on a certain lattice, despite the module itself being separate from the core MAD-X code.

RF-Track was written and developed by A. Latina at CERN, in parallel and optimised C++. It offers extremely fast tracking utilities for partially and fully relativistic particles. Beams of arbitrary energy, particle and bunch composition can be defined through generated/imported phase space vectors, or with Twiss parameters and emittance. It is capable of modelling the effects of both space-charge and RF acceleration on these beams, allowing for numerous applications of the code such as the aforementioned studies on photo-cathode based uniform beam generation [188]. Elements can be defined either in a **Lattice** or **Volume** object for rapid computation of tracking, or full modelling in a 3D space, respectively. In either case, elements can be rotated or translated to study effects of jitter or misalignment on the beam. Recent updates to the code allow MCS in materials of arbitrary thickness and composition to be modelled. These have been used to study muon cooling, and RF-Track has been successfully benchmarked with relevant codes for this purpose [209, 211, 212]. The main interest in its use for these studies was RF-Track's speed; if results were comparable with the more established PTC code, it is reasonable to assume that RF-Track's description of tracking through lattices in the VHEE regime would be reliable, whilst also running significantly faster (well over a factor of 10) than PTC and with more flexibility.

To perform the benchmark, initial parameters of the beam particles were first set. The beam was composed of 50 000 particles randomly distributed within the unit phase-space circle defined in Section 3.2.1, with 0 energy spread. The final beam distributions from both RF-Track and PTC tracking through the designed beamline are shown in Figure 3.6. The lattice design clearly produced

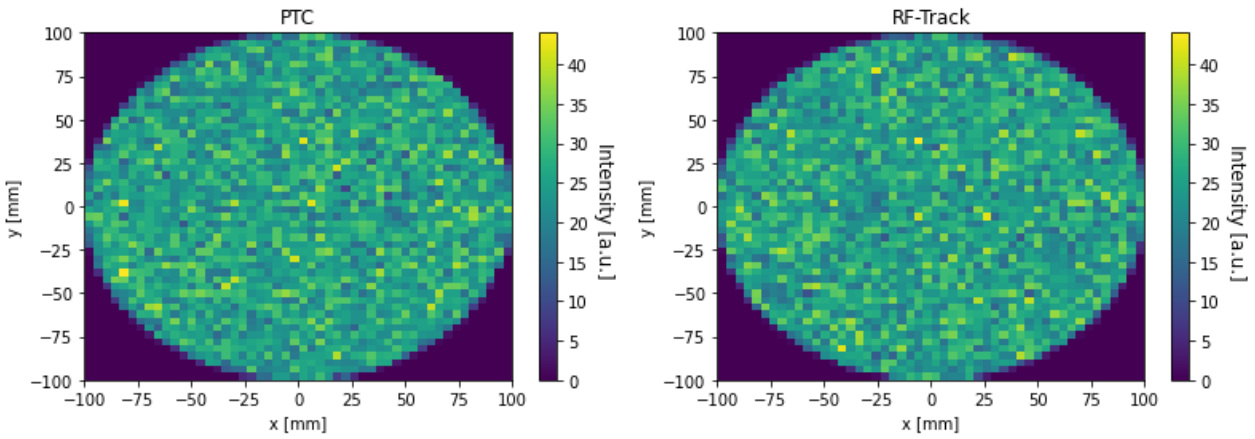

Figure 3.6: Transverse beam density histogram at isocentre from beam tracked through Riesenrad lattice with PTC (left) and RF-Track (right).

a uniform beam with a radius of 100 mm at the isocentre as predicted. The results from the two tracking systems were indistinguishable when viewed as an ensemble, with any differences well within statistical variation. To more explicitly demonstrate the agreement between the two codes, single particle tracking was carried out for an array of 4 particles with one of initial parameters x, p_x, y, p_y set to 1 mm or 1 mrad respectively and all other initial parameters set to 0. Figure 3.7

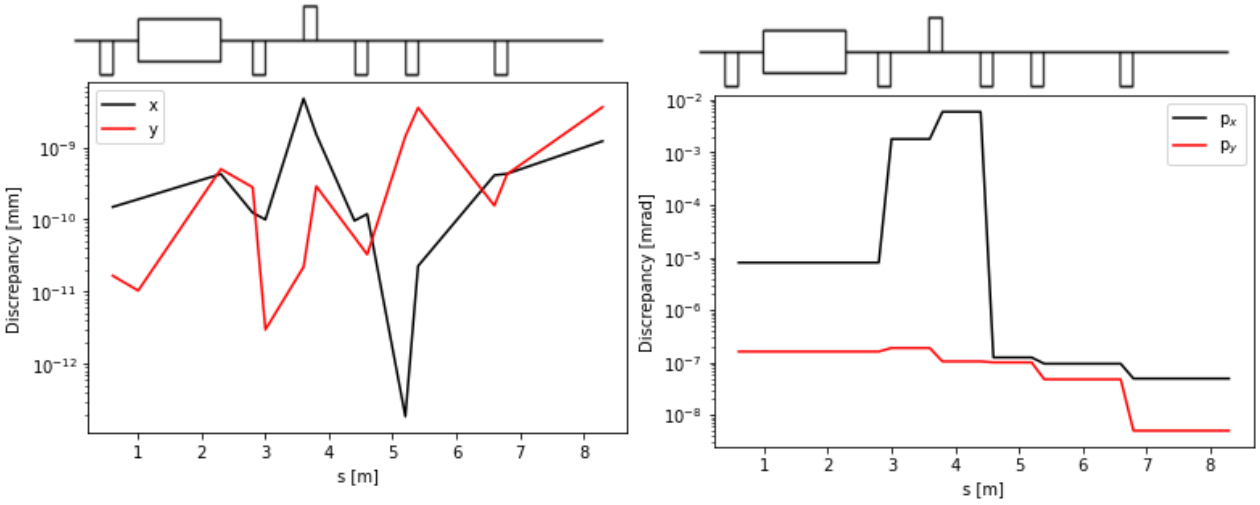

Figure 3.7: Single particle discrepancies between PTC and RF-Track against displacement along Riesenrad beamline, in position (left) and divergence (right), in both transverse axes. MAD-X lattice overlaid on both sub-figures.

demonstrates the accuracy of the two codes relative to each other whilst being tracked through the lattice. Discrepancies in physical space was on the order of 10 nm at most, and as such can be assumed to be effectively non-existant. Even the largest disagreement for the initial p_x = 1 mrad case was very small - on the order of 10 µrad. The agreement of the two codes showed that the design was successful for transferring the beam with the desired requirements, and that RF-Track and PTC results compared well in this energy regime.

3.3 Merit Based e-GaToroid Optimisation

3.3.1 System Geometry and Initial Beam

The work in Section 3.2.2 confirmed that RF-Track is capable of accurately modelling beam propagation through short, linear beamlines with quadrupoles and dipoles in the VHEE regime, whilst being orders of magnitude faster than PTC. Additionally, it demonstrated a method for retention of uniformity using matrix matching. This method became more complex when attempting to include initial beams with non-zero energy spreads into the design process, especially when further dipoles were required in the beamline for progressing from the Riesenrad model to a more typical gantry geometry.

The power of RF-Track was thus used for an alternative approach to the lattice design for the e-GaToroid system. Rather than the two-stage process of transfer-matrix matching and subsequent tracking to analyse dispersive and higher order effects, the beamline could be designed through analysis of the final profile quality using iterative runs of the tracking code itself. This would allow any effects not fully implemented by the matrix formalism in MAD-X to be accounted for without additional steps and iterations. It would also simplify consideration of initial beams with different parameters. The speed of RF-Track runs is under a second for a short beamline with a limited number of particles ($<10^5$). This makes it extremely well suited to automated beamline design which may require many thousands of runs to converge to an appropriate solution (again dependent on the particle number, complexity of beamline and constraints on the final beam profile).

The prescribed geometry of e-GaToroid was initially flexible for the design process, but within certain constraints. The system was set to be composed of the linear toroidal optical elements as described in Section 3.1 and shown in Figure 3.8. The true toroidal nature of e-GaToroid was neglected, with the design carried out assuming a linear beamline; each element was modelled as typical component in RF-Track with the presence of possible higher order fields left for future work. The consequences of this simplification are discussed in Section 3.5. The beamline was defined as bending in the y-axis, with positive quadrupole strengths referring to focusing in the x-axis and vice versa as in standard convention. The initial vector magnet was modelled as a thin (zero length) 5° dipole kick in the negative y-axis, followed by a drift tube to increase physical separation from axis of symmetry. This was required so that the following magnification dipole (**Mag dipole**) was of a sufficient radius to be feasibly manufactured with passage of the 7 beamlines. The magnification dipole was modelled as a 25° sector-bend in the same direction. This was simply

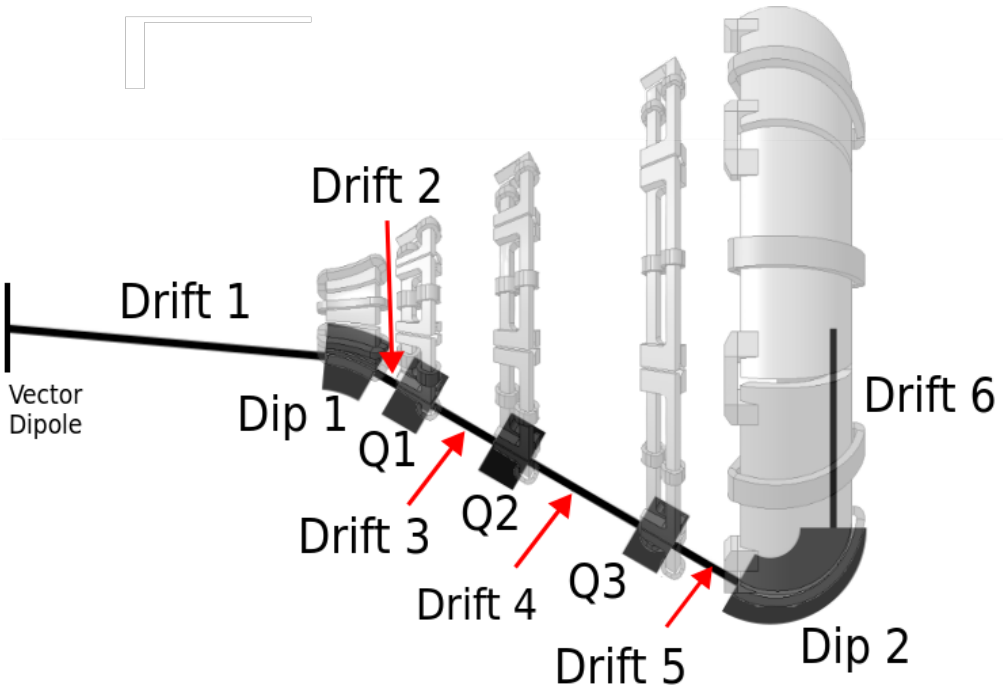

Figure 3.8: Generic 1D representation of e-GaToroid system showing main components, with conceptual e-GaToroid side-profile courtesy of T. Lehtinen overlaid. Beam entering from left.

for ease of future work and treatment of magnetic field imports with a 30° angle. Beyond this was a matching section with three quadrupoles. Their positioning was initially undefined. The final optical component was the 120° bend to deliver the beam to the isocentre, representing the final large toroid. Changing the angles of the pole-tips was deemed plausible for producing a quadrupole magnetic field moment along with the dipole field. Thus, this final bend was modelled as a combined function magnet (referred from here onwards as the **CF dipole**). A 1.5 m drift section between the final bend and isocentre was chosen to leave sufficient space for beam diagnostics, collimation and/or focusing or scanning components in future studies, as with the Riesenrad design in Section 3.2.1. The constrained element lengths are illustrated in Table 3.2. The variables for the design consisted

Table 3.2: Geometrical e-GaToroid lattice constants, referring to the labels in Figure 3.8.

Element	Length [m]
Q1	0.3
Q2	0.3
Q3	0.3
Dip 1 (Mag dipole)	0.4
Dip 2 (CF dipole)	1.0
Drift 1	2.5
Drift 6	1.5

of the strengths of the 3 quadrupoles and the CF-dipole quadrupole component, and the positioning of the 3 quadrupoles (explicitly, the lengths of Drift 2, Drift 3 and Drift 4 in Figure 3.8). The length

of Drift 5 was always modified such that the length of Drift 6 was 1.5 m whilst ensuring the beam returned to the axis of symmetry. A minimal drift space (0.1 m) was always retained at each end of the magnetic elements to allow for disparities between physical and magnetic lengths, as well as diagnostic or corrector elements.

3.3.2 Isocentre Beam Requirements and Constraints

The principle aim of the design was for the beam to have a uniform component in both transverse axes out to a radius of 75 mm at the isocentre. This was deemed an appropriate requirement for such a beamline design for medical applications, and could describe an approximate upper bound for maximal tumour size (of course, some extremely large and irregularly shaped tumours may exceed this). This requirement for beam-size at the patient was also used for the studies in Chapter 4, for consistency. The definition of uniformity here was chosen such that the variation was within 10%, not including statistical error from simulations - as such, the uniform radius would be analogous to the concept of r_{90} for the super-Gaussian beam models introduced in Chapter 2. Whilst a rather generous definition and rather more lenient than clinical requirements, this reflected the use of this as a first iteration study. The beam was assumed to be perfectly collimated outside of this region for calculation of transmission through the system. Thus, the proportion of the beam within this radius should be maximised as much as possible. A transmission above around 50% would be higher than that after collimation of Gaussian tails achieved with scattering foils [213], still allowing UHDR to be achieved given UHPCI currents. Ideally, dispersion in the beamline would be reduced as much as possible to minimise the dependence of initial beam momentum spread; high dispersion values in clinical beams can result in deviations [214].

The aim for the first iteration of the e-GaToroid design was to reach these requirements within the described geometry of the system. Care was taken to carry out the optimisation within appropriate constraints on the normal-conducting magnets. For the quadrupoles and CF dipole, this introduced dependencies on the beam-size inside the magnets, as this would change the requirements on the pole-tip fields to achieve the required gradients well under the limits for iron saturation. The maximal limit for magnetic field in any of the magnets was set at 1.5 T (to give a reasonable error band around the the saturation limit). Beam-sizes and magnetic gradients in the toroidal quadrupoles were minimised wherever possible to simplify the physical designs and reduce the required currents. The initial beam was identical to that described in Section 3.2.2 in terms of transverse phase-space, again representing a simplified UHPCI accelerated beam. In this case, the beam was also given a 0.25% uniform momentum spread such that dispersive effects could be addressed in the optimisation. In

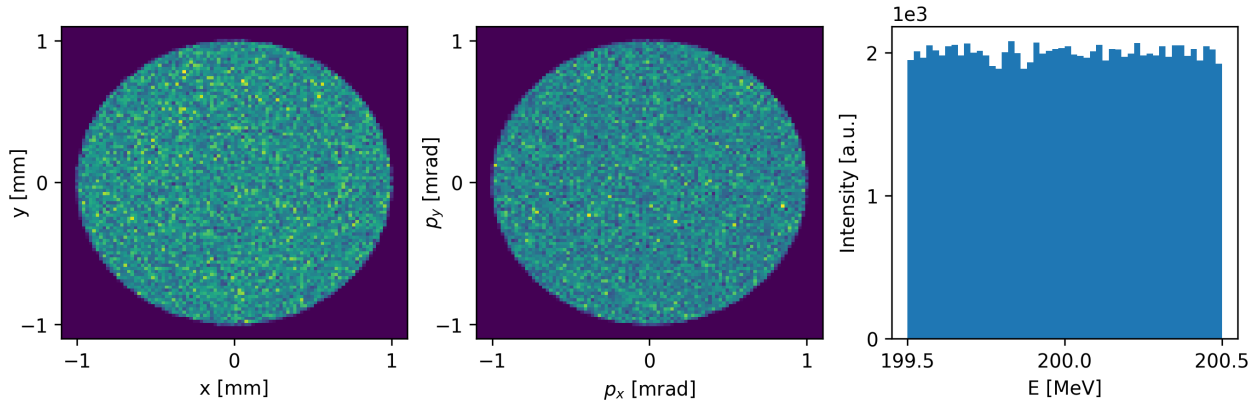

:

Figure 3.9: Intensity distributions of initial beam used for e-GaToroid design. 2D density histograms in $x - y$ (left) and $p_x - p_y$ (middle), and 1D beam density histogram of particle energy (right).

reality, the momentum spread of a UHPCI beam may be small, but is unlikely to be uniform. The energy was assumed to be 200 MeV for the e-GaToroid design, such that the beam could feasibly reach deep-seated tumours in a patient.

3.3.3 Initial Merit Function

The optimisation was carried out using minimisation of an objective function. The simplex (or Nelder-Mead [215]) algorithm is a rapid minimisation method based on simple mathematical formulae, and is capable of handling numerous constraints and variables during optimisation. The desired beam at the isocentre of the e-GaToroid system was thus characterised with a merit function which would be minimal for a beam meeting the desired attributes for the system. For this optimisation, the merit function was simply a weighted sum of terms with additional penalty functions.

$$M_{Gat1} = M_{beam} + M_{penalties} + M_{transmission} \tag{3.1}$$

$$M_{beam} = M_{beam_x} + M_{beam_y} \tag{3.2}$$

where

$$M_{beam_y} = W_{y1}M_{\mu y} + W_{y2}M_{\sigma y} + W_{y3}M_{kurt_y} + W_{y4}M_{D_y}. \tag{3.3}$$

W_{yN} are weighting factors and M_{beam_x} is of the same form, but with different weights and no dispersion term. $M_{\mu y}$ and $M_{\sigma y}$ terms were minimised when the beam's transverse position and standard deviation were within a certain reasonable band. M_{kurt_y} was minimised with increasing uniformity of the final beam. This uniformity was quantified through measurement of the kurtosis and comparing it with the ideal uniform beam kurtosis of 2, as described in Chapter 2. M_{D_y} was propor-

tional to the absolute value of the dispersion function $D_y(s)$ at the isocentre. $M_{penalties}$ contained bundled penalty functions to suppress the maximum magnetic field strength for the variable magnetic elements. These were practically defined in such a way that if constraints on magnet pole-tip fields were not satisfied, the merit terms grew exponentially and dominated the merit function. The penalty functions were defined to minimise the beam-size in the three quadrupoles to further reduce the required apertures and pole-tip fields. The magnet half-apertures were chosen as 5σ to minimise losses. $M_{transmission}$ was a simple function which exponentially rose when the number of particles within a 75 mm perfect (virtual) collimator at the isocentre was below 50% of the particle number at the entry of the beamline.

3.3.4 Optimisation Summary

The optimisation for the lattice followed an iterative process. Repeated runs were necessary as the simplex algorithm is likely to converge to local minima where there are many variables in the optimisation, as in this case with a total of 7 (4 k_1 values including that from the CF-dipole, 3 drift lengths). Thus, initial conditions were randomised to reach appropriate solutions of the merit function within prescribed constraints.

1. Initial variables were randomised within hard constraints
2. Drift 5 length was calculated and beamline defined in RF-Track
3. Initial 1000 particle beam was generated and tracked through beamline to isocentre
4. Isocentre phase-space and beamline transport table was extracted and merit function calculated
5. Free variables were updated according to Nelder-Mead algorithm
6. Steps 2-5 were repeated until a local solution was found
7. Steps 1-6 were repeated until a general solution was found

The weightings of the various terms of the merit function in both x and y were continuously modified during this process to guide the optimisation and produce more desirable beamline designs. The choice to minimise beam-size in the quadrupoles resulted in the optimisations being biased towards the magnification being principally carried out by the combined function dipole. This was deemed acceptable, as its large size around the isocentre would allow ample space for the magnet gaps and passage of larger beams. The initial magnet values retrieved from the kurtosis based optimisation process are shown in Table 3.3, with drift lengths shown in Table 3.4. The final beam was mostly

uniform within the 75 mm radius in y and with a slightly larger uniform extent in x. There were more significant Gaussian tails in in the dispersive y axis than x, as shown from the final transverse beam profile in Figure 3.10. Losses in the beamline were negligible.

The transverse profiles of the initial design demonstrated significant losses of uniformity particularly in y in the regions near the virtual collimator - it was found that the aim of retaining 10% uniformity inside the virtual collimator was not reached , with uniformity extending to around 65 mm in y. This was directly determined through binning of the 2D dose distribution across the collimated region. A more advanced method for beam characterisation at the isocentre was used to

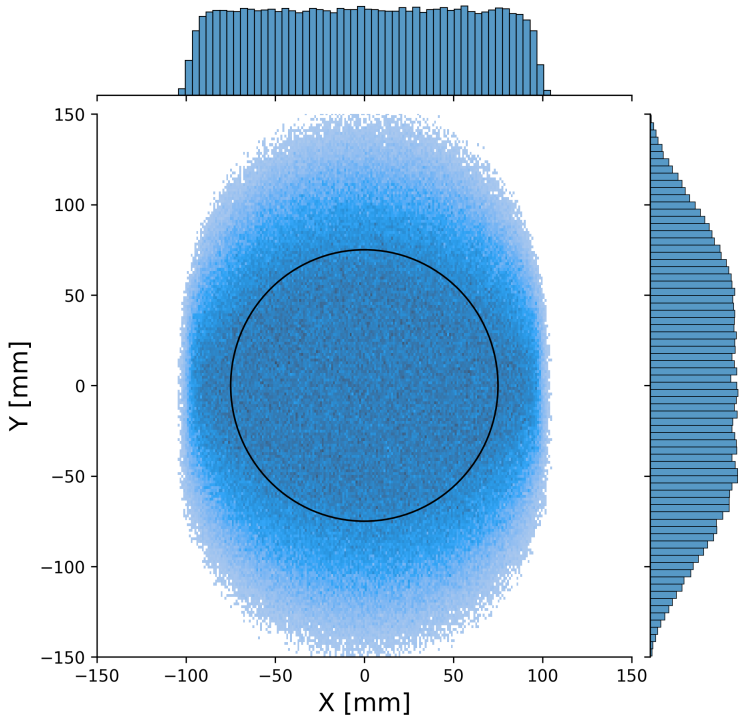

Figure 3.10: Transverse beam intensity histogram at e-GaToroid isocentre from initial kurtosis based RF-Track optimisation, with 75 mm radius virtual collimator region highlighted. 1D distributions in respective axes also shown.

optimise this initial design. In the first optimisation, the uniform radius was implicitly increased using a combination of kurtosis and σ measurements - this rather approximate method is what resulted in a larger than desired uniform extent in x, and lower than desired uniform extent in y. Statistical variations in the 1000 particles additionally made the measurements of kurtosis unreliable. To adjust the uniform region more precisely, the super-Gaussian functions described in Chapter 2 were used for the first time. These could be fitted to the transverse beam profile during optimisation, and the value of r_{90} used as input to the merit function for optimising beamsize and flatness.

A similar optimisation to that outlined above was carried out to retain a 50% transmission and ensure uniformity out to 75 mm in both x and y. The geometry of the gantry (positioning of the

quadrupoles) was constrained to that of the initial design here for simplicity and consistency; this geometry is visualised in the optimised result in Figure 3.11. Dispersion was again minimised as far as possible during this process. As asymmetry in flatness in x and y was present from the initial design, 1D fits across transverse slices were used to determine the uniform extents in the transverse axes (these are referred to as x_{90} and y_{90} from here onwards, and are effectively the elliptical equivalents of r_{90}. Thus, they are also referred to as "elliptical axes"). These slices were chosen to be of 5 mm thickness to balance statistics for fitting with effects of the beam curvature at the profile fringes. During this process, the required quadrupole strength of the CF dipole was reduced to simplify the eventual design.

3.3.5 Results

Table 3.3: Quadrupole strengths in initial (**init**) design and subsequent reference (**ref**) design. Quadrupole positioning visualised in Figure 3.11, with drift tube lengths explicitly quantified in Table 3.4.

	Q1	Q2	Q3	CF
k_1^{init} [m^{-2}]	-6.196	5.43	-24.48	3.83
k_1^{ref} [m^{-2}]	-6.196	5.41	-29.52	1.94

Table 3.4: Lengths of unconstrained drifts in e-GaToroid system as designated by initial lattice design optimisation results, consistent for both initial and reference design. Drift 5 defined to retain constant Drift 6 length.

Variable Drifts	Length [m]
Drift 2	0.200
Drift 3	0.544
Drift 4	0.956
Drift 5 (semi-constrained)	0.579

This optimisation was successful in producing a result with 75 mm uniformity across the beam profiles and transmission above 50%, verified by the super-Gaussian fits outlined in Table 3.5. 1D slices of the final beam intensity profile at the isocentre for this design are shown in Figure 3.12. The uniformity across the 75 mm region also shown in Table 3.5 was lower than the 10% requirement for uniformity, confirming the validity of the results from the fits. The design was chosen to have a slightly larger uniform extent than the 75 mm requirement to allow some deviation of the transverse beam position at the isocentre without loss of uniformity, whilst still ensuring the transmission was above 50% for the perfectly aligned case. Whilst reduced as far as possible, the final result still had a dispersion in the bending axis of $D_y(s)$=-10 m. The slight asymmetry of y_{90} compared to x_{90} was also a deliberate choice; statistical fluctuations were higher in the dispersive axis y. This more

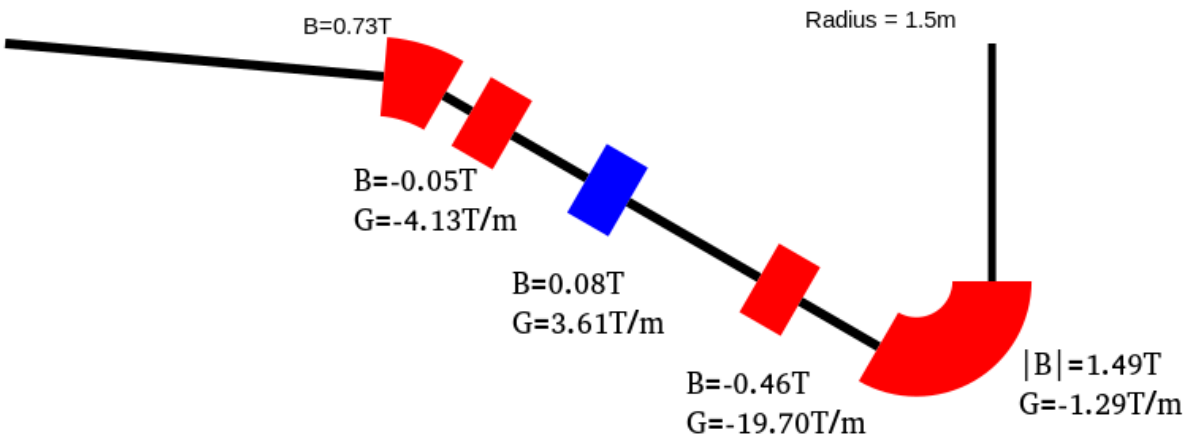

Figure 3.11: 1D e-GaToroid design geometry and required magnetic strengths for reference magnet values, with quadrupole gradients shown where necessary. Beam entering from left, with vector magnet not shown.

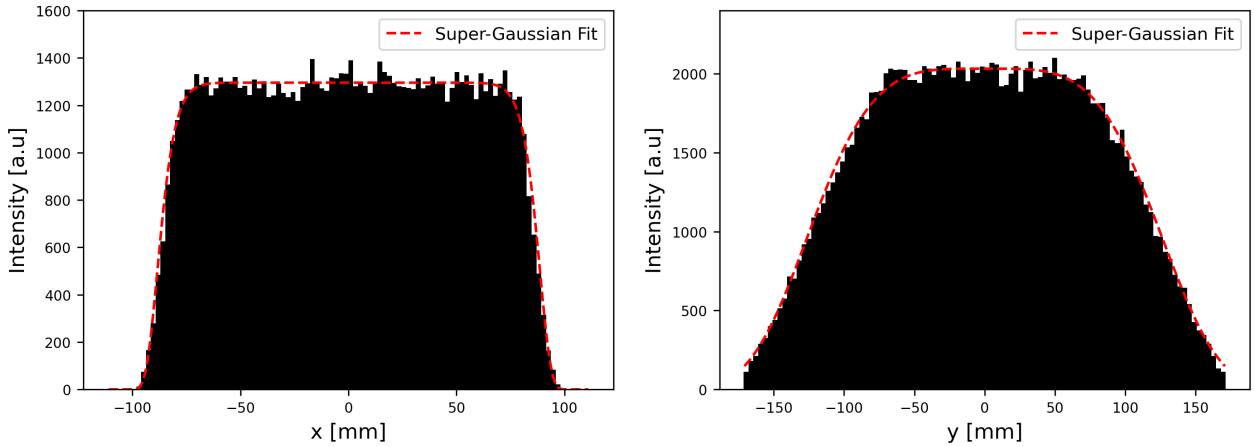

Figure 3.12: Histograms of beam intensity against x (left) and y (right) across slices of beam profile at e-GaToroid reference design isocentre, with super-Gaussian fits indicated. Extracted from simulation in RF-Track.

optimised design is referred to as the "reference" design, compared to the "initial" design. This optimal result in terms of uniformity and transmission still had a significant value of the dispersion function as shown in Figure 3.13. The divergence profile would have to be taken into account during treatment planning, but this is not uncommon for conventional treatments with flattening filters, or electron/proton treatments with dual-scattering foils [216]. Evolution of the beam envelope function and dispersion through the beamline for the reference design is shown in Figure 3.13. As a final confirmation step, PTC was used to successfully verify the RF-Track results of this system design.

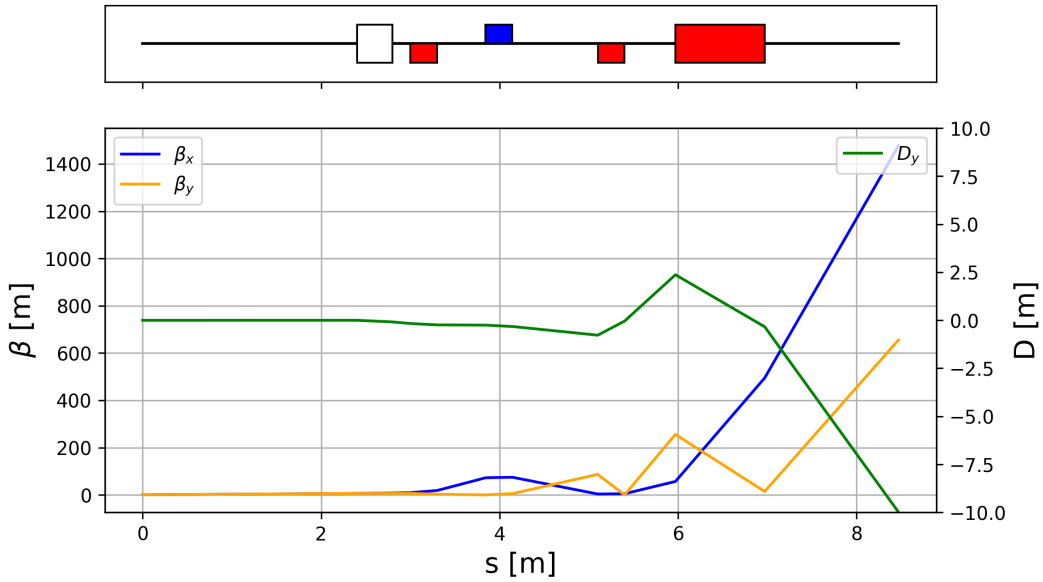

Figure 3.13: Beam envelope function and dispersion in bending axis against displacement through reference e-GaToroid beamline, with element geometry displayed above.

Table 3.5: Fitting and direct parameters for initial and improved reference design. r_{90} values derived from Equation 2.70 from fits shown in Figure 3.12. Transmission and uniformity directly measured within 75 mm virtual collimator. Errors retrieved from running multiple cycles with 10^7 particles.

Design	x_{90} [mm]	y_{90} [mm]	Uniformity [%]	Transmission [%]
Init	92.8±0.4	65.3±0.4	15.0±0.6	54.3±0.1
Ref	78.1±0.1	79.7±0.5	4.0±0.5	51.9±0.1

3.4 Sensitivity Analysis of Lattice Design

3.4.1 Individual Scans

A crucial component of beamline design (especially those for medical applications) is a thorough analysis of the sensitivity of the lattice to deviations in magnetic field, beam energy and distribution or element position (misalignment). Here, the sensitivity of the reference design is presented for the purpose of analysing the key sources of insensitivity, the results of which could be implemented into a future merit-based optimisation process. This would then allow a robust and efficient pipeline for any future iterations to be developed. The areas investigated for sensitivity to small deviations and justifications for their interest in the VHEE GaToroid system are as follows:

- Magnetic field strength - typical consideration. Toroidal quadrupoles are a novel concept and deviation from ideal field is likely. Information on the sensitivity of beamline to deviations in the field and any elements with lower tolerances is crucial.
- Element misalignment - transverse and longitudinal position, rotation (roll, yaw and pitch).

Typical consideration for any beamline. Lateral imperfections in particular could modify uniformity due to dispersion.

- Initial beam conditions - phase space, mean energy, energy spread. System was designed with ideal on-energy beam with small, uniform spread. Realistic beam is likely to have deviations in phase space and energy spread.

Simulations with ensembles of 10^7 initial particles were used for this process to reduce statistical uncertainty whilst balancing computational load. This was a significantly larger ensemble than that used for the optimisation routines, as few simulations were required compared to the many thousands used during the simplex minimisations. Scans across the relevant sources of error were carried out with newly generated beams with 5 different random seeds for each step, to allow statistical error to be determined and plotted. This was deemed sufficient to demonstrate non-negligible offsets resultant from misalignments. All deviations were made with respect to the reference design. Super-Gaussian fits to the reference profile with no offsets are shown in Figure 3.12.

Tolerance of the final profile against offsets in magnetic field strengths for the focusing elements was studied. The quadrupole fields were scanned from 99% to 101% of their reference values individually, for each element. The results of these scans are shown in Figure 3.14. Fits are shown for cases with statistically significant correlations within offsets of this magnitude x_{90} was found to be more dependent than y_{90} on the quadrupole strengths - particularly that of Q2, where x_{90} varied by approximately 20% within the 1% scanning range. For Q1 and Q3, there were correlations between field strength offsets and both x_{90} and y_{90}, but with much shallower gradients. There was a similar relationship between x_{90} and offsets in the quadrupole strength of the CF dipole. All isocentre beams retained uniform extents above the 75 mm virtual collimator when neglecting the Q2 and x_{90} case however. These scans produced negligible variations in the transverse mean in both axes at the isocentre. The direct uniformity and transmission measurements confirmed the fitting results, with uniformity being worse than 10% only during the Q2 scan. Transmission was found to evolve inversely proportionally to the uniformity, as expected (a higher proportion of the Gaussian component inside the virtual collimator would increase transmission whilst uniformity would worsen).

Element misalignment was carried out by introducing progressive offsets in each element individually, and plotting the resultant statistical deviations as before. This was done for both transverse and rotational offset. The magnitude of the translation scans was specified to an arbitrary offset of 10 µm. Whilst a very tight tolerance, this was still deemed sufficient to characterise sensitivities of

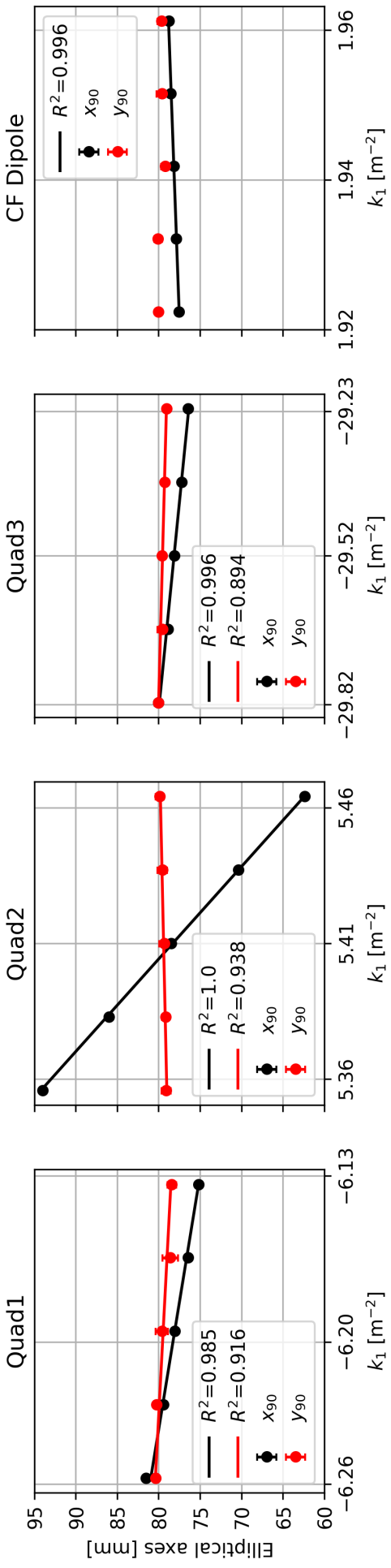

Figure 3.14: Fitted uniform ellipse parameters x_{90} and y_{90} at e-GaToroid isocentre against quadrupole strength for each relevant element in beamline, for scan taken around reference k_1 values. Linear fits and coefficient of determination R^2 indicated for correlations between deviations and fitted parameters.

the system. An offset of 1 mrad in all three axes (roll, pitch and yaw) was chosen for the rotation offset scans. Longitudinal offsets were practically achieved by simply changing the position coordinate of the magnetic elements in the Lattice class of RF-Track. This had the added benefit of maintaining the consistency of the total beamline length, as the geometry of the system was hard-coded to retain the 1.5 m final drift length. Thus, this could model the flexing of the system, for example due to changes in temperature or pressure. An initial scan across a 10 µm longitudinal displacement was carried out. Deviation in the uniform extent or in the mean position was within statistical error in all cases. Changes in uniformity and transmission were also minimal across these scans.

The transverse translation and angular deviations were inputted directly into the dedicated arguments of the RF-Track element classes (a new feature in RF Track 2.1). As shown in Figure 3.15, transverse misalignments manifested themselves as offsets in the same axis of the three quadrupoles, as was rather more sensitive than the longitudinal positioning. Similarly to the magnetic strength scans, this effect was rather stronger in the x axis rather than y axis. The beam was again more sensitive to Q2 in x, with the beam centre deviating by approximately 2.2 mm at the maximal scan extents. y_{90} was most sensitive to Q1, although this sensitivity resulted in only around a 1 mm deviation in position. Offsets in position due to misalignments in the magnification and CF dipoles were very small. These misalignments had negligible effect on x_{90} and y_{90} - these values always remained above 75 mm. Direct uniformity also remained better than 10% even during the Q2 scan - this was a benefit of the slightly larger uniform extents of the reference design from optimisation. Beam transmission also remained stable within 1%. The magnification of such small errors in transverse positioning of the quadrupoles was still a significant cause for concern, and likely due to a relatively high β function in Q2.

Rotational misalignment in the z axis (roll) was not found to cause any significant change in either the offset in μ_x or μ_y at the isocentre, or any deviation in the uniform extents, with any variations being well within statistical uncertainty. As shown in Figure 3.16, misalignment in x axis rotation (pitch) caused rather more significant deviations particularly in μ_y at the isocentre for all elements. The dependence was highest for Q1, with a deviation of above 10 mm for a 1 mrad offset and a failure to meet the 10% uniformity criteria beyond 0.5 mrad deviation. There was no evidence for a change of shape or uniform extents with these deviations, with the loss in uniformity entirely accounted for by deviations in the transverse beam position.

The most significant effects of element misalignment are shown in Figure 3.17 for rotation around the y-axis (yaw). All three quadrupoles were extremely sensitive to these variations, with μ_x offsets an order of magnitude above most previous cases. The highest dependence was again

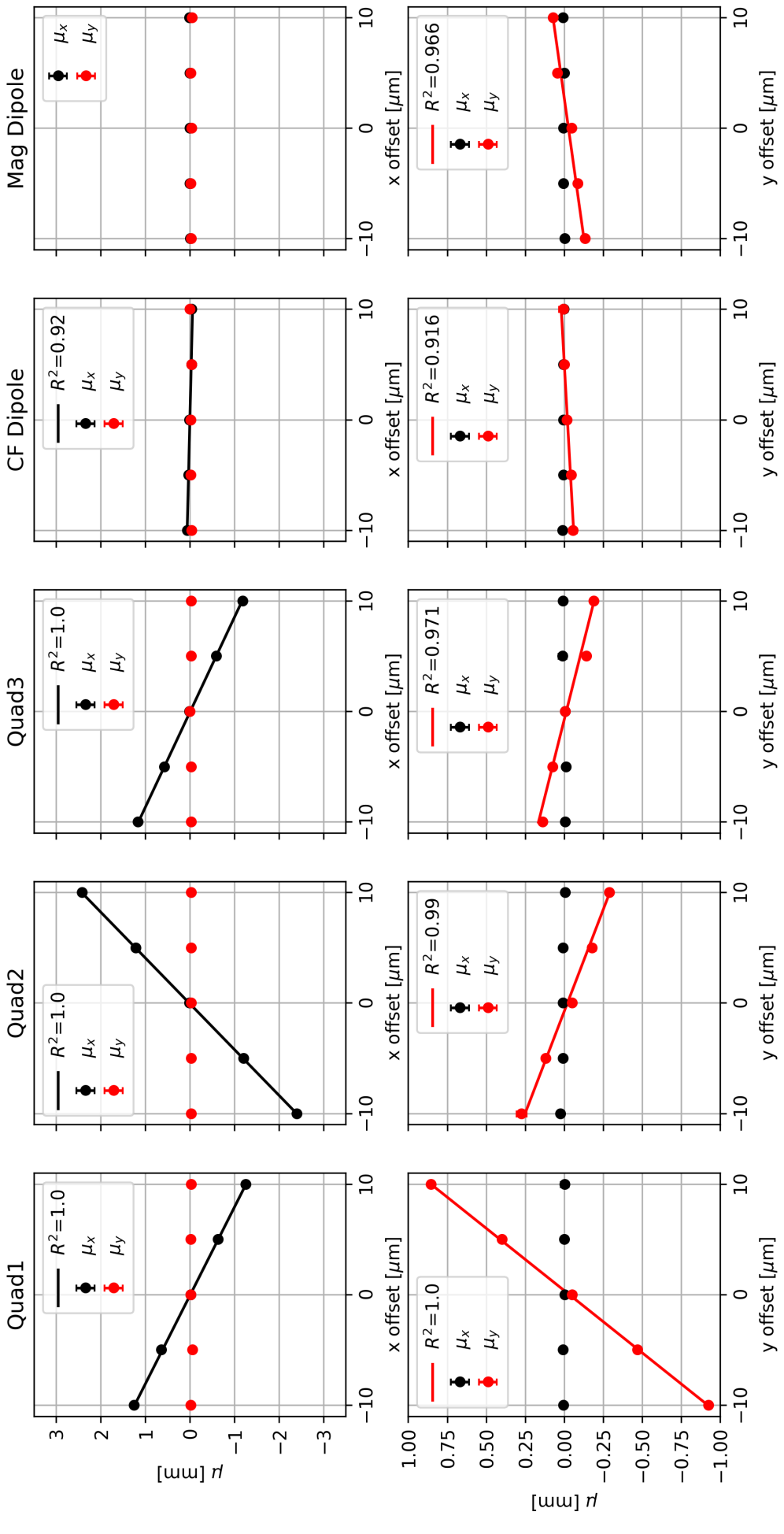

Figure 3.15: Fitted mean transverse beam position $\mu_{x,y}$ at e-GaToroid isocentre against translation offsets in x (top) and y (bottom) for each element in beamline, as indicated above each column. Linear fits and coefficient of determination R^2 indicated for correlations between deviations and fitted parameters.

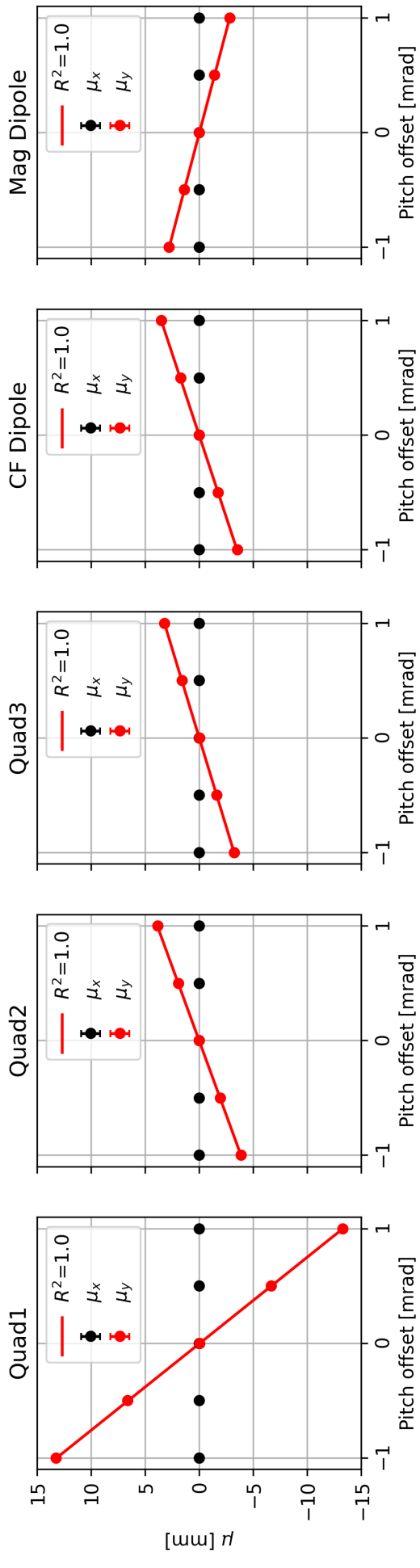

Figure 3.16: Fitted mean transverse beam position $\mu_{x,y}$ at e-GaToroid isocentre against offsets in angular pitch for each element in beamline, as indicated above each figure. Linear fits and coefficient of determination R^2 indicated for correlations between deviations and fitted parameters.

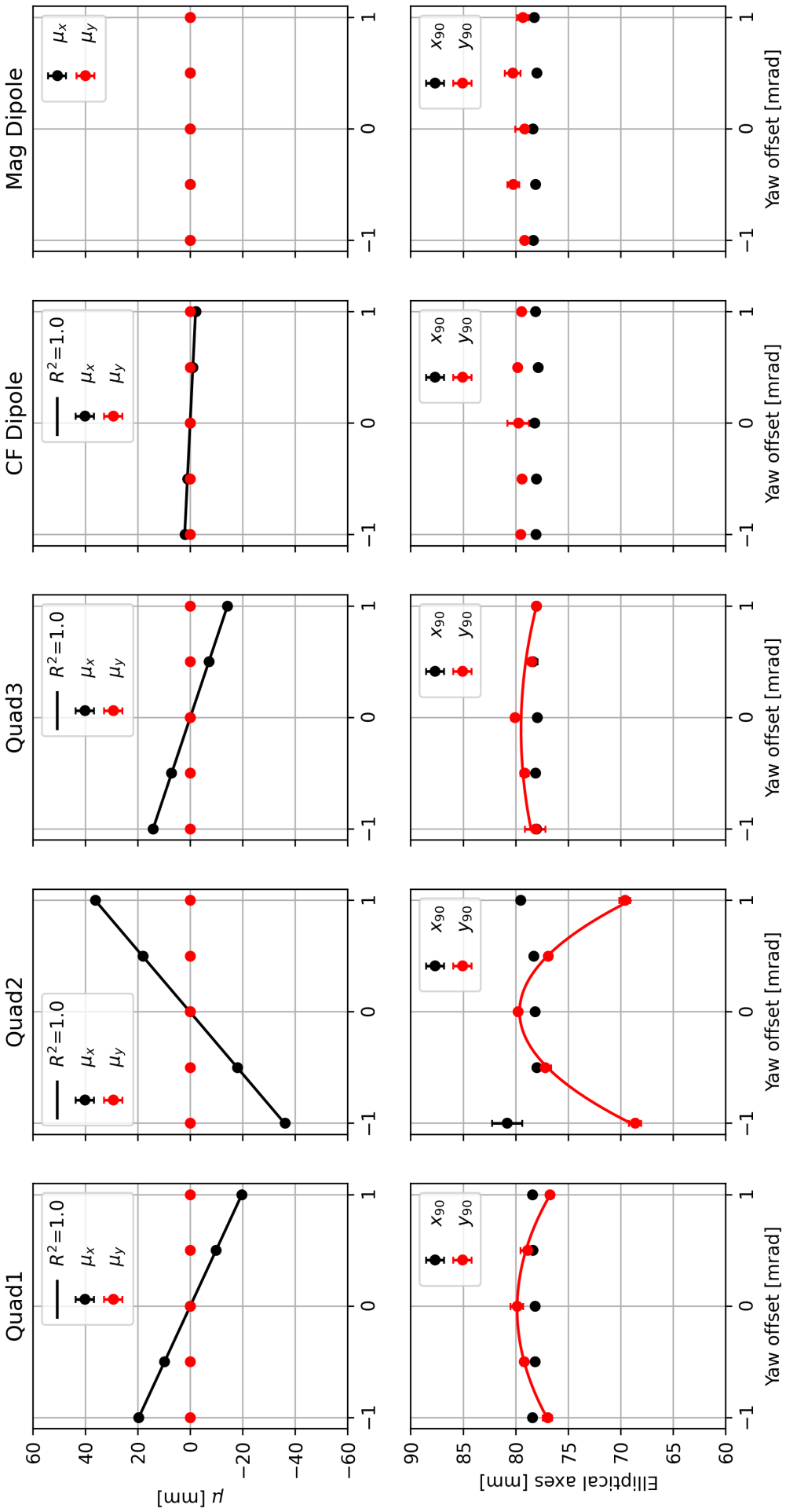

Figure 3.17: Fitted mean transverse beam position $\mu_{x,y}$ (top) and uniform ellipse parameters x_{90} and y_{90} (bottom) at e-GaToroid isocentre against offsets in angular yaw for each element in beamline, as indicated above each column. Linear and parabolic fits and coefficient of determination R^2 for the former indicated for correlations between deviations and fitted parameters.

on Q2, which produced a beam with almost 40 mm transverse displacement from the central axis with a 1 mrad deviation. Whilst less sensitive than Q2, misalignments in Q1 and Q3 still produced very large offsets in beam position. The sensitivities to magnet yaw are of extreme concern for the system as a whole (although the process of alignment would be rather unique for GaToroid). The effects of the yaw offset for the quadrupoles also translated to variations in the uniform extent. These variations were inversely parabolic with the misalignment for Q1 and Q2, with y_{90} smaller than the virtual collimator beyond around 0.6 mrad yaw offset in Q2. Variations in y_{90} during the scan for Q3 and the dipoles were within statistical error. The combination of the loss of flatness and position deviation (moreso the latter) across all three quadrupoles produced a very significant loss of uniformity at the isocentre with 1 mrad offset in either direction, as also shown in Figure 3.17. Transmission through the virtual collimator was also reduced. The mean offset was slightly counter-balanced by the reduction in beam-size; hence, the transmission remained above 40% even during the Q2 scan.

To measure the dependence on the initial beam, the input beam into the system was scanned in a phase space circle with magnitude 0.1 mm mrad (10% deviation from isocentre) around the central axis in both $x - p_x$ and $y - p_y$ phase spaces. Energy was linearly scanned around its reference value of 200 MeV, and the energy spread also varied from its nominal value of 0.5 MeV. Care was taken in specifying the energy offsets, as the RF-Track model for the lattice was defined using the normalised quadrupole strength k_1. As such, altering the reference beam energy would implicitly alter the quadrupole gradients in RF-Track. The energy was thus changed at definition in the generation module outside of RF-Track, with the element definitions still assuming a reference particle with energy 200 MeV. The system typically magnified errors in $y - p_y$ phase space, particularly in the angular divergence of the initial beam. Changing the divergence by 0.1 mrad in y resulted in a shift in the beam position on the order of 10 mm. Deviations in initial position typically resulted in offsets on the order of a few mm at most, and were well compensated by the collimation and slightly larger uniform beam component. The jitter magnification factor was computed in x and y by comparing the area enclosed by the mean position and **absolute** transverse momentum components (P_x and P_y) ellipses traced out from the scans at isocentre and injection. For $x - P_x$ space this was equal to 1, suggesting little amplification of initial phase space errors. For $y - P_y$ however, this value was approximately 50, demonstrating the severe amplification of initial phase space error in y.

Small deviations in the mean energy of the distribution was found to negligibly affect either the beam position or uniform extent in x and y with both decreasing and increasing mean energy. Increasing energy spread from the nominal value of 0.5 MeV had little effect on transverse beam

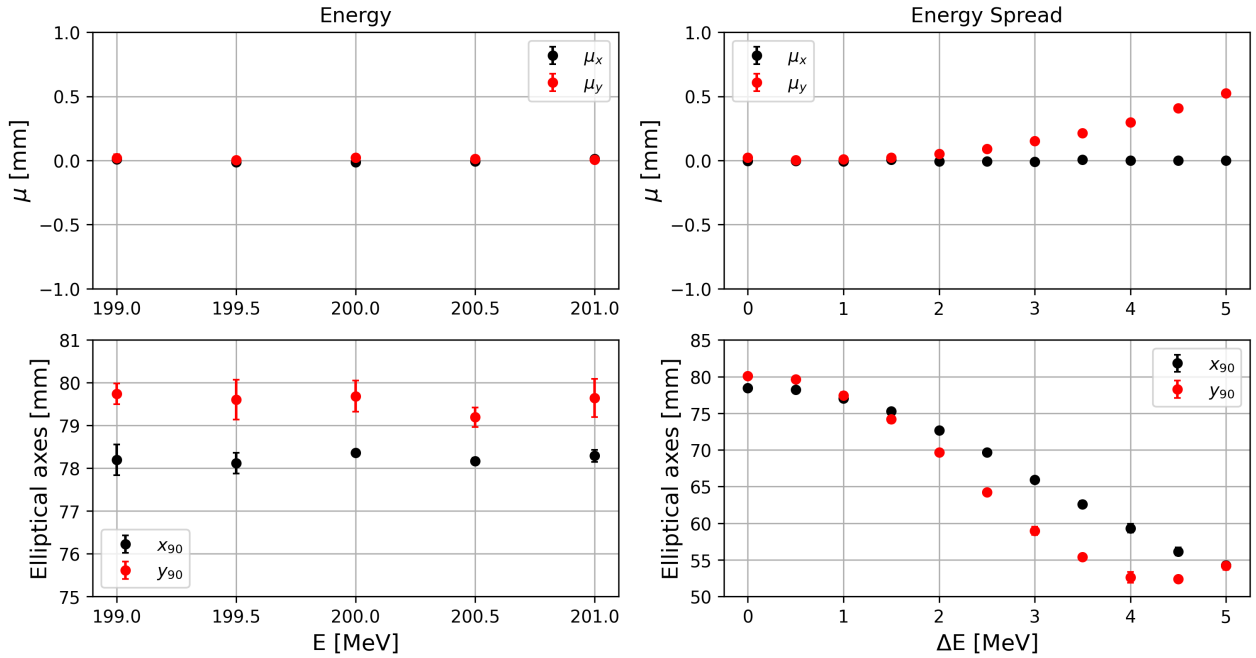

Figure 3.18: Fitted mean transverse beam position $\mu_{x,y}$ (top) and uniform ellipse parameters x_{90} and y_{90} (bottom) at e-GaToroid isocentre against mean energy (left) and absolute energy spread (right).

positioning up to around 2 MeV, beyond which μ_y began to drift off-axis. This was likely due to non-zero dispersion at the isocentre. The magnitude of this drift was fairly small however, with an energy spread of 5 MeV only resulting in an offset of 0.52 mm. More concerning was the dependence of x_{90} and y_{90} on this spread - these both reduced rapidly, decreasing beneath the 75 mm virtual collimator at an energy spread of around 1.5 MeV and continuing to decrease beyond this. This corresponded to a similar decrease in directly measured uniformity within the 75 mm collimator with the more significant energy spreads.

3.4.2 Sensitivity Study Summary

Table 3.6: Summary table displaying statistically significant correlations between offsets in elements and deviation in mean position, within scanning ranges described in Section 3.4. Highest sensitivities highlighted in **bold**. Uncertainties not displayed here for clarity - typically below 1%.

μ Offsets	μ_x^{Q1}	μ_x^{Q2}	μ_x^{Q3}	μ_x^{CF}	μ_x^{Mag}	μ_y^{Q1}	μ_y^{Q2}	μ_y^{Q3}	μ_y^{CF}	μ_y^{Mag}
Trans X[mm μm^{-1}]	-0.12	**0.24**	-0.12	-0.0061	-	-	-	-	-	-
Trans Y[mm μm^{-1}]	-	-	-	-	-	**0.089**	-0.027	-0.018	0.0040	0.010
Pitch[mm mrad^{-1}]	-	-	-,	-	-	**-13.24**	3.87	3.22	3.50	-2.80
Yaw[mm mrad^{-1}]	-19.64	**36.08**	-14.17	2.08	-	-	-	-	-	-

The linear scans and fitting demonstrated the specific effects of these misalignments in terms of transverse beam positioning and the resultant changes in the uniform radius, with the effect inside the virtual collimator being verified with the direct uniformity and transmission measurements. It was found that Q1 and Q2 were the elements most sensitive to both alignment (particularly in

Table 3.7: Statistically significant correlations between offsets in elements and uniform radius, within scanning ranges described in Section 3.4. Yaw row values taken from local gradient at maximal scanning extent. Highest sensitivities highlighted in **bold**. Uncertainties not displayed here for clarity - typically below 1%.

r_{90} Offsets	x_{90}^{Q1}	x_{90}^{Q2}	x_{90}^{Q3}	x_{90}^{CF}	x_{90}^{Mag}	y_{90}^{Q1}	y_{90}^{Q2}	y_{90}^{Q3}	y_{90}^{CF}	y_{90}^{Mag}
Strength [mm/%]	-2.89	**-15.85**	-1.77	0.63	NA	-0.93	-0.39	-0.47	-	NA
Yaw [mm mrad^{-1}]	-	-	-	-	-	-6.12	**21.14**	2.64	0.53	-

transverse rotations) and in magnetic field strength. This was expected, as these were the elements which were most crucial in retaining the uniformity of the beam before magnification in Q3 and the CF dipole.

The linear scans above were all carried out assuming uncorrelated, distinct and singular alignments. In a realistic system, beams would be affected by a combination of all the offsets discussed throughout Section 3.4. Whilst the measurements of x_{90} and y_{90} were useful for characterising the sensitivities, a successful design could be characterised entirely with the direct transmission and uniformity measurements - a system with sufficient values of each of these *must* then have $\mu_{x,y} \approx 0$ and sufficiently high uniform radius. The sensitivity was thus more broadly characterised by introducing combined, randomised offsets and evaluating whether the system passed or failed against the criteria for the system as a whole. Practically, this was the requirement for large-scale uniformity of better than 10% and transmission of over 50% within the virtual collimator.

Each of the sources of offset in the elements above was grouped together: quadrupole strength offsets, element translation misalignment, and element rotational misalignment (the initial beam was neglected from this analysis). For each group, the offsets were randomly generated within a normal distribution of a set scale, and the final distribution ranked as "pass" or "fail". The size of the distribution under which these offsets were being drawn was then decreased until at least 68% of the randomised runs passed. This then allowed a parameter for each offset to be retrieved, characterising the sensitivity of the combined misalignments. This was 1.6% for the magnet strengths, 33 µm for transverse misalignments, and 0.23 mrad for the rotational misalignments. Thus, if the strength and alignment values across all magnets were generally kept below these values, the system would be expected to have sufficient transmission and uniformity within the virtual collimator in 68% of cases. The tolerances for transverse and rotational offsets were thus infeasibly small. These values provide a summary of the overall sensitivity for the overall system, and could be compared with results from the various plots of Section 3.4 to determine more detailed results (for example, the extreme sensitivity to rotational alignment here was shown to originate primarily from the yaw component).

3.5 Discussion, Current Status and Future of VHEE GaToroid

The sensitivity analysis of the VHEE GaToroid demonstrated several key points. The beamline design process above whilst successful in reaching the desired beam parameters and reasonable transmission within the given geometry did not take concerns of sensitivity into account. It was unsurprising to find that extreme precision would be required to retain the appropriate beam and only very small deviations from the reference conditions could be tolerated, particularly in rotation alignment. The designs were also based on a highly idealised initial beam, and thus a more realistic beam may produce rather different results due to demonstrated dependence on the initial beam parameters. The collimation required to mitigate some of these concerns whilst beneficial, would likely significantly reduce the beam transmission, and indeed even this transmission would be variable and dependent on the accuracy of the magnet alignment, magnet strength and specific beam parameters. Before further optimisations of a more advanced system would be carried out, a crucial characteristic of the system which has been neglected in this chapter would have to be addressed - the magnets themselves. The initial design was valuable for estimations on required field strengths and radii of the novel magnets in the system system. This allowed conceptual designs (for example, the drawings shown in Figures 3.2 and 3.8) and cost estimates to be carried out for e-GaToroid .

More advanced studies on these toroidal magnetic systems were carried out by two final-year students at the University of Oxford for their MPhys projects. The first of these was based upon the analysis of the fields generated from the novel toroidal e-GaToroid magnets. OPERA. This was carried out with finite element analysis. All five principal magnetic components were modelled in 3D, with fields generated from appropriate currents in the system. The combined function characteristics of the final dipole were neglected for simplicity of the studies at this stage. The desired fields for each magnet were generated after several design iterations and studies of required currents in the magnet coils. Additional studies were carried out following this to optimise the fields further, utilising finer mesh sizes and more precisely defining the magnet geometry [205].

The second MPhys project was based on analysis of the generated fields themselves, and their implementation in RF-Track. These studies identified small but significant discrepancies between the true fields of the quadrupole magnets and ideal quadrupoles - specifically, the presence of higher order multipole moments and skew terms identified from Fourier decomposition. The fringe fields of the toroidal quadrupoles were also found to deviate significantly from the models in RF-Track. These higher order moments and fringe fields resulted in some discrepancies in beam-tracking, which could drastically affect the beam at the isocentre without further modification of the lattice.

Further studies (specifically, the implementation of the magnification and CF dipoles in RF-Track) would be desirable to allow a more advanced optimisation taking the true nature of these unique magnets into account. Such an optimisation would also be an opportunity to use a more thorough design process. The sensitivity studies and lessons learnt from the work carried out in this chapter could produce a more robust, rapid and reliable optimisation in conjunction with these more realistic magnet models. This advanced optimisation method could utilise some or all of the following points:

- Rather than randomly generating an initial, idealised beam for each optimisation run, a realistic UHPCI beam with expected parameters from photocathode based uniform beam generation of the type discussed in Chapter 2 could be used as input, if available from current studies or experimental data.
- Sensitivity could be implicitly constrained by placing more stringent bounds on the Twiss parameters in the magnetic elements of the beamline. The dependence of the initial design on Q2 in particular was due to the large β_x value at this point in the lattice. Suppressing these values in the elements further where possible would be beneficial to the total sensitivity of the system.
- Sensitivity could be explicitly constrained by using a condensed sensitivity analysis with each negative increment of Nelder-Mead algorithm during the automated optimisation process. For example, a minimal version of the random sampling method outlined in Section 3.4.2 could be used to return a general element sensitivity score in addition to the usual isocentre merit function values.

3.6 Summary

GaToroid is a novel static gantry concept, which could allow multi-directional treatment to be carried out within an UHDR timescale for FLASH treatment. The first iterations of the GaToroid concept were developed for use with protons and hadrons, assuming the use of superconducting toroids and very fast and accurate scanning magnets for transverse tumour coverage. A system for use with VHEE would require only normal conducting magnets, allowing additional magnetic components for beam magnification and retention of transverse uniformity to be included in the design. MAD-X was used to demonstrate beam magnification and uniformity in an arbitrary gantry geometry for a 100 MeV beam, with results verified and benchmarked between PTC and RF-Track. In both cases, the beam at the isocentre had a uniform radius of 100 mm.

The speed and accuracy of RF-Track allowed a tracking and optimisation based design routine to be developed for the lattice design of e-GaToroid itself. This routine was based upon a merit function characterisation of the beam at the isocentre, and its characteristics and constraints of magnets in the beamline. A lattice of 3 quadrupoles and 2 dipoles (one of which included a quadrupole focusing term) was developed to magnify a 200 MeV beam with a small, uniform transverse intensity profile up to a uniform region of 78.1 mm in x and 79.7 mm y, and ensuring a large-scale uniformity of better than 10% within this region. Relatively low quadrupole magnet gradients were required, particularly for the first two quadrupoles in the beamline. Transmission was $51.9 \pm 0.01\%$ within a virtual collimator of 75 mm radius. Super-Gaussian fits were used for this optimisation.

A sensitivity study on small offsets in magnet strengths, alignment and initial beam was carried out using large particle ensembles and dedicated element positioning methods in RF-Track. The uniformity of the final beam within 75 mm was found to be rather sensitive to offsets in strength and magnetic field strength of the first two quadrupoles, and particularly to misalignment in the horizontal (yaw) rotation axis of the magnetic elements. A more general sensitivity characterisation technique was demonstrated to give a measurement for combined element misalignment field strength deviations; this found that the system as a whole would be very sensitive to angular misalignment of the beamline elements, as expected. Randomised studies suggested alignment within 0.23 mrad in the angular components would be required to produce an acceptable beam at the isocentre in 68% of cases. Future studies using a more advanced optimisation, realistic initial beam and RF-Track models of toroidal magnetic components would be desirable for developing future iterations of e-GaToroid.

4 Scattered Beams in the VHEE Regime

4.1 Introduction

4.1.1 Motivation

The results from Chapter 3 showed that even for a fairly constrained beamline in terms of space and available optics, an initially uniform beam could be magnified up to the size of a large tumour and uniformity retained for transverse coverage. This was still very dependent on the initial profile of the beam, with optical components privy to misalignment resulting in significant changes in the final beam distribution. More advanced optimisations may reduce these errors, however the effect of misalignment is dependent on the β function, and thus any magnification solution would likely be rather sensitive to such misalignments. An alternative for providing a uniform beam profile is the use of either a single or dual-scattering system. These are commonly used methods of beam flattening across all operational modalities of external beam RT. The former would simply enlarge the beam sufficiently such that local uniformity within a certain region could be achieved, subject to an arbitrary definition. The principle of the latter is similar to the concept of the X-ray flattening filter as discussed in Chapter 1.

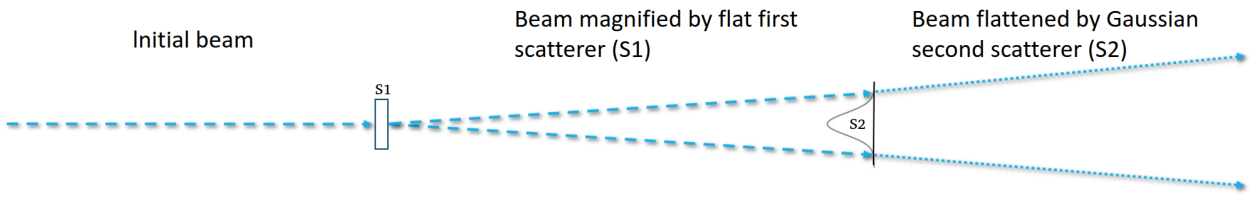

Figure 4.1: Illustration of dual-scattering foil principle with initial beam of arbitrary intensity profile entering system from left-hand side.

As shown in Figure 4.1, the initial beam (presumed not to have been magnified after acceleration, but of arbitrary transverse profile) is firstly scattered by a material of uniform thickness. This first scatterer is referred to from here onwards as S1. According to the Moliere scattering theory of Chapter 2, the beam will be enlarged with a profile approximated by a Gaussian, with a divergence and thus physical profile given by Equation 2.59. The beam then passes through a 2nd scatterer which itself is Gaussian to complement the scattered beam profile (the second scatterer will be

referred to as S2). The non-uniform S2 thus preferentially scatters the more intense central portion of the beam, resulting in a flat-topped beam, very similar to the transverse profiles retrieved at the isocentre from the optimisation in Chapter 3 and modelled with the super-Gaussian functions described in Chapter 2. As before, the beam can then be appropriately collimated to provide a uniform beam profile at the patient position for conformal tumour irradiation.

A crucial advantage of the scattering methods for achieving uniformity is that depending on the resulting scattering angle, the effects of the initial beam divergence profile may be minimal. The scattering contribution from Equation 2.59 is added in quadrature to the initial divergence of the beam, so may be the dominant contribution to the final phase-space profile, depending the specifics of the system and beam energy. This can allow a system for providing uniformity which is more robust to changes in initial beam than that from magnification optics. An initially uniform beam profile is also not required to produce a uniform beam at the isocentre using this method, meaning these could be implemented in more general beam-lines not necessarily developed for medical applications (see Chapter 5). There are some drawbacks to this method however. A dual-scattering system is typically only capable of providing a flat-topped beam of a single radius, although initial beam conditions may cause some variation. Collimators with different radii can be inserted to allow delivery of smaller beams, but this would significantly reduce the beam transmission. Even with collimation just of the Gaussian tails and none of the uniform component, 60-70% of the total beam is removed from typical scattering based systems [213]. Additionally, the introduction of any materials into the beam will result in particle production, energy and beam losses, and energy spread (the latter of which could result in increased chromatic effects if flattening were to take place in combination with magnetic elements). The extent of these effects is dependent on a number of factors: the required beam size, longitudinal positioning, and the beam energy and particle.

Little consideration has been given to the use of scattering systems in the VHEE regime; studies are rather sparse and many questions remain. A key concern is that at comparably high energies compared to clinically available electrons, the rate of Bremsstrahlung production will be significantly higher. Equation 2.59 demonstrates an inverse linear proportionality between beam energy and scattering angle from a flat foil; in the VHEE regime, much thicker or higher density scatterers would be required to produce the same scattering angles as low energy electrons. Bremsstrahlung production would also be far higher than that of hadron beams. The generated photons would occupy a higher energy spectrum (Equation 2.61) than those generated from low energy electrons, and thus may contribute more to the total dose. Neutron production could also be a concern for VHEE beams in both the scatterers and collimator, as discussed in Chapter 2.

Simulation based studies have been carried out to assess dose distributions generated from dual-scattering systems in the VHEE regime with both MC simulations and an analytical approximation [198]. It was found that for a typical setup for production of 100x100 mm^2 uniform fields, 1 m downstream of a dual-scattering system, secondary photons could indeed contribute significantly to the final dose distribution. This component could be detrimental to production of transverse dose uniformity, as scattered photon distributions are of a different shape to the Moliere profiles expected from the primary beam. This study only formed a small part of the work however, and more general characterisation of dual-scattering foil usage in the VHEE regime should be carried out. The use of the word "foil" may not seem appropriate in many cases due to the required thicknesses for VHEE scattering; this is simply a convention and not necessarily representative of the system geometry, especially when such a system is composed of plastic or aluminium. For example, the 3D printed dual-scattering system described in Chapter 5 has an S1 and S2 longer than 1 cm.

4.1.2 Aim

The purpose of this chapter is to summarise the concerns and considerations for scattering foil operation in the VHEE regime more broadly than previous work, assessing appropriate setups, materials and typical assumptions for provision of dose uniformity in the patient. This is carried out through the study of systems with the aim of delivering a 75 mm uniform radius beam to the virtual patient for coverage of a large transverse tumour size. Discussions of practical implementation of dual-scattering foils are also given, with studies on misalignment, collimation and modelling of evolution of flattened beams in water (as an approximation to patient tissue). These also represent the basis of the simulation work carried out for comparison with experimental values in Chapter 5. Methods for designing and optimising scattering foils in the VHEE regime based on arbitrary constraints are also discussed, culminating in an automated design pipeline using MC dose calculations and a similar optimisation of the dose profile as that used in Chapter 3.

4.2 Methodology of Monte-Carlo Simulations

TOPAS [217, 218] is a wrapper and extension for the MC beam tracking code GEANT4 [100], allowing detailed and complex simulations to be initialised and run using a far higher level, script based interface than that available in GEANT4. This can be optionally extended with custom GEANT4 scripts. Beams of arbitrary particle, energy and distribution can be generated, from phase-space distribution, Twiss parameters, or imported from a phase-space file (for example, from the

output of tracking codes). Users should note however that the TOPAS implementation of emittance must explicitly include a line defining the proportion of the phase-space ellipse defined by emittance as equal to 0.395 to be equivalent to the relationships in Chapter 2 (this value is the fraction of particles enclosed within 1σ radius for a 2D, Gaussian beam profile). For the purposes of this thesis, the physics packages were kept to their default settings, which were deemed appropriate for these moderately simple geometrical setups. This was with the exception of the studies on neutron production carried out in Section 4.6, where the `QGSP_BERT_HP_EMZ` physics list was used to simulate photo-nuclear interactions, which was otherwise unnecessary. The default physics package of TOPAS MC includes the Wentzel-VI MCS GEANT4 model [219] for accurate computation of the beam scattering in foils and transverse evolution in water.

All TOPAS simulations in this chapter (and Chapter 5) were carried out using a bundled set of scripts in Python 3, acting as an interface to the already high-level TOPAS. The parent class in this module initialised the TOPAS `.txt` script, set file-paths and defined the computational availability of CPUs (number of threads). Several child classes were available to insert components of the simulation; beams, materials, magnetic field elements, scoring surfaces and phantoms of arbitrary characteristics. The finalised script was then run and output files passed to scripts for analysis. Functions were defined such that many series of TOPAS scripts could be rapidly generated and run with simple functions and relatively little input from the user. Consideration of packaging of these functions into a graphical user interface was given (hence the naming of the parent class as "guiScript.py"), but time constraints prevented this idea from coming to fruition. These TOPAS wrapper scripts and all scripts used for analysis throughout this thesis are publicly available at `https://github.com/gilettejr/dosimetry`.

Unless otherwise stated, simulations were carried out with 10^7 primary particles for phase-space intensity scoring, and 10^6 particles for voxel dose scoring in water phantoms. Statistical errors were retrieved from repeating simulations in 5 cycles - in most cases, these errors were dominated by uncertainties in fitting, however. The University of Oxford Particle Physics batch processing farm utilising HTCondor was heavily used during these extensive MC simulations. The analysis scripts (also available at the same Github repository) were comprised of various sorting and fitting routines, capable of taking TOPAS phase-space, dose profiles, and images of YAG or radiochromic film data (see Chapter 5) as input for comparative analysis. As previously, the goal of uniformity for transverse profiles was such that large-scale variation was under 10%, with this characteristic primarily verified with fitting functions for applicability to experimental data with noise or anomalous values.

4.3 Single Scattering

Consideration was firstly given to the single-scattering of VHEE beams for uniform beam production. Sufficient beam magnification would clearly result in uniformity within an arbitrary definition, and for some applications where dose transmission is not important, this method may be used. However, for the purposes of UHDR and FLASH, such a high loss of transmission would be undesirable. Integration of Equation 2.63 from zero to r_{90} demonstrated that transmission of the uniform radius without any flattening would be under 10%. Whilst single scattering was likely to be the most straightforward method, the higher transmission of the uniform component in a dual-scattering system was much preferred. Instead, studies of VHEE scattering in S1 alone were carried out to assess particle production, beam enlargement and effects on dose before flattening would take place with S2.

In line with typical dual-scattering systems and previous studies [198, 220, 221], S1 was chosen to be composed of tantalum. The target position was initially defined 1 m downstream of the upstream edge of this scattering foil, again a typical placement in scattering studies. The "patient" in this case was modelled as a 300x300x300 mm^3 water phantom split into 50x50x15 voxels for dose scoring. The beam was defined immediately at the upstream edge of S1; effects of scattering from vacuum windows or air were neglected, as the effects particularly from air in the VHEE regime was shown to be minimal in comparison to the foils. The initial beam was chosen to have a small Gaussian transverse intensity distribution, with σ_x=σ_y=0.1 mm and 0 divergence (a pencil beam, for simplicity). The beam energy was retained at 200 MeV unless stated otherwise with zero initial energy spread. This geometrical layout taken from the graphical user interface in TOPAS showing the beam location, S1 and water phantom is shown in Figure 4.2.

Simulations to evaluate the evolution of the beam-size with increasing thickness of S1 were carried out, particularly in reference to the predictions of Equation 2.59. The values of σ were determined from Gaussian fits of the transverse electron density profiles at the patient surface, using the phase-space scoring capabilities of TOPAS. An example of these fits displayed in a manner typical of visualising transverse beam distributions throughout both this chapter and Chapter 5 is shown in Figure 4.3. These profiles are displayed both in 2D, and in 1D from 1 mm slices in x and y. The 1D fits shown were typically used for beam characterisation particularly from Section 4.5 onwards for both consistency with the other chapters of this thesis, and the rather excessive number of variables in the 2D shaped and skewed super-Gaussian functions resulting in inconsistencies with 2D fitting. Slice thickness was dynamically chosen based on the beam-size to balance statistics

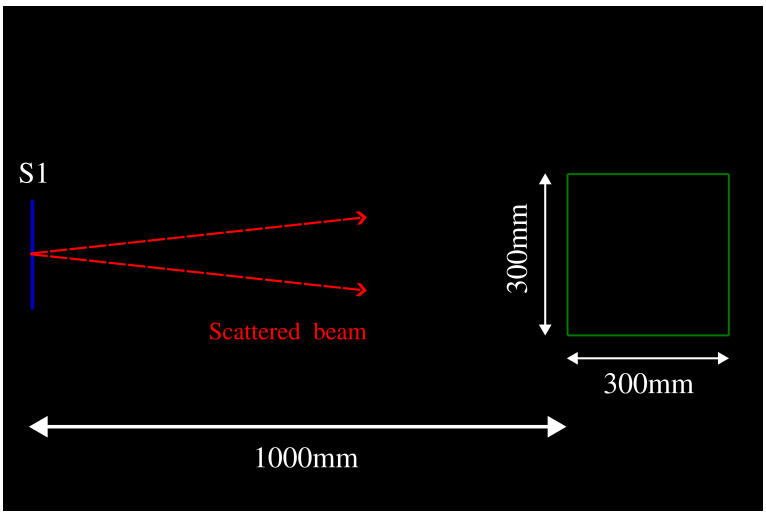

Figure 4.2: Reference setup in TOPAS, with beam in red entering from left-hand side, being scattered by S1 and entering green water phantom on right-hand side.

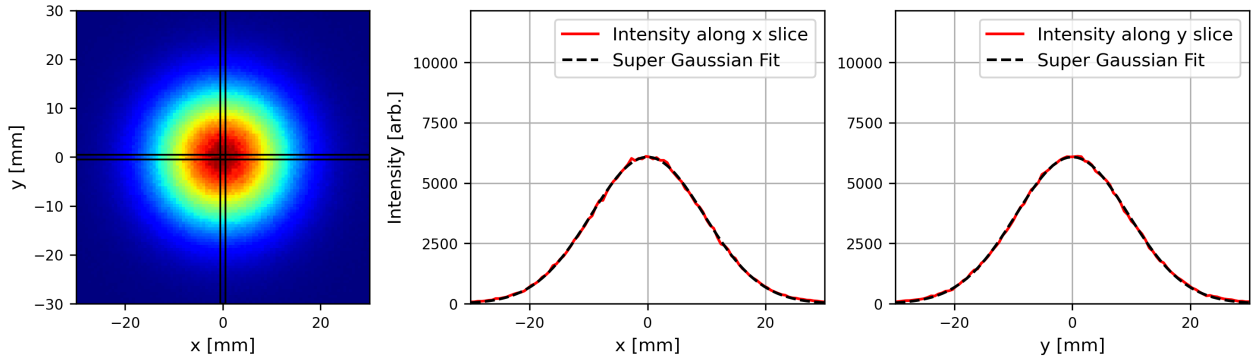

Figure 4.3: 2D transverse primary beam intensity histogram (left), beam intensity against x (middle) and y (right) from indicated slices across distribution, with (super) Gaussian fits shown. Extracted from TOPAS simulation of arbitrary single-scattered beam.

with curvature of the profiles. Errors from fitting were extracted from the covariance matrices of the fits and propagated appropriately. The thickness of the tantalum S1 was scanned from 0.1 mm to 4.91 mm, to produce a range of beam-sizes up to 75 mm according to Equation 2.59. Generated secondary particles were also captured by the phase-space scorer. The evolution of the transverse primary beam-size at the water phantom surface with increasing S1 thickness is shown in Figure 4.4.

Whilst the Gaussian approximation and simulations were in excellent agreement for small scattering angles (below 10 mrad), these diverged significantly with thicker scatterers - especially above 30 mrad where the discrepancies rose above 10%. This was explained by the significant rise in photon production and mean energy reduction with thickness. The secondary photon transverse distributions were non-Gaussian as expected from previous work, confirming likely challenges in treating the primary and secondary components as homogeneous when designing scattering foils. The more sharply peaked photon distributions could be reasonably well modelled with Lorentzian

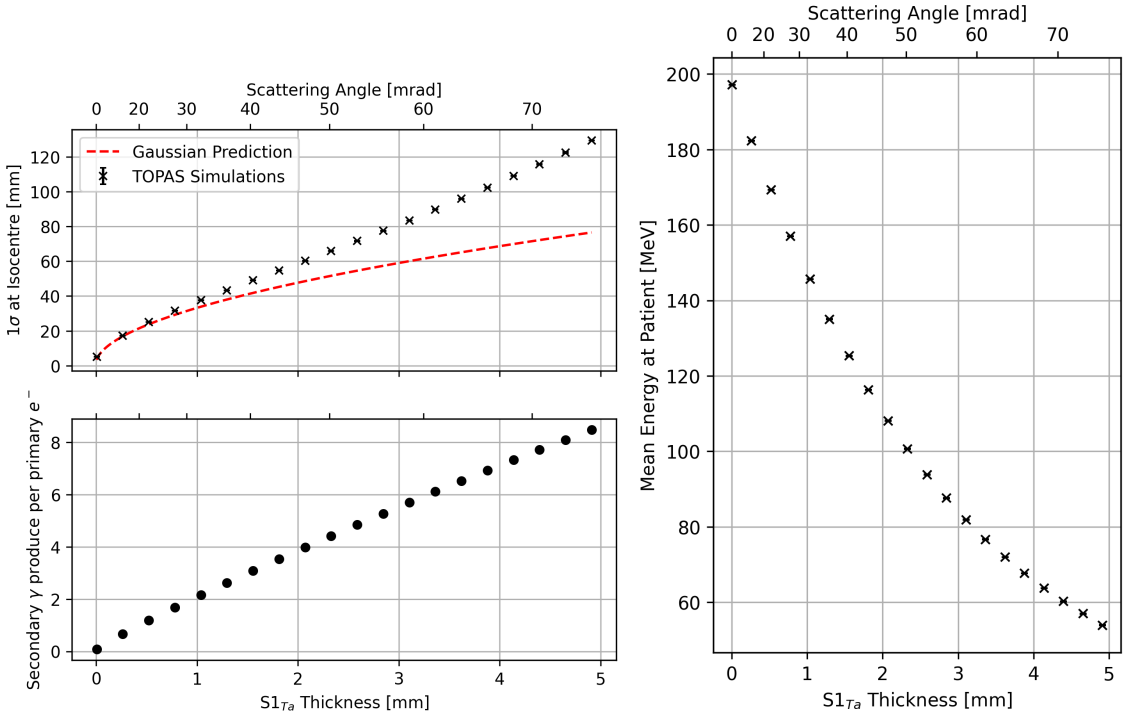

Figure 4.4: Beam-size from Gaussian fits with prediction from Equation 2.59 indicated (upper-left) and photon production (lower left), against thickness in tantalum S1. Beam energy at surface of water phantom against tantalum S1 thickness (right). Scattering angles also indicated. Extracted from TOPAS simulations with single-scattering reference setup.

functions to describe their transverse size. The photon distribution generated from the initial reference beam passing through a 0.1 mm tantalum foil (identical setup as that used to generate the electron distribution shown in Figure 4.3) is shown in Figure 4.5.

When repeating these simulations with lower energies (and thus lower tantalum thicknesses to cover the same predicted scattering range), agreement between Equation 2.59 was retained at progressively higher scattering angles. This confirmed that the discrepancies were likely dependent on the losses from passage through the material. This was verified through direct measurements of the photon profiles produced from beams with different energies but constant scattering angle (from Equation 2.59 as before). Photon production was still high in terms of the gross number of generated particle compared to the primary beam, but significantly lower for the lower energies - even at small scattering angles where the approximation and simulations were in good agreement. These comparisons for a production of a 30 mrad scattering angle are shown in Figure 4.6. The reasoning for using a high-Z material for S1 according to the convention set by [213] is clearly demonstrated also in Figure 4.6. Photon yield from scattering at a certain angle is higher for lower-Z materials such as aluminium, or plastics like nylon, Poly-Lactic Acid (PLA) or Polyether-Ether-Ketone (PEEK). Thus, a higher-Z material would scatter with improved efficiency. Difference in gross photon yield between tantalum and nylon were 29% at 200 MeV. An additional concern with

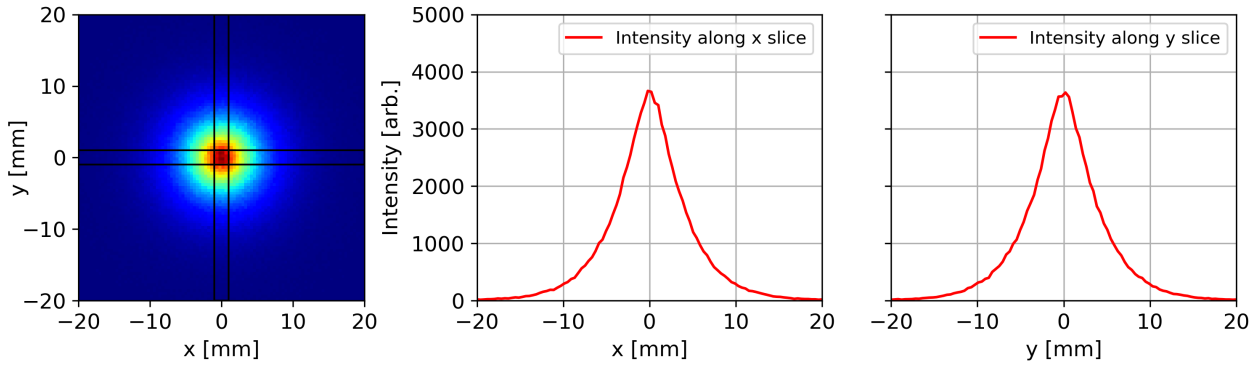

Figure 4.5: 2D transverse secondary photon beam intensity histogram (left), beam intensity against x (middle) and y (right) from indicated slices across distribution. Extracted from TOPAS simulation with reference single-scattering setup, at water phantom surface.

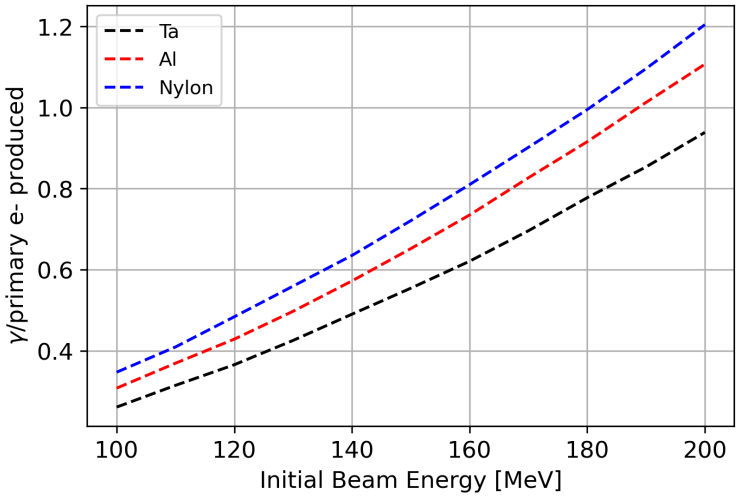

Figure 4.6: Photon yield per primary electron against initial beam energy measured at water phantom surface from S1 producing constant 30 mrad scattering angle according to Equation 2.59 (0.9 mm Ta at 200 MeV). Results from three scattering materials for S1 shown, produced from TOPAS simulation with single-scattering reference setup.

the use of thicker, lower-Z foils for scattering would be the physical space required - PLA and PEEK scatterers have been implemented in some scattering foil experiments (see Chapter 5), but to produce equivalent scattering angles to 5 mm tantalum for example, a thickness of approximately 20 cm PLA would be required.

Whilst the above simulations confirm many of the concerns regarding photon production and resultant energy loss and spread from significant scattering of VHEE electrons, the main area of investigation was the impact on the dose distribution itself. The wide energy spread and relatively lower mean energy of the photon distributions (shown in Chapter 2) was predicted to result in lower dose deposited per particle than the electrons, although these would still be expected to penetrate deeply into the water phantom. Dose in the water phantom in the reference setup was scored to investigate the dose components for three tantalum foil thicknesses: 0.12 mm, 0.42 mm and 0.90 mm

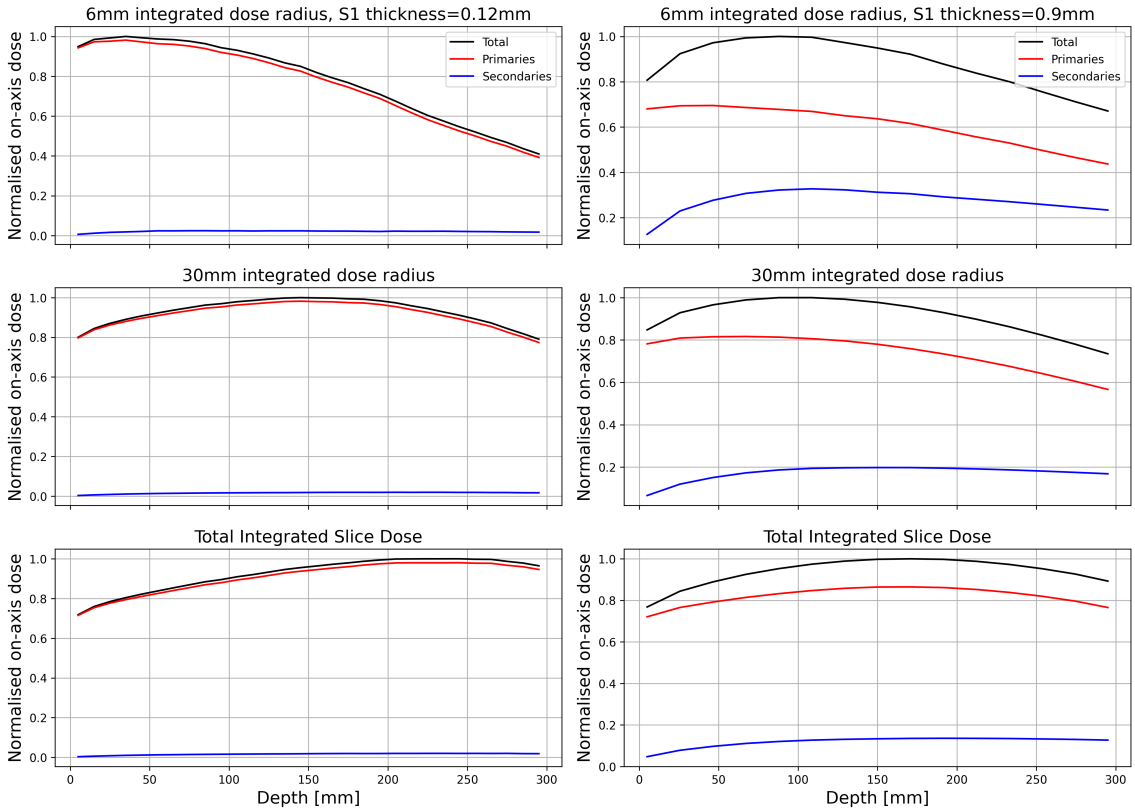

Figure 4.7: Normalised dose scored in water phantom against depth in water, from TOPAS simulations of reference setup. Components from total, primary and secondary (generated in S1) beams indicated. Shown for 0.12 mm (left), and 0.9 mm (right) tantalum foil thicknesses (10 and 30 mrad scattering angles respectively). Dose integrated across 6 mm (top), 30 mm (middle) and total (bottom) transverse radii.

These thicknesses were chosen to produce scattered beams with of 1σ = 10 mm, 20 mm and 30 mm at the water phantom surface in the single-scattering reference setup respectively from Equation 2.59 (corresponding to scattering angles of 10, 20 and 30 mrad from S1).

On-axis dose measurement results are shown in Figure 4.7 for the first and last case, with Figure 4.8 displaying a sample of the transverse dose profile for the highest scattering angle case (30 mrad). Dose components were explicitly split into dose arising from the primary electron beam, and dose arising from the secondary electrons and Bremsstrahlung photons from the scattering foil (in Figure 4.7, the majority of secondary dose was from photons rather than the small number of secondary electrons). This was achieved by inserting a "splitting" phase-space scorer immediately downstream of the scattering foil and regenerating the individual components separately from the same location. This removed any ambiguity in the origin of the particle histories imparting dose into the water phantom.

The dose distributions in Figure 4.7 demonstrated significant photon dose contributions for the 30 mrad (0.90 mm) scatterer, particularly in the central regions of the dose profiles where the sharp

photon peaks would be most dominant. This represented over 30% of the total on-axis dose at the peak depth. At higher scattering angles, the photon distribution would eventually become locally dominant over the primary electron contribution to dose. The relative contribution of the secondary photons grew further into the phantom, with the primary component gradually decreasing and secondary component remaining relatively constant throughout.

This contribution from secondary particles have to be considered when approaching the design of the dual-scattering foil, which would typically base the design of S2 on a near-Gaussian MCS dominated primary electron beam. The secondary X-rays would not be scattered at the same angles as the electrons and thus whilst a uniform electron dose contribution may be generated, the photon component would not be uniform. As expected, the Bremsstrahlung dose contribution decreased with beams of progressively lower energies as expected from reduction of the total photon yield shown in Figure 4.6. These results demonstrated that production of secondary particles in S1 could be very significant even for small scattering angles of VHEE beams.

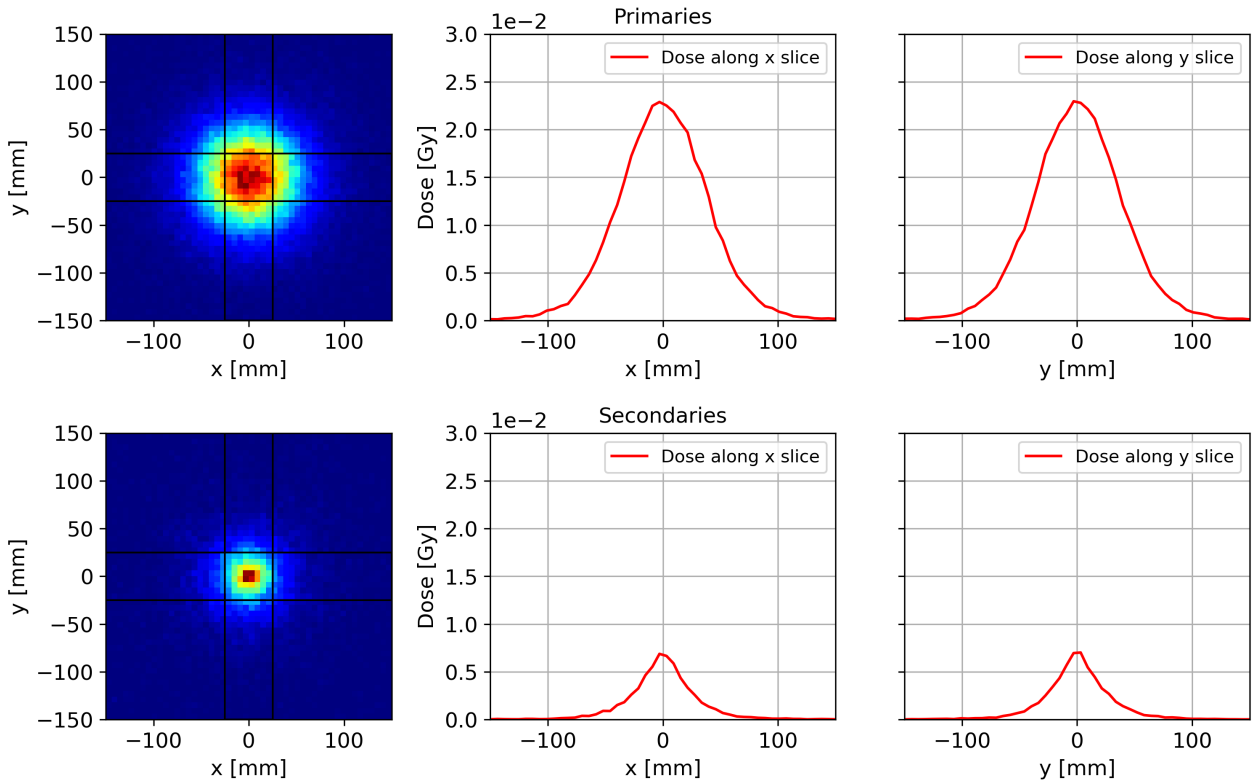

Figure 4.8: 2D transverse dose histograms (left), dose against x (middle) and y (right) from indicated slices across distributions. Primary beam dose component (top) and secondary beam dose component (bottom) shown. Extracted from TOPAS simulations with reference single-scattering setup and 0.9 mm Ta S1 (30 mrad scattering angle). Measurement taken at peak of on-axis total dose, 80 mm depth in water phantom. 1 nC accumulated charge in simulation.

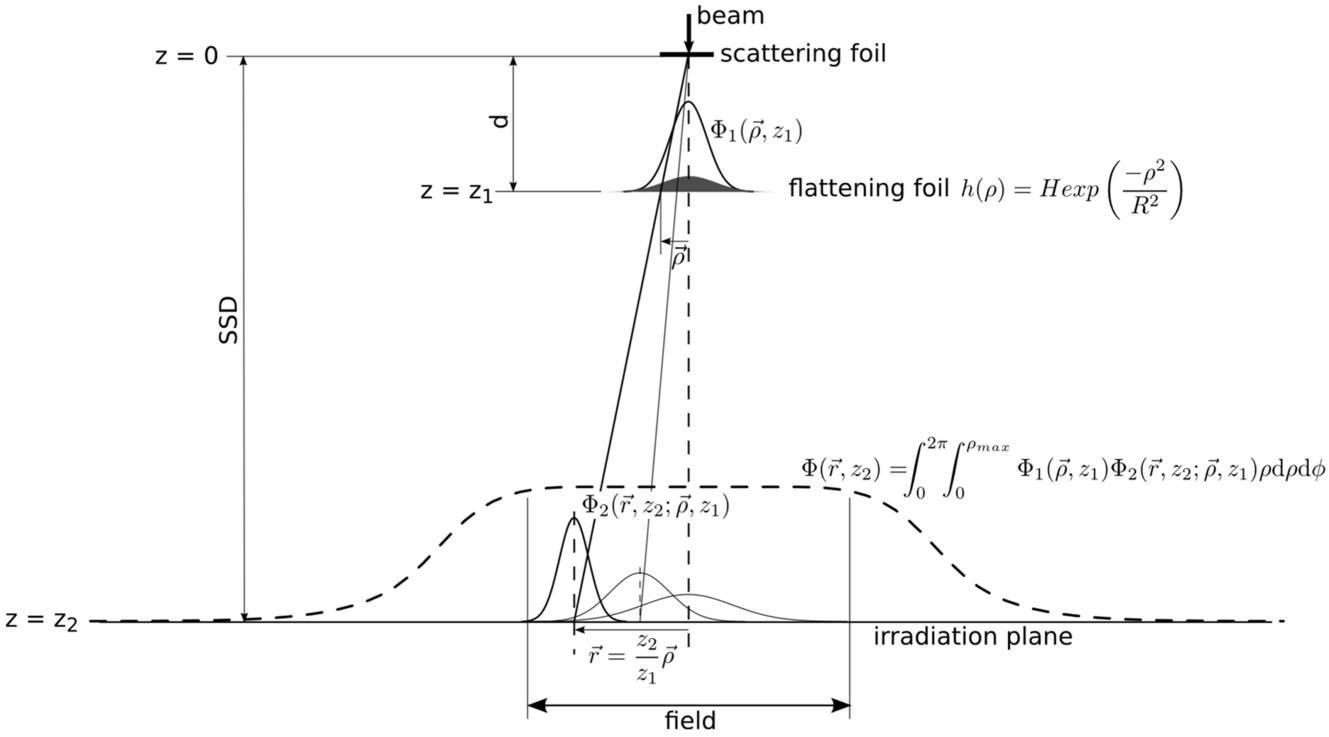

Figure 4.9: Relevant scattering parameters for analytical design method. Image from [220][02].

4.4 Analytical Design of Dual-Scattering Foils

Despite the likely challenges from scattering in the VHEE regime, design of the dual-scattering foil was initially approached using the typical methods developed for other modalities of RT. The analytical method of [213] was used, inserting S2 10 cm downstream of S1 in the reference setup of Figure 4.2 as is standard convention in such geometry [198]. A brief description of this typical design process as also covered by [222, 220] is given here.

The dual-scattered *fluence* (intensity) profile can be modelled as a convolution of the two scattered distributions. Mathematically, this is given by

$$\Phi(\vec{r}, z_2) = \int_0^{2\pi} d\phi \int_0^{\rho_{max}} \Phi_1(\vec{\rho}, z_1)\Phi_2(\vec{r}, z_2; \vec{\rho}, z_1)\rho d\rho \tag{4.1}$$

where $\vec{r}$, $\vec{\rho}$, z_2 and z_1 are shown in Figure 4.9, Φ_1 is the scattered fluence distribution from S1 approximated with Equation 2.59 with $t = t_{S1}$, the thickness of S1, and Φ_2 is given by

$$\Phi_2 = \frac{1}{2\pi}\exp\left(-\frac{-(\vec{r} - ((z_2/z_1)\vec{\rho})^2)}{2\sigma_1}\right). \tag{4.2}$$

σ_1 is split into three components:

$$\sigma_1^2 = \sigma_{init}^2 + \sigma_{sec}^2 + \sigma_{air}^2 \tag{4.3}$$

where these components are derived from the initial beam divergence, scattering in S2 and the air between the scatterers respectively. σ_{init} and σ_{air} can be simply calculated using Equation 2.59 once again, although the former is very small for 200 MeV electrons traversing 10 cm in air and can thus be generally neglected for this application with electrons at 200 MeV. σ_{sec} is slightly more complex due to its dependence on the shape of S2 and as such is given by inserting the thickness of S2 at a certain radial distance ρ:

$$h = H \exp\left(-\frac{\rho^2}{R^2}\right) \tag{4.4}$$

into the Moliere approximation once again. H is the maximal thickness of S2 and R is the "width" of S2, equivalent to $\sqrt{2}\sigma_{S2}$ where σ_{S2} is the standard deviation if the physical shape of S2 were translated into a distribution. Thus, σ_{sec} has a functional form $\sigma_{sec}(h)$. This equation could not be analytically solved mainly due to the multiple exponentials in the convolution equation. It is normally numerically solved and optimised by adjusting H and R according to the desired flat radius, uniformity requirements and geometrical constraints. The first stage of dual-scattering foil design is typically [213] defining the thickness of S1 such that the Gaussian profile is at 60% of its maximum, i.e

$$f(r) = 0.6 = \exp\left(-\frac{r^2}{2\sigma^2}\right) \tag{4.5}$$

where r is the desired uniform radius. Thus,

$$\sigma = \sqrt{\frac{r^2}{2\ln(0.6)}} \approx 0.99r \tag{4.6}$$

It is immediately clear from the studies of Section 4.3 that magnification up to σ=75 mm as required to reach a uniform radius of 75 mm with S1 would result in extremely high photon production. It would also require modification of σ_{init} in Equation 4.3 to account for the deviation from Equation 2.59 to appropriately flatten even just the uniform component. Thus, when outlining this design process here, production of uniform beams with r_{90}= 10, 20 and 30 mm uniform radii in the original 1 m configuration of Figure 4.2 was studied before scaling up of the system geometry for the 75 mm goal case described in Section 4.5. An aluminium S2 was assumed as this is commonly chosen for ease of manufacture; the shaping of S2 is simpler with lower Z and thus thicker materials. The impact in terms of scattering efficiency from using a low or high-Z S2 is minimal, as

[02]Reprinted from Przemysław Adrich: "A new method for designing dual foil electron beam forming systems. I. Introduction, concept of the method". Nuclear Instruments and Methods in Physics Research Section A: Accelerators, Spectrometers, Detectors and Associated Equipment 817. Copyright (2016), with permission from Elsevier.

discussed also in Section 4.5. One of the key approximations (and reasons for development of a more advanced method) of the technique described here is assumption of an initial beam where the beam-size was dominated by scattering as the position of S2. This was the reason for the choice of a very small initial beam for the reference setup rather than the larger 1 mm beam used for the studies of Chapter 3.

Optimisation of the H and R parameters of Equation 4.4 was carried out again using the Scipy minimization routine in Python to find an analytical fluence function with 10% or better uniformity across the 10, 20 and 30 mm radii for a 200 MeV VHEE beam. This optimisation was based upon minimisation of a transmission merit function term, and a uniformity term. The former was minimised with increased value of the integral of the analytical function within the flat-top radius. The latter was minimised when peak-to-valley uniformity within the desired flat-top radius reached 10%. Numerical integration was also carried out using the Scipy library. The algorithm was poor at accounting for cases where the S1 scattered beam was much larger than S2. Attempts were made to modify the method to include initial beam parameters, but given the other approximations involved, it was determined that this would not be worthwhile and an alternative method was eventually devised (see Section 4.7). Figure 4.10 demonstrates the solution found for the 10 mm r_{90} case along with the evolution of the beam loss index (transmission merit function term) and peak-to-valley uniformity during optimisation of the merit function.

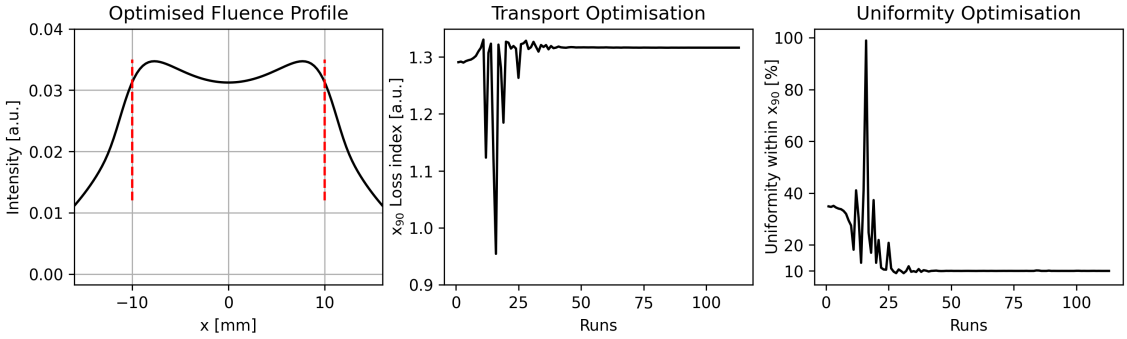

Figure 4.10: Predicted optimised fluence against radial displacement from 10 mm uniform radius design with analytical formalism of [213] (left), beam loss index (middle) and uniformity across 10 mm radius (right) against iteration number during optimisation.

Validity of the analytical solutions was confirmed by inputting the foil designs into TOPAS and studying the resultant transverse intensity profiles from the MC simulations. For the generation of S2 in TOPAS, a routine in the Python module was implemented. A smooth Gaussian function was generated from inputs (maximum thickness and value of σ_{S2}, along with the maximum radial extent (cutoff) of the physical shape; typically this was chosen to be $3\sigma_{S2}$ to prevent generation of extremely thin slices). The shape was then constructed up by incrementing along the x-axis from

the maximum radius and generating slices under the distribution until the final shape was formed. The number of slices could be defined to produce an effectively smooth shape, or alternatively only compose the shape out of a few slices for ease of manufacture. The effect of these choices on final distributions is described at the end of this section. Additionally, a minimal slice thickness could be explicitly enforced (this was often necessary for generation of very smooth scatterers as TOPAS has a tendency to return stuck tracks for extremely thin material slices).

Thus, for these TOPAS comparisons, the output of the analytical optimisation was inserted directly into the scatterer generator and 100 slices were used to mimic the ideal, smooth shape assumed by the analytical formalism. The geometry of each S2 was verified between the TOPAS and analytical models to confirm successful translation between the codes. Characterisation of the dual-scattered profiles produced by the designed systems was achieved using the shaped super-Gaussian functions described in Chapter 4. The optimised objective profiles were typically hollow; these were well described by allowing the shaping parameter of Equation 2.74 to rise above zero. During simulations of optimal setups, there was no source of asymmetry and thus the skew parameter $k_{x,y}$ could be constrained to zero (although this can be used to characterise misalignment as described later in this section).

The results of the TOPAS simulation are shown for the 10 mm case in Figure 4.11 with specific foil geometry for all three cases in Table 4.1. Even with these fairly small scattering angles com-

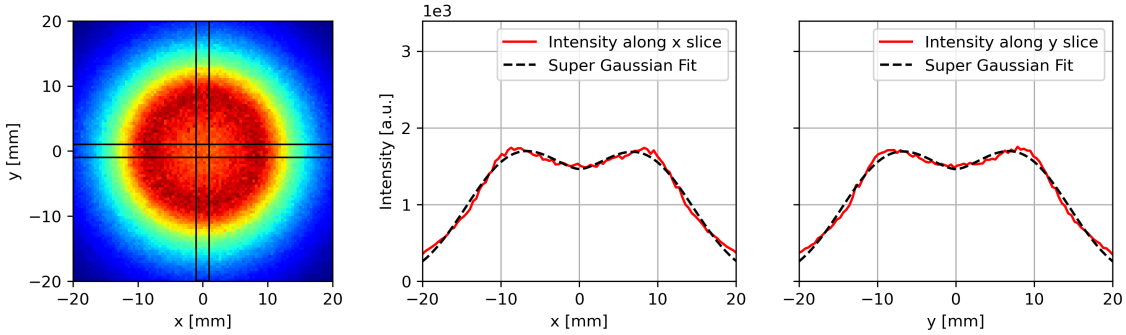

Figure 4.11: 2D transverse primary beam intensity histogram (left), beam intensity against x (middle) and y (right) from indicated slices across distribution, with super-Gaussian fits shown. Extracted from TOPAS simulation of beam after passage through dual-scattering system with geometry described by Row 1 of Table 4.1. Measurement taken at water phantom surface in reference setup.

pared to that required in a more compact clinical system, there were notable discrepancies between the analytical prediction and results from TOPAS in terms of the transverse beam profile. With increasing foil thickness, there were progressively sharper double peaks in the 1D profiles in the TOPAS simulations compared to the analytical predictions, thus worsening the local uniformities. In all three cases, directly using the analytical designs did not produce the desired objective profiles

in terms of electron fluence at the patient - due to both increasing of peaking in the profiles and size of the profiles. The character of these profiles was best represented by two measurements: the r_{90} referring to the region outside of which the intensity decreased to 90% of the maximum, and the uniformity assessing any variation inside this r_{90} - necessary to prevent large rings (double peaks in 1D) in the profiles. The fits were used to characterise these values - these were preferred over the direct measurements as dose scoring in the water phantoms of this chapter were typically limited by resolution. Accuracy between fits and direct measurements for profile characterisation was verified through comparisons with intensity profiles. At higher scattering angles, the thickness of

Table 4.1: Comparison between analytical ($an.$) predictions and TOPAS results for dual-scattering foil designs for different uniform extents at water phantom surface. TOPAS measurements taken from fits to profiles; within statistical uncertainty of direct measurements. "Uni" refers to full (peak-to-valley) variation of fitted profiles within uniform radius r_{90}.

$r_{90}^{an.}$ [mm]	t_{S1} [mm]	H [mm]	σ_{S2} [mm]	Uni.$_{an.}$ [%]	Uni.$_{TOPAS}$ [%]	r_{90}^{TOPAS} [mm]
10	0.12	0.53	0.42	10.0	12.7±0.5	10.2±0.1
20	0.42	1.859	0.92	10.0	17.8±0.2	21.7±0.6
30	0.90	4.26	1.2	10.0	22.0 ± 0.2	33.0±0.5

the required scatterers and reduction in mean energy resulted in even more heavily ringed profiles due to the substantial particle production and energy spread from passage through S1. These results demonstrated that the analytical method alone was unlikely to be sufficient for scattering foil design in the VHEE regime, with additional concerns likely to arise from the secondary particle contributions to dose shown in Section 4.3.

The analytical solutions could be tweaked by modifying the shape directly in TOPAS to retrieve appropriate uniformity in the electron fluence profile. This would have been a rather arduous process when using the direct uniformity measurements as these required around 10^7 particles for each iteration to reduce statistical uncertainty; the shaped super-Gaussian fits were in this case a useful tool for optimising uniformity, as they accounted for noise and fluctuations were fairly small for simulations of 10^6 particles. The double peaking could be reduced by increasing the radius of S2, and any resultant increase in the width of the uniform extent decreased by reducing the height H of S2. For these corrections, the effect on transmission of the scattered beam was not taken into account; within the virtual collimator, this still remained significantly higher than predicted results from uniformity with single scattering, at around 30%. This process of approximation and slight modification of S2 was deemed an appropriate basic method for minimal scattering design, which was also initially used for the design of the system for general characterisation in Section 4.5. A more advanced and general optimisation technique for application to numerous scenarios is discussed in Section 4.7.

4.5 Characteristics and Practical Considerations of Large, Flattened Beams from Dual-scattering Foils

From the results of Section 4.3, it was clear that the secondary Bremsstrahlung profile could be a considerable contribution to dose in the local on-axis region, for scattering angles of 30 mrad and above, or even below this depending on the irradiation depth and geometry of the setup. Thus, the goal for this section was to determine the impact of the secondary photons on the uniformity for the three scattering angles covered in the previous two sections - 10 mrad, 20 mrad and 30 mrad. Of more interest than the small beams generated from these scattering angles in the reference layout were the characteristics of the ideal 75 mm beam at the water phantom surface, generated from the dual-scattering foil; the geometrical setup was thus scaled up appropriately.

TOPAS could be used to study and characterise the evolution of the flattened beam in water, and consider effects of misalignment of the scattering foils given this geometry. The 1 m distance requirement between S1 and phantom from the reference setup in Section 4.3 was thus relaxed for these studies. The initial transverse phase space distribution, energy, S1 material (tantalum), S2 material (aluminium) and water phantom geometry were retained. Ideally, the specific results on scatterer optimisation, particle production and produced beams would be compared to previous work of Deut et al. [198]; this was not possible as the geometry of the scattering system was not specified in that work. The three new scattering systems were designed as specified in Section 4.4 with their geometry described in Table 4.2 and their positioning shown in Figure 4.12. The principle of S1 producing approximately 1σ equal to the desired uniform radius and S2 being placed 10 cm downstream of S1 was initially retained to define the system geometries. The designed dual-scattering systems are shown in Figure 4.13. From here onwards, these 3 simulation and scatterer setups as referred to as the 10 mrad, 20 mrad and 30 mrad setups, respectively.

Table 4.2: Scatterer geometries and required phantom positioning for production of 75 mm uniform component for 3 scattering angles. H and σ_{S2} refer to quantities for S2 geometry described in Section 4.4. t_{S1} is the thickness of S1.

S1 scattering Angle [mrad]	Phantom Position [mm]	t_{S1} [mm]	H [mm]	σ_{S2} [mm]
10	7500	0.10	0.521	0.42
20	3750	0.29	2.01	0.95
30	2500	0.80	3	1.5

Simulations of dose deposition in the same water phantom were carried out to assess the beams from these three setups. As before, the dose was separated into primary and secondary components from particles generated inside the dual-scattering system. Secondary particle generation was heav-

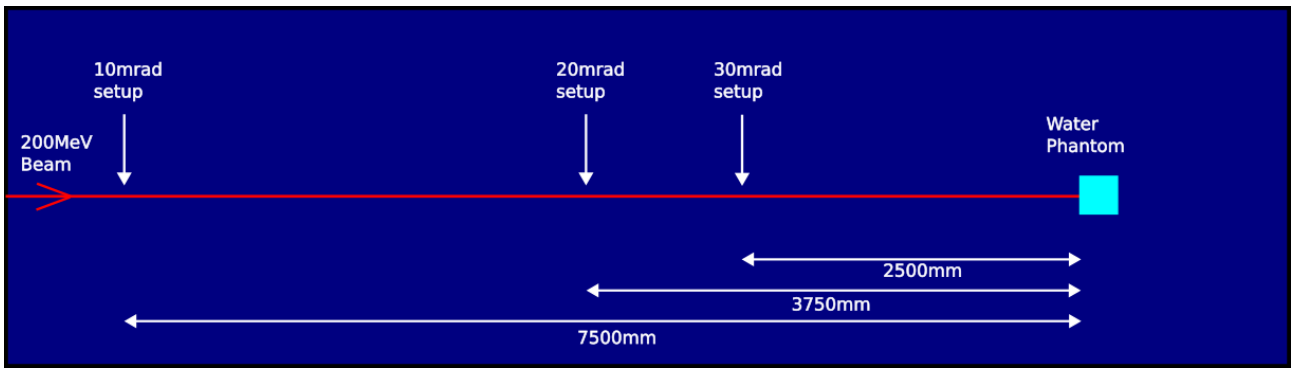

Figure 4.12: Schematic showing locations of S1 in the three scattering setups relative to water phantom as described in Table 4.2 used in TOPAS simulations. S2 placed 100 mm downstream of S1 for each setup.

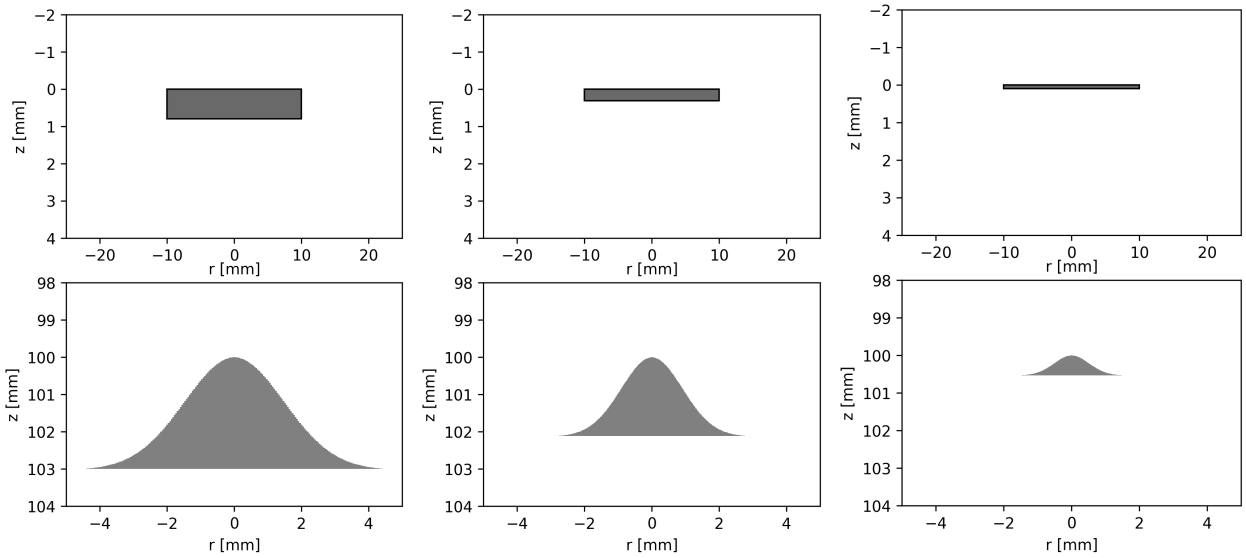

Figure 4.13: Geometrical visualisation (longitudinal positioning vs radial extent of slice) of scattering systems for production of 75 mm dual-scattering profile with 30 mrad (left), 20 mrad (middle) and 10 mrad (right) divergence angles, described quantitatively in Table 4.2. Systems are composed of tantalum S1 and aluminium S2.

ily dominated by S1, as expected due to the far higher scattering power than even the thickest portion of S2. This was a consequence of the choice to position S2 rather close to S1 - extensive simulations showed that this was the most efficient configuration overall in terms of particle production. For the 30 mrad setup, local dose contribution was rather high beyond the entrance bin of the water phantom as expected, especially very close to the centre of the distribution from the sharply peaked secondary photon beam. This was demonstrated by slices taken of the transverse dose distributions, displayed at the entrance, centre and exit of the phantom in Figure 4.14.

Whilst the total dose distribution at the entrance to the phantom was uniform up to 75 mm as expected from the fluence distribution achieved during design, the significant secondary component resulted in a loss of uniformity beyond the first 20 mm voxel into the phantom for the 30 mrad case.

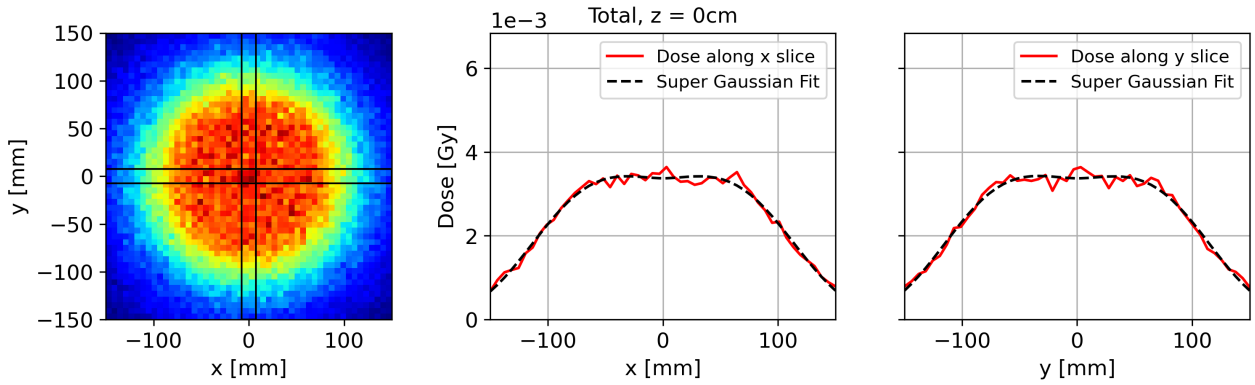

(a)

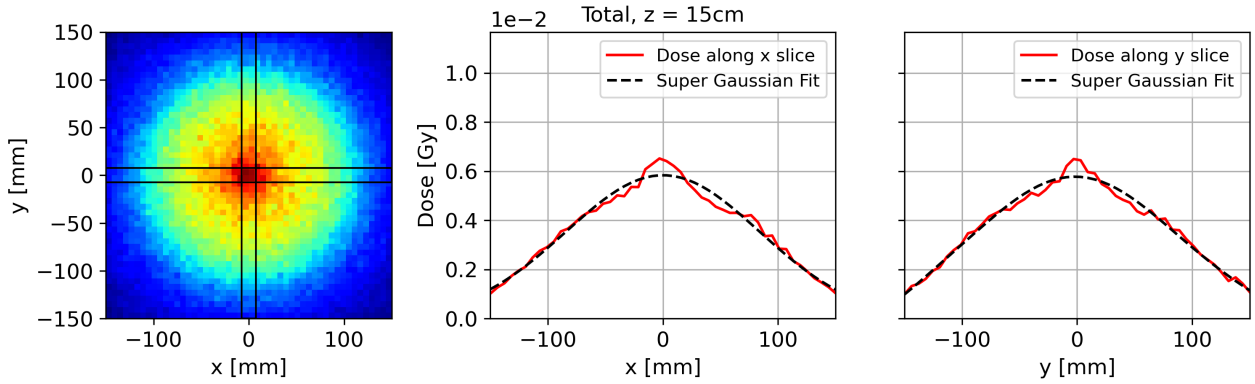

(b)

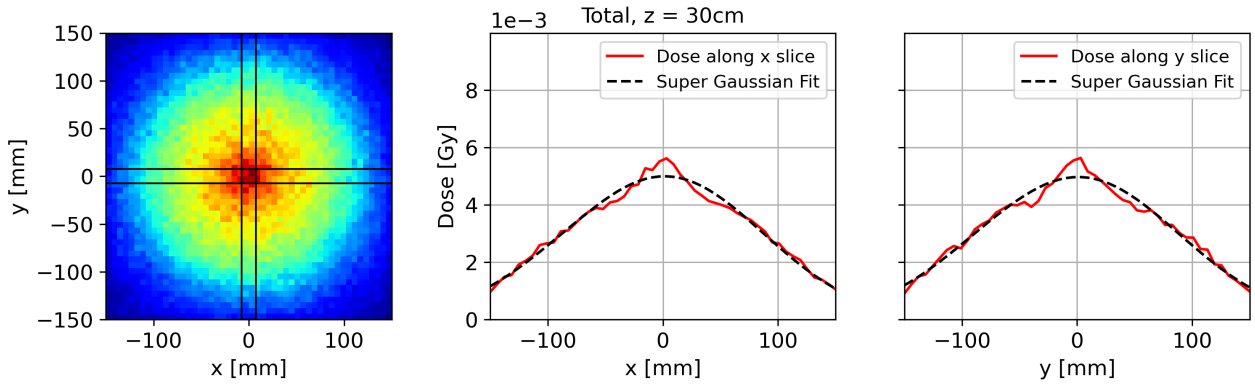

(c)

Figure 4.14: 2D transverse total dose histograms (left), total dose against x (middle) and y (right) from indicated slices across distributions, with super-Gaussian fits shown. Extracted from TOPAS simulations with 30 mrad dual-scattering setup. Profiles shown at entrance (a), middle (b) and exit (c) of 30 cm depth water phantom, with measurement positions indicated. Sharp central peak visible at depth from photon contributions generated in dual-scattering system.

The total dose component was poorly modelled by the super-Gaussian fits due to the photon component beyond this depth; arising as an additional sharper peak from the broader primary electron contribution. The dose contribution from photons generated from the scattering system was highest at the exit of the phantom, accounting for almost half of the total dose in the central bins. The primary dose component could be modelled separately, and its evolution through the phantom successfully characterised by the super-Gaussian fits. Evolution of the r_{90} and uniformity within this radius for the primary beam dose contribution are shown in Figure 4.15. r_{90} gradually increased, with local uniformity within a constant region gradually decreasing. This was due to both the lateral spread and reduction of double-peaks through the water phantom. Lateral parameters were moderately stable throughout the water phantom with an increase in 5.8% of the uniform region size due to scattering.

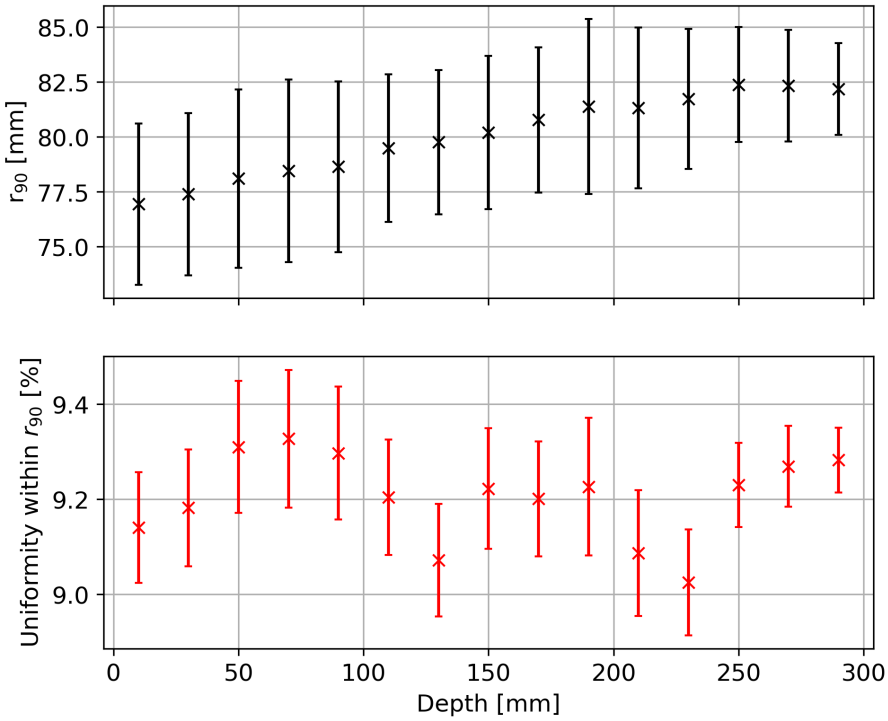

Figure 4.15: r_{90} (top), and peak-to-valley uniformity within r_{90} (bottom) against depth in water phantom, calculated from shaped super-Gaussian fitting of **primary** transverse dose components. Extracted from TOPAS simulation with 30 mrad setup in TOPAS. Errors propagated from covariance matrix of fitting results and statistical uncertainty derived from multiple simulation runs (errors dominated by the former).

When the 20 mrad setup was used, the total dose was well described by the super-Gaussian fits throughout due to the reduced particle production, with local photon dose becoming substantial only close to the exit of the phantom. Uniformity was also successfully retained throughout the entire phantom, although this diminished as the secondary dose component became more dominant throughout, with r_{90} decreasing from 73.0 mm at the surface bin to 57.3 mm at 300 mm depth.

Residuals of the fits demonstrated the presence of the localised photon contribution throughout; however, this was always within 10% of the flat-top dose. For the treatment of deep-seated tumours, uniformity would be retained as deeply as possible into the patient, as was the case for the 20 and 10 mrad cases where r_{90} of the total dose remained above 50 mm throughout the entire water phantom. The evolution of uniformity and uniform radius for both cases is shown in Figure 4.16. Unlike the primary component, the total dose component uniformities diminished through the phantom principally due to the eventual contributions from the secondary photon components. Thus, this occurred at a lower rate for the 10 mrad case compared to the 20 mrad case, with the uniform radius in the former setup reducing to 67.7 mm after passage through the phantom - a decrease of less than 10%. For this case, there was no evidence of the localised photon component in the fitting residuals.

For practical purposes and for ease of manufacture (for example, the systems utilised in Chapter 5) it may be appropriate to design Gaussian scatterers with only a few transverse steps. This would be expected to have some effect on the dose distributions, especially given the minimal scattering of VHEE beams from air. The 20 mrad scatterer from above was modified to a sliced composition, and intensity and dose distributions measured for systems with successively fewer slices. These altered scatterers are shown in Figure 4.17. All other parameters from the scatterer generator input were kept constant. The defining characteristic of the coarsely sliced systems was a series of "rings" created by the steps, most prominent very close to the scatterer itself (this phenomenon was also viewed experimentally during the work carried out in Chapter 5). With appropriate space downstream of S2 (depending on the specific system, geometry and step number), the beam divergence effectively "smeared" out the presence of these ridges inside the uniform radius itself, with the sharpest ridges present outside this and thus not of extreme concern. These rings were minimal in magnitude even when composing S2 from 5 steps.

In general, the recommendation of placing the scattering systems further upstream to reduce energy losses would serve the dual-purpose of also minimising the stepping effects. Even this would likely be unnecessary however; dose measurements using the 5-step S2 demonstrated that effects from the ridges were immediately removed due to MCS upon entry to the water phantom; transverse profile measurements in the water phantom from the 5 different step cases displayed in Figure 4.17 returned r_{90} and uniformity measurements within statistical uncertainty of each other throughout the water phantom. The intensity distribution displaying these rings from the 5-step S2 at the water phantom surface is shown in Figure 4.18.

Misalignment in the dual-scattering systems could produce tilts in the flat tops of the transverse distributions. This could be modelled by the fits with non-zero skew ($k_{x,y}$) parameters in

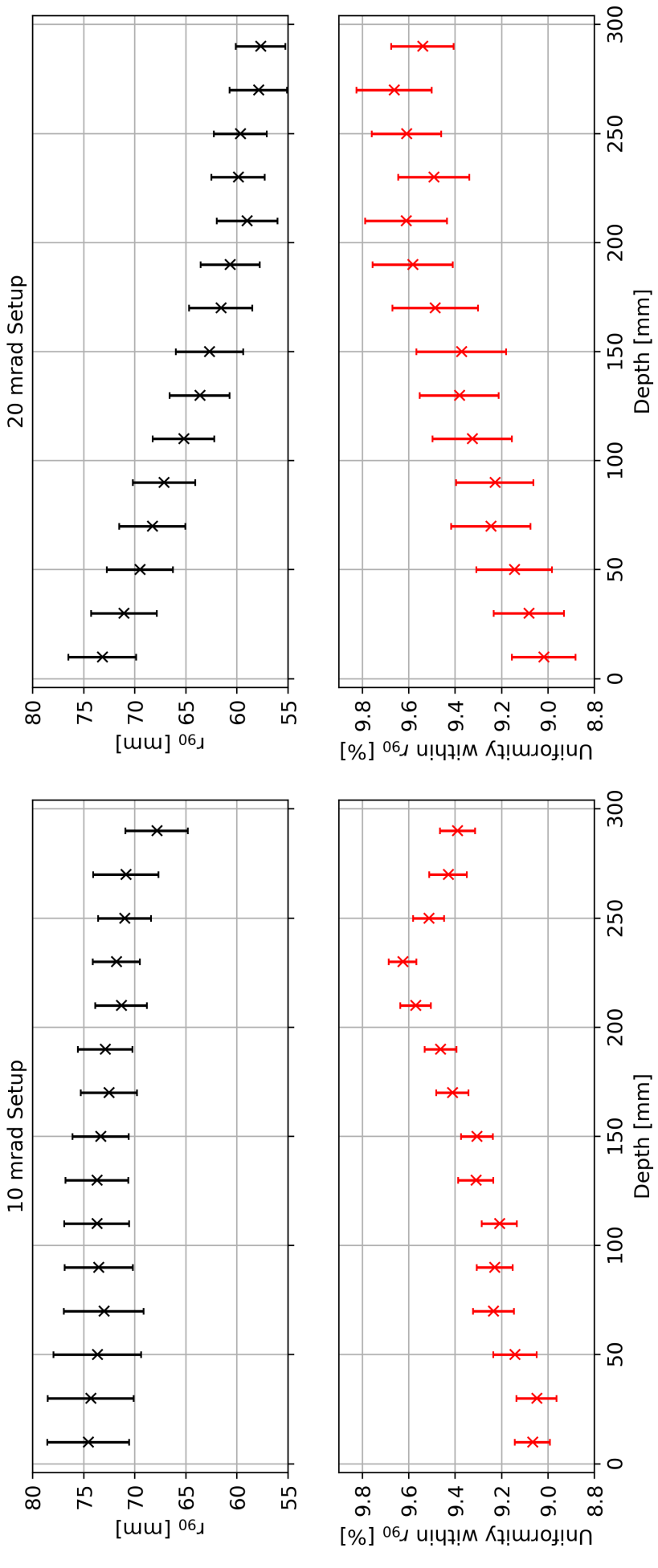

Figure 4.16: r_{90} (top), and peak-to-valley uniformity within r_{90} (bottom) against depth in water phantom, calculated from shaped super-Gaussian fitting of **total** transverse dose. Extracted from TOPAS simulation with 10 mrad (left) and 20 mrad (right) setups in TOPAS. Errors propagated from covariance matrix of fitting results and statistical uncertainty derived from multiple simulation runs (errors dominated by the former).

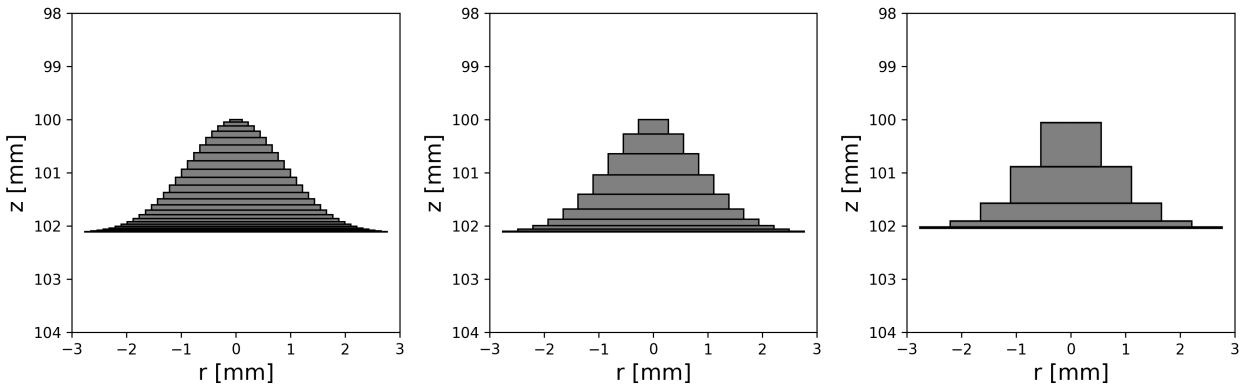

Figure 4.17: 2D visualisations of physical 20 mrad S2 geometry (longitudinal coordinate against radial coordinate for circularly symmetrical systems) as composed by 25, 10 and 5 slices, from left to right.

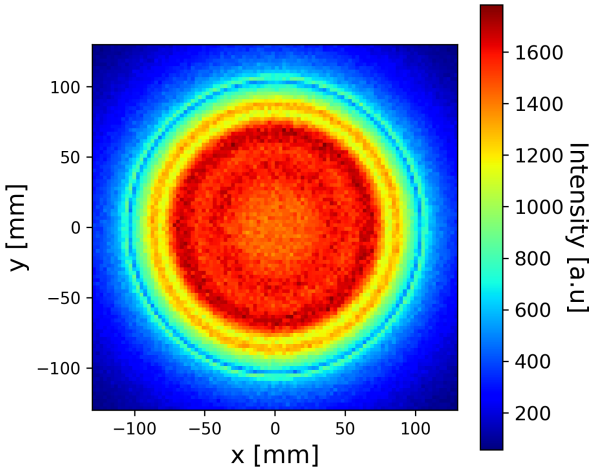

Figure 4.18: Transverse density histogram of primary electron beam generated from dual-scattering system with 5 step S2. Extracted from TOPAS simulation with 20 mrad setup, measured at water phantom surface. Density rings from multiple steps clearly visible.

Equation 2.74 and used to establish misalignments for certain scattering system. As shown in Figure 4.19, there was typically a linear relationship between the values of the fitted skew parameters and the transverse misalignment of S2. This fitting method for quantifying the misalignment of the scattering system could be extremely valuable for operation of such a system. Given either sufficiently flexible optics in the beamline or S2 mounted on a stage, the position of S2 or the beam could be automatically shifted until the fitted skew parameters reached zero. A mock-up of such a system using TOPAS was written and verified; this was capable of returning an arbitrarily offset initial beam to the centre of S2 only by minimising k in both x and y. This code could be used to correct e.g. YAG scintillation intensity from a camera rather than simulated data to provide an online scatterer alignment correction system during operation.

A very similar code for detecting misalignment in a known setup was also written; effectively this operated in reverse. Given a single transverse profile measurement in a system with known

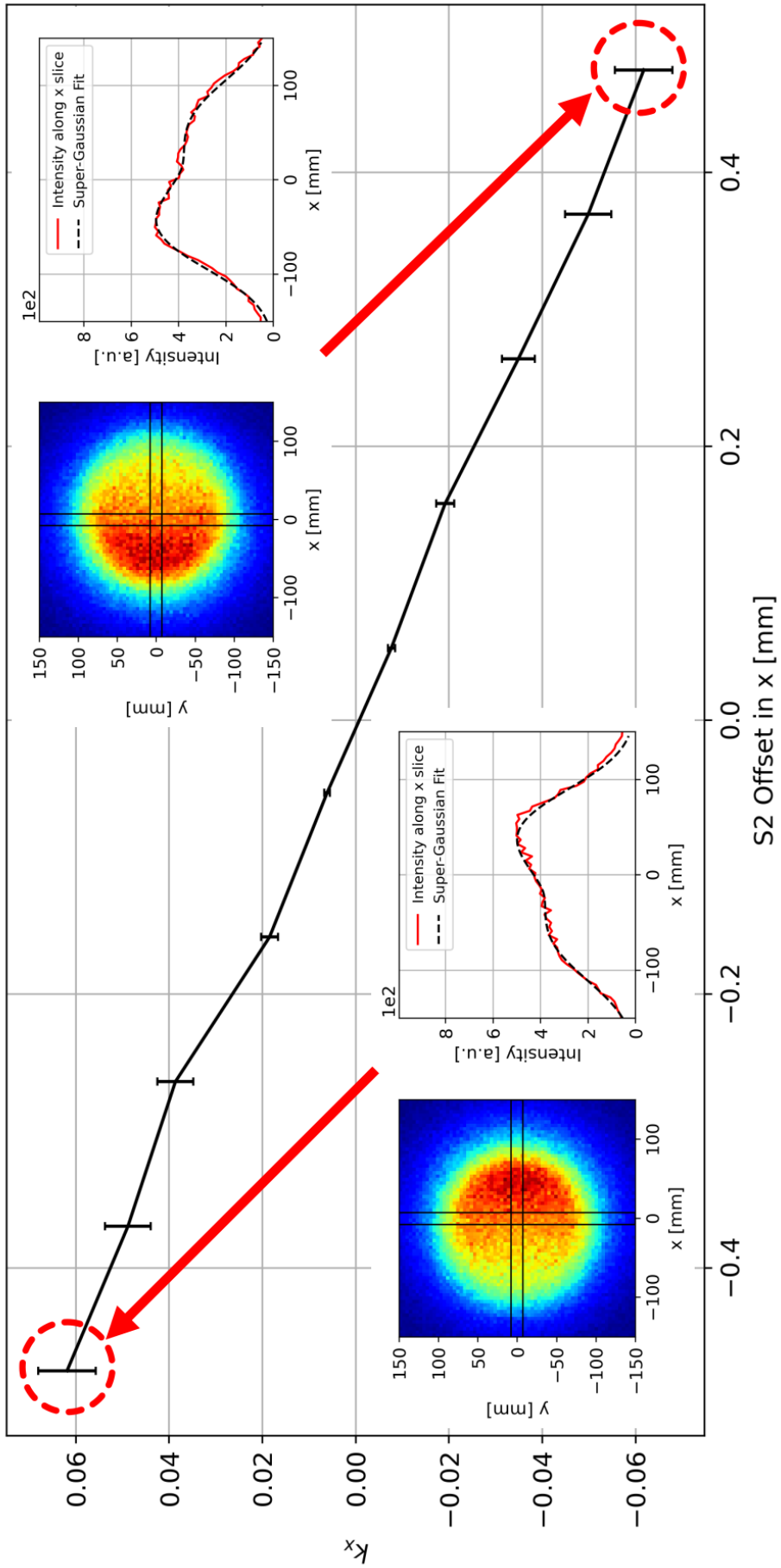

Figure 4.19: k_x parameter from fit of Equation 2.74 to transverse intensity distribution at water phantom surface against S2 misalignment in x. 2D density histograms and 1D slices with fits in x at extrema of misalignment scan shown in insets. Results from TOPAS simulations with 20 mrad setup. Errors from covariance matrix of fits and statistical fluctuations calculated from multiple scanning runs.

geometry, this version attempted to replicate the fitting results by aligning S2 in simulation. Upon reaching a similar profile within certain minimisation constraints, this would give an approximate offset of S2. It was shown that offsets in angle could be corrected for by adjusting the position of the scatterer accordingly. If the beam is aligned on the tip of the scatterer, the effects from angular misalignment are minimised, although this was found to create a slightly smaller uniform radius in the tilting axis, due to the smaller area in the transverse plane. An example of such a profile from a corrected misalignment is shown in Figure 4.20. The dual-scattering systems in these examples were thus found to be fairly robust to variations in scatterer angle if realigned at the scatterer tip. This was the case for both smooth scatterers and sliced scatterers, as before. The relevant code for implementation is available at the same GitHub repository.

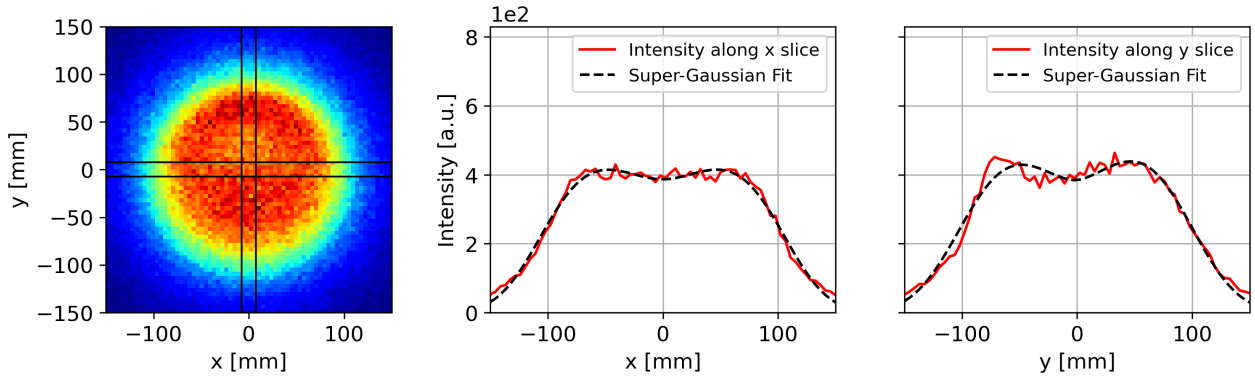

Figure 4.20: 2D transverse primary beam intensity histogram (left), beam intensity against x (middle) and y (right) from indicated slices across distribution, with super-Gaussian fits shown. Extracted from TOPAS simulations with 20 mrad setup at water phantom surface, after correction from 300 mrad tilt in S2 alignment. Correction algorithm based upon minimising skew $k_{x,y}$ parameter of fits from Equation 2.74.

4.6 Collimation and Neutron Production from VHEE Beams

Whilst again touched upon by [198], a study was carried out to determine appropriate characteristics and materials for collimation in the VHEE regime. During the studies on VHEE GaToroid, "virtual" collimation was assumed: perfect collimation of the beam within the defined radius. In reality, the final distribution is dependent on the material and length of the chosen collimator. For low energy electrons, the beam can be mostly blocked with fairly thin collimators. For electrons in the VHEE regime, the required collimating material was expected to be more comparable to those used in conventional X-ray therapy. For VHEE beams, the X-ray energy spectrum is indeed even higher than that of conventional RT, so it was likely that these would need to be even thicker to completely block the dose.

Collimators of varying geometries were investigated to determine appropriate thicknesses for reduction of dose outside r_{90} in the water phantom. The setup for the 20 mrad case from Section 4.5 above was retained, for consistency. Material slabs were inserted 20 mm upstream of the water phantom - an arbitrary choice but deemed appropriate, as MLCs are often positioned very close to a patient during conventional treatment. Dose was scored and integrated across the whole water phantom. For a suitable collimating system, this total dose would be zero or very close to zero. Tungsten, lead and steel were studied; the former is most common in conventional systems, whilst the latter two were utilised in the experimental studies of this thesis. The results from these simulations with varying collimator thicknesses are shown in Figure 4.21. Suitably thick tungsten was successful in

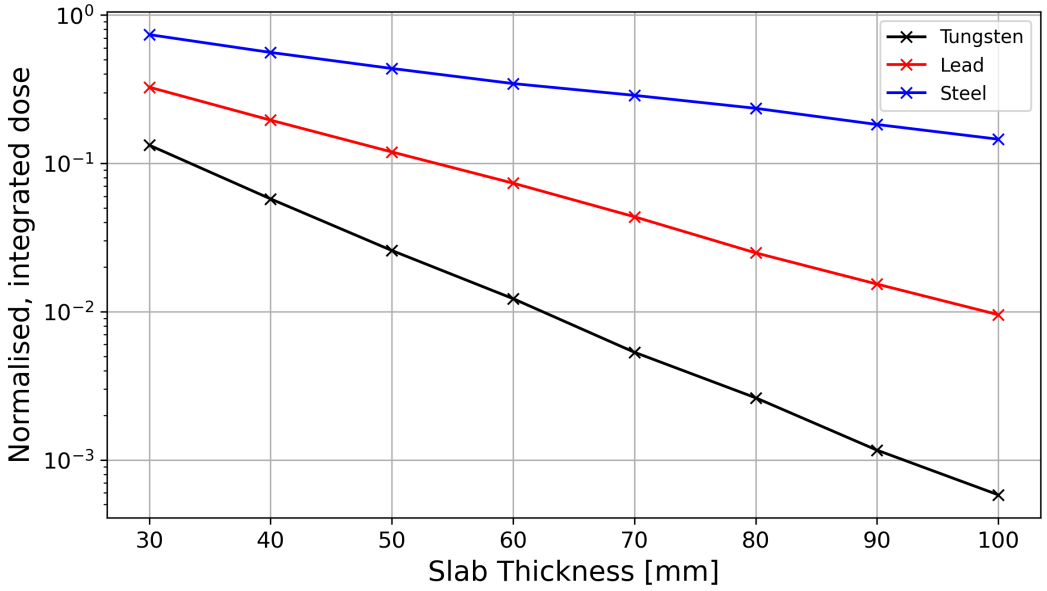

Figure 4.21: Integrated dose deposition in water phantom against collimator slab thickness, from simulations in TOPAS with 20 mrad setup. Normalised to total absorbed dose in phantom without collimation.

reducing integrated dose compared to the case with no material present, with reduction of 99% at 62 mm thickness and 100 mm of tungsten reducing integrated dose throughout the phantom to less than 0.1%.

The true primary objective of such collimation system is to retain only the desired portion of the beam - in this case, the uniform component; in a clinical setting, the beam may also be shaped to account for a realistic tumour profile. The collimation is carried out to prevent the transverse Gaussian tails from damaging healthy tissues around the tumour; thus providing the conformal irradiation - described as reducing the lateral penumbra of dose. The lateral penumbra can be defined [159] as the relative width of the transverse dose component between 90% and 10% of the maximum (r_{10} - r_{90}) - very simply computed from the super-Gaussian fits used throughout this thesis. This measure-

ment would ideally be small directly after collimation, but gradually increasing due to scattering in the patient. Studies were carried out to investigate the lateral penumbra for VHEE beam taking into account the effects from both dual-scattering and collimation. A 10 cm tungsten collimator was used for this study, due to its success in blocking almost all of the 200 MeV beam used to produce Figure 4.21. This collimator was given an aperture with 75 mm radius to retain only the uniform component at the water phantom surface, and inserted 2 cm upstream of the patient in the 20 mrad setup.

Dose was scored in the water phantom using TOPAS as before and lateral penumbra measured both with collimator inserted and extracted. For the extracted measurements, the water phantom transverse geometry was extended to 500x500 mm^2 to ensure the tails were captured for fitting. Voxel size was decreased to 1x1x20 mm^3 due to the sharp gradients of the collimated penumbrae at shallow depths. The results are shown in Figure 4.22, demonstrating consistent reduction of lateral penumbra at the surface and throughout the water phantom. The combination of dual-scattering system and tungsten collimator was successful in providing a large beam satisfying uniformity requirements of 10%, with a minimised lateral penumbra outside of this region, even deep into the water phantom. At the entrance to the phantom, the lateral penumbra was reduced from 80.0 to 3.6 mm. At the phantom exit bin, the lateral penumbra was 49.0 mm with collimation, compared to 110.3 mm without this collimation.

An additional concern for operation in the VHEE regime and particularly at UHDR is neutron production. Neutrons could be generated from the scattering foils and collimator, as well as the patient themselves. As previously stated, the default packages in TOPAS MC were changed to the `QGSP_BERT_HP_EMZ` physics list to carry out this study, as photo-nuclear processes are not typically simulated in TOPAS due to the significant additional computation and time required. Previous studies on neutron production have used the same package and verified that the non-neutron dose was within statistical error - this was not explicitly verified for the work of this thesis [223]. A 500x500x500 mm^3 water phantom was used for this short study, to ensure measurement of the complete transverse dose profile. Relative neutron dose at the patient originating from the scattering foils and collimator is shown in Figure 4.23. S2 was found to contribute negligibly to the total neutron dose as with the total photon contribution and with the majority originating from the 10 cm tungsten collimator. A small but notable contribution was from S1- accounting for 5% of the neutron dose at the surface. The dose contribution from neutrons as a function of total dose was small however - approximately 0.1% at maximum, at the entrance bin of the water phantom.

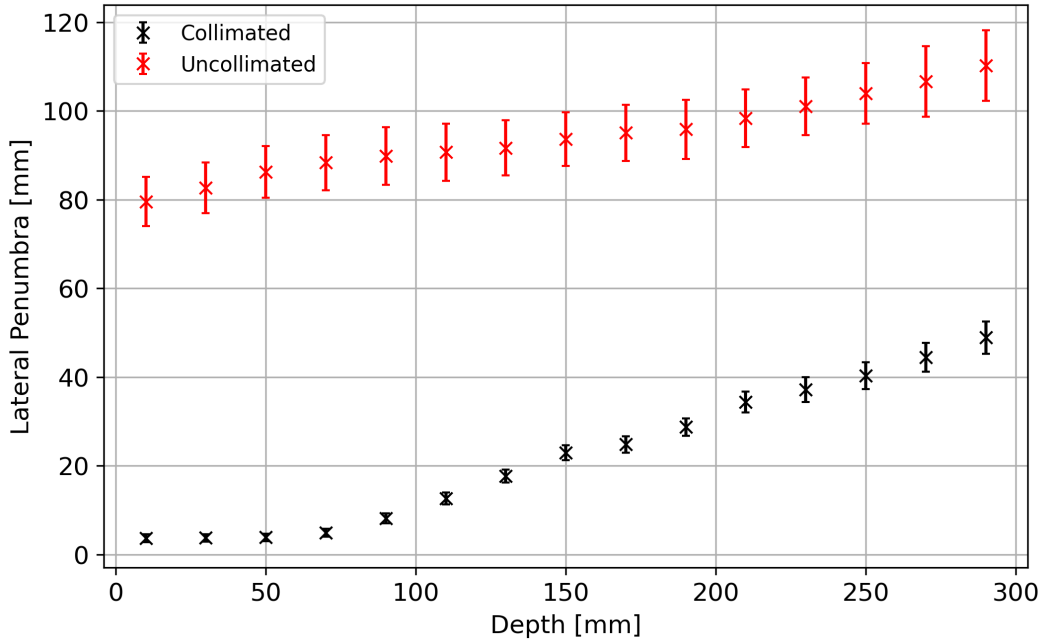

(a)

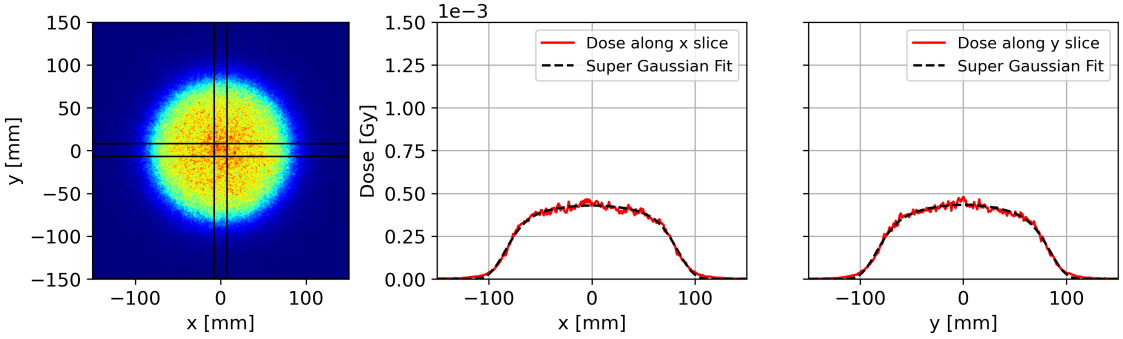

(b)

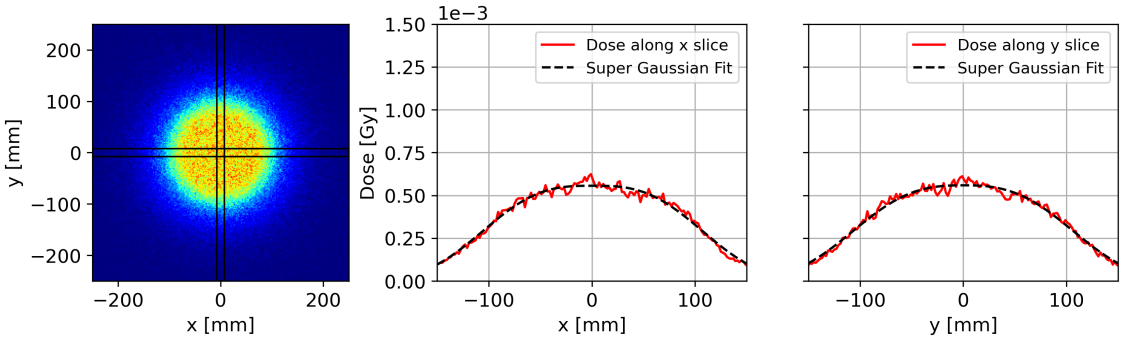

(c)

Figure 4.22: Lateral beam dose penumbra against depth in water for dual-scattered beam in 20 mrad setup with collimator inserted and extracted (a), 2D transverse primary beam intensity histogram (left), beam intensity against x (middle) and y (right) from indicated slices across distribution, with super-Gaussian fits shown (b,c). Dose profiles in water at phantom exit for collimator inserted (b) and extracted (c). Extracted from TOPAS dose simulations.

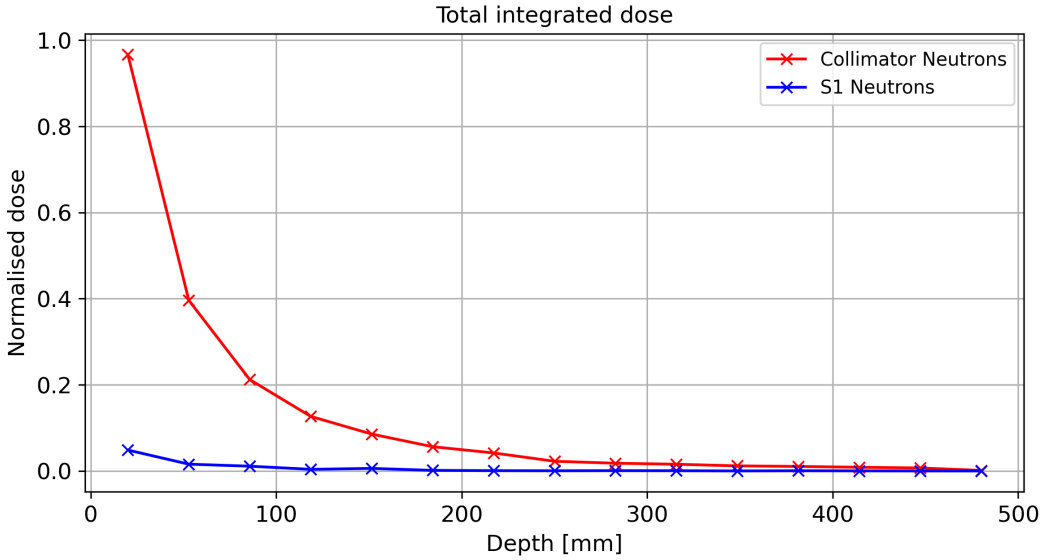

Figure 4.23: Normalised relative neutron contributions to dose from external sources against depth in water phantom, from TOPAS simulations with 20 mrad setup and extended water phantom.

4.7 Optimisation of Dual-scattering Systems with TOPAS

The analytical method described by [213] and shown in Section 4.4 is commonly utilised and in theory applicable to particles of arbitrary energy. As discussed however, this does rely upon the accuracy of the MCS model used and neglecting effects of particle production, losses and their effects on dose when using the typical Gaussian approximation to MCS. Even in a setup with lower scattering angles than 10 mrad, dose contribution from secondary particles generated in the scattering foils could be significant (for example, at higher energies in the VHEE regime such as 250 MeV). The analytical method also relies upon a Gaussian shaped S2, which may not be the most appropriate shape for the design of scattering foils. It requires an initial beam with Gaussian divergence and assumes that any scattering will dominate the initial spatial distribution, which may not be accurate depending on the application. It would require additional calculations to be made for production of a uniform profile at a certain point in e.g. a water phantom rather than simply providing a uniform beam at the surface of a patient. A solution to this could be the use of an dose model in the design process to target uniformity deeper in the patient [198]. Nevertheless, verification with MC simulations would be required to assess the accuracy of the analytical methods in a range of setups. A method of scattering foil design utilising both the analytical method and MC verification to generate appropriate solutions has been suggested [220]. This method whilst efficient and rapid, was still developed for the regime where particle production was negligible and would be expected to lose accuracy with large scattering angles and particle production, as before.

For flexibility and ease of extension, accuracy and adaption, an automated routine fully based on MC simulations was developed for VHEE dual-scattering foil design in this thesis. This routine was broadly analogous to the minimisation method utilised for VHEE GaToroid design in Chapter 3, and is a more advanced version of that described in [224]. This process is visualised in Figure 4.24. Initially, the constraints of the setup were defined. These would typically be the materials for S1

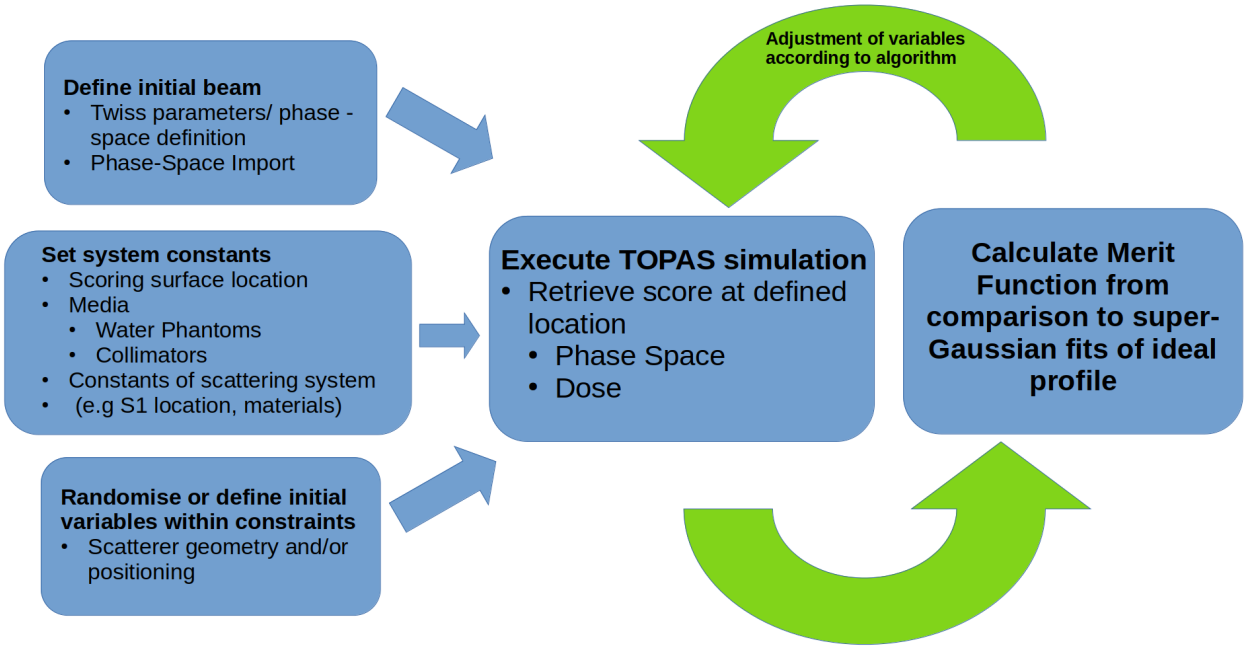

Figure 4.24: Summary of MC based dual-scattering foil optimisation process.

and S2, and the position of the merit dose scoring surface. Limits on the minimal slice thickness of S2 could be set for ease of manufacture, or conversely many slices could be used to create a smooth Gaussian shape as in Section 4.5. The system geometry could include additional components and materials such as vacuum windows, magnetic fields, water phantoms or collimators; these could be simply entered into the TOPAS script. An initial beam of arbitrary energy, energy spread and profile could be defined using transverse beam-size and divergence, Twiss parameters and emittance, or directly imported from an external file into the simulation. This then alleviated the constraint of the analytical method above assuming that the initial beam size was negligible compared to the scattered beam. Parameters could be set as variables or constants appropriately.

Typical variables in the system could be the positioning of S2 and S1, the thickness of S1, and the width and maximal thickness of S2 (as in the analytical method). An additional variable was introduced to warp the shape of S2 to a non-Gaussian three dimensional shape. This "warp factor" would produce a function with heavier or lighter tails, depending on its deviation from 1. The slices of S2 were then generated beneath this function with arbitrary slice thickness as described for

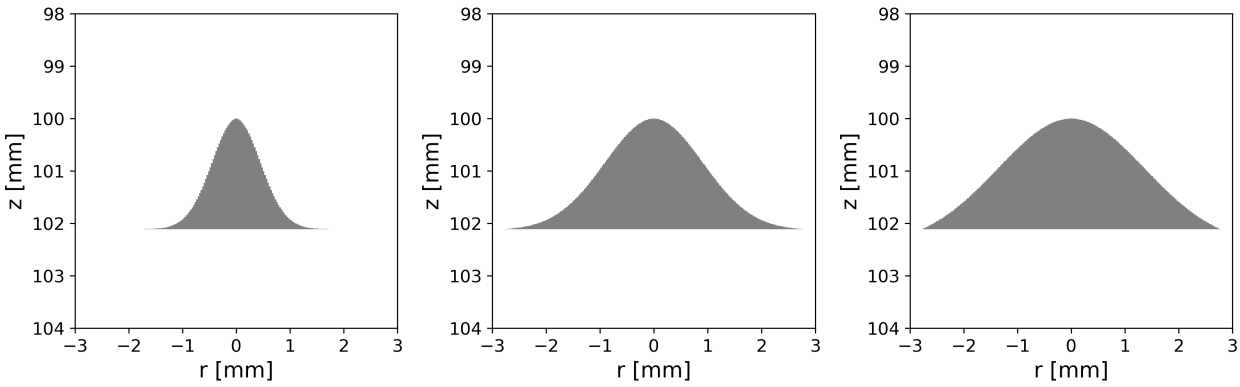

Figure 4.25: Transverse slice of arbitrary S2 (longitudinal positioning vs radial extent) with consistent σ_{S2} and H generated from differing warp factors. 0.5 (left), 1 (middle) and 1.5 (right).

the TOPAS implementation in Section 4.5. Variants of S2 created from generation functions with differing warp factors are shown in Figure 4.25. Given an asymmetrical initial beam, an elliptical S2 could also be generated such that flatness (i.e the power term in the 2D super-Gaussian equations) would be symmetrical.

Initial variables in the system could be fully or entirely randomised as defined by the user during initialisation. If desired, the analytical approximation optimisation could be carried out and used as an initial guess; alternatively, the randomisation could be defined within certain bounds. The optimisation could be based on either intensity profile or directly for dose profile. The simulation was carried out and the distribution of the dual-scattered beam scored at the required surface. If a beam of a certain distribution was required at a certain depth in a patient, the surface could simply be inserted at the chosen depth in the water phantom. This allowed uniformity at arbitrary depth to be achieved, rather than relying on preservation of uniformity throughout the patient (in this case, dose was always scored rather than intensity). Physical collimation could be included here if desired, although this resulted in a significant increase in simulation time; virtual collimation (removal of all particles outside of a specified radius) was typically preferred before verification runs.

The super-Gaussian fitting functions were used to determine uniform radii, as these were shown to successfully model flattened beams both when collimated or uncollimated, accounting for double peaking or rounder transverse distributions. $k_{x,y}$ parameters could be set to zero during optimisations with symmetrical beams to reduce the variables for the fits, although initially asymmetrical beams of the type extracted from accelerator tracking codes could be accounted for with these parameters, as well as quantifying misalignment during optimisation as previously described. The double-peaks across the uniform portion were suppressed using measurements of uniformity across the fits. The merit function result was returned according to the similarity between the fitted parameters and that

of the ideal beam desired. The result was then optimised according to the desired algorithm until convergence.

The repeated randomised optimisations of the Nelder-Mead algorithm were used in combination with optimisation through differential evolution [225]. The latter was found to be more efficient in terms of time and computation and as such was generally preferred. In some cases, the Nelder-Mead algorithm was used to converge towards a solution, with differential evolution used for the final stages. In many cases, a small amount of manual tweaking was also required with higher particle population to reduce statistical uncertainty in the final design, but this was typically fairly minor. The above process was flexible, reliable and applicable to a range of setups. A basic iteration of this code with limited variables was used to produce the finalised designs of the 10, 20 and 30 mrad scatterers for the work of this thesis shown in Table 4.2, aiming for the ideal beam in primary electron phase-space at the phantom entrance. Aside from the insertion of collimators and verification with additional particles, little additional work was required after a solution was found, since MC simulations were deemed the most convincing verification of successful design other than experiment. Examples of this process applied to design dual-scattering foils for numerous experiments are shown in Chapter 5.

4.8 Future and Ongoing Work

4.8.1 Rapid Design of Dual-scattering Foils in RF-Track

The principle limitation of the design process outlined above was the length of time taken for the TOPAS MC runs. The entire process could be greatly simplified if a reasonable approximation of the required scatterer geometry for production of the desired final beam could be made with much more simple calculation. The analytical method could be used to provide this as shown in Section 4.4, but as also described, this would not take precise initial beam distributions or the effect of magnetic field elements into account. RF-Track would allow balance between the analytical simplicity and the full MC detail of TOPAS to provide an approximate dual-scattering foil design for additional study - be it for first order estimations of required geometries, or for further optimisation in TOPAS. This would also allow scattering to be directly modelled during beamline design and optimisation.

Numerous MCS models are available in RF-Track, with materials of arbitrary radiation length and density defined during initialisation of the beamline. Scattering is defined across a number of steps through each material by the user. Implementation of the flat S1 in RF-Track for the dual-

scattering foil design would be trivial; S2 can be constructed using the *Absorber* aperture capabilities, composing the Gaussian shapes out of many smaller scatterers as in TOPAS. RF-Track does not currently model particle production, so this would have to be used for setups with few secondaries.

4.8.2 Bremsstrahlung Reduction or Production?

The significant number of Bremsstrahlung photons generated during the production of large, uniform electron beams at the patient could be harnessed to treat the first scatterer as a target, using the second as a flattening filter specifically for the secondary beam contributing more significantly to the cumulative dose, in a similar fashion to conventional RT. Whilst this would not allow the benefits of VHEE to be utilised, it may still be a worthwhile area of investigation, since X-rays characteristically have a small lateral penumbra, and thus higher energy distributions would be expected to have further reduced penumbrae. Using just a flat scatterer, the thickness of a tantalum was extended to determine where maximum yield of photons would be extracted from a 200 MeV, before the beam would be "self-collimated". As shown in Figure 4.26, this was at a tantalum thickness of approximately 12 mm. With this generating target, a full-width-half-maximum of 3.4 mm photon profile was measured at the water phantom surface bin.

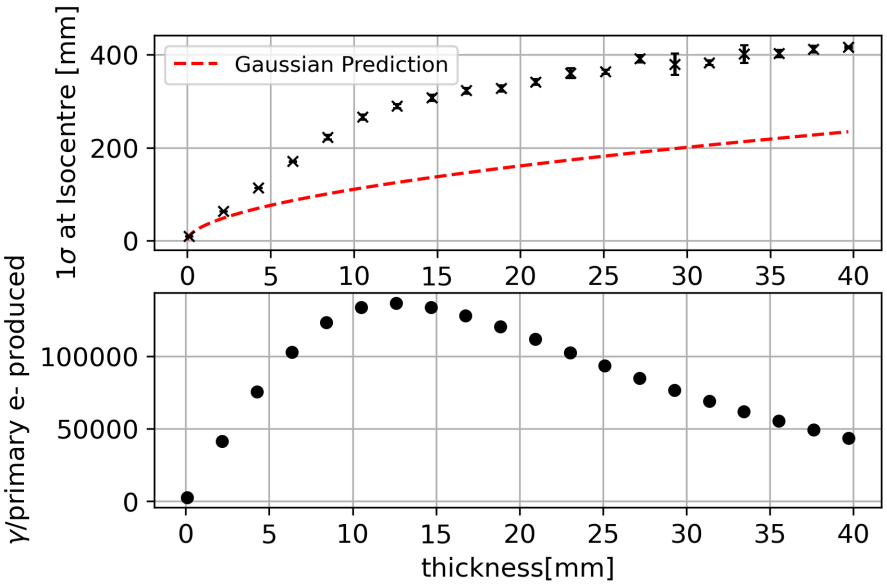

Figure 4.26: Scattering angles (top) and photon yield (bottom) generated from 200 MeV primary electron beam against tantalum S1 thickness. Results from TOPAS simulations with single-scattering reference setup.

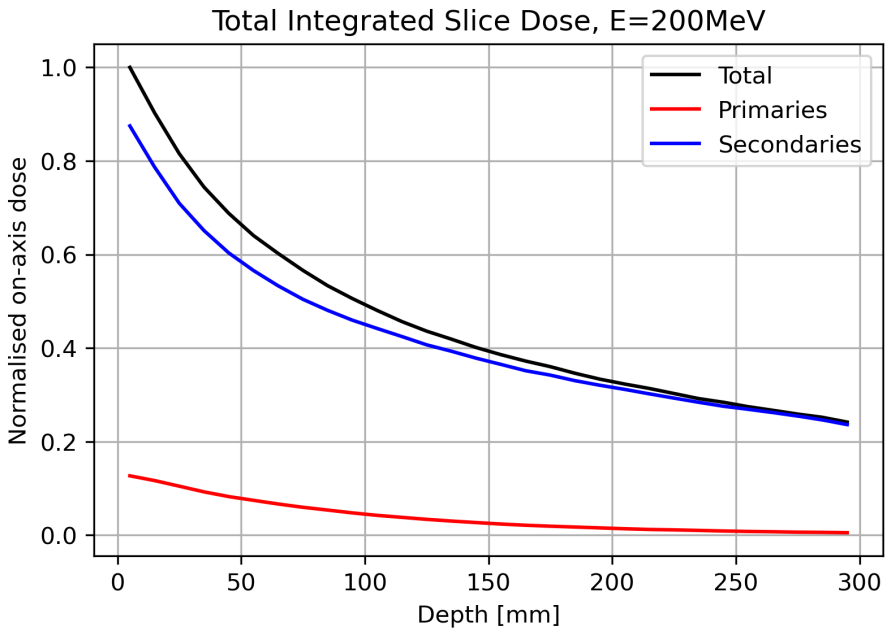

Figure 4.27: Integrated dose against depth in 30 cm water phantom, data generated from TOPAS simulation of a 200 MeV beam scattering from 12 mm tantalum target 10 cm upstream of phantom. Total, primary and secondary contributions to dose indicated.

4.8.3 Outlook of Dual-Scattering Foil use for VHEE

The studies carried out for this chapter confirmed some of the concerns raised from previous authors regarding the use of dual-scattering foils for practical delivery of magnified and flattened beams for VHEE therapy. Particle production was found to be significant even for rather modest scattering angles, such that production of large, uniform beams with such systems would require extended geometry well beyond desired gantry sizes for treatment. For example, even taking the 30 mrad divergence case from above, a 1.5 m gantry radius would only be able to provide a beam with 45 mm uniform dose radius; even this scattering angle was shown to result in a loss of uniformity at shallow depths within a patient due to the photon dose from Bremsstrahlung in S1. Uniformity requirements may depend on the specific patient and setup, but it is reasonable to assume that at scattering angles greater than the 20 mrad case described above, many of the benefits of flattening from the dual-scattering system would be lost due to these secondary photons. For a clinically applicable solution, there would be limitations on the field size, or future work on novel solutions for mitigating these effects would be required.

An alternative to the use of a dual-scattering system could be to remove the first scattering foil entirely, enlarging a beam with a Gaussian transverse intensity profile with quadrupoles and only utilising the Gaussian S2 for flattening. Whilst this could greatly reduce particle production and energy losses from scattering since the vast majority originate from S1 in upstream designs, this would

result in increased sensitivity to the initial beam as with the GaToroid design (although in this case, an initially uniform beam would not be required, with a Gaussian beam of the same size as S2 likely most appropriate). The sensitivity could be alleviated by positioning S2 in a further downstream configuration - this would increase particle production from S2 itself and as such an appropriate balance between sensitivity and particle production would once again be required. These combined optical and scattering studies could be investigated using a combination of the optimisation tools outlined in this chapter - either in RF-Track or a combined RF-Track and TOPAS optimiser. With this purpose in mind, an interface was developed to feed RF-Track data into TOPAS and an extension added to the optimiser of Section 4.7, such that an optimisation routine varying both quadrupoles and scatterer geometry could be carried out.

Similarly, the study of combined scatterer and scanning beamline studies may be worthwhile to strike an appropriate balance between the drawbacks of both methods: the speed and accuracy of the scanning magnets, and the particle production of dual-scattering foils. Further study on neutron production particularly from collimators is required - while the single case here demonstrated low dose contributions, neither the local profiles nor neutron production from the patient were studied. Low dose contributions from neutrons have been found in other simulated VHEE studies, but again within a limited setup [198].

4.9 Summary

Scattering foils present an alternative to the use of magnification optics for providing conformal transverse tumour coverage on a FLASH timescale. These have been extensively used for low energy electron and hadron treatments; these are regimes where secondary photon production is low however, which was not expected to be the case for VHEEs when significant beam enlargement in a compact space is required. Transmission was predicted to be extremely low when using a single scatterer to achieve uniformity; typically around 10%, which was not deemed appropriate for UHDR applications. Initial studies in a geometrical setup with 1 m between a single scatterer and patient phantom demonstrated significant photon production contributing heavily to the dose even at a scattering angle of 30 mrad for a 200 MeV beam. At this angle, the Gaussian approximation of MCS significantly underestimated the primary component beam-size, with this discrepancy and photon contribution to dose increasing further at higher scattering angles. The photon dose distribution represented 29% of the on-axis dose distribution at the peak of total dose in this case.

Beams with uniform radii of 75 mm were thus produced with extended geometries and scattering systems with 10, 20 and 30 mrad scattering angles from S1 rather than the more compact system, using a combination of analytical formalism and MC simulations to achieve uniformity within 10%. Beam transmissions for these designs within a virtual collimator were typically around 30%, significantly higher than that achievable with single scattering. Uniformity of the dose profiles was retained deep into the phantom for the 20 mrad and 10 mrad cases; the uniform radius decreased from an initial value of 75 mm to 57 mm for the former and from 75 mm to 68 mm for the latter after passage through the water phantom. This demonstrated the dependence of scattering angle and photon production on the evolution of the beam. The secondary component of the 30 mrad case dominated the transverse dose profiles even at shallow depths, with large scale variation above 10% beyond the first voxel (2 cm) of the phantom. Evolution of the primary dose components was consistent for each case, with the homogeneous extent at entry to the phantom retained throughout. Artificial misalignments in S2 were well characterised by skewed and shaped super-Gaussian fits, and could be related to the k fitting parameter depending on the specific geometry. Stepped rather than smoothed scatterers produced rings in intensity distributions which were smeared out after passage through a small amount of water.

A 10 cm tungsten slab was successful in blocking 99.9% of the integrated dose in a water phantom. For the 20 mrad case, insertion of a collimator with the same thickness and 75 mm half-aperture reduced the lateral penumbra at the phantom surface from 80 mm to 3.6 mm; the reduction of penumbra was retained throughout the phantom, with decrease between the uncollimated and collimated cases at 300 mm depth (110.2 to 49.0 mm). Neutron production for this 20 mrad setup was found to be minimal, accounting for 0.1% of the integrated dose at most. The neutron dose was dominated by the collimator, with 5% originating from S1. A more advanced tool for designing dual-scattering foils in TOPAS based on fitted transverse profiles was developed for use with beams of arbitrary initial profile and in beamlines with arbitrary geometry and constraints, such as those in Chapter 5. Future studies may be based upon alleviating concerns of Bremsstrahlung emission with combined optical and scattering systems, or indeed utilising the photon production to treat with higher energy conventional X-rays.

5 Uniform Beams at CLEAR

5.1 Introduction

5.1.1 Aim

The aim of this chapter is to describe how the extensive MC simulations and design procedures of Chapter 4 were put into practice. The CLEAR facility was deemed an excellent location to demonstrate the practical use of dual-scattering foils in the VHEE regime and characterise the evolution of the flattened beam in a patient model (water phantom). Successive experiments were carried out to achieve this and investigate the practical use of the system for irradiation of samples for pre-clinical VHEE studies.

5.1.2 The CLEAR User Facility

CLEAR is an experimental User Facility located at CERN. It can trace its origins back to the days of the Large Electron Positron (LEP) collider. LEP accelerated positrons and electrons up to 209 GeV in the synchrotron ring, and was responsible for extensive studies of electroweak interactions [226]. Before injection into the LEP ring, the leptons were first accelerated by a chain of accelerators including the proton synchrotron and super-proton synchrotron - in a similar manner to the current chain used for injecting hadrons into the LHC [227]. The initial generation and acceleration of the positrons and electrons was carried out by the LEP Injector Linac (LIL), followed by the LEP positron accumulator (LPA) to increase the intensities of the electron and positron beams and to match the operational frequency of the PS - together these components made the LEP pre-injector complex. LIL itself was composed of two accelerators operating together; LIL V and LIL W. LIL V was an S-band linear accelerator bringing electrons up to 200 MeV after generation from a thermionic gun. Beyond this point, the beams were fed into LIL W for production of positrons, and for acceleration up to 500 MeV before entry into the LPA [228]. LEP was dismantled in 2001 during construction of the LHC.

During development of CLIC, there was a requirement for testing the novel acceleration scheme outlined briefly in Chapter 2. In particular, this was the drive beam for generation of X-band RF

power to the primary beam after increasing the bunch frequency to X-band with the combiner ring and delay loop systems. After the decommissioning of LIL, many of its components (for example, the RF-cavities [229]) were repurposed for use in CLIC Test Facility 3 (CTF3). A schematic of this is shown in Figure 5.1. CTF3 [230] was composed of the drive beam complex, and the probe

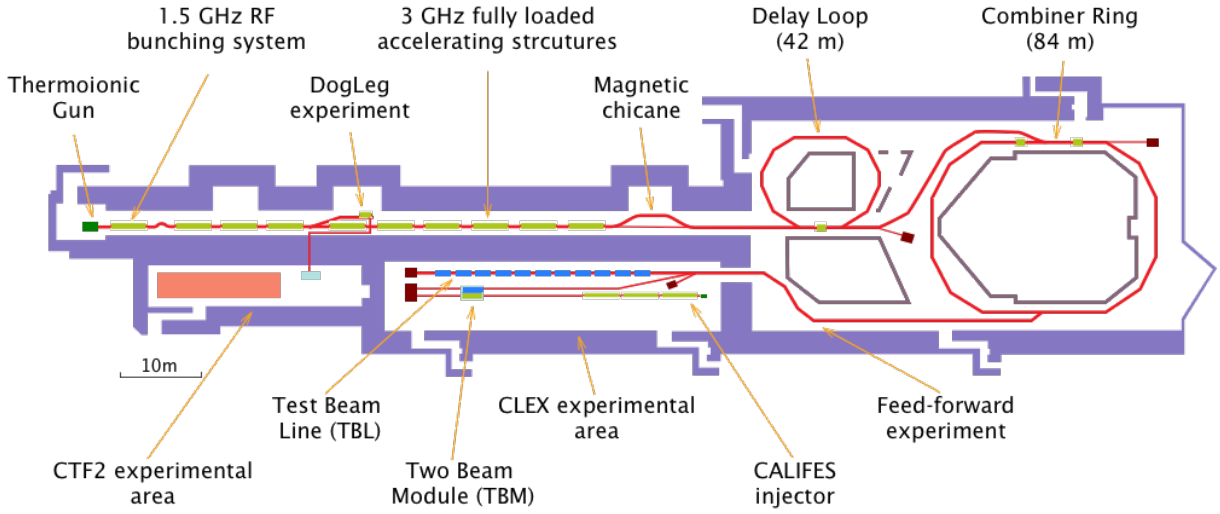

Figure 5.1: Schematic of CTF3 layout, taken from [230].

beam. In the former, electrons were generated from a thermionic gun and accelerated to 150 MeV, with bunching at 1.5 MHz. The beam then entered the delay loop and combiner ring as shown in Figure 5.1 to increase this bunch frequency to 12 GHz, as would be carried out during operation of CLIC as described in Chapter 2. The beam was then delivered to the CLEX complex to provide acceleration to the probe beam. The probe beam itself was generated from a photocathode-based gun, and was accelerated up to 200 MeV in the CALIFES injector.

CALIFES was composed of the same S-band structures used in LIL-V. The drive beam was decelerated to produce X-band RF power for the further acceleration of the probe beam, thus serving as a scaled down version of the primary CLIC line. CTF3 successfully demonstrated both the bunching frequency increase in the delay loop and combiner ring, and two-beam acceleration concepts required for CLIC. It was also used extensively for R&D for studies of high gradient acceleration and beam diagnostics [231, 232, 233]. Upon decommissioning of CTF3, the CALIFES injector and the probe beam were converted into a new accelerator complex with the primary purpose of carrying out research and development for general accelerator physics purposes: CLEAR.

CLEAR [234] was commissioned in 2017. An overview of the beamline is shown in Figure 5.2 - note that the beam in these schematics travels from right to left, a legacy from its time as the CTF3 probe beam. Electron acceleration is carried out in a broadly unmodified CALIFES injector,

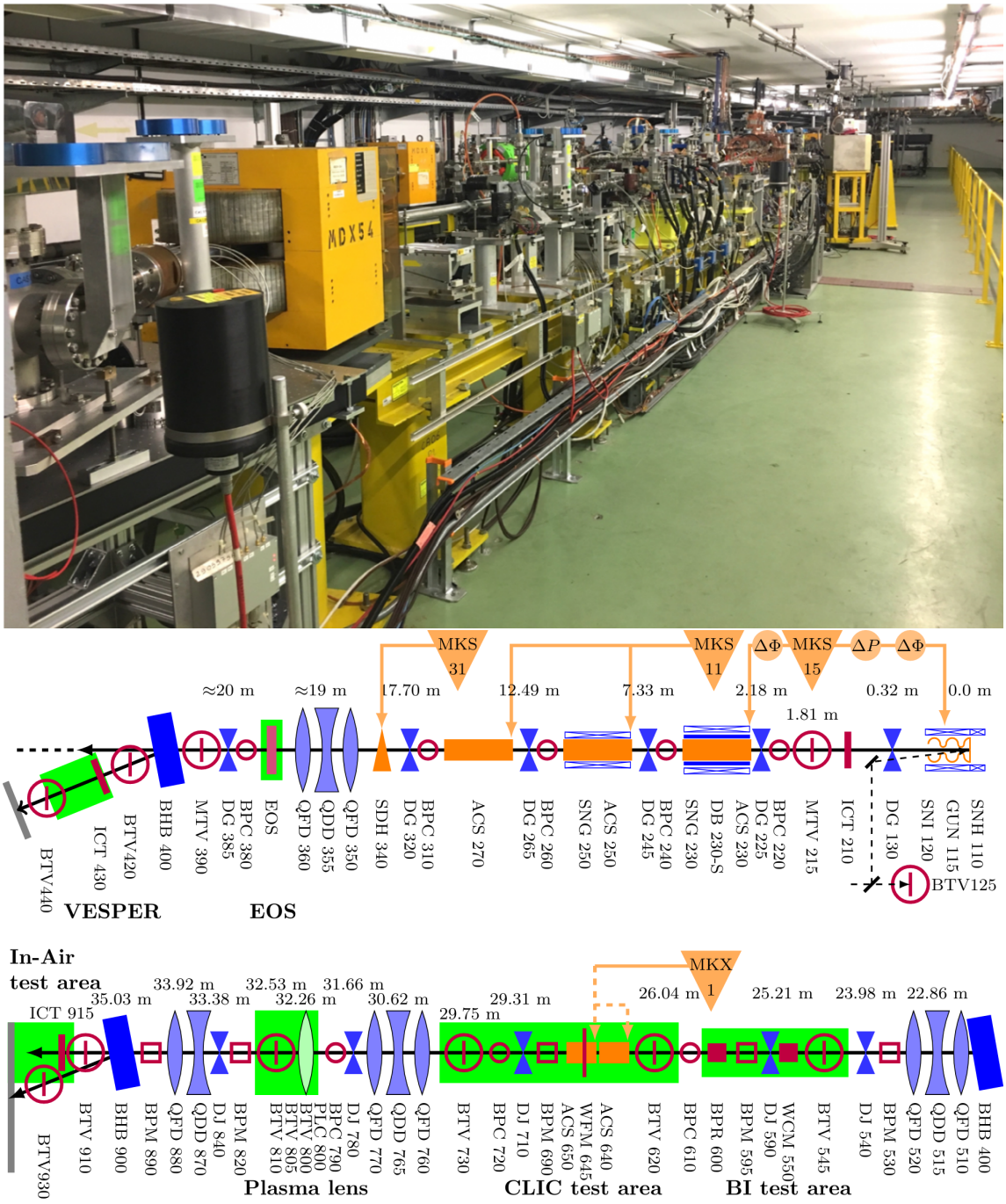

Figure 5.2: The CLEAR User Facility, photograph inside bunker (top), schematic of accelerator (middle) and schematic of experimental beamline (bottom). Images from [235].

as in CTF3 [234, 236]. Bunches are generated from a caesium telluride photocathode. The laser spot size and position can be tuned to optimise the conditions of the initial beam in the gun. The electron gun is fed by an S-band klystron, with the beam reaching a kinetic energy of 5 MeV at the exit; the gun is enclosed by solenoid magnets to compensate for the space-charge effects at lower energies [237]. After passing through diagnostics and magnetic kicker magnets, the beam enters the first full accelerating structure. This is fed by the same klystron as the gun, taking the beam energy to around 60 MeV. Velocity bunching can be carried out in this cavity to deliver variable bunch lengths, depending on the requirements of the user. The beam is then accelerated to its 200 MeV nominal energy through two further structures, fed by the MKS11 klystron which also operates at S-Band RF-frequency.

The beam then leaves the CALIFES injector portion and enters the CLEAR test line. The first notable component here is a dipole allowing the beam to be directed to the *VESPER* in-air test stand. This has been used for both medical irradiation studies [238] and research on radiation hardness of electronics for space applications [239]. During typical operation, the dipole is used to measure the energy of the beam using a diagnostic screen. When the dipole is deactivated, the beam passes through a section dedicated to vacuum installations, also including quadrupoles and further diagnostics and kickers. This section has been used for numerous installations and diagnostic studies including Cherenkov diffraction radiation based beam monitoring for applications at the AWAKE plasma wakefield accelerator [240] in the BI test area outlined in Figure 5.2. Further in-vacuum experiments studying CLIC beam diagnostics and novel focusing with a plasma lens have been carried out at CLEAR [241]. The beam exits the vacuum pipe through a thin Kapton window, leading to the main CLEAR in-air test stand, capable of hosting numerous experiments with the assistance of stages and water phantoms. An additional dipole is installed upstream of this window, allowing the beam to be diverted to a separate screen.

The design of CLEAR allows for significant flexibility in beam parameters and installation of experiments. An overview of the available parameters is given in Table 5.1. The machine can operate with bunches in every RF bucket (3 GHz) or in alternating buckets (1.5 GHz), with variable repetition rate. The CLEAR train structure is shown in Figure 5.3. Bunch lengths can be modified using velocity bunching with the first accelerating structure. Measurement of the bunch length at CLEAR is carried out using a transverse deflecting cavity, indicated as SDH 340 in Figure 5.2. CLEAR can operate with up to 200 bunches per train, and as such is capable of reaching the required dose rates for UHDR experiments. Medical research activity has been supplemented by several developments at CLEAR to improve operation for sample irradiations and dosimetric studies.

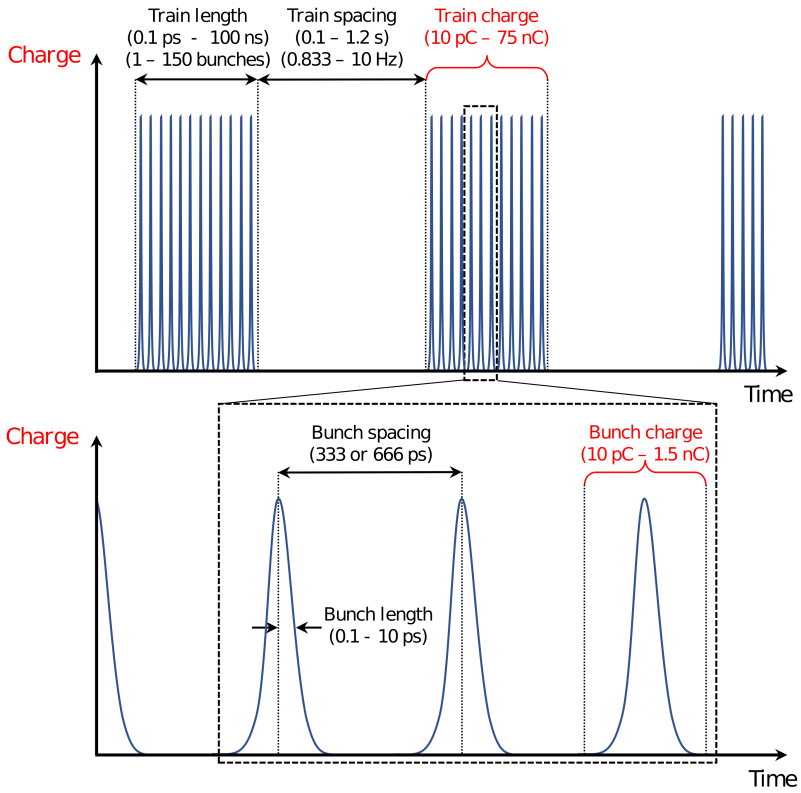

Figure 5.3: Transmitted charge against time demonstrating length and spacing of trains (top) and bunches (bottom) at CLEAR. Image from [242].

The most significant of these developments is the C-Robot. This is a remotely operated system composed of three individual linear stages controlling a grabber. This grabber can be used to hold samples or radiochromic films in custom holders developed and manufactured by the CLEAR operators. Samples and films are typically shielded by lead bricks. An image of the C-Robot is shown in Figure 5.4. During operation, the C-Robot can individually insert up to 32 holders from its storage rack. Typically, each film holder consists of slots for two radiochromic films, and a slot for insertion of samples. Various modifications of this initial design exist however. Extended holders with slots for 23 films are available to construct depth-dose distributions. Additionally, a holder with a scintillating YAG screen is routinely used during operation; the C-Robot is equipped with a camera on its arm with which to measure the transverse beam parameters from this YAG screen.

5.2 Dosimetry at CLEAR

Measurement of dose during experiments at CLEAR is carried out primarily with radiochromic films [243]. Films used throughout the work of this chapter were Gafchromic EBT3 and EBT-XD, with dynamic dose ranges from 0.1 to 20 Gy and 0.1 to 60 Gy respectively [244, 245]. These are composed of a radio-sensitive polymer, darkening with exposure deposited dose. This is indepen-

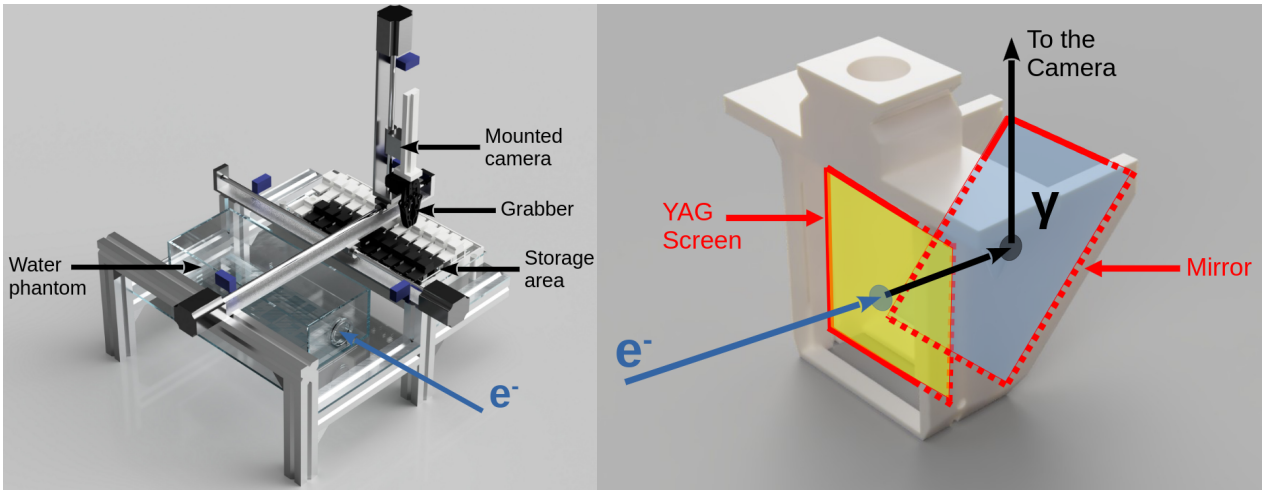

Figure 5.4: C-Robot (left) and holder held by C-Robot and used for diagnostic YAG beam imaging in the in-air test stand during operation (right). Images from [241].

Table 5.1: CLEAR Beam Parameters in 2023 [241].

Parameter	**Value**
Beam Energy	$30 - 220$ MeV
Beam Energy Spread	$< 0.2\%$ rms (< 1 MeV FWHM)
Bunch length RMS	$0.1 - 10$ ps
Bunch frequency	1.5 or 3.0 GHz
Bunch charge	$0.01 - 1.5$ nC
Norm. emittance	$1 - 20$ μm
Bunches per pulse	$1 - 200$
Max. pulse charge	87 nC
Repetition rate	$0.8333 - 10$ Hz

dent of the dosimetric time structure, and allows the transverse profile to be quantified, rather than just an integrated value as with typical ion chambers. The radiochromic films require calibration to known doses, since their response to dose is not linear. One of the manufacturer recommended equations to describe this response is:

$$d = a + b/(D - c) \tag{5.1}$$

for each colour channel (red, blue and green), where d is the optical density, D is the dose, and a, b and c are the calibration coefficients. Calibration is carried out by the CLEAR operators for each batch using the eRT6 linac at CHUV in Lausanne, with dose measured using an ion chamber [246]. It is assumed that the calibration of these films is energy independent, as no facility provides reliable dosimetry for calibration of films in the VHEE regime.

Films at CLEAR are scanned using a 16-bit Epson Perfection V800 Photo scanner at 300 dpi with a custom template ensuring consistent positioning of the films on the scanning surface. Images

of films irradiated at CLEAR are processed from raw data into optical density for each colour channel using a simple conversion, then into dose using Equation 5.1 with coefficients from calibration. Typically, only the green colour channel from the scanning is used at CLEAR, as this has been reported to be most accurate for doses in the range of 5 to 50 Gy [247]. Dosimetry at CLEAR and characterisation of dose profiles typically relies on automated fitting routines to determine the beam centre, followed by 1D fitting in x and y with slice profiles to determine the transverse beam size. The raw dose data, rather than fits, is used to determine the dose itself at any particular location or region in the film. For irradiation of samples, the CLEAR team irradiate one or several holders containing an Eppendorf tube between two films, with lead/mercury covering a similar dimension to the sample sizes. This creates an outline of the sample region in the downstream film. The size and relative location of this dose region on the film is then used for the films irradiated with the samples themselves. The mean and standard deviation of the dose within the region can be calculated. Thus, dose measurements throughout this chapter typically use a similar method, defining a small region and directly extracting mean dose and error from standard deviation of the dose within this region.

Analysis of all dosimetric data for the purposes of this thesis were carried out in collaboration with the operators at CLEAR, and followed a similar procedure to their standard routines with modifications in fitting functions for flat-topped beams. As briefly discussed in Chapter 4, the analysis module for fitting simulated dose and intensity data from TOPAS was extended to allow YAG and film image data to be processed with identical routines. This allowed reasonable comparisons to be drawn from TOPAS simulations and reduced errors arising from differences in methodology. The film processing class contained the appropriate calibration constants to convert raw image data into a dose-map image. YAG images taken with a digital camera were simply converted directly from MATLAB files to intensity histograms.

5.3 Single Scattering Experiments

Firstly, a simple experiment at CLEAR was run to evaluate the agreement between TOPAS and experiment for single scattering of the beam. This also allowed initial considerations for the setup of future experiments to be taken into account with respect to the logistics of this first experiment. The experiment would also demonstrate whether any energy spreads from long trains or initial dispersive effects from the steering throughout the beamline would cause a dramatic discrepancy with MC simulations. The experiment was installed in the in-air test stand at the end of the CLEAR beamline to carry out these measurements and comparisons. A diagram of the setup in the in-air test

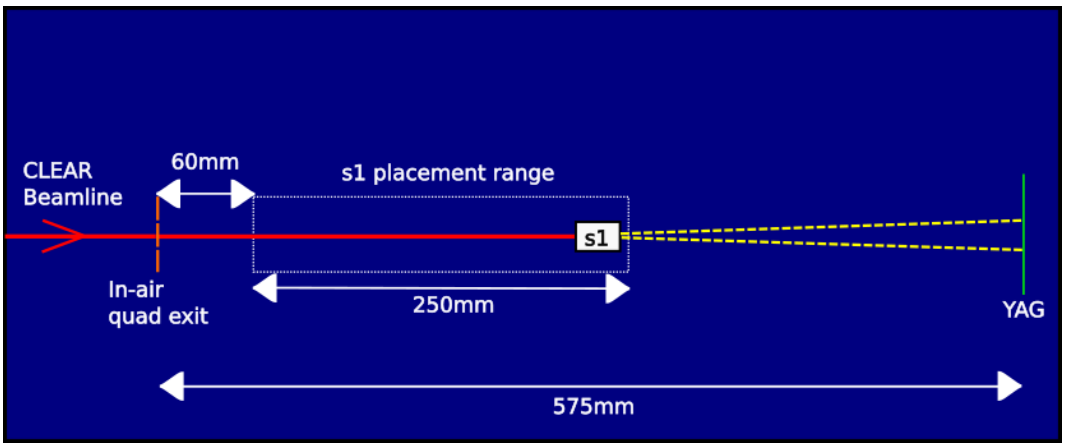

Figure 5.5: Schematic of pre-scattering experiment in CLEAR in-air test stand.

stand at CLEAR is shown in Figure 5.5. A small beam with transversely Gaussian intensity profile was envisaged at the position of the scatterer. S1s of three different thicknesses (10 mm, 20 mm and 30 mm) were 3D printed in PLA. These thicknesses were predicted to magnify the beam by an factor of approximately 10-30 across the test stand. The scatterers were mounted on film holders and held in the path of the beam by the C-Robot. The geometrical layout of the experiment was defined by the available space in the CLEAR in-air test stand at the time. The beam profiles after the single-scattering were measured using a YAG screen situated at the beam dump. Whilst CLEAR is optimised for operation at 200 MeV, it is possible to operate at lower energy. Thus, additional measurements at 150 MeV were also taken to verify the predicted increased scattering at reduced energies. This lower energy was achieved by modifying the RF phase of MKS11 during operation.

The beam at CLEAR during this experiment was approximated to simplify the TOPAS simulations. To do this, a simple image comparison algorithm was used to estimate the phase space distribution of the beam at the position of the scatterers using the profiles from these two YAG screen measurements at different longitudinal positions in the in-air test stand. The initial beam was assumed to have a Gaussian profile in both physical and angular phase space. Comparisons between TOPAS and experiment were carried out using 2D Gaussian fits. The 3D printed PLA blocks were not assumed to be pure, and as such their densities were individually calculated from the mass of printed filament used to improve the comparability of the TOPAS simulations. There was a slight variation in density with increasing length of these 3D blocks, presumably due to the additional layering by the printing nozzle. There were some issues with misalignment and magnification beyond the YAG screen during the experiment, likely causing some error which would be difficult to quantify. This was far more significant for the data taken at 150 MeV, where the beam was often extremely large, asymmetrical and not entirely captured by the YAG screen. A sample of the transverse profiles is shown in Figure 5.6, and a summary of the predicted and actual values from TOPAS

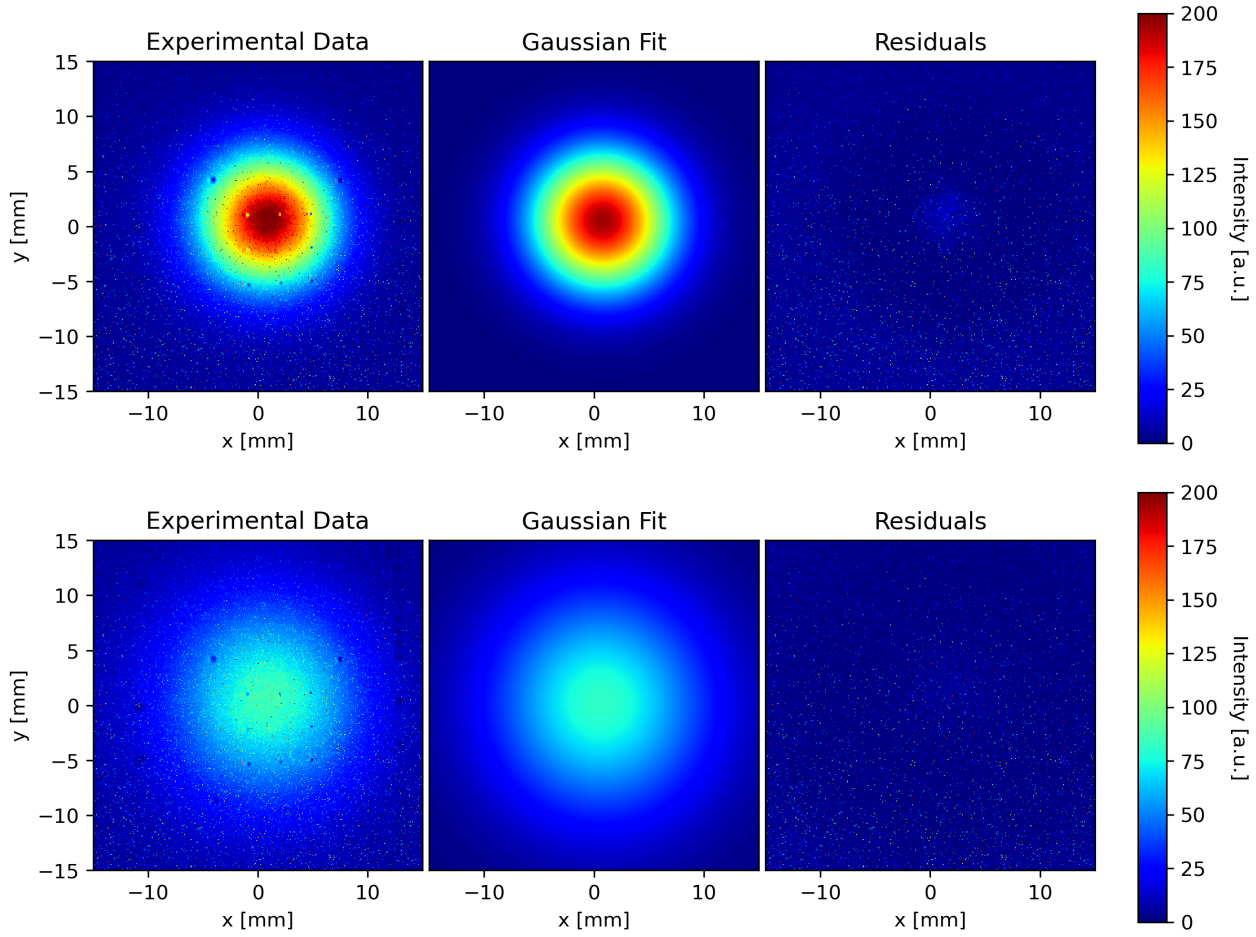

Figure 5.6: Sample of single scattering experimental data. YAG screen images of scattered beam showing transverse intensity profile (left), 2D Gaussian fit to YAG data (middle), and fitting residuals (right), for 10 mm S1 inserted (top) and 30 mm S1 inserted (bottom).

and experiment for 200 MeV in terms of the Gaussian fitting values is shown in Figure 5.7.

There was reasonable agreement between simulation and experiment for the measurements taken at 200 MeV, even with the approximations made for simulation of the initial beam. Higher discrepancies were seen for the 150 MeV results. This was expected however, due to a general lack of stability in the beam, jitter and variance in charge per pulse during operation, captured from the significantly higher errors particularly in x on the right-hand side of Figure 5.7. The only clear conclusion from the measurements taken at 150 MeV was that the scattering was significantly larger at the lower energy; consistent with the Gaussian approximation to the Moliere PDF. The results and reasonable agreement between experiment and simulations at 200 MeV validated that the CLEAR beamline was sufficiently stable and well characterised to be used for scattering comparisons with MC tracking codes. It was noted at this stage that the well matched profiles only took electrons into account rather than the significant photon beam predicted from the TOPAS simulations. There was no evidence of the non-Gaussian component in the YAG images. This was predicted due to the thin

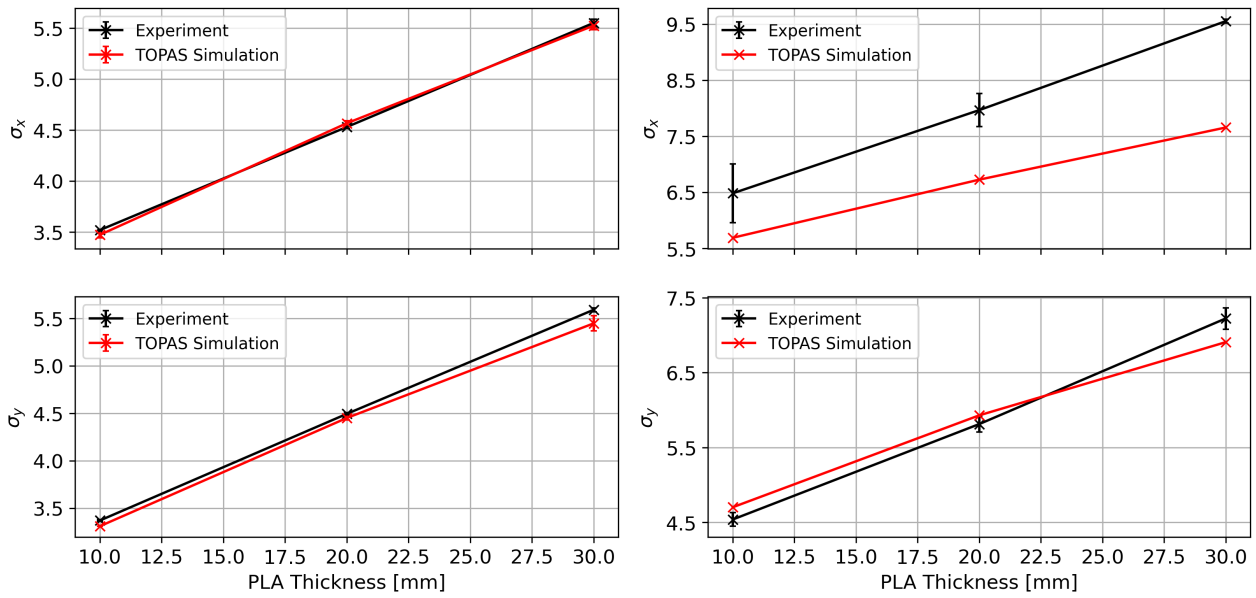

Figure 5.7: Beamsize from Gaussian fits in x (top) and y (bottom) against S1 thickness for single scattering experiment. Experimental data measured with in-air test stand YAG screen, and comparative TOPAS simulations indicated. S1 placed 250 mm upstream of YAG for measurement. Beam energy of 200 MeV (left) and 150 MeV (right). Experimental errors from deviations of ten measurements (trains).

screen being within the buildup region for photons, and the fairly low scattering angles (between the 10 mrad and 20 mrad cases from Chapter 4).

Later, a study was carried out to assess the scattering powers of additional materials in CLEAR; this was to verify predictions of TOPAS for higher density materials, which may be useful for construction of future dual-scattering systems due to their higher scattering efficiency compared to plastics, as also shown in Chapter 4. Quadrupole scans would be used in this case to explicitly measure the beam parameters for comparative simulations, with. More time was taken to ensure the stability of the beam, especially at energies below the nominal 200 MeV to gather more data on single scattering of the different materials. Four materials were studied: Tantalum, Tungsten, PLA, and PEEK. Tantalum and tungsten were chosen due to their frequent use in medical applications. PEEK is a commonly utilised plastic in accelerator physics, which is robust and resistant to radiation. It also has applications in medicine and has been heavily utilised in surgery [248]. It was chosen for this study due to its eventual use as the principal material for dual-scattering foils in CLEAR. The PLA was chosen to compare with the initial scattering experiments. Equation 2.59 was used as before to estimate the required thicknesses of each material, such that the scattered beam profiles would be significant but entirely captured by the C-Robot YAG screen at the in-air test stand.

There were limitations on the thickness of materials which could be attained - the tungsten and tantalum foils were only available with certain thicknesses so the scattered profile sizes would be

varied but still predictable from TOPAS and used for comparisons. The PEEK was carved out with a lathe by the CLEAR operators, and the same 30 mm 3D printed scatterer from the first scattering experiment was utilised for the PLA test. The manufacturer's website quoted no tolerance or error for foil thickness; thus, uncertainties in the foil thicknesses were due to the resolution of measurement from the digital calipers. Uncertainties on the PLA and PEEK were from the estimated variation of material thickness across their upstream and downstream surfaces, which was larger than this resolution. The material thicknesses and predicted scattering angles for this experiment are shown in Table 5.2.

Table 5.2: Manufactured materials and uncertainties, and resulted predicted scattering angles (generated from 2D Gaussian fitting to intensity profiles at scoring surface in TOPAS).

Material	Thickness	Predicted Scattering Angle at 200 MeV
PLA	30 mm±100 µm	18.7±0.1 mrad
PEEK	20 mm±100 µm	14.7±0.1 mrad
Tantalum	200±20 µm	13.8±0.6 mrad
Tungsten	200±20 µm	15.1±0.7 mrad

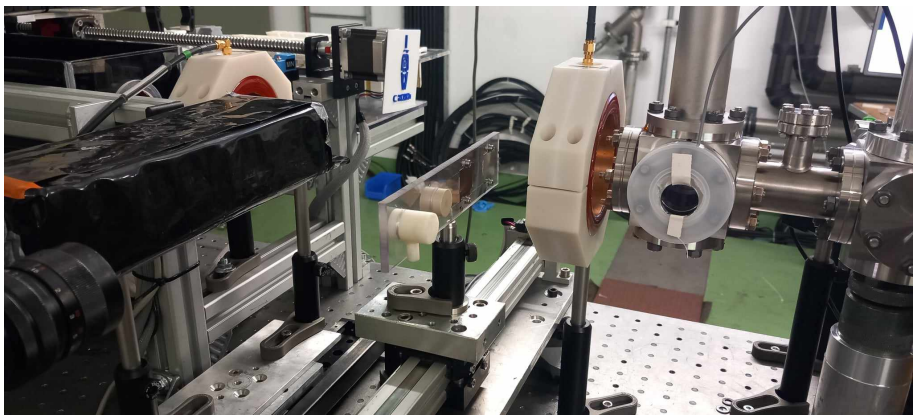

Figure 5.8: Photograph of setup for more precise single-scattering experiment, beamline entering from right with PMMA holder and materials in centre. Water phantom hidden by enclosed fibre experiment on left.

The experimental setup was altered from the first single-scattering experiment displayed in Figure 5.5, with the C-Robot being used to hold the YAG screen for transverse beam measurement rather than the scattering blocks themselves. The scattering materials were attached to a PMMA holder and mounted on a linear stage in the in-air test stand. This allowed the respective materials to be inserted in turn into the beam with appropriate motion of the stage. A photograph of this setup is shown in Figure 5.8. The YAG screen was held 380 mm downstream of the PMMA holder.

Beam current for these irradiations was largely arbitrary assuming sufficient intensity such that the YAG camera was neither dominated by noise nor saturated. The charge per train was kept constant, as the beam parameters of CLEAR (particularly the measured emittance and energy spread

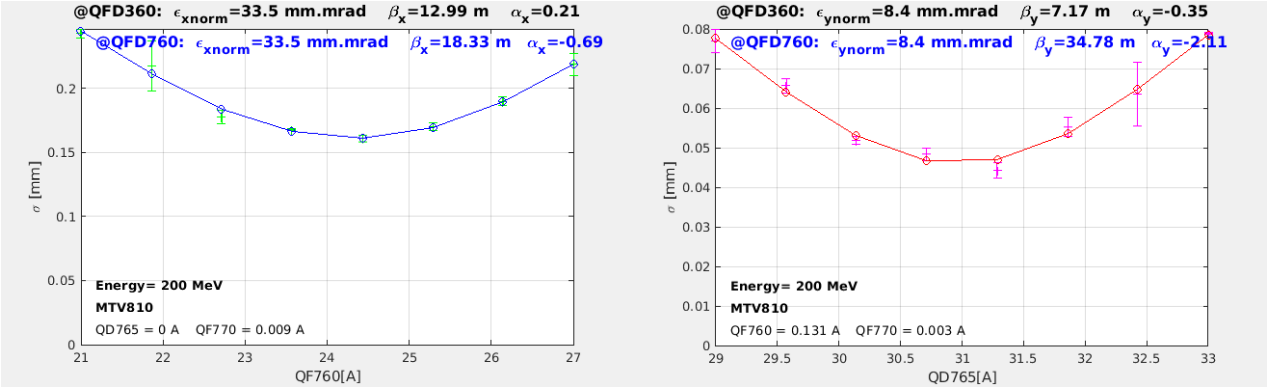

Figure 5.9: Measured beamsize against current of relevant quadrupole magnet shown along with fits for derivation of Twiss parameters in x (left) and y (right). Parabolic fits indicated. Quadrupole scan results measured with 7XX triplet at CLEAR, lower (blue values) taken for input to TOPAS simulations for comparison with scattering experiment, at 200 MeV. Twiss parameters extrapolated back to 3XX triplet shown (black values). Also carried out for operation at 180 MeV and 160 MeV.

profile) change significantly at very high intensities. Initially operating at 200 MeV, 25 YAG images of the scattered beam were taken for each material being tested. Quadrupole scans were taken using the method described in Section 2.2, with the results of these in x and y at 200 MeV shown in Figure 5.9. These were carried out numerous times to ensure consistency of the results. YAG screen images were also taken for scattered profiles with all materials at 180 MeV and 160 MeV. To improve stability compared to the lower energy operation of the previous experiment, the beam energy was changed by reducing the power of MKS11 and adjusting the phase appropriately to ensure that the bunches remained on the crest of the RF waves. Each YAG image was taken after irradiation from a single train with approximately 1 nC charge.

Comparative TOPAS simulations were carried out more precisely than the previous experiment, and formed the basis of the model used for simulation comparisons from Section 5.7 onwards. The quadrupole scan data was used for input data to a minimal model of CLEAR built in RF-Track, using the locations of lattice elements directly from the CLEAR MAD-X `.seqx` file. This did not take the effects of steering magnets into account, instead only including the appropriate linear focusing elements (in this chapter, only the 7XX quadrupole triplet shown in Figure 5.2 was used during operation). The model was used to propagate the beam through the remainder of the beamline from the location of the quad scan. After passage through the beamline, the bunch was exported and fed into TOPAS to simulate interactions with the scattering foils. The RF-Track exported and TOPAS imported phase spaces were compared against each other to verify the transfer between the two codes. The results of this more systematic scattering experiment at 200 MeV are shown in Figure 5.10, with comparative TOPAS simulations also displayed.

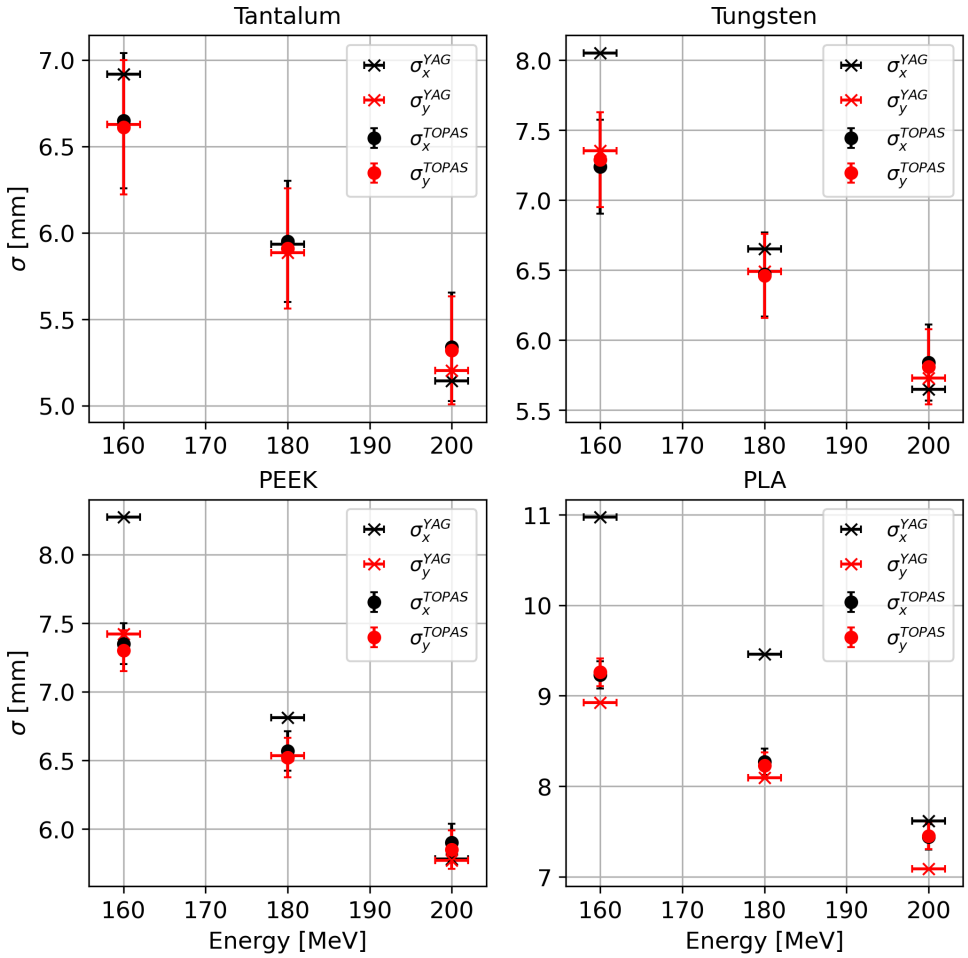

Figure 5.10: Beam σ from Gaussian fitting of transverse intensity profiles against energy for each material under investigation, indicated above each figure. Experimental C-Robot YAG screen results and those from comparative TOPAS simulations indicated. Vertical error bars for experimental data represent standard deviation of 25 train measurements. Simulated data errors dominated by material thickness uncertainty.

At 200 MeV, the scattering from tantalum and tungsten were well within experimental error, although this was rather high due to the significant uncertainties in thickness. At the slightly larger scattering angles, there were significant asymmetries in experimental beam-sizes in x and y, with the difference increasing at lower energies across all scattering materials. This suggested either an error with the model implementation, or effects arising from dispersion in the CLEAR beamline. The latter explanation could be justified by the large emittance derived from the quadrupole scan during the day of experiment in Figure 5.9, well outside of the typical CLEAR parameters of Table 5.1. There were strong horizontal corrections required throughout the beamline from the steering magnets for alignment, which may have given rise to this dispersion. In addition, there was a small, off-energy bunch present during operation which may have exacerbated the dispersive effects. There was nevertheless excellent agreement in scattering in y between experiment and simulation for tungsten, tantalum, and PEEK across all energies. There was an offset for PLA even for the y beamsize which

was not within experimental error of the TOPAS predictions. Future experiments would ensure beam conditions such that the scattering would be typically symmetrical .

These experiments demonstrated some of the likely challenges to be faced with the use of dual-scattering foils in CLEAR. With the somewhat smaller scattering angles from the foils compared to those required for clinical systems, initial beam conditions could have a significant effect on the scattered beam sizes. For the design of scattering foils and particularly those scattering at low angles, a range of initial conditions should be taken into account to assess the effects on the flattened profile, and ideally during operation a standard set of conditions should be retained to reduce any variation. This was carried out for characterisation of the CLEAR scattering system described in Section 5.7. It was assumed that collimation during operation of a dual-scattering system could reduce variance in the resultant beam in a similar manner to the virtual collimation shown in Chapter 3.

5.4 Uniform Intensity Profiles at In-air Test Stand

With broad agreement of scattering in TOPAS and that measured at CLEAR (particularly at 200 MeV), experiments with dual-scattering systems were carried out in the in-air test stand. The aim of the first dual-scattering foil experiment was to demonstrate a flattened electron beam intensity profile, as well as verifying and comparing with simulations given the same geometry as available at CLEAR. The three 3D printed PLA scatterers which had been manufactured for the first scattering experiment outlined in Section 4.3 were used. These S1s were mounted on a linear stage in the in-air test stand at CLEAR. Typical beam parameters at CLEAR were assumed for the design of the dual-scattering system (initially Gaussian in both size and divergence, with 1 mm σ and 4 mrad angular spread). These beam parameters and spatial constraints were given as input arguments to the optimisation process outlined in Section 4.7, although for this case the thickness of S1 was constrained to that of the chosen S1 - 30 mm. The goal of the design was to produce a flattened beam intensity profile at a YAG screen in the in-air test stand. S2 was also designed in PLA to be 3D printed. The manufactured design was based upon a placement of S2 335 mm downstream of S1; this was chosen for ease of insertion at the CLEAR in-air test stand.

The PLA S2 is shown in Figure 5.11, and was composed of 7 cylindrical slices. It was mounted on a film holder for compatibility with the C-Robot's grabber. The film holder could then itself be inserted into the beamline with the C-Robot to produce an enlarged and flattened beam with S1, with this setup shown in Figure 5.12 The CLEAR beam was operated at typical conditions with 200 MeV energy and again with trains of approximately 1 nC (5-10 bunches). Profiles were captured using

Figure 5.11: PLA S2 visualised in CAD (left) and photograph of 3D printed system set in C-Robot holder (right).

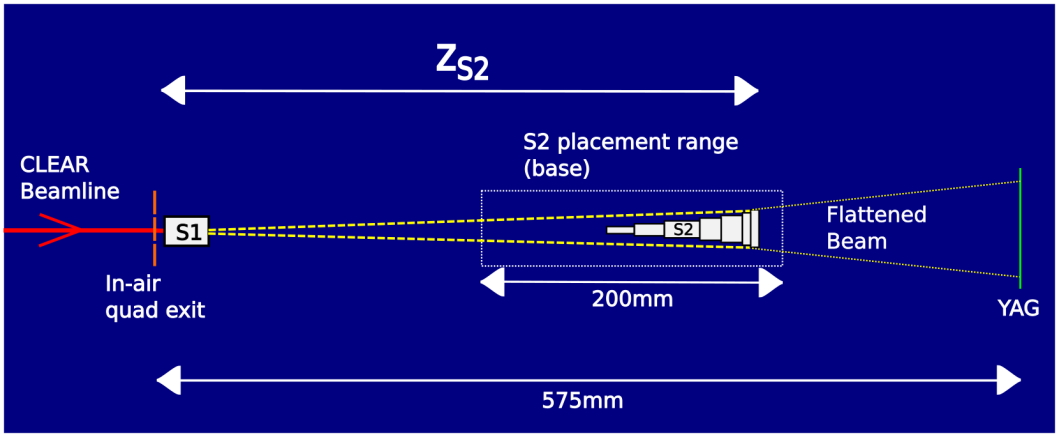

Figure 5.12: Schematic showing layout of dual-scattered profile experiment on CLEAR in-air test stand.

a camera directed at the YAG screen. Measurements were carried out initially with the same S1 (30 mm) and predicted ideal positioning as the design. Profiles were also captured with different longitudinal positioning of S2 and thickness of S1 to investigate the effect on the beam profiles and further benchmark TOPAS results with experiment. Simulations were run to generate transverse electron profiles for these comparisons. The primary beam for these simulations was composed of 10^7 electrons, using the same generic parameters for the CLEAR beamline as for the design.

Flattened beam profiles were retrieved at the YAG screen, with varying uniformity depending on the geometrical layout and S1 used. Experimental profiles were typically smaller than predictions from simulations, but significant uniform extents were still achieved. Comparisons between transverse characteristics from fitting of profiles from TOPAS simulations and YAG data for those results with evidence for uniform regions of over 10 mm radius are shown in Table 5.3. The transverse profiles were described as before with super-Gaussian fits, and 1D slices. x_{95} and y_{95} were used in this case; the stricter uniformity condition was deemed appropriate to distinguish between the effects of enlargement and true flattening. Misalignments between beam and S2 are demonstrated by non-zero $k_{x,y}$ parameters. Experimental errors may have been underestimated particularly for the images with larger beam sizes, where the screen did not capture the entire profile.

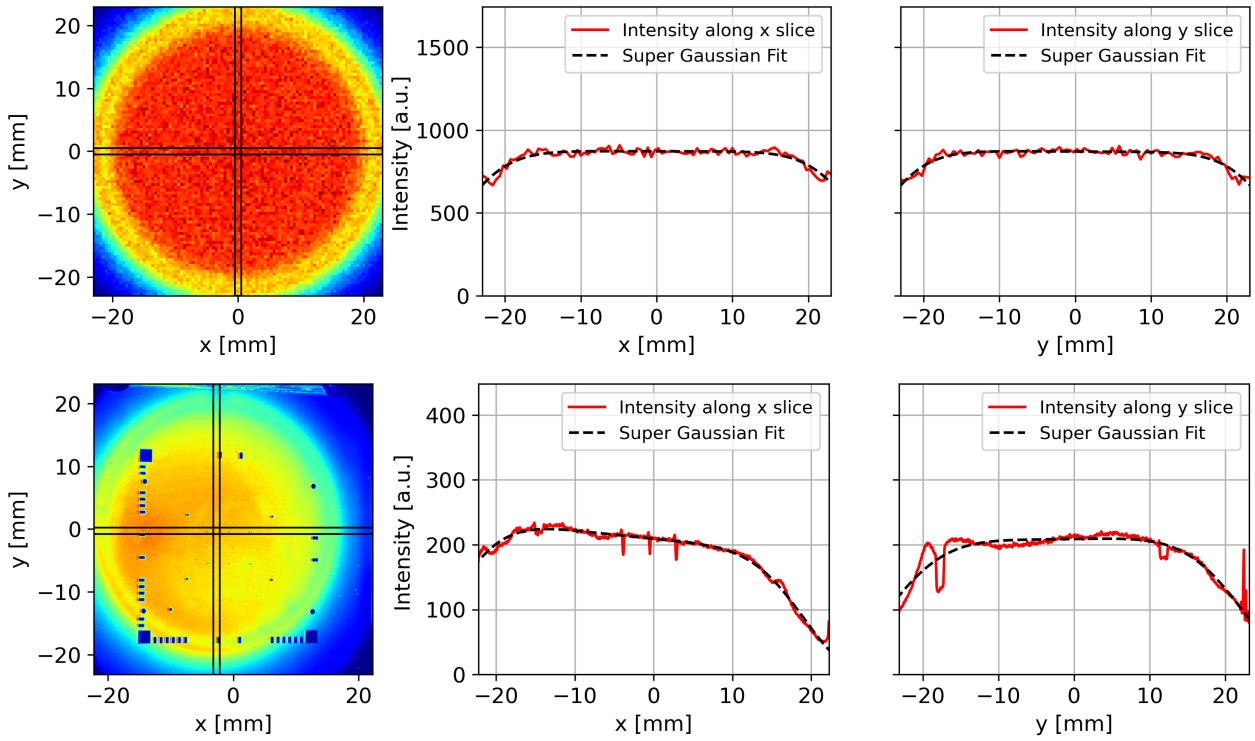

Figure 5.13: 2D transverse beam intensity histograms (left), beam intensities against x (middle) and y (right) from indicated slices across distributions, with super-Gaussian fits shown. Results from TOPAS simulation (top) and in-air test stand YAG screen at CLEAR (bottom), with PLA dual-scattering system inserted. 30 mm S1 and S2 placed 335 mm downstream of S1 (corresponding to Row 4 of Table 5.3).

Figure 5.13 and Figure 5.14 display samples of the measured profiles, for the 30 mm S1. The dark spots on the YAG screens were utilised for calibration purposes during operation, and were omitted from the fitting process as necessary. The YAG measurements from the PLA scatterer experiment were in fairly good agreement with the electron intensity profile in TOPAS. There are a number of possible explanations for the discrepancies in beam sizes between experimental and simulation results. The simulated S2 model in TOPAS had uniform PLA density calculated from the mass of filament and dimensions of the final prints; this may have not accurately represented the structure of the filament based printing. An uneven distribution of filament with variable densities in the scatterers could explain the systematically smaller measured beam profiles in experiment compared to simulation, and would be essentially undetectable otherwise. Additionally, the generic beam parameters at CLEAR used for simulation may have slightly deviated from the experimental beam distribution as differences in the asymmetries in beamsize in the transverse plane between both sets of results and simulations indicate.

Nevertheless, super-Gaussian fitting demonstrated uniform components for many of the retrieved profiles, and particularly that corresponding to the geometry used for the design optimi-

Table 5.3: Super-Gaussian fitting parameters in experiment and simulations of PLA dual-scattering setup, for results with evidence for uniformity region of 1 cm radius. t_{S1} is the thickness of S1; z_{S2} is the distance from the upstream face of S1 to the downstream face of S2, as shown in Figure 5.12. Line in **bold** is setup from design optimisations. Units of mm unless otherwise specified. Errors from fitting covariance output.

Row [#]	z_{S2}	t_{S1}	Sim x_{95}	Exp x_{95}	Sim y_{95}	Exp y_{95}	Exp k_x [a.u.]	Exp k_y [a.u.]
1	335	20	10.9±0.4	10.1±0.1	11.0±0.3	8.3±0.3	1.3±0.1	-0.4±0.1
2	381	20	13.9±0.2	10.0±0.1	13.6±0.2	10.0±0.1	0.6±0.1	0.2±0.1
3	281	30	9.7±1.6	11.4±0.1	11.2±1.0	13.8±0.6	0.5±0.1	1.5±0.1
4	**335**	**30**	**17.7±1.0**	**13.5±0.1**	**17.7±0.8**	**13.4±0.3**	**-0.6±0.1**	**0.1±0.1**
5	381	30	18.9±0.3	12.7±0.1	18.8±0.3	12.5±0.2	0.2±0.1	0.4±0.1

sation. With the use of the thinner 20 mm S1, the uniform region was found to decrease slightly as shown in Table 5.3. This was due to the beam being small compared to its location at S2 and thus relatively less of the beam being flattened by S2. Use of the 10 mm scatterer resulted in a more Gaussian shaped beam; the smaller beam essentially passed through S2 as it were a second flat scatterer. The comparative simulations and those utilised for the design of the dual-scattering system was based upon the desired intensity distribution of the primary electrons rather than all particles taken together, with the secondary component apparently having no quantifiable effect on the YAG profile.

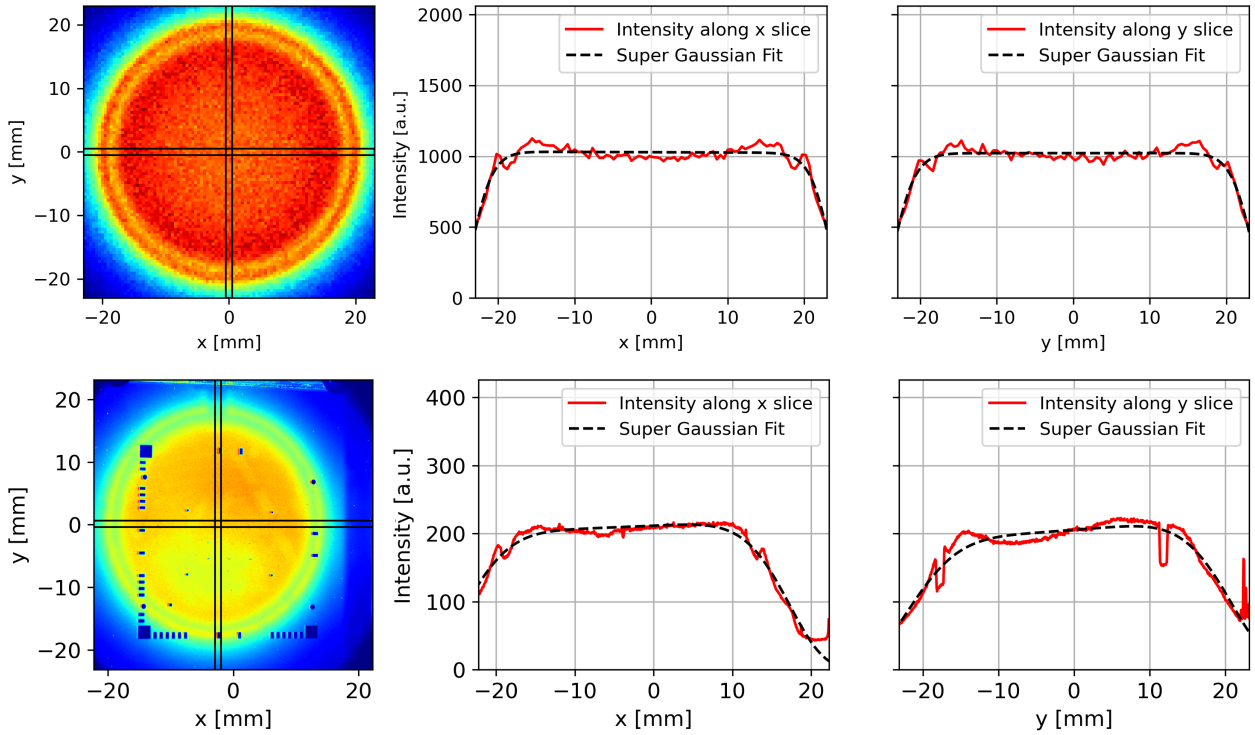

Figure 5.14: 2D transverse beam intensity histogram (left), beam intensities against x (middle) and y (right) from indicated slices across distributions, with super-Gaussian fits shown. Results from TOPAS simulation (top) and in-air test stand YAG screen at CLEAR (bottom), with PLA dual-scattering system inserted. 30 mm S1 and S2 placed 381 mm downstream of S1 (corresponding to Row 5 of Table 5.3).

5.5 Uniform Dose Profiles at In-air Test Stand

With enlarged and flattened profiles successfully demonstrated in beam intensity, the next goal was to measure dose profiles with radiochromic films as a more clinically valid confirmation of uniformity. Multiple designs were carried out to verify the flexibility and validity of the design process. EBT3 films [249] were used for all irradiations, with analysis carried out as described in Section 5.2.

The CLEAR setup was adapted to allow numerous dose measurements to be taken in the in-air test stand. The 30 mm S1 remained in its upstream position, but the positioning and thus design of S2 were modified to allow films to be mounted on to the C-Robot for the measurements. Aluminium was the preferred material choice for S2 for this experiment. The higher density of the material was required to reduce the size of the scatterers to be able to physically fit into the allocated space provided on the vertical stage, and still demonstrate beams with a significant uniform component. Three new S2s were designed to be mounted in 3 different longitudinal positions in the test stand, which could individually be moved into the beam path using a vertical stage. These are named Al 1, Al 2 and Al 3 moving from downstream to upstream positioning, as shown in Figure 5.15. The flattened profiles from the first two of these were measured in one location and the other was measured at a slightly further downstream location to smear out any artefacts from the steps in the scattering blocks (these locations are also indicated in Figure 5.15). The scatterers were mounted in PMMA holders, which slightly impinged upon the beam profile. This was not taken into account during the initial design simulations before manufacture of the scatterers. Thus, TOPAS MC simulations with the PMMA holders added were run and the positioning of the scatterers modified so as to mitigate the loss of uniformity that the PMMA was predicted to cause.

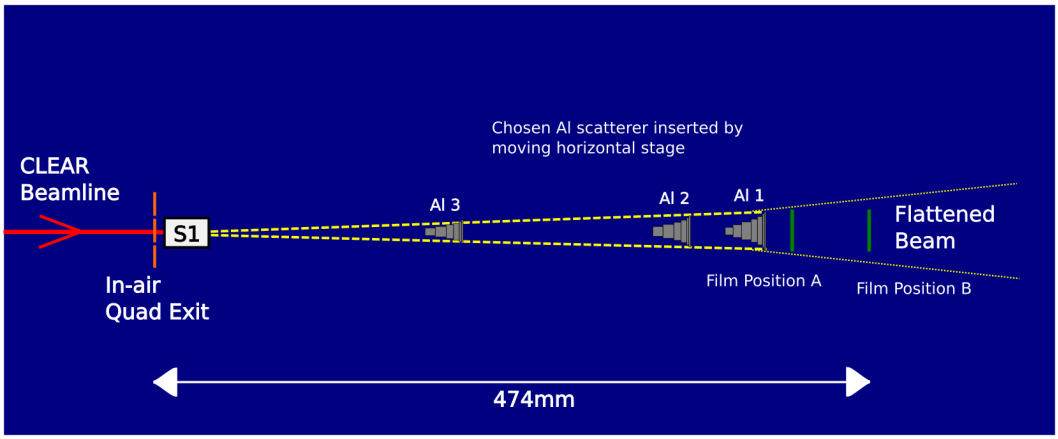

Figure 5.15: Schematic showing layout of dual-scattering dose experiment on CLEAR in-air test stand. Al 1, Al 2 and Al 3 inserted respectively at positions indicated. Film positions A and B used for measurements also indicated.

Table 5.4: Super-Gaussian fitting parameters from transverse experimental dose profiles and TOPAS simulated intensity profiles for aluminium dual-scattering setup. S2, Loc column refers to the choice of scatterer and positioning of transverse profile measurement, as shown in Figure 5.15. Errors from fitting covariance output.

Row	S2, Loc	Sim x_{95} [mm]	Exp x_{95} [mm]	Sim y_{95} [mm]	Exp y_{95} [mm]	Exp k_x [a.u.]	Exp k_y [a.u.]
1	Al 3, A	11.3±0.3	16.3±0.1	11.6±0.3	14.4±0.2	-0.8±0.1	-0.5±0.1
2	Al 3, A	11.3±0.3	15.0±0.1	11.6±0.3	13.0±0.2	-1.2±0.1	-0.6±0.1
3	Al 2, A	8.1±0.3	7.9±0.1	8.2±0.2	6.7±0.1	0.3±0.1	-1.1±0.1
4	Al 2, A	8.1±0.3	8.2±0.2	8.2±0.2	7.0±0.2	0.0±0.11	-0.8±0.1
5	Al 1, B	8.5±0.3	8.9±0.2	8.4±0.3	7.4±0.1	-0.5±0.1	-0.3±0.1
6	Al 1, B	8.5±0.3	9.5±0.2	8.4±0.3	7.9±0.2	-0.0±0.1	-0.2±0.1

Radiochromic film irradiations were carried out for each of the three scattering setups in pairs, with two different intensities (3 nC/train and 25 nC/train) to investigate any significant effect on the scattered profile from the changed beam conditions. The total charge delivered by the beam was effectively arbitrary, as it was primarily the profiles on the films rather than the actual doses that were of concern for this experiment. Transverse fitting parameters retrieved from radiochromic films and TOPAS simulations are shown in Table 5.4, with a sample of the flattened profiles displayed in Figure 5.16. No evidence of photons from Bremsstrahlung was visible (as expected from dose simulations in thin films), with the general character of the profiles agreeing well with the electron intensity distributions predicted from TOPAS, verified from comparison of super-Gaussian fits. An additional irradiation pair with the films held very closely downstream of Al 1 was carried out to verify the predicted presence of the ringed structure (such as that shown in Figure 4.18). Two sets of irradiations with S1 removed were carried out for additional comparisons with simulations.

The higher intensity film results generally displayed some discrepancies between those at lower charges, although without a distinctive trend. Some differences were expected due to the effects of beam loading at these high intensities, but significant uniform (or skewed uniform) dose components were still achieved in all cases with two scatterers inserted. All films were EBT-3, which would be expected to be dose-rate independent, and thus any discrepancy would not be expected to originate from the films themselves. A further justification for the assumption of some errors in the previous experiment arising from the PLA filament structure was that the discrepancies between experiment and simulation were overall decreased here compared to the previous PLA S2 experiment of Section 5.4 (especially from Row 3 onwards in Table 5.3). The best agreement was found in the results with only the aluminium scatterers inserted, not displayed in this table but found in Appendix A.

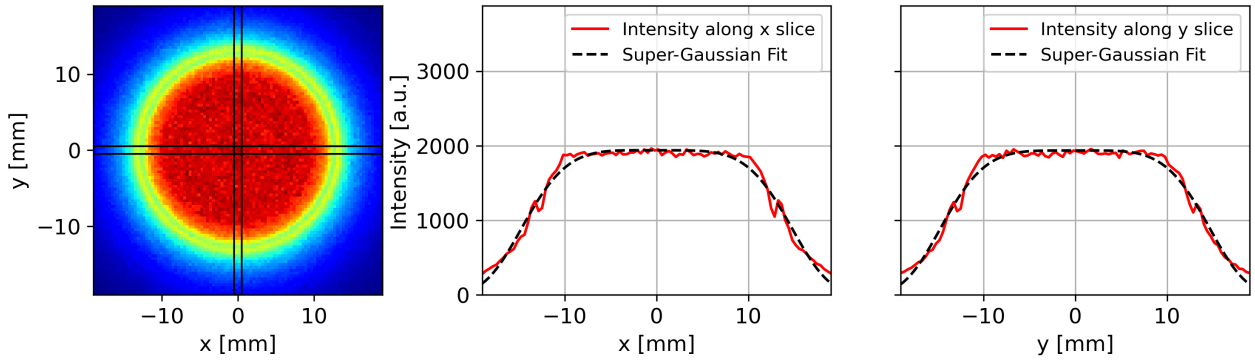

(a)

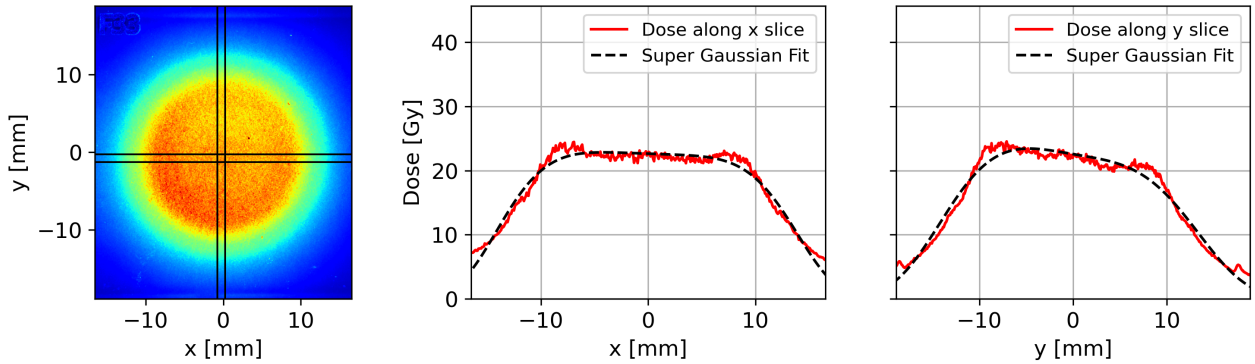

(b)

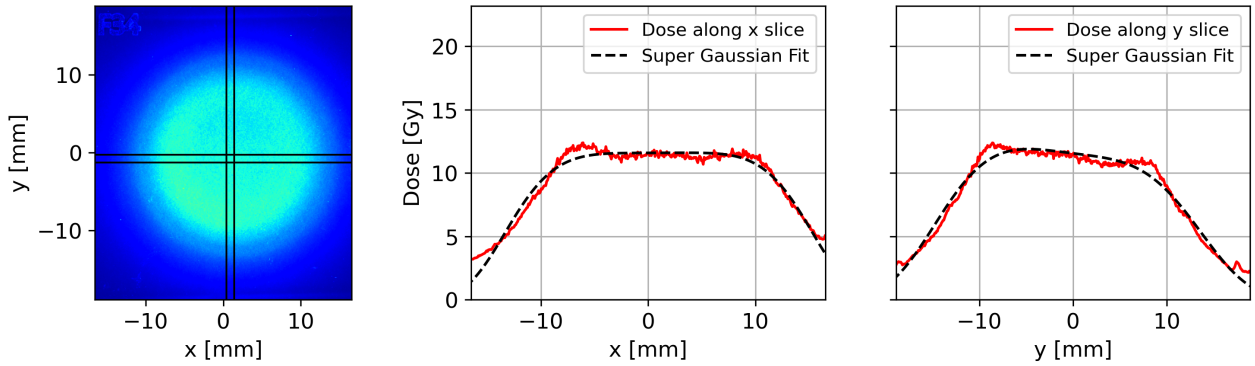

(c)

Figure 5.16: 2D transverse primary beam intensity histogram (left), primary beam intensities against x (middle) and y (right) from indicated slices across distributions, with super-Gaussian fits shown, from TOPAS simulation (a). 2D transverse beam dose histograms (left), beam doses against x (middle) and y (right) from indicated slices across distributions, with super-Gaussian fits shown, from EBT3 film measurements at CLEAR at 3 nC/train (b) and 25 nC/train (c) intensities. Simulation/experiments carried out with Al 2 inserted and measurements taken at Film Position A. (b) and (c) correspond to Rows 3 and 4 in Table 5.4, with (a) used for comparisons to both.

5.6 CLEAR Vacuum Dual-Scattering System I

5.6.1 Positioning, Design and Installation

A condensed description of the installation and initial experiments of concern in this section is given in [250]. Due to the limited space available in the in-air test stand and numerous stages required for installation of the scatterers at this location, a water tank could not be installed with the above experiments. Dose measurements in water were desired however to compare with predictions from TOPAS and assess the effects of collimation and flattening on uniformity for conformal treatment (though the beams would be far smaller than those studied in Chapter 4). Furthermore, the position of the previous setups so close to the tank was predicted to result in significant energy loss and photon production; even if the latter did not contribute to dose measured by dosimetric films in air, it was predicted to contribute a significant dose at depth in water. In collaboration with CLEAR operators, the installation of a dual-scattering system in the CLEAR beamline itself was preferred. Not only would this allow flexibility and reduce losses for these experiments, but the capability of CLEAR to provide flattened and enlarged beams without taking up space in the experimental test stand could be extremely desirable for users at CLEAR in general.

Three locations in the CLEAR beamline for the dual-scattering system were proposed by the operators. These locations were those where the vacuum chambers could be realistically installed in the beamline. Consideration was given to installation of both scatterers in the same vacuum chamber for "upstream" operation and minimisation of secondary production; this was not deemed practical however, and as such all simulations were carried out assuming foils located in separate chambers. Preliminary designs were carried out for systems located in available positions for chamber instal-

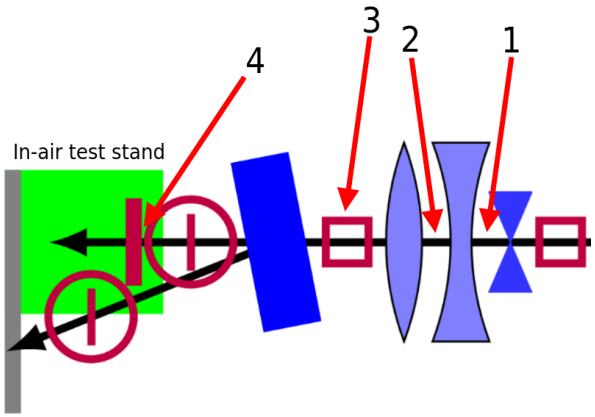

Figure 5.17: Schematic showing end segment of CLEAR beamline (enlarged from Figure 5.2) with available options for installation of vacuum chambers indicated. Beam passage from right to left.

lation shown in Figure 5.17, initially with nylon as this was the intended material at first. The aim of these designs (and that of the final system) was to achieve a uniform radius of approximately 15 mm (this was predicted to depend on the initial beam conditions more heavily than in previous experiments). Installation of a downstream system in positions 1 and 2 would have been the most straightforward for modification, but would still require relatively thick scatterers to achieve significant magnification of the beam. Furthermore, the distance of 1.1 m between S1 and S2 resulted in difficulties during optimisation and significant double-peaking even in heavily optimised profiles. Installation in positions 2 and 3 was more desirable, with the shorter distance between the scatterers producing more effective results from the optimisation.

Table 5.5: Initial designs for vacuum systems placed in reference to Figure 5.17. Designs based upon nylon S1 and S2 unless otherwise stated, S2 split into 5 slices. Initial symmetrical beam conditions of $\beta_{x,y}$ =20 m, $\alpha_{x,y}$=0 and **normalised** emittance $\epsilon_{x_n,y_n} = 10\,\mathrm{mm\,mrad}$. t_{S1}, H and σ_{S2} as defined in Chapter 4. Transmission defined within virtual collimator of 15 mm radius.

Positioning	t_{S1} [mm]	H [mm]	σ_{S2} [mm]	Transmission	E_{mean} [MeV]
3 & 4 (S2 Al)	7.0	6.0	6.0	54%	193.27
2 & 3	3.0	8.0	2.2	50%	197.35
1 & 2	1.7	5.8	2.0	47%	198.16
1 & 2 (PEEK)	1.8	4.5	2.0	47%	198.17

The main concern with installation in positions 2 and 3 was this would require the removal of BPM 890. This was used for diagnostics and was critical for CLEAR machine development work at the time. The final installation location choice was in positions 3 and 4 in Figure 5.17. The distance from the system to the in-air test stand (2.2 m upstream of typical sample placement in the C-Robot) was a cause for concern, as this would require very thin, precisely machined scatterers and would likely be sensitive to variations in the initial beam. Conversely, the scatterers would also produce very few X-rays to contaminate the uniformity of the beam in water, and were predicted to reduce the average beam energy by less than 1%. Furthermore, installation here would not require the removal of any diagnostic components in the beamline. Thus, the new scattering system would be installed in positions 3 and 4.

The scattering system was optimised further within these positional constraints once again using the method developed in Chapter 4 in PEEK rather than nylon due to its aforementioned heat resistance, robustness, and radiation hardness. The original choice of nylon had been due to the ease of implementation of this material in the comparative TOPAS simulations. Two vacuum chambers were installed at CLEAR for placement of the scattering system in the described locations in the beamline. The aim for the final optimisation was to produce a transverse profile with 15 mm uniform radius exactly halfway along the in-air test stand, for a weakly focused beam at CLEAR with

idealised parameters as shown in Table 5.5. The minimal thickness of the layers on the second scatterer was limited as many of the optimisation runs would tend towards shapes with extremely thin bases when constraints were removed, which would create manufacturing challenges. A successful design in TOPAS using PEEK was achieved and is shown in the final row of Table 5.5, with results of TOPAS predictions of the beam profile at the C-Robot shown in Figure 5.18.

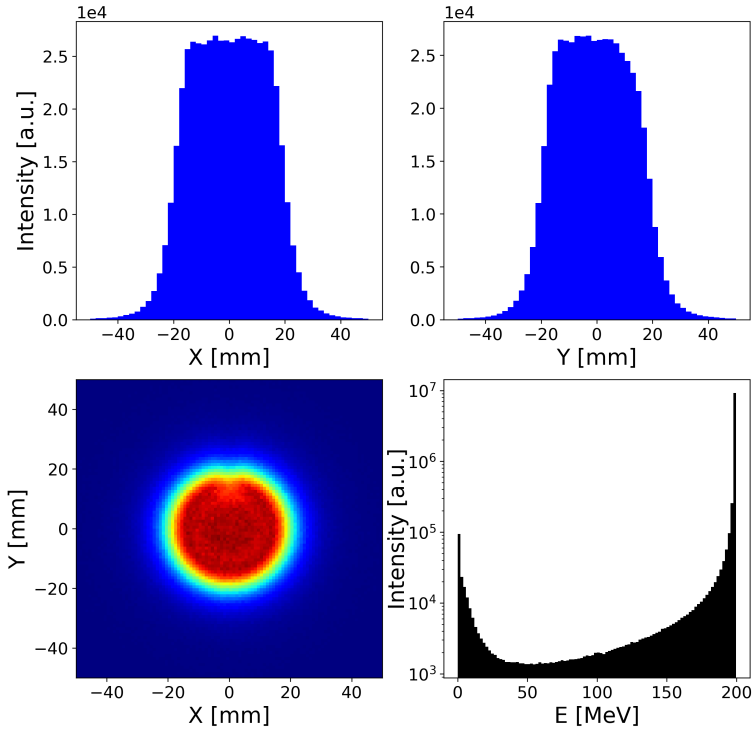

Figure 5.18: Simulated profile generated by PEEK in-vacuum dual-scattering foil from 200 MeV initial beam in TOPAS, using generic positioning of C-Robot YAG screen at CLEAR. Primary beam intensity against x (upper left) and y (upper right) from thin slices across distribution. 2D transverse intensity histogram (bottom left) and intensity against primary particle energy (bottom right).

This first iteration of vacuum scatterer (referred to as V1 from here onwards) was machined by CLEAR operators with a lathe. Schematics of the design and final system installed in the CLEAR beamline are shown in Figure 5.19. The system was mounted on linear stages in the vacuum chambers, with each scatterer held by a 500 µm diameter steel stem. The effect of the stem particularly on S2 (the base of the shape was too thin to use for mounting, so the next layer was used) was simulated in TOPAS and is visible in the 2D profile and y slice in Figure 5.18. This was predicted to cause a slight loss of uniformity in the profiles. The stage of the first scatterer was pneumatic with only "inserted" and "extracted" position. The S2 stage was variable to assist with alignment of the beam through the complete system during operation.

Figure 5.19: Schematic of first vacuum dual-scattering system components at CLEAR (left), camera images of S1 (middle) and S2 (right) installed in beampipe vacuum chambers.

5.6.2 Profile Measurement

Alignment of the beam to this system during operation proved difficult due to the small transverse size of the first scatterer and lack of diagnostics beyond the CLEAR Beam Position Monitors (BPMs) and profile measured on the C-Robot YAG screen to estimate the beam position. Once correctly aligned however, the system was found to produce a large, hollow transverse distribution when measured at the CLEAR in-air test stand, as shown in Figure 5.20. This was predicted by the preliminary simulations for certain beam parameters, and could be corrected through appropriate focusing with quadrupoles in the experimental beamline. As also shown in Figure 5.20, the large extent of the beam from this system resulted in the edge of the beampipe being clipped, with a diagnostic in-vacuum YAG screen also infringing on the profile.

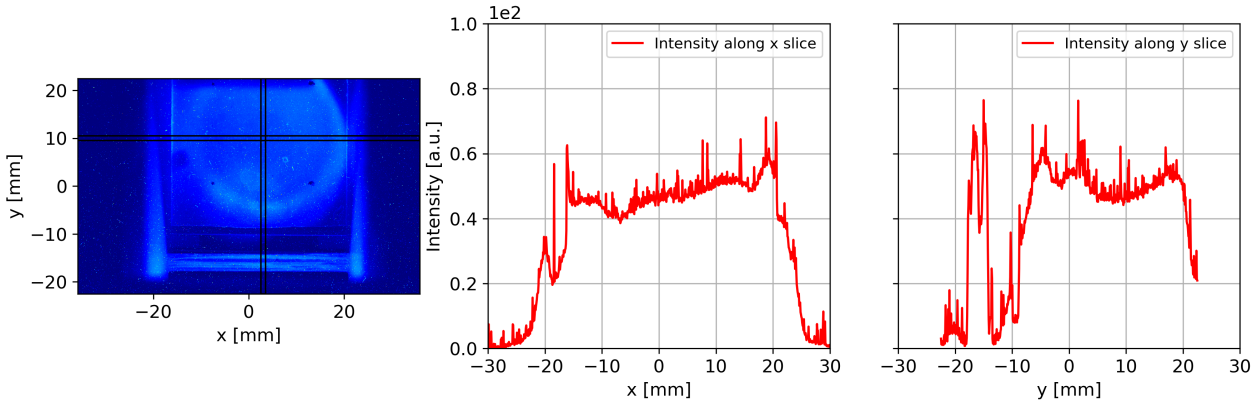

Figure 5.20: 2D transverse intensity histogram (left), intensity against x (middle) and y (right) from indicated slices across distribution. Extracted from image of C-Robot YAG screen with V1 system inserted in CLEAR. Beam cut by diagnostic YAG screen 910 in beamipe at top of profile, and edge of beampipe itself. Anomalies visible from edge of screen and holder.

Despite success in retrieving an enlarged and flattened profile, the size of the beam covering the entire YAG screen and associated issues with clipping made it difficult to characterise or compare

this profile. Large scale variation across the "uniform" component could be reduced to less than 10% however, although characterisation of the fringes of the beam were impossible due to the clipping and extension of the profile beyond the YAG screen. The infringements in the beam were rectified by introducing a collimator to the system for the first time. This initial collimator was composed steel, 30 mm thick with a 21.5 mm full-aperture, positioned 2 cm immediately downstream of the beampipe exit. This smaller aperture size than the predicted uniform extent was chosen to improve the robustness of the system to beam jitter. The geometry of the V1 system and generic positioning of C-Robot for measurement in the CLEAR in-air test stand is shown in Figure 5.21. With appro-

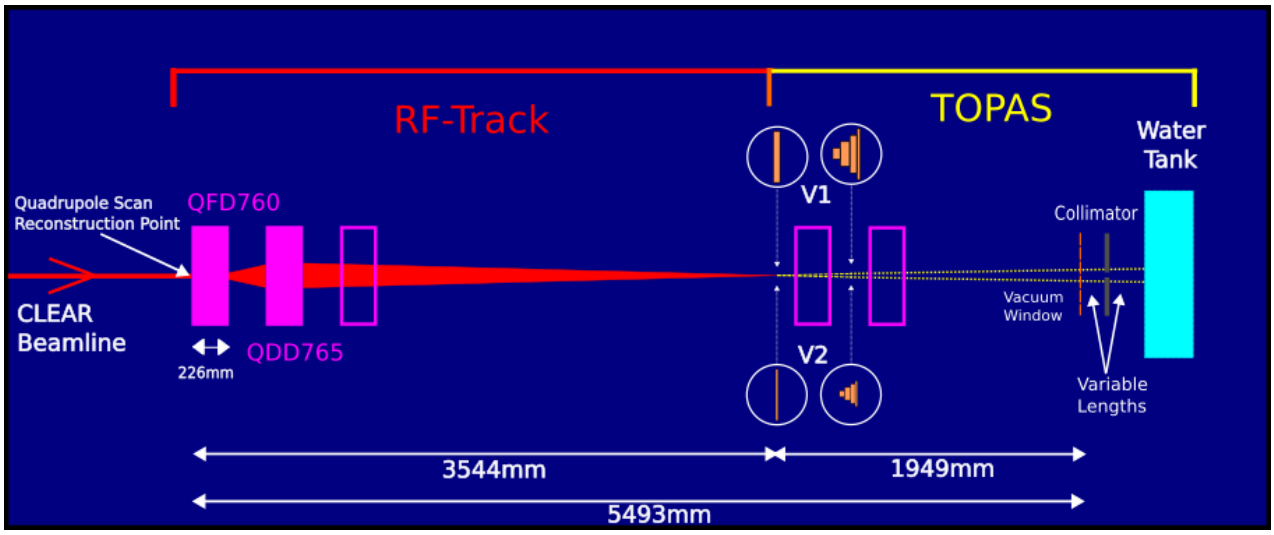

Figure 5.21: Schematic of in-vacuum experiments, indicating components, relevant regions and code choices used for comparative simulations. Inactive quadrupoles represented by open pink boxes.

priate adjustments and alignment, a partially uniform beam profile was achieved at CLEAR for the first time, with a sample shown in Figure 5.22. In x, this could be successfully characterised with a super-Gaussian fit as in the previous studies, with x_{90} determined as 10.27 mm as measured by the YAG screen.

Following the successful retrieval of a uniform beam profile, studies on the evolution of the intensity and dose profiles in water were carried out for comparison with predictions by TOPAS. These would represent the first studies of magnified, uniform VHEE beams in a patient model (water). Initial intensity measurements were carried out using the C-Robot YAG scintillating screen in water. The screen was moved longitudinally downstream through the water tank from the surface (20 mm from tank window) to 140 mm depth, at 10 mm increments up to 60 mm depth and in 20 mm increments beyond this. Images were saved at each increment, with a sample of these displayed in Figure 5.22. Fits to the profiles in x could be made, although the YAG screen artefacts and markings may have added some uncertainty to these measurements. Data in y is not displayed here due to the

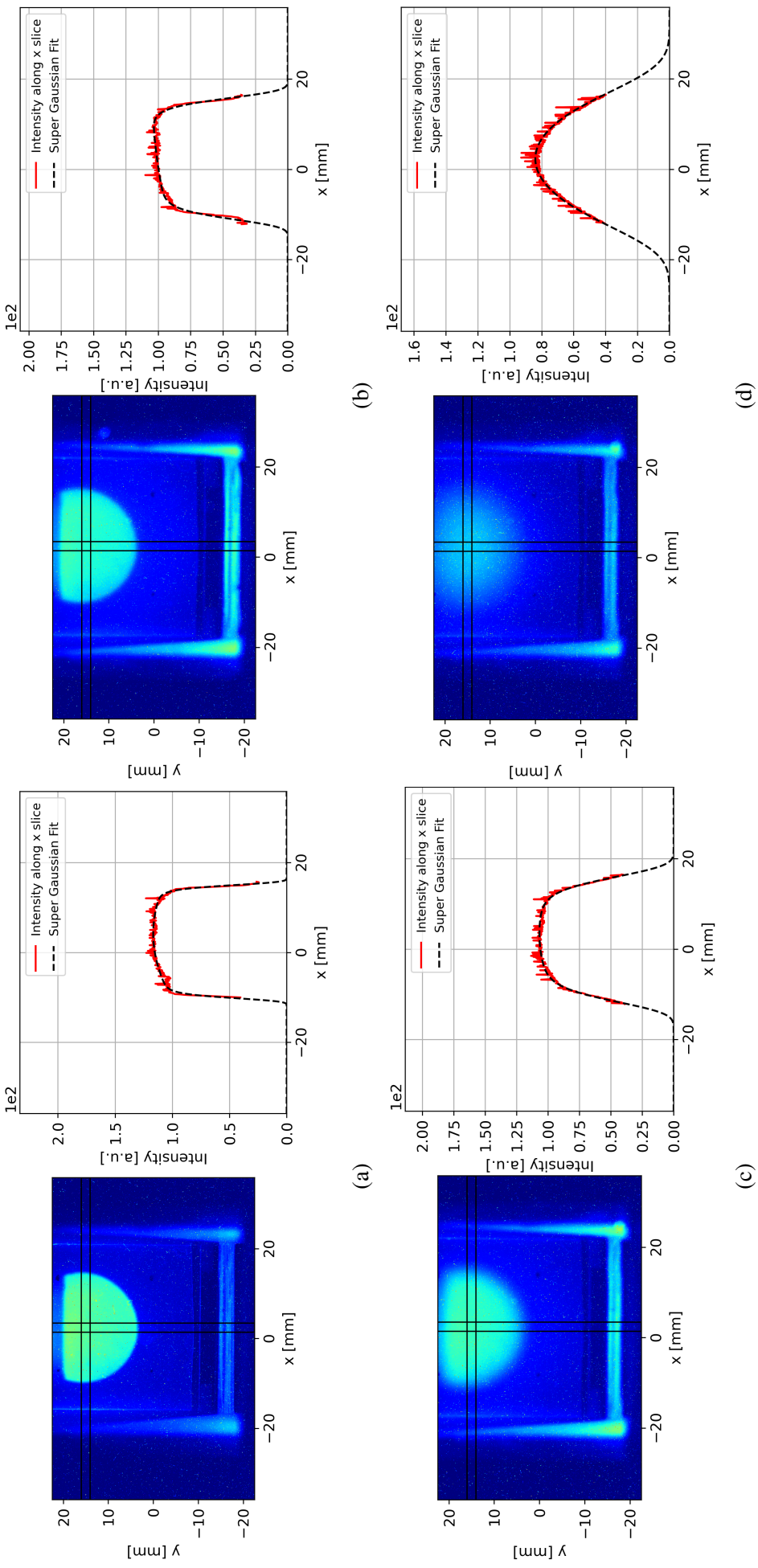

Figure 5.22: Transverse profiles with V1 inserted, measured with C-Robot YAG screen in air (a), 20 mm (b), 60 mm (c) and 100 mm (d) depths in water. 2D transverse intensity histogram (left), intensity against x (right) from indicated x slice with super-Gaussian fit shown in each sub-figure. Clipping from diagnostic YAG screen visible.

Table 5.6: Quadrupole scan results taken with 7XX triplet and used for input into RF-Track/TOPAS combined model for studies in Section 5.6 and 5.7.

Parameter	β_x,β_y [m]	α_x,α_y	ϵ_{x_n},ϵ_{y_n} [mm.mrad]
Value	5.45, 22.54	0.18, 0.58	12.9, 8.5

interference of the diagnostic YAG screen. These profiles were trimmed to remove the effect of the YAG screen holders visible at the fringes of the images.

Evolution of the fitted uniform radius parameters is shown in Figure 5.23. Comparative TOPAS simulations were carried out in a similar manner to that discussed in the latter of the single scattering experiments of Section 4.3, using a combined RF-Track and TOPAS model to propagate the beam through the CLEAR beam lattice, dual-scattering system, and collimator and water phantom. The simulated beam for these comparisons was initialised with the quadrupole scans taken for a later experiment discussed in Section 5.7; these beam parameters displayed in Table 5.6. Measurements taken on the day of experiment were used to build the TOPAS component of this model - the accuracy was verified through comparisons of in-air intensity profiles (x_{90} = 10.2±0.3 mm) from simulations, comparable to the value from the in-air YAG measurement of x_{90}. Uniformity decreased in alignment with simulations, with an initial uniform extent in x of 10.06 mm, decreasing to 6.36 mm at a depth of 140 mm. Qualitatively, this was explained by the evolution from a uniform

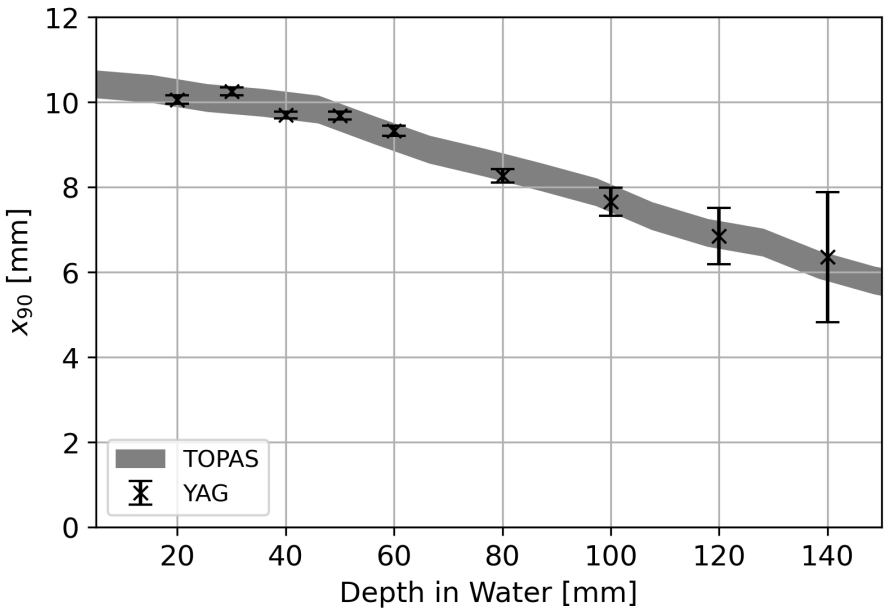

Figure 5.23: x_{90} of transverse beam intensity against depth in water with V1 system inserted. Measured with C-Robot water tank positioned 2245 mm downstream of S1, taken from fits to YAG images with comparative TOPAS simulation results also shown. Beam operated at 1 nC per train. TOPAS error margin taken from simulation resolution, with experimental errors propagated from fitting covariance matrix.

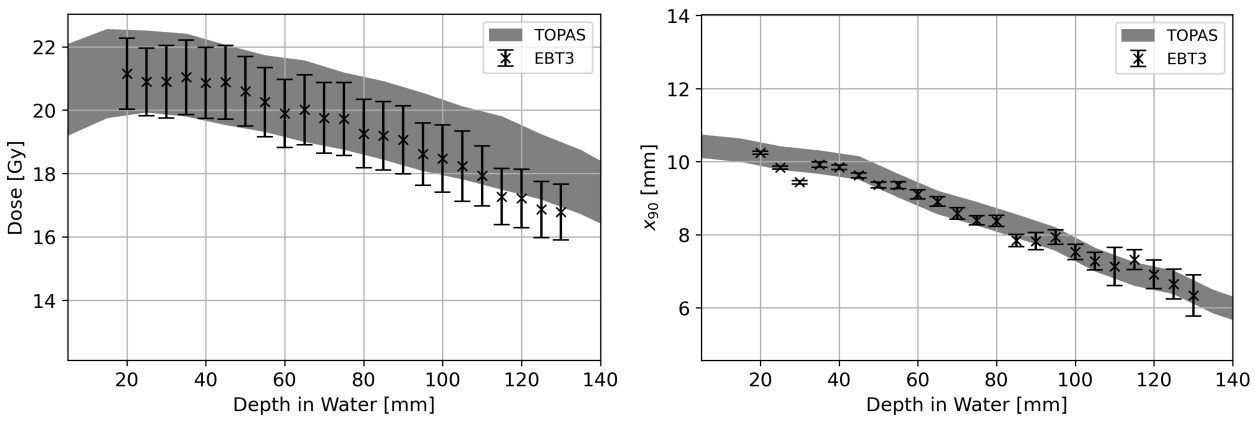

Figure 5.24: Dose (left) and x_{90} (right) against depth in water for single holder irradiation with V1 dual-scattering system inserted. Measured in test stand water tank with long EBT3 film holders, with dose directly extracted from 5x5 mm^2 large sample region, and x_{90} taken from fits to transverse profiles on films. 104.6 nC accumulated charge, delivered at 1 nC/train intensity. Water tank positioned 2245 mm downstream of S1.

beam profile to a more Gaussian shape with extended tails, despite the increasing lateral spread of the beam. A similar scan was performed in-air to study the resultant beam divergence from the dual-scattering system. This was found to be minimal, and with only small effects at the fringes of the transverse profile indicating the effects of in-air scattering (x_{90} increased by 0.5 mm in 200 mm travel through air, although simulations demonstrated that this was more due to divergence from the scattering foils rather than scattering in air). Thus, the choice to generally neglect simulating air for design and comparative studies in TOPAS was justified in the VHEE regime.

Whilst a useful general benchmark, dose measurements were taken in preference to the YAG data to determine agreement between simulation and experiment for the evolution in water, both in terms of the transverse profiles of the beam and to measure the dose. Typically, films were less susceptible to noise than the YAG screen. It has also been demonstrated at CLEAR that YAG images are sensitive to beam intensity due to saturation of the camera. However, EBT3 films are dose rate and thus intensity independent with a measurement accuracy of 5% [249]. Measurements of beam evolution in water with the V1 system were carried out using the long holders at CLEAR with space for 23 films with 0.5 mm spacing. These holders allowed dose profiles at numerous depths to be measured simultaneously, ensuring no variation in delivered charge. The irradiation was carried out in water, with the beam operating at a 1 nC/train intensity and accumulating 52.3 nC total charge. The results in terms of raw dose measurements and the evolution of the fitting parameters and longitudinal profiles as before is shown in Figure 5.24. These dose measurements were carried out across a "large" sample size of 5x5 mm^2. Due to the fairly fine resolution of the TOPAS simulations, standard deviation across the uniform regions was typically around 7% from statistical fluctuations

- comparable to the dose error in the films of 5%. x_{90} from the films was initially 10.2±0.1 mm, at 20 mm depth, decreasing to 6.3±0.6 mm at 130 mm depth. Increased errors with depth were due to emergence of non-Gaussian tails predicted from simulation.

With appropriate adjustment, it was possible to direct the beam through the dual-scattering system such that screen 910 did not impinge on the profile. Steering magnets were used to achieve this effectively through a dog-leg. Thus, the first symmetrical, uniform dose distribution was measured at CLEAR with the V1 scattering system, as shown in Figure 5.25.

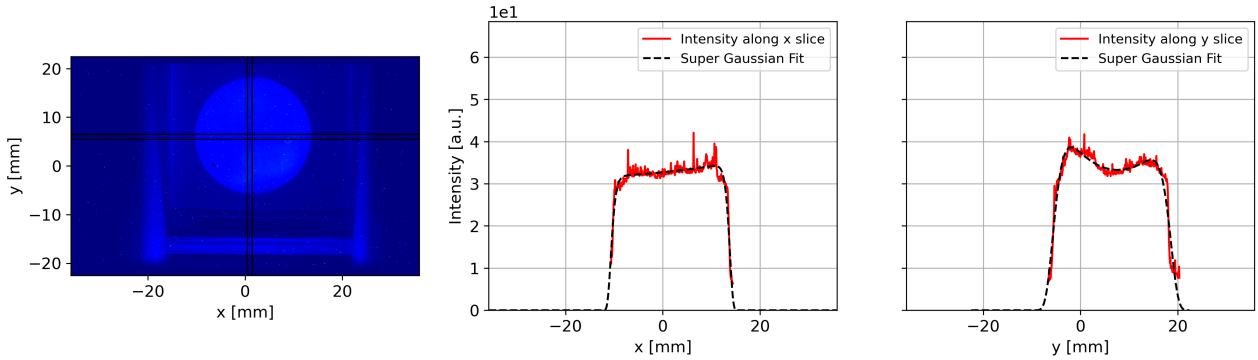

Figure 5.25: 2D transverse intensity histogram (left), intensity against x (middle) and y (right) from indicated slices across distribution, with super-Gaussian fits shown. Measured with C-Robot YAG screen in-air with V1 inserted and aligned with steel collimator to avoid diagnostic YAG screen and beampipe clipping.

5.6.3 Removal of V1

Despite the general success of this system for providing such a large and flattened beam, it was deemed unsuitable for use as a permanent installation at CLEAR. The large uniform radius was only just measurable with the C-Robot YAG and films, and much of the beam profile extended past the size of the films or YAG screens when uncollimated. This was in addition to the issues with clipping which prevented further characterisation of the beam. Studies run by CLEAR often require UHDR irradiation of samples; for a dual-scattering system to be a useful upgrade to CLEAR for this purpose, a smaller beam would be required. The beam generated from the V1 dual-scattering system could only provide a maximum dose of around 15 Gy per train according to TOPAS simulations and experimental results when operating at the maximum charge/train of 86 nC - even without considering the effects of increased jitter and beam-loading at high intensity. A further design was envisaged to address these concerns; to produce a smaller flat top to allow the entire profile to be captured without collimation, providing a significantly higher charge-dose ratio. Steps would also be taken to improve the ease of use in terms of alignment.

The steel collimator whilst broadly successful at removing dose outside the aperture still resulted in a significant background distribution, demonstrated by the non-0 values around the profile fringes in the film doses. This prevented measurements of the lateral penumbra of the beam from being carried out. The dosimetric results confirmed that indeed a thicker and/or higher density collimator would be required to further reduce the dose outside of the aperture (this would also be expected from inspecting the blockage of charge from Figure 4.21 in Chapter 4). At the shallowest water phantom depth, background dose outside of the collimator aperture was measured to be 36±5% of the flat-top dose (in agreement with predictions from TOPAS simulation).

5.7 CLEAR Vacuum Dual-Scattering System II

5.7.1 Design Overview

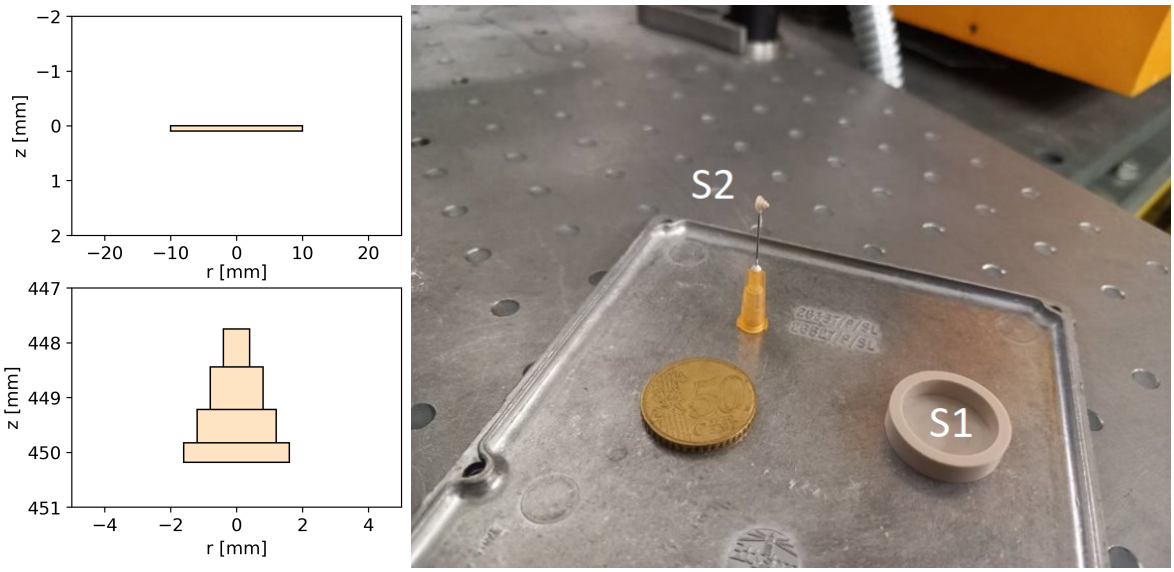

Figure 5.26: Design schematic showing longitudinal coordinate in TOPAS component of design simulations for S1 and S2 against radius of transverse PEEK V2 slices (left) and photograph of manufactured components (right).

A final design was carried out using the previous method, but this time aiming for a system with a uniform radius r_{90} of 7.5 mm. The material and location of installation were maintained. The production of such a small uniform beam required great care during the optimisation process, as slice limits were often reached before successful designs were retrieved. The resultant design is shown in Figure 5.26. This far smaller radius was predicted to allow beams with flat top doses of 50 Gy to be produced with a single train at CLEAR, assuming maximum beam intensity was achieved. In reality, it was predicted that losses of stability and effects of beam loading would make this challenging. During the design process, it was clear that the final distribution would be more

dependent on the initial beam than previous designs, due to their lower scattering power. Hence, it was expected that time would have to be spent investigating the ideal optical conditions for operation with the scattering foils at CLEAR.

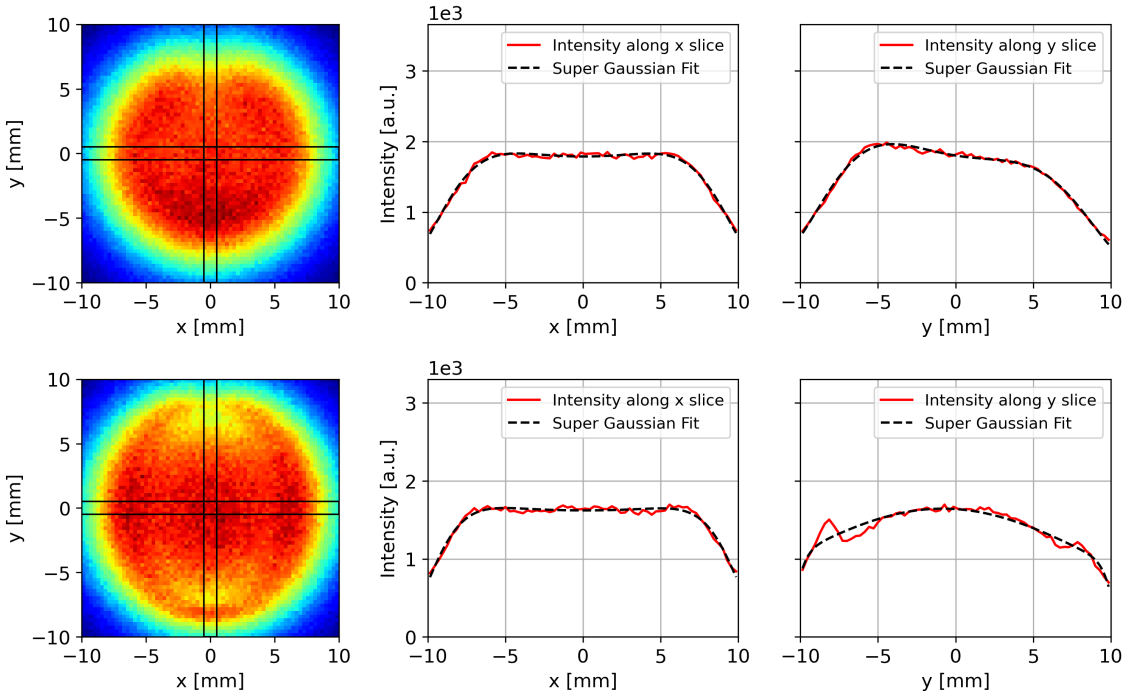

Figure 5.27: 2D transverse primary beam intensity histograms (left), intensities against x (middle) and y (right) from indicated slices across distributions, with super-Gaussian fits shown. Extracted from combined RF-Track/TOPAS simulations of CLEAR with V2 inserted with different optics settings. No focusing (top) and with typical quadrupole settings used during operation to reduce jitter (bottom). Quadrupole strengths of QFD760 and QDD765 were 3.44 and $-3.94\,\mathrm{m}^{-2}$ respectively, for this latter case. Initial beam conditions of Table 5.6 assumed to assess changes from conditions of design simulations (caption of Table 5.5) including steel mounting stem.

The system was again mounted with thin steel stems. Several experiments were run throughout spring and summer of 2023, with the two principle aims being the further comparisons of uniform beam evolution in water, and the characterisation of the system for general operation. Simulations predicted approximately 0.5 nC total transmitted charge would be required to produce 1 Gy on the flat top in-air, with this charge-dose ratio experimentally verified in water as described in Section 5.7.3. The design was carried out for the ideal beam conditions as described in Table 5.5. TOPAS simulations demonstrating the predicted beam intensity at the CLEAR in-air test stand are shown in Figure 5.27.

5.7.2 Initial Characterisation and Beam Evolution

After installation of the new scattering foil itself, the steel collimator was replaced with a thicker, composite collimator to prevent transmitted dose and charge so that the system could be better

characterised for practical use. This was composed of 49 mm of steel and 47 mm of lead. The aperture was chosen to be 10 mm diameter to improve robustness of the system to changes in initial parameters or beam jitter, in a similar manner to the collimator chosen for use with the V1 system. The same procedure for simulations as before was replicated with slightly altered positioning of the C-Robot, verified through measurement during installation.

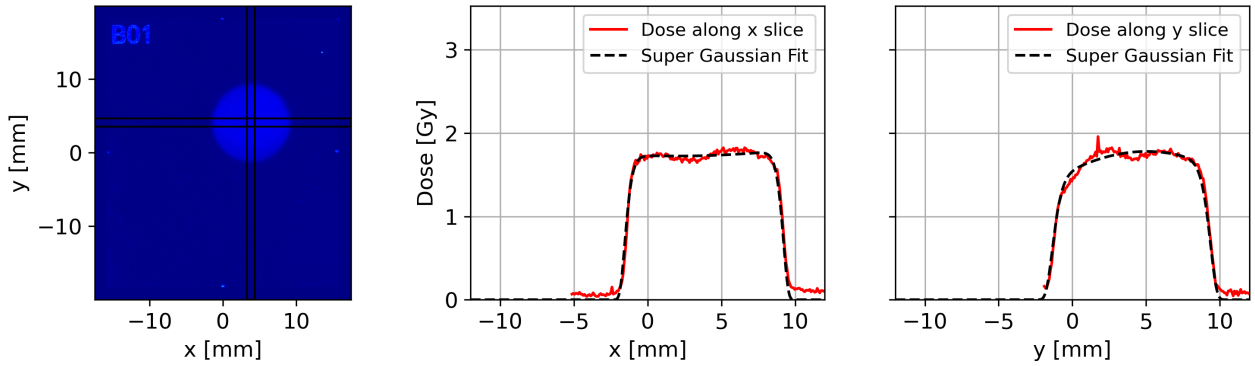

Figure 5.28: 2D transverse dose histogram (left), dose against x (middle) and y (right) from indicated slices across distribution, with super-Gaussian fits shown. Sample profile of dual-scattered beam measured with EBT3 film at in-air test stand with V2 system inserted. 2.02 nC accumulated charge measured at THz1, at 200 pC/ train.

The new collimator was again mounted on a linear stage immediately downstream of the beampipe exit. This collimator was verified to reduce passage of charge through the non-aperture region. This was tested using two Beam Current Monitors (BCMs) - one positioned upstream and one positioned downstream of the collimator. These are referred to as THz1 and THz2 respectively (a legacy from previous experiments at CLEAR). Alignment of the beam with the scattering foil was again rather challenging given the very small size of the S2 tip and initial lack of diagnostics to ensure alignment. It was difficult to verify accuracy of the thickness of S1 in particular. The steel stem was also expected to have more of an impact than the previous scatterer due to its larger relative scattering compared to the V1 scatterer. A sample EBT3 dose profile from the V2 scattering system and collimator inserted with super-Gaussian fits is shown in Figure 5.28.

Initial tests were carried out for the new scattering system at a number of charges in-air, measured with EBT3 films. The aim was to characterise the collimated charge-dose ratio and uniform radius at low intensity operation. This represented one of the key benefits of irradiations with the dual-scattering system: assuming a consistent profile within the collimation region, dose targeting could be extremely simple (effectively a simple conversion factor could be used to convert between charge and dose, at a defined depth). This was carried out as before for a large sample size of 5x5 mm. The results from this study are shown in Figure 5.29. Super-Gaussian fitting retrieved values of x_{90} and y_{90} to be 4.71±0.04 mm and 3.95±0.95 mm respectively in these tests. Transmission

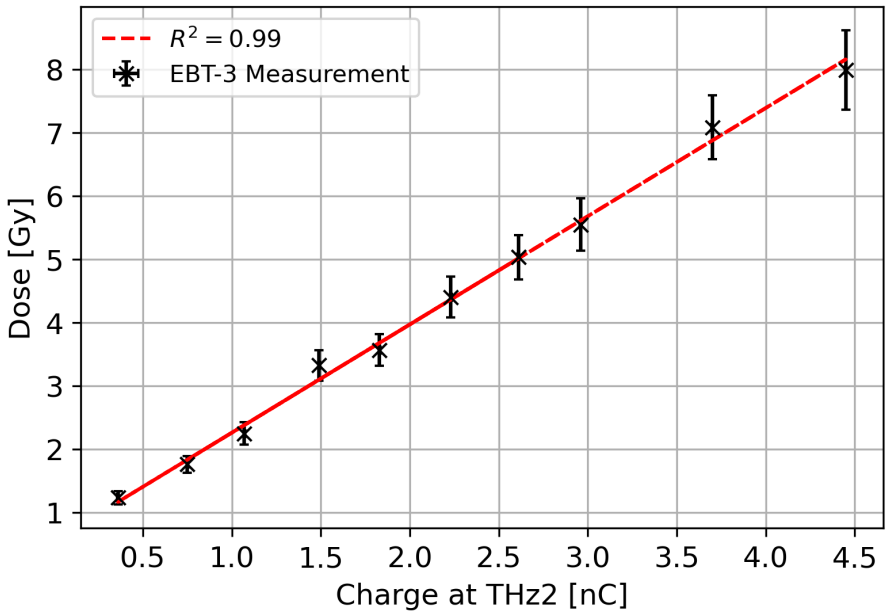

Figure 5.29: Dose measured across 5x5 mm^2 region on dual-scattered EBT3 film profiles in-air at test stand, against accumulated charge measured by THz2 BCM. Beam operated at 200 pC/train. Errors from standard deviation across sample region. Linear fit to data and coefficient of determination R^2 displayed.

after collimation was 27.2±0.02%. Simulations yielded r_{90}≈5mm and transmission≈25%, subject to initial beam conditions. The beam shape did vary slightly from shot to shot, but this was typically well quantified by the super-Gaussian fits. The beam in the x axis was found to be slightly double-peaked and the beam in y to be under-scattered (rounded, with negative h_y values in fitting). This asymmetry originated from the steel stem impinging on the profile, also resulting in some instability in the fitting process. The impact of the stem was more significant at higher beam intensities, as discussed in Section 5.7.3.

Depth-dose measurements with the V2 scattering system were done using the same long holders as before, each with 23 radiochromic EBT3 films to compare characteristics of the smaller flattened beam with TOPAS simulations. These irradiations were carried out subsequently, but at two beam intensity settings to evaluate any change in dose characteristics. For both sets of irradiations, 20 nC accumulated charge at THz1 was targeted; one in 4x5 nC pulses, and the other set in a single 20 nC pulse. The resulting distributions are shown in Figure 5.30, with comparative TOPAS simulation predictions for the true charges measured at THz1. As discussed above, at higher intensity the effects of the stem were more severe; in x, the more severe double peaking could be quantified by the fits, but the fitting in y was very inconsistent as in the initial charge scan of Figure 5.29. Thus, only the evolution of x_{90} was evaluated, as can be seen in Section 5.6. Evolution of this and the fitting parameters as the beam travelled through water is shown in Figure 5.31.

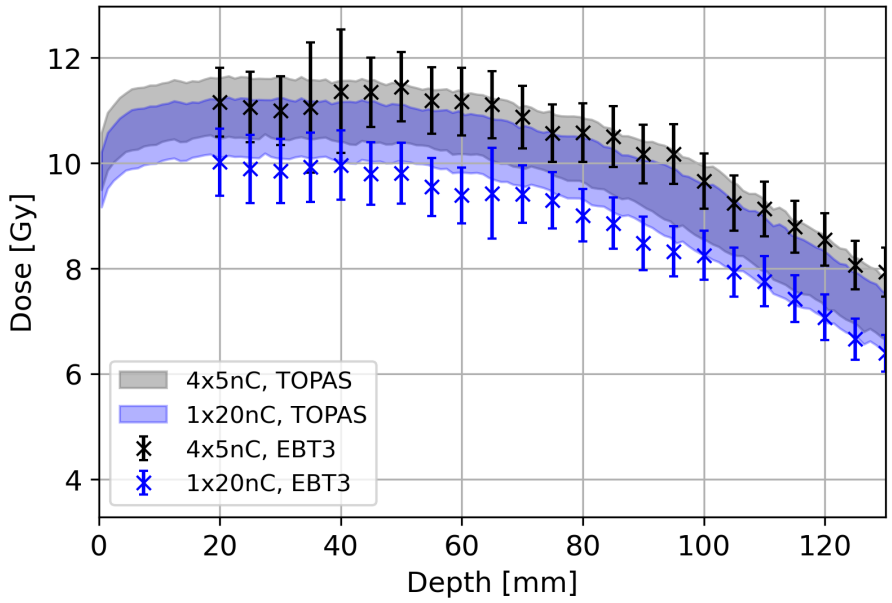

Figure 5.30: Dose measured across 5x5 mm region in centre of uniform profile against depth in water with V2 system inserted. Experimentally measured with long C-Robot EBT3 film holders in water tank, with comparative TOPAS simulations indicated. Four train and single train measurements shown. Errors from standard deviation of dose across measurement region. Approximately 20 nC total charge delivered at THz1 BCM for each set. 5.81 and 4.85 nC transmitted charge measured at THz2 BCM for four shot and single shot measurements, respectively (simulations scaled accordingly). Water tank positioned 2378 mm downstream of S1.

A number of factors could be responsible for discrepancies in dose between the two irradiation sets, beyond the slight difference in delivered charge. The high number of bunches per train may have resulted in beam loading and thus a larger energy spread and/or reduction in mean energy. This would likely explain the systematically lower dose than predicted for the single shot irradiation shown in Figure 5.30. The evolution of x_{90} was comparable for both cases, with the uniform radius decreasing by approximately 50% on passage through the film holder to a depth of 130 mm. When combining both measurements, x_{90} was found to evolve from 4.8±0.1 mm, to 2.6±0.3 mm at 120 mm depth. This was in excellent agreement with the comparative TOPAS simulations, although there were some discrepancies between simulation and experiment in the evolution of x_{90} between these depths, particularly for the lower intensity irradiation.

There were more significant discrepancies in the lateral penumbra as shown in Figure 5.31. Fits to the experimental data derived values of the lateral penumbra in x to be 1.0±0.1 mm at 20 mm depth and 7.0±0.2 mm at 100 mm depth. Beyond 120 mm in water, the fitting uncertainties became extremely high and were thus excluded from this analysis. This showed the limitation of this method for quantifying uniformity of the dose.

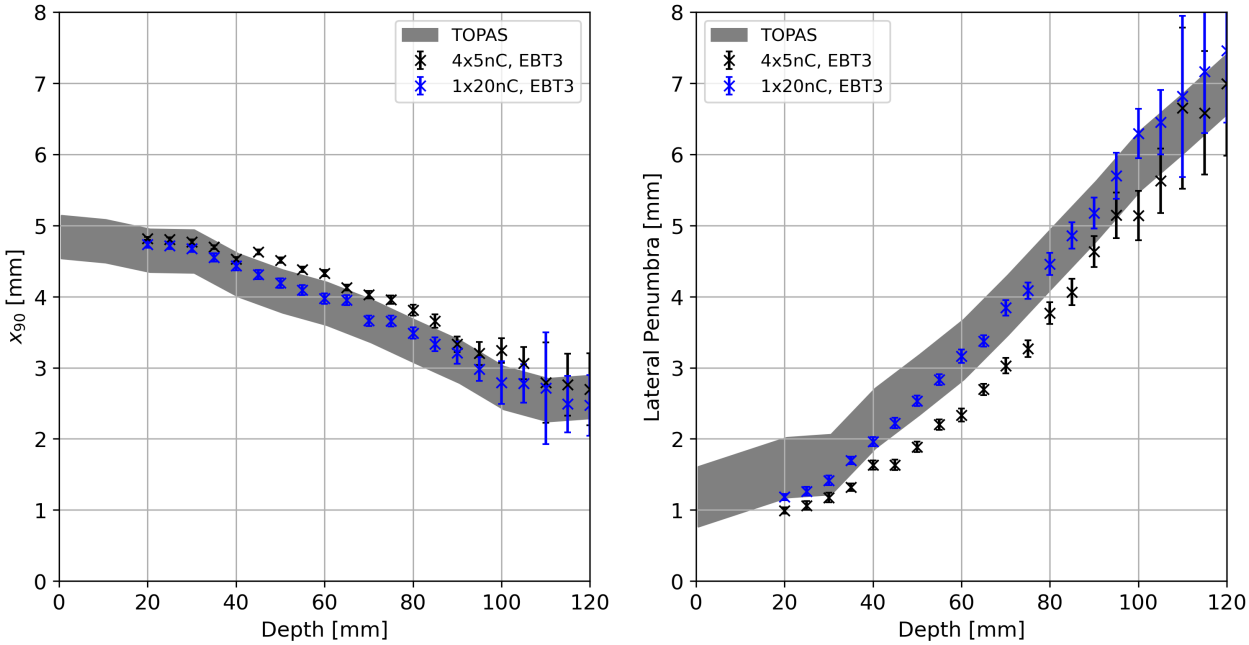

Figure 5.31: Dose x_{90} (left) and lateral penumbra (right) against depth in test stand water phantom from beam with V2 system inserted. Taken from super-Gaussian fits to transverse dose profiles captured by EBT3 films in long holders, with errors propagated from covariance matrix. Four train and single train measurements indicated. Approximately 20 nC total charge delivered at THz1 for each. Results from comparative RF-Track/TOPAS simulations indicated. Error region defined by simulation resolution. Water tank positioned 2378 mm downstream of S1.

5.7.3 Optimisation and Robustness of Charge-Dose Relationship

The results from experiments with both scattering systems, particularly those outlined in Figures 5.24, 5.30 and 5.31, represented the original goal of these dual-scattering experiments at CLEAR. The first enlarged, uniform VHEE beams were generated and measurements of their transverse characteristics and dose evolution carried out in water. In general, these agreed well with predictions from TOPAS MC simulations, with discrepancies typically explained by differing initial beam conditions. General operation of such a system for irradiations at CLEAR would require further optimisation and characterisation of predicted doses retrieved at sample positions.

The transverse size of the PEEK S1 was rather small due to the ordered material, and alignment with S2 and the collimator aperture took significant time during operation for the above experiments. This was essentially carried out through trial and error whilst changing steering magnet conditions, positioning of S2 in the beamline, and assessing the result on a YAG screen. Therefore, this was replaced with a 100 µm aluminium foil, which had an equivalent scattering power to the PEEK S1, but was larger and had a more accurately defined and homogeneous thickness. Due to the dependence on beam alignment on S2 for symmetry of the final distributions, a diagnostic camera was installed to view S2 during operation to aid with positioning of the beam during operation. The new instal-

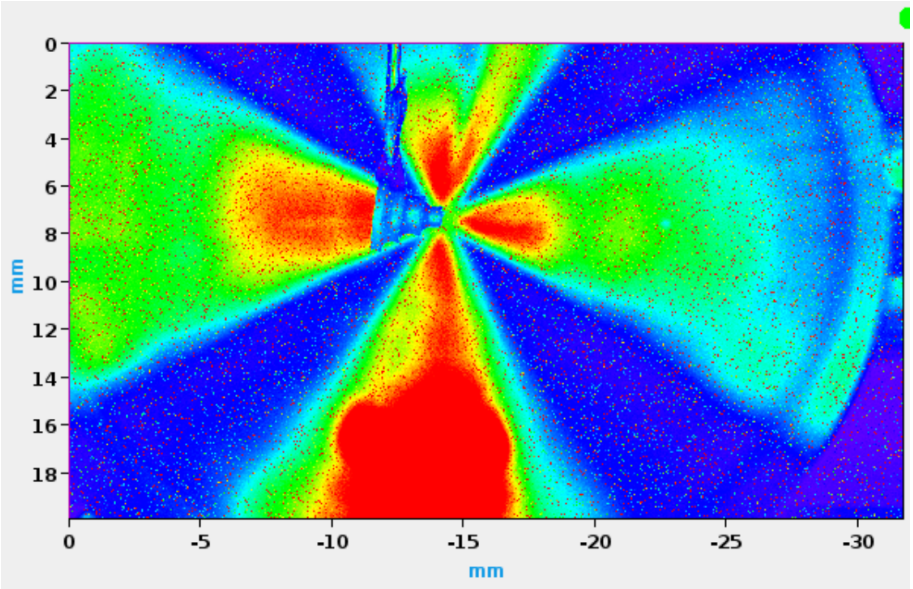

Figure 5.32: Image of V2 S2 scatterer in beam pipe during operation from digital camera, with steel stem mounting visible.

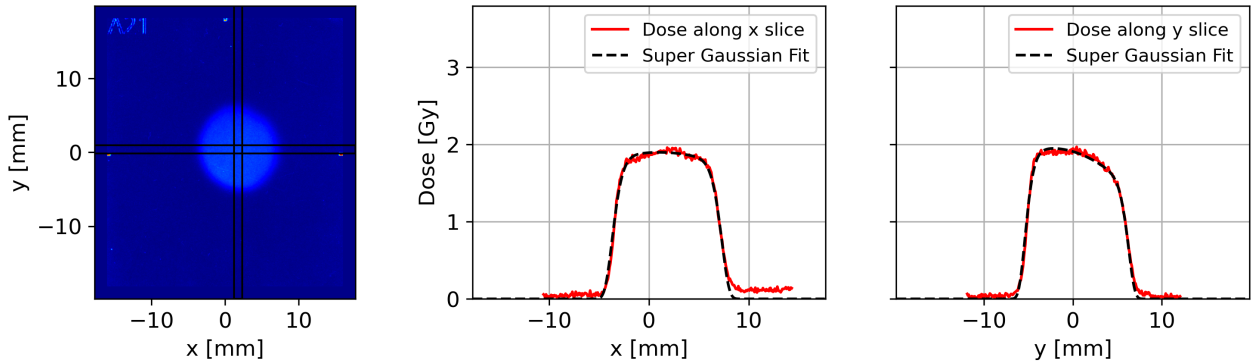

Figure 5.33: 2D transverse dose histogram (left), dose against x (middle) and y (right) from indicated slices across distribution, with super-Gaussian fits shown. Sample profile of dual-scattered beam measured with EBT3 film at in-air test stand with modified V2 system using 100 µm aluminium S1 inserted. 3.8 nC accumulated charge measured at THz1, delivered in 2x1.9 nC trains.

lation with aluminium foil and camera greatly simplified operation of the dual-scattering foil, with alignment achievable in a matter of seconds by an experienced operator. With this complete, the principle purpose of this final experimental programme was to ensure the repeatability of the dose delivery from the scattering system with a number of initial conditions, determine their variation and stability at certain depths in water, and investigate practical considerations and optimal conditions for general use of the system for irradiation experiments at CLEAR.

To improve the validity of comparative simulations, fresh quadrupole scans were taken using the procedure outlined in Chapter 2. These scans retrieved the values shown in Table 5.6, and thus were used for the retrospective simulations carried out for the earlier experiments of this section and Section 5.6. Irradiation sets during this experiment were carried out in each of the following

conditions, with collimators both inserted and extracted:

- S1 IN, S2 OUT, in-air
- S1 IN, S2 IN, in-air
- S1 IN, S2 IN, 20 mm water depth
- S1 IN, S2 IN, 60 mm water depth
- S1 IN, S2 IN, 100 mm water depth

This allowed the reduction in lateral penumbra from the collimator to be explicitly verified. Typically the setup was rechecked for alignment at around the halfway point of irradiations, as phase shifts in the accelerating cavities resulted in slight changes. Single-scattered distributions were taken to study the effect of increasing bunch per train on the dual-scattered profiles. YAG images were also taken to complement the transverse profile distributions from the films; whilst not explicitly shown in this analysis, they were used to crosscheck the transverse beam parameters. The YAG images were found to show discrepancies of up to 10% in terms of beam size when compared to the values from the films. There are numerous reasons for this discrepancy, and its true origin is under active research at CLEAR. The Twiss parameters were again fed into a model of the CLEAR beamline in RF-Track and exported into TOPAS to simulate the dose deposition for these comparisons, as previously.

Table 5.7: Summary of irradiation conditions for V2 charge-dose study.

Intensity	Approx Accum. Charge at THz1 [nC]	Charge/train at THz1 [nC]
Low	2	0.1
Low	20	0.5
Low	20	1.2
Low	9	2
Low	20	2
Low	20	20
High	40	40
High	40	40

Focusing with the final quadrupole triplet at CLEAR was successful in producing a stable and mostly symmetrical beam profile; these parameters were slightly altered during the experimental programme to produce the most stable results. A sample profile retrieved from EBT3 radiochromic film with the new aluminium S1 is shown in Figure 5.33. This irradiation procedure was carried out for a number of total doses and dose rates to cover a significant proportion of the parameter space required for irradiations. For the purposes of analysis, these could be separated into "low" and "high" intensity categories, as shown in the summary Table 5.7. The low intensity measurements were taken with EBT3 films; the high intensity measurements were taken with EBT-XD films as the predicted dose was beyond the EBT3 film dynamic range [249].

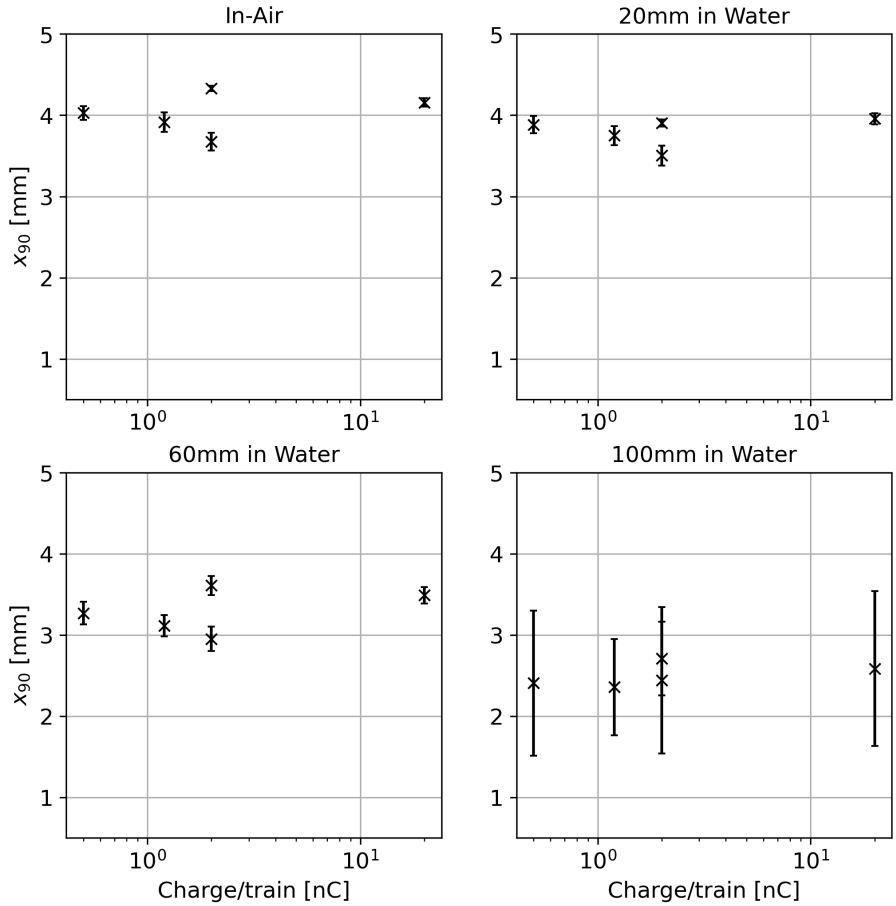

Figure 5.34: Fitted x_{90} parameter measured from radiochromic EBT3 and EBT-XD films at in-air test against charge per train measured at THz1 BCM, with modified aluminium-PEEK V2 inserted. Measurements carried out by C-Robot in-air, and at 20 mm, 60 mm, and 100 mm depths in water, as indicated. V2 inserted; positioning in water or in-air measurement indicated. Errors from propagation of covariance matrix output.

The resultant uniform extent in x_{90} for the beams at each depth in water is shown in Figure 5.34. Due to the scattering from the steel stem, measurements were only taken in x. The evolution of the beam size was consistent with that seen in the previous studies with V2, retaining some flatness out to around 6 cm depth before becoming almost fully Gaussian at 10 cm; the increased spread of

Table 5.8: Summary table of low charge results from characterisation experiments, from combined data. Showing uniform extent in x (x_{90}) and lateral penumbra in x (LP_x).

Depth	$x_{90}^{Uncollimated}$ [mm]	$x_{90}^{Collimated}$ [mm]	$LP_x^{Uncollimated}$ [mm]	$LP_x^{Collimated}$ [mm]
In-air	6.24± 1.56	4.02±0.22	6.78±1.83	2.22±0.31
Water, 20 mm	6.52±0.85	3.80±0.16	7.03±1.43	2.70±0.23
Water, 60 mm	6.35±0.98	3.28±0.24	7.84±0.89	4.34±0.28
Water 100 mm	5.96±0.74	2.5±0.13	10.0±1.22	6.90±0.19

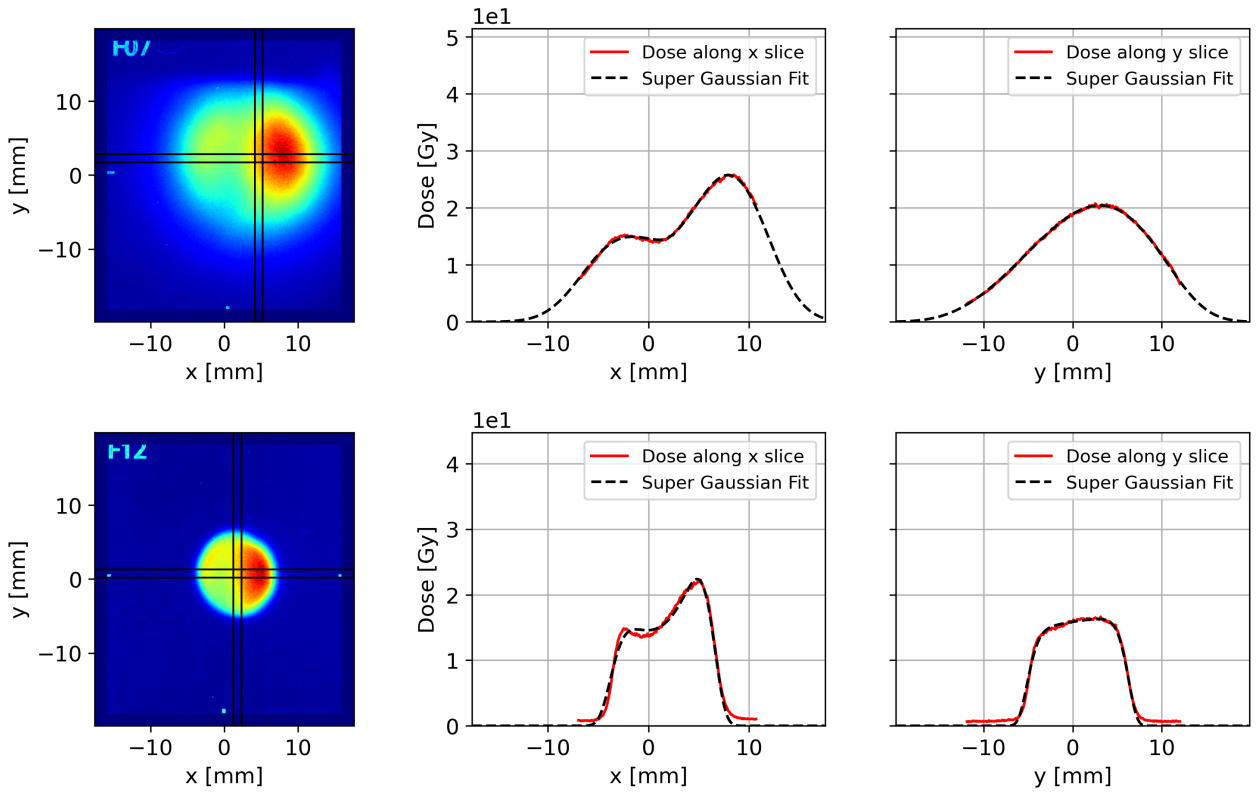

Figure 5.35: 2D transverse dose histograms (left), dose against x (middle) and y (right) from indicated slices across distribution, with super-Gaussian fits shown. Measurements with V2 inserted, taken with EBT-XD films in-air, with collimator extracted (top) and inserted (bottom). High-charge 40 nC in single train at THz1 delivered. Significant misalignment in x shown.

the beam somewhat reducing the loss of flatness through the water phantom. The initial beam was typically slightly smaller in x than predicted from simulations however, likely due to the angle of entry of the beam entering the collimator. The lateral penumbra of the beam was measured using fits and dose as previously. The collimator significantly reduced the transverse penumbra of the beam in all cases, with this effect diminishing deeper in water. The results are summarised in Table 5.8. The high charge measurements were significantly offset from the low charge measurements - the explanation for this was clear from inspection of the dose profiles, for example those shown in Figure 5.35. There was significant jitter leading to misalignment of these measurements. The impact of this diminished at depth in water, as demonstrated by the convergence of the low and high charge values of x_{90}, shown in Figure 5.34. Even when correctly aligned, the high intensity measurements

were more heavily affected by the presence of the steel stem, with double peaking in x and loss of uniformity in y. This was replicated in simulations by increasing the beam emittance and thus the divergence and beamsize before scattering.

For general operation of the system, quadrupole scans and repeated adjustment would not be appropriate due to time constraints of irradiation experiments. A key aim of the system was to provide a constant charge-dose ratio, irrespective of some changes in the initial beam. The same 5x5 mm^2 large sample size was used to assess this charge-dose ratio at the varied intensities used for irradiations in this experiment. When remaining at consistent depths, the charge-dose ratio measured from THz2 and the flat top dose region on the films was reasonably consistent, particularly for the lower intensity measurements. It was found to be approximately constant in shallow water, before diminishing (as predicted from the depth-dose profiles in e.g. Figure 5.30). From fitting to the complete dataset, charge-dose ratios of 2.2±1.0, 2.10±0.3 and 1.7± 0.1 Gy nC^{-1} at THz2 were found; the large uncertainties for the shallower results were due to the skewed high-intensity profiles, hence the more precise results deeper into the phantom where these effects were reduced due to scattering. Excluding the high charge data produced far more precise results of 2.15±0.08, 2.10±0.05 and 1.75±0.05 Gy nC^{-1}at the three water depths across the 5x5 mm region (shown in Figure 5.36).

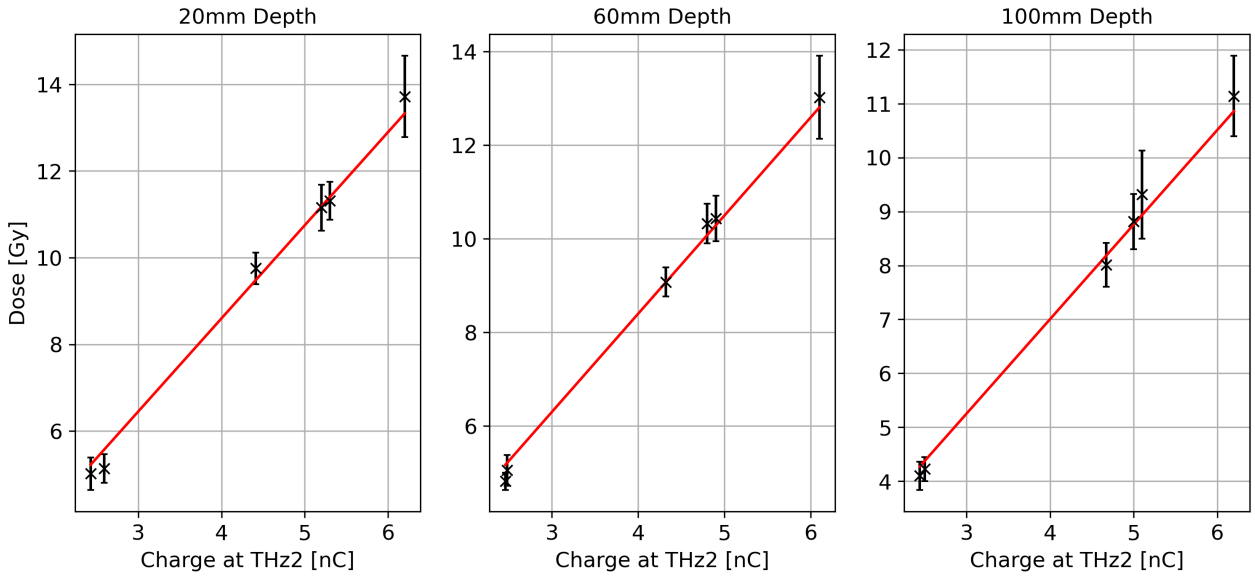

Figure 5.36: Dose across 5x5 mm central region against accumulated charge measured at THz2 at 20 mm (left), 60 mm (middle) and 100 mm (right) depths with EBT3 films in C-Robot water phantom. Error bars represent standard deviation across dose region. High intensity data points from Table 5.7 excluded. Line of best fit indicated in each sub-figure.

These results demonstrated reasonable uniformity within the 5x5 mm large sample region despite the steel stem, and were consistent with both simulation and the results shown in Figure 5.30. Standard deviation of the dose within this region was typically close to 5% - approximately equivalent to the prescribed dose uncertainty within the dynamic range of the EBT3 and EBT-XD films. Thus, the requirement of uniformity within even this large sample region was met. Variance within the typical CLEAR 1x1 mm^2 sample region was well within the 5% accuracy of the films. Whilst the change in beam profile with higher intensity would require correction, in theory uniform beams with the V2 system at CLEAR could reach dose per train of up to 50 Gy, assuming typical transmission of 27% measured throughout this experiment. Finally, the jitter correction algorithm discussed in Chapter 4 was used with the simulation model to determine the magnitude of offsets for the two high-charge cases in-air; this returned values of approximately 500 µm.

5.7.4 X-ray Production from V2

The final dedicated dual-scattering foil experiment for this thesis was based upon measuring the X-ray dose generated from the scattering system. Whilst predicted to be rather high for some cases (such as those outlined for production of 75 mm beams in Chapter 4), simulations suggested a low contribution from X-rays due to the low required scattering angle from the CLEAR scattering foils. Nevertheless, this was experimentally verified to confirm these predictions; agreement would also confirm the predictions of the secondary dose contributions for scaled-up systems required for eventual clinical treatment, such as those outlined also in Chapter 4.

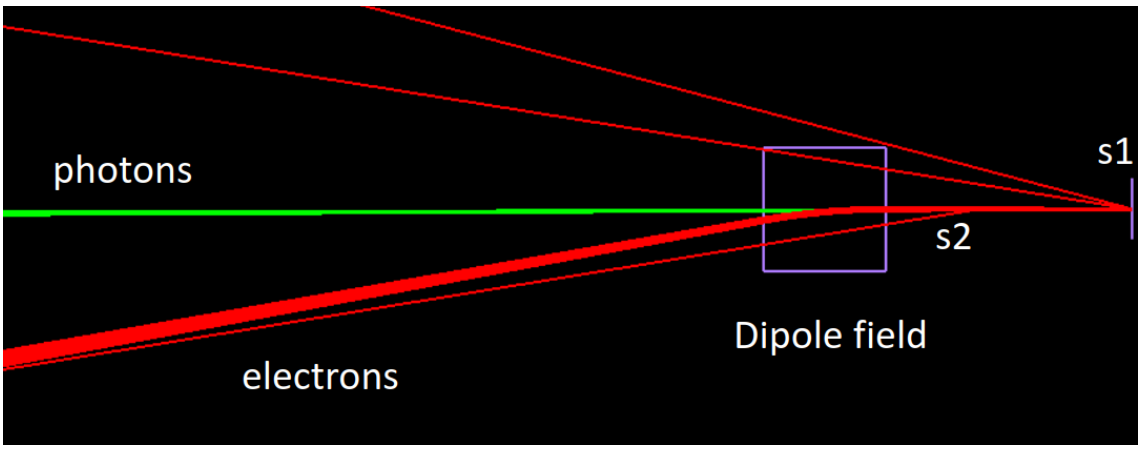

Figure 5.37: Dipole field separating secondary photon beam from electron component after dual-scattering, visualised in TOPAS GUI. Beam entering from right-hand-side.

Within the same geometry as that shown in Figure 5.21, this X-ray contribution was measured by inserting the CLEAR V2 system, with the spectral dipole (BHB900 in Figure 5.2) switched on. This split the beam into charged and uncharged components allowing the Bremsstrahlung X-ray

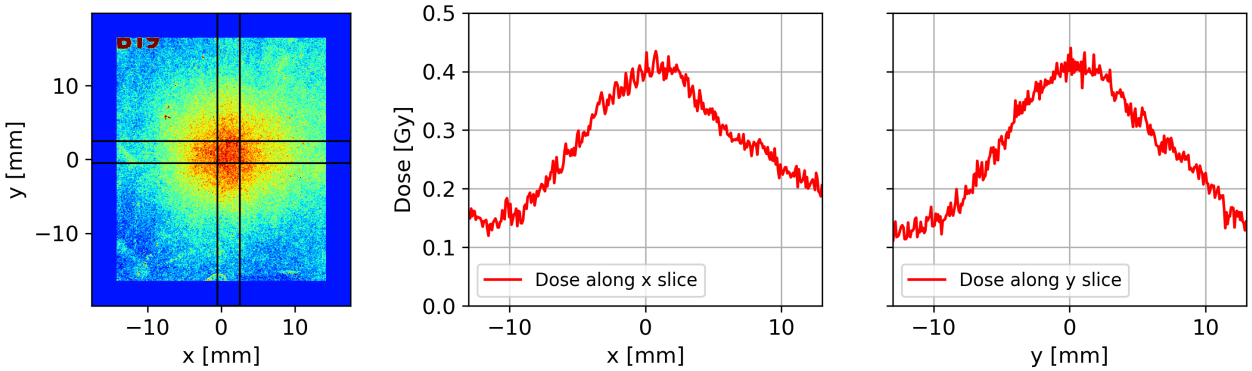

(a)

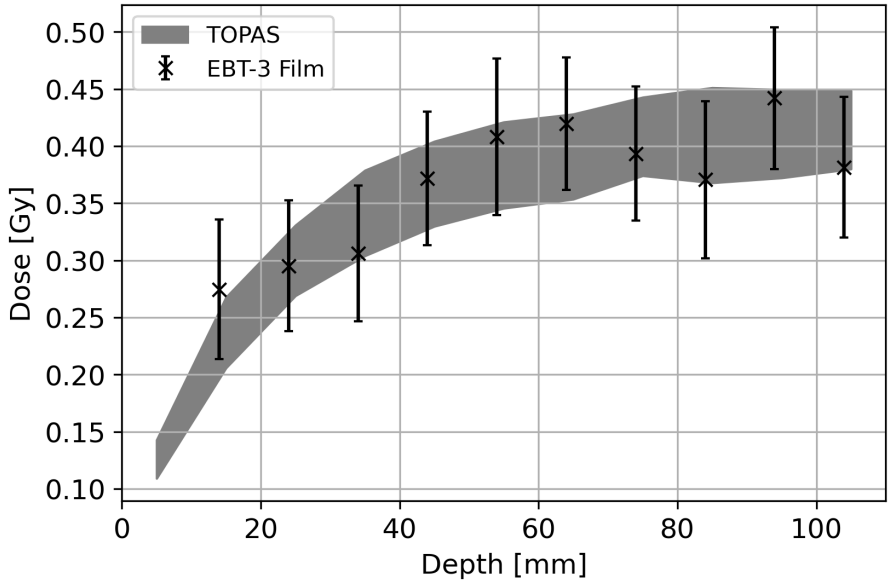

(b)

Figure 5.38: 2D transverse X-ray dose histogram (a, left), X-ray dose against x (a, middle) and y (a, right) from indicated slices across distribution, measured with EBT3 film at 105 mm depth in water and V2 inserted. Dose across 5x5 mm large sample size against depth in water phantom from X-rays (b) displaying experimental EBT3 measurements and comparative RF-Track/TOPAS simulations. Errors from standard deviation across dose measurement region in both cases. 400 nC estimated accumulated charge at THz1.

contribution to the dose to be isolated, as outlined in Figure 5.37. EBT3 films were inserted from 14 mm to 104 mm depths in water, at 10 mm increments and exposed to 20x20 nC trains delivered to THz1. This was verified by measuring 20 trains through THz1 with the dipole turned off, followed by the 20 trains with the dipole turned on, as the dipole was situated before the BCM and thus on-line measurement of the accumulated charge could not be carried out. The low total doses resulted in significant noise on the films. The non-Gaussian shape of the profiles required the peaks to be manually defined, rather than relying on the automated procedure for defining the beam centre used throughout this chapter. The X-ray profiles were of the characteristic shape predicted throughout Chapter 4, with a peak and extended non-Gaussian tails. A sample profile and the measured evo-

lution of dose across a 5 mm region and comparisons to equivalent simulations with the combined TOPAS and RF-Track model is shown in Figure 5.38.

Excellent agreement both in the predicted transverse distributions and dose measured across the peak was retrieved from this experiment compared to the results from TOPAS. This demonstrated that the photon contribution to dose from the dual-scattering foils at CLEAR was negligible, representing approximately 0.2% of the total dose contribution even at 100 mm depth (assuming beam transmission of 30% and charge-dose ratio derived from Figure 5.36). The agreement of simulations suggested that the predictions for X-ray dose contribution would be accurate for the scaled up systems such as those studied throughout Chapter 4.

5.8 Recent Developments and Future Outlook

5.8.1 Performance of Scattering Foils for Sample Irradiations

The above experiments demonstrated agreement with TOPAS simulations and displayed the effect of collimation on lateral penumbrae of VHEE beams. For the provision of dose rates up to 10 Gy/train (in air or shallow water), consistency in the ratio between charge and dose was confirmed and the system sufficiently stable and uniform in the x axis. X-ray contamination was very small, accounting for around 0.2% of the localised dose, also in agreement with comparative simulations. It was shown throughout the previous section and associated simulations that whilst excellent uniformity was typically achieved in x, the steel mounting stem impinged on the profile in y, with this being very dependent on the alignment of the system during operation. Whilst the standard deviation across a typical sample size was low, this would be improved with a symmetrical profile, and ensure that the charge-dose ratio was not dependent on vertical positioning. The solution to this was the replacement of the steel stem holding S2 with a silica mounting. With a far higher radiation length than steel, this was predicted to greatly improve the symmetry of the beam. With the stem replaced, the dual-scattering foil at CLEAR with the collimator was used to provide uniform, symmetrical beams in water for irradiation experiments for the first time.

Throughout the autumn of 2023, the CLEAR operations team ran numerous tests to ensure the robustness and consistency of the dual-scattering foils for general use - in particular, determining more precisely the charge-dose ratio for experiments. The ratio was typically measured immediately before user experiments to minimise changes in the initial beam conditions, as these were predicted to still have some effect. Generally this was defined at the lower end of dose rate range, for irra-

diations of up to 10 Gy per train. The first radiobiological irradiations using the V2 dual-scattering system took place at the end of 2023. It was used to provide conventional and FLASH dose rates to far larger sample sizes than previously carried out at CLEAR. With appropriate alignment, an increase in local uniformity and consistent dose targeting has been achieved using this system, representing a permanent upgrade to the capabilities of CLEAR as a user facility. Due to the time independence of the dual-scattering system and ease of operation, it is a useful tool for studying FLASH RT and is likely to be used in the future CLEAR user programme. The system has also been used in UHDR dosimetry studies to provide large, uniform beams for measurement with silica fibres of the kind proposed by Bateman et. al [174].

5.8.2 Proposed Experiments and Extensions of Dual-scattering Systems at CLEAR

The current V2 system is well characterised, stable, and well suited for provision of beams with low variation and dose targeting up to sample sizes of around 1 cm. It is envisaged that general purpose irradiations at CLEAR within the dose range of the system will be carried out with the dual-scattering foils. The CLEAR operation team is developing a system for real-time dose targeting, using the measured charge from the BCMs and intensity measured with a diagnostic YAG screen. With appropriate calibrations, dose at a certain depth could be measured in real time for irradiations. The use of the dual-scattering foil and collimation would greatly simplify the calculations for this, as the beam would ideally be uniform within the collimator. Any variations could be quantified using the measured brightness of the YAG screen. This additional YAG screen could have some effect on the uniformity due to MCS in the material, depending on its positioning. With appropriate consideration and minimisation of this effect, this could allow real-time dosimetry to be carried out at CLEAR during irradiations. This would be desirable for radio-biological applications, allowing explicit dosimetric conditions to be measured and optimised during operation.

Additional flexibility in dose delivery could be provided at CLEAR with numerous scattering systems installed on the same mounting stems as the current system. One of the main drawbacks of dual-scattering foils is their inflexibility in terms of beamsize, with collimation required to reduce the beamsize from a maximum (thus limiting the uniform dose to that achieved for the maximal beamsize). There could be some flexibility at CLEAR to install several systems for applications which may require larger beam sizes than those currently provided, or indeed those which may require smaller uniform regions but with higher charge. The former could be achieved by simply installing the PEEK V1 system in tandem with PEEK V2, and boring out a larger aperture in the col-

limator. Additional systems could be developed to provide numerous beamsizes, but the scattering design methods of outlined in Chapter 4 allow this to be a fairly simple process.

Finally, CLEAR is currently developing a secondary beamline and a new test stand to act as the primary location for radiobiological experiments. This second beamline would begin from a dispersion free bending section splitting off from the main beamline at the current location of the VESPER dipole. A diagram of this proposed scheme is shown in Figure 5.39. A new, improved

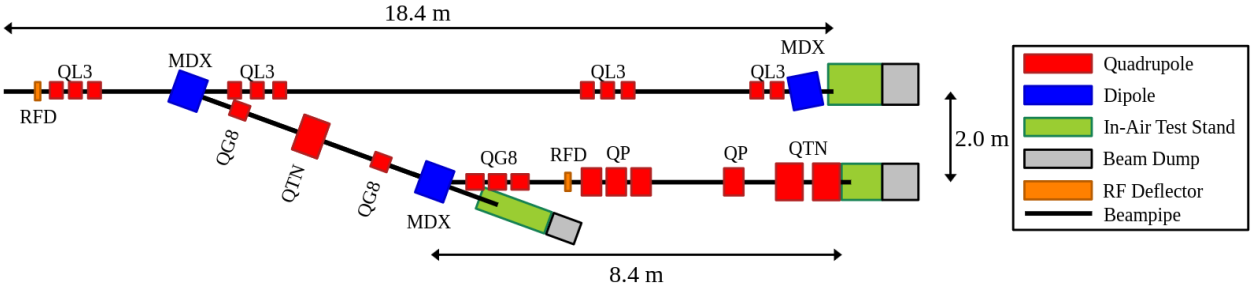

Figure 5.39: Schematic of proposed 2nd beamline at CLEAR. Image from [251].

C-Robot 2.0 has been built for installation in the second beamline. C-Robot 2.0 would be capable of carrying significantly more holders than the original C-Robot, reducing the number of accesses required during operation for replacing of films and/or samples. Its permanence would also reduce installation times, as the current C-Robot is regularly installed and removed from the test stand.

Another feature of the new beamline is a larger beampipe. This could allow significantly larger beams to be produced with appropriate dual-scattering foil designs, again increasing the flexibility of beam conditions provided to users at CLEAR. This could also allow studies of larger beam evolution in water to be carried out to again compare with TOPAS simulations and verify the predictions from Chapter 4. With the optics envisaged for the 2nd beamline at CLEAR, studies on the interactions between quadrupole focusing and dual-scattering foils could be carried out. The optics settings throughout the experiments described here were principally defined for the purpose of reducing beam jitter, ensuring uniformity and consistent dose delivery through the system. The study of combined optical and scattering systems for beam enlargement could be of significant interest to the field, particularly due to the issues with secondary particle production at higher scattering angles as discussed in Chapter 4.

Similar studies could likely be carried out in facilities other than CLEAR. For example, the second phase of CLARA [252] will reach energies of 250 MeV, and is expected to be used for experiments in wide-ranging applications. Similarly, ARES [253] based at DESY is currently operational within the VHEE regime and is expected to carry out in-vitro and eventually in-vivo radiobiological studies [253]. Whilst not operational at currents typically compatible for FLASH studies with very

large beams, installation of dual-scattering foil experiments with extended geometry may still be compatible with the in-air experimental area. Facilities under development for clinical translation may also be appropriate for further testing or gain benefit from use of dual-scattering foils for high energy electrons [254].

5.9 Summary

The CLEAR User facility at CERN is the only experimental beam-line capable of hosting experiments for VHEE-FLASH studies, as well as general accelerator R&D. Its flexibility, expertise of operators and extensive collaborations made it an ideal location to experimentally verify the TOPAS based design techniques and predictions of dual-scattering foil use in the VHEE regime for FLASH. Single scattering experiments were carried out to verify the models of MCS used in TOPAS MC code and assess material choice for development of dual-scattering systems; an initial experiment with 3D printed PLA displayed reasonable agreement at 200 MeV. More detailed studies to assess a variety of materials also displayed good agreement for scattering in tantalum, tungsten and PEEK at 200 MeV using a combined RF-Track and TOPAS model of the CLEAR beamline, although there were some systematic discrepancies between simulation and experiment particularly at high scattering angles. A dual-scattering system was developed and 3D printed in PLA, producing a uniform beam with approximately 13 mm uniform radius measured with a YAG screen. Modifications to the design setup retrieved intensity profiles with varying uniformities. The resultant profiles were consistent with the predicted transverse electron intensity distributions in the in-air test stand from TOPAS, using an input beam with generic CLEAR parameters and low emittance. Three additional designs in aluminium were carried out to successfully produce enlarged and flattened transverse dose profiles, measured with radiochromic EBT3 films.

To allow measurement of uniform beam profiles in water, a vacuum dual-scattering system was designed in PEEK and installed upstream in the CLEAR beamline, capable of being inserted or extracted remotely. The first iteration provided a beam with a large uniform region, with a steel collimator installed to produce a uniform beam in x, with x_{90} of 10.27 mm measured in-air. Depth-dose measurements were carried out with this system to quantify the evolution in uniformity and dose throughout the water phantom. Results from these studies agreed well with the TOPAS predictions, with the uniform region in x in water reducing to 6.3 mm at 120 mm depth, measured with radiochromic films. Agreement was also found from similar measurements with a YAG screen. The steel collimator was not of sufficient thickness to block the beam outside of the aperture, with

significant fringe doses in the film results. Additionally, the large dual-scattered beams from this system resulted in limitations in maximal achievable dose per train.

A second vacuum dual-scattering system to produce a beam with a smaller uniform region was installed, in addition to a thicker, composite lead and steel collimator with 10 mm full aperture. Depth-dose studies confirmed the more rapid loss of uniformity for the smaller beam on passage through the phantom, with some discrepancies in TOPAS simulations likely due to changes in the initial beam. x_{90} was 4.8 mm at 20 mm depth in water, decreasing to 2.6 mm at 120 mm depth. The thicker collimator allowed the lateral penumbra of the beam to be measured for the first time, evolving from 1.0 mm to 7.0 mm over the same range of depth. Studies with the collimator extracted and inserted confirmed the reduction of transverse penumbra from collimation before the water phantom. The system was found to produce consistent flattening of the beam and ratios between dose after collimation and dose measured on the flat top at varying intensities up to 20 nC/train measured before collimation. With typical transmission of 25% through the collimator and charge-dose ratio of 2.2 Gy nC^{-1} at 20 mm depth, this would allow consistent large sample irradiation with up to 10 Gy per train.

The CLEAR in-air test stand dipole was used to explicitly measure the secondary photon dose component generated in the dual-scattering system; this was minimal compared to the primary component due to the low scattering angles. The CLEAR dual-scattering system has been further optimised to provide uniformity in both x and y with installation of a silica stem, and is now used for regular experimental irradiations in the user programme.

6 Conclusions

6.1 Summary

This thesis detailed the studies carried out for the enlargement and flattening of VHEE beams to enable conformal UHDR delivery. Specifically, this research was focused on the production of a beam with a homogeneous transverse profile to deliver uniform dose whilst minimising losses and lateral penumbra.

Beam focusing, deflection with magnetic fields and beam-matter interaction were relevant for achieving dose conformality. The evolution of electron beams in a transfer line can be described through matrix formalism of linear elements and treating the ensembles with envelope functions - the Twiss parameters - and emittance. These parameters in a beamline can be derived using a quadrupole and diagnostic screen. Electron scattering in matter can be modelled using Moliere's theory of multiple coulomb scattering. This was demonstrated in Chapter 2 using the derivations of Bethe in a later work, with the final PDF composed of a Gaussian term, a hard scattering term, and a correction. For most purposes however, the resultant profile can be modelled with a Gaussian approximation with the width of the angular distribution calculated from the beam and scatterer properties. A partial or complete transversely uniform beam could not be modelled by the typical Gaussian functions used in beam physics; thus, modified super-Gaussian functions were described with additional terms allowing function fitting to asymmetrical or ringed, flattened profiles. Inelastic processes in the VHEE regime are dominated by Bremsstrahlung production and pair-production from the resultant photons which may span a large energy spectrum from the primary beam energy to zero. It should be noted that neutron production may also be significant due to the giant-dipole resonance.

The GaToroid concept presents a solution for provision of beams from multiple angles within a short timescale. Treatment with multiple beams would be desirable to provide conformal FLASH-RT. A compact, cost-effective VHEE variation of the original gantry concept has been proposed, using novel, normal-conducting magnets to enlarge initially uniform beams to cover the size of a large tumour. This was first demonstrated in an arbitrary Riesenrad gantry layout using MAD-X matrix element matching. The results were verified with a successful benchmarking of both PTC and

RF-Track codes, with a 100 MeV beam. The more complex design for the 200 MeV e-GaToroid was carried out using objective function minimisation with RF-Track, to enlarge a similar initial beam with non-zero energy spread, retaining uniformity within 10% to at least 75 mm. The resulting beam met these requirements with a predicted transmission of over 50%. Whilst losses were substantial, this would still allow sufficient dose rates to induce the FLASH effect given achievable currents in UHPCIs. Required quadrupole strengths were minimal for two out of three of the required quadrupoles, with gradient magnitudes under $5\,\mathrm{T\,m^{-1}}$. The final quadrupole required a stronger gradient, but was still within realistic specifications.

Studies carried out in RF-Track demonstrated sensitivity of the final beam to the angular positioning of the second quadrupole in the lattice, as well as the energy spread and angle of the initial beam. Randomised studies with combined misalignments confirmed the sensitivity to angular element offsets on the final beam profile. This design demonstrated that the general goal could be achieved within the desired compact e-GaToroid and with only linear optics, realistically attainable focusing strengths and with fairly small apertures. These characteristics were desirable due to the novelty of the toroidal beamline elements required, and the typical goals of efficiency and cost-effectiveness in such a gantry. The design allowed cost estimates and detailed studies on practical design of the toroidal components to be carried out and progress the concept towards fruition. The automated lattice design methodology was shown to be flexible and capable of arbitrary modification; future studies for the preservation of uniformity in e-GaToroid could implement terms to minimise sensitivities to alignment as far as possible during the design process. Nevertheless, some sensitivity would always be expected due to the required beam magnification in this system.

Further studies should be dedicated towards removing the simplifications of the designs described in this research - a natural extension would be the implementation of the realistic field maps extracted from finite element magnetic field analysis of the toroidal elements. The ideal quadrupoles in RF-Track could be replaced with these and the changes to the beam at the isocentre studied. Additional optimisation using a similar automated process may be required if the impact of these realistic fields were significant. This may also include a more realistic UHPCI initial beam of the kind described in Chapter 2. Outside of the lattice design, specification of the novel vector magnet and its capabilities are required to ensure the feasibility of multi-directional beam delivery on a FLASH timescale.

The use of scattering foils was studied as an alternative method to magnification optics for VHEE beams. Production of a uniform VHEE beam from a single scatterer was demonstrated to be inefficient, from integration of a 2D Gaussian function. 10% transmission was resultant when retaining

the portion of beam with 10% dose inhomogeneity within a virtual collimator. Thus, this would be not be an appropriate system for beam delivery when UHDR would be required for FLASH. The true scattering angle and the approximations from the Gaussian approximation to MCS diverged with thicker scatterers, depending on the energy. At predicted angles above around 30 mrad for a 200 MeV beam, inelastic scattering resulted in the discrepancy becoming rather significant. Photon production was found to be lower for high-Z materials than low-Z materials for scattering to the same angle; thus, the choice of dense materials such as tungsten or tantalum in design wherever possible was justified for practical use. The photon dose distributions were typically sharply peaked with non-Gaussian tails. This component accounted for a third of the peak on-axis dose in a 300 mm depth water phantom when scattering a 200 MeV beam at 30 mrad angle. Extension of these studies to the design of dual-scattering foils demonstrated dependency of optimised profiles on the scattering models used for analytical approximations. Thus, additional considerations would be required for design in this regime with increased inelastic scattering compared to clinically available electrons.

Further TOPAS optimisation resulted in successful scattering systems providing enlarged and flat-topped beams, with improved transmission from virtual collimation compared to single-scattering solutions . Due to the intensity of the secondary beam, production of a 75 mm uniform beam in 1 m with a similar system was not deemed appropriate for further study; a dual-scattered beam with significant secondary photon dose would not retain a significant uniform dose component, even at the phantom surface, and thus would be clinically infeasible. Hence, the simulation geometry was extended to study the evolution of a 75 mm uniform radius beam in water, produced from thinner scatterers. Appropriate characterisation of the beam in water was desirable for future clinical implementation of VHEE. This would also verify the impact of the different dual-scattering foil designs on the dose distributions. Uniformity within 10% was immediately lost in water due to Bremsstrahlung photons when scattering with an angle of 30 mrad; the primary dose component however retained uniformity throughout the 300 mm water phantom. This component was well modelled by super-Gaussian fitting. These results confirmed that even the 30 mrad dual-scattering system produced a beam with too high a secondary component to produce a homogeneous transverse dose distribution at significant depth in water. Thinner scatterers would thus be required for delivery of conformal treatment at 200 MeV.

For the lower 10 and 20 mrad scattering angles, 10% uniformity in total dose was retained, with the uniform radius reducing to 57 mm in the latter and 68 mm in the former at 300 mm depth in water. Thus, retention of 10% homogeneity over a large transverse region could be retained deep

within a patient, using these systems. However, extended beamline lengths of 7.5 and 3.75 m were required for the 10 and 20 mrad systems respectively. The use of dual-scattering foils alone for conformal treatment with large beams would place limitations on the minimal size of the delivery beamline or gantry. More compact systems would likely require optics to provide uniformity deep in water, rather than relying entirely on dual-scattering foils if a 75 mm uniform radius were required.

10 cm of tungsten in the form of a stopper slab was shown to block passage of 99.9% of dose. A collimator of this thickness and material with a 75 mm aperture was thus capable of reducing the lateral penumbra of a 75 mm beam at both the surface and at 300 mm depth in the water phantom. This penumbra was defined as the radial extent between 90% and 10% of the maximum dose. This would be crucial for reducing dose delivered to healthy tissues during treatment and improving tumour conformality. The reduction even deep into the phantom demonstrated the necessity and benefit of a similar collimation procedure which would be required for the treatment of deep-seated tumours. Neutron production from these dual-scattering foil setups was dominated by the collimator, although the first scatterer composed of tantalum contributed up to 5% of the dose from neutrons when scattering at an angle of 20 mrad.

Future studies should investigate the modification of the collimator thickness to reduce the neutron dose contribution. In addition, a clinical system would likely benefit from more precise beam shaping than the simple circular aperture described here. Application of MLCs to VHEE could be relevant for this purpose, although considerations of the effects on the penumbra and neutron production would be required. A novel method for dual-scattering foil design was developed, based entirely on optimisation of dose or intensity profile at an arbitrary location from a generalised initial beam. This was preferred to the analytical method for the purposes of VHEE scattering design due to its reliance on TOPAS MC simulation for modelling rather than approximations to MCS. It would thus take inelastic scattering and particle production into account during optimisation. This optimiser could be run with arbitrary geometry and initial beam conditions, or include modification of magnetic elements alongside the scattering geometry by importing RF-Track results into TOPAS. Future simulation studies for VHEE beam delivery could use a similar optimisation procedure to investigate the operation of systems with combined magnification optics and dual-scattering foils. This could allow the provision of large, uniform beams in a compact space with reduced Bremsstrahlung. Other novel solutions for operation of scattering foils in the VHEE regime could also be of interest.

The CLEAR User Facility was used to successfully test and verify the effectiveness of the MC based approach for dual-scattering foil design and benchmark predictions from MC simulations.

The first goal of these experiments was to study and compare the evolution of uniform VHEE beams in water with simulation. This would be a scaled-down version of the previous simulations studies with comparatively small uniform beams. However, agreement between TOPAS and experiment would verify the description of uniform beam evolution in TOPAS and enforce the conclusions of Chapter 4. The second goal was to determine the usefulness of such a system for irradiation of large samples at CLEAR, where numerous radiobiological studies on FLASH VHEE are carried out by Users. Single-scattering studies demonstrated agreement between the MCS models of TOPAS and experiment at 200 MeV for PLA scattering. A separate experiment demonstrated agreement for the scattering angles predicted by simulation for a number of materials, such as PEEK, tantalum and tungsten at 200, 180 and 160 MeV in one axis. There were notable discrepancies in the orthogonal axis possibly due to dispersion and an off-energy bunch present during operation.

The automated process outlined above was used to design the first ever dual-scattering system for 200 MeV electrons, 3D printed in PLA. This successfully produced an enlarged and flattened beam with an approximate uniform radius of 13 mm measured on a YAG screen in-air. Component positions and thicknesses were modified and compared with simulation, with broad agreement despite a systematically smaller beam produced in experiment - this was likely due to filament structure of the scatterers. For this reason, it may be preferred to rely on materials with more reliable densities to manufacture dual-scattering foils for clinical use. A more compact set of scattering systems in aluminium was installed to successfully measure uniform dose profiles in-air with radiochromic films. This again verified the success of the automated design process, with broadly better agreement between simulation predictions and experiment than the PLA system. To allow measurement of beam evolution in water, a dual-scattering system was designed in PEEK and installed in the CLEAR beamline. Using a steel collimator, a uniform beam was measured in water, with evolution of both dose and transverse profile in the medium well modelled using a combined RF-Track and TOPAS comparative model. The 10% uniform region in x decreased from the initial value of 10 mm after passage through 120 mm of water, accounted for by loss of uniformity counterbalanced by increasing lateral spread.

A second iteration of the PEEK system with a thicker lead and steel collimator was designed, developed and installed to allow operation with higher doses across the uniform region. Similar studies on beam evolution in water compared well with MC simulations in terms of both uniform region and lateral penumbra, with discrepancies likely caused by sensitivities of the system to the exact initial beam parameters. The uniform region again decreased with depth, accounted for by the loss of uniformity and within reasonable agreement with simulations. The lateral penumbra was

initially 1 mm due to the successful collimation, also increasing with depth generally in line with simulations. This verified the predictions of beam evolution in water from TOPAS, with a reasonable assumption that it would also remain accurate for the larger uniform beams required for clinical use. Further studies confirmed the relative robustness of the system to beam intensity up to 20 nC/train, equivalent to approximately 10 Gy/train delivered in shallow water for the purposes of carrying out irradiations of large samples for pre-clinical FLASH studies at CLEAR. X-ray contributions to total dose were found to be negligible, with the magnitude and dose-profile in excellent agreement with MC calculations. This again served as a benchmark of the MC predictions of secondary dose contributions from scattering foils in the VHEE regime. The PEEK scattering system system is now a permanent upgrade to the capabilities of the CLEAR accelerator, and is used for general purpose operation of the User Facility. Study of larger dual-scattered beams would be desirable for comparison with simulation; this would however be challenging in non-dedicated research accelerators such as CLEAR where the beam pipe and limited size in the in-air test stand were a constraint. Upon completion of a secondary beamline at CLEAR dedicated to radiobiological experiments, study of slightly larger VHEE beams at CLEAR with greater secondary particle production may be feasible. Future electron facilities operating in the VHEE regime may also be appropriate for carrying out these studies.

6.2 Final Remarks

When taken together, the main conclusions of this thesis are: large beams with transverse homogeneity in dose can be delivered for FLASH VHEE-RT. The principle methods of either magnification optics of a uniform beam or dual-scattering of an arbitrary beam have respective caveats. The former is likely to be sensitive not only to the initial beam, but also to the alignment and field consistency of the required magnets; design in a compact gantry such as e-GaToroid should take these sensitivities into consideration during the optimisation process. Simulations of the latter demonstrated that typical dual-scattering foil design processes and geometries would be incompatible with 200 MeV electrons. Therefore, more extended geometries or assistance with optics may be required, together with MC assisted scatterer design. Nevertheless, uniformity of beams and reduction of lateral penumbrae for conformal treatment particularly with the use of collimators could be achieved with sufficient space between the scattering system and treatment location. The validity of the conclusions from simulations and the novel design process with TOPAS was confirmed through smaller-scale experimental studies. Despite the possible drawbacks of dual-scattering foil use in compact, clinical VHEE settings, they can be worthwhile for pre-clinical studies and irradiations

where Bremsstrahlung is negligible. They represent a cheaper and simpler solution to providing these beams than bulky, expensive magnification optics. Online alignment may also be feasible for their use. The lifetime of the system may be a concern, but PEEK or metal based systems would both be resistant to radiation damage. Operation with magnetic elements could allow dual-scattering foils to be feasibly implemented clinically in the VHEE regime, but additional studies on such combined systems are required.

Bibliography

[1] Abi Rimmer. "UK's progress on cancer survival has slowed in past decade, figures show". *BMJ* 384 (2024). DOI: 10.1136/bmj.q290.

[2] CR Smittenaar et al. "Cancer incidence and mortality projections in the UK until 2035". *British journal of cancer* 115.9 (2016), pp. 1147–1155. DOI: 10.1038/bjc.2016.304.

[3] J Maddams, Martin Utley, and Henrik Møller. "Projections of cancer prevalence in the United Kingdom, 2010–2040". *British journal of cancer* 107.7 (2012), pp. 1195–1202. DOI: 10.1038/bjc.2012.366.

[4] Daniela S Gutiérrez-Torres et al. "Changes in smoking use and subsequent lung cancer risk in the Alpha-Tocopherol, Beta-Carotene Cancer Prevention Study". *JNCI: Journal of the National Cancer Institute* (2024), djae012. ISSN: 0027-8874. DOI: 10.1093/jnci/djae012.

[5] Michelle C. Turner et al. "Outdoor air pollution and cancer: An overview of the current evidence and public health recommendations". *CA: A Cancer Journal for Clinicians* 70.6 (2020), pp. 460–479. DOI: https://doi.org/10.3322/caac.21632.

[6] Janet S de Moor et al. "Access to cancer care and general medical care services among cancer survivors in the United States: an analysis of 2011 medical expenditure panel survey data". *Public Health Reports* 131.6 (2016), pp. 783–790. DOI: 10.1177/0033354916675852.

[7] Katie Wakeham et al. "Towards world-class radiotherapy in the UK: time for transformation". *The Lancet Oncology* (2024). DOI: 10.1016/S1470-2045(24)00103-7.

[8] Theo Rashid et al. "Mortality from leading cancers in districts of England from 2002 to 2019: a population-based, spatiotemporal study". *The Lancet Oncology* 25.1 (2024), pp. 86–98. DOI: 10.1016/S1470-2045(23)00530-2.

[9] Didem SM Bernard, Stacy L Farr, and Zhengyi Fang. "National estimates of out-of-pocket health care expenditure burdens among nonelderly adults with cancer: 2001 to 2008". *Journal of Clinical Oncology* 29.20 (2011), p. 2821. DOI: 10.1200/JCO.2010.33.0522.

[10] Annie Bygrave et al. "Australian experiences of out-of-pocket costs and financial burden following a cancer diagnosis: a systematic review". *International journal of environmental research and public health* 18.5 (2021), p. 2422. DOI: 10.3390/ijerph18052422.

[11] Lu Han et al. "The impact of transportation mode, socioeconomic deprivation and rurality on travel times to radiotherapy and surgical services for patients with prostate cancer: a national population-based evaluation". *Radiotherapy and Oncology* 192 (2024), p. 110092. DOI: 10.1016/j.radonc.2024.110092.

[12] Elaine Douglas et al. "Socioeconomic inequalities in breast and cervical screening coverage in England: are we closing the gap?" *Journal of medical screening* 23.2 (2016), pp. 98–103. DOI: 10.1177/0969141315600192.

[13] Barbara Bachtiary et al. "Financial Toxicity in Swiss Cancer Patients Treated with Proton Therapy: An Observational Cross-Sectional Study on Self-Reported Outcome". *Cancers* 15.23 (2023), p. 5498. DOI: 10.3390/cancers15235498.

[14] Alexander Fabian et al. "Financial toxicity in cancer patients treated with radiotherapy in Germany—a cross-sectional study". *Strahlentherapie und Onkologie* 198.12 (2022), pp. 1053–1061. DOI: 10.1007/s00066-022-01936-z.

[15] Frank A Sloan, Hellen Gelband, et al. "The cancer burden in low-and middle-income countries and how it is measured". *Cancer control opportunities in low-and middle-income countries*. National Academies Press (US), 2007. URL: https://www.ncbi.nlm.nih.gov/books/NBK54028/.

[16] CS Pramesh et al. "Priorities for cancer research in low-and middle-income countries: a global perspective". *Nature medicine* 28.4 (2022), pp. 649–657. DOI: 10.1038/s41591-022-01738-x.

[17] Shailja C Shah et al. "Cancer control in low-and middle-income countries: is it time to consider screening?" *Journal of global oncology* 5 (2019), pp. 1–8. DOI: 10.1200/JGO.18.00200.

[18] Isabelle Soerjomataram and Freddie Bray. "Planning for tomorrow: global cancer incidence and the role of prevention 2020–2070". *Nature reviews Clinical oncology* 18.10 (2021), pp. 663–672. DOI: 10.1038/s41571-021-00514-z.

[19] Gilles R Dagenais et al. "Variations in common diseases, hospital admissions, and deaths in middle-aged adults in 21 countries from five continents (PURE): a prospective cohort study". *The Lancet* 395.10226 (2020), pp. 785–794. DOI: 10.1016/S0140-6736(19)32007-0.

[20] Valerie McCormack and Ajay Aggarwal. "Early cancer diagnosis: reaching targets across whole populations amidst setbacks". *British journal of cancer* 124.7 (2021), pp. 1181–1182. DOI: 10.1038/s41416-021-01276-2.

[21] Rebecca L Siegel et al. "Cancer statistics, 2023". *Ca Cancer J Clin* 73.1 (2023), pp. 17–48. DOI: 10.3322/caac.21763.

[22] M Dalmartello et al. "European cancer mortality predictions for the year 2022 with focus on ovarian cancer". *Annals of Oncology* 33.3 (2022), pp. 330–339. DOI: 10.1016/j.annonc.2021.12.007.

[23] Milena Falcaro et al. "The effects of the national HPV vaccination programme in England, UK, on cervical cancer and grade 3 cervical intraepithelial neoplasia incidence: a register-based observational study". *The Lancet* 398.10316 (2021), pp. 2084–2092. DOI: 10.1016/S0140-6736(21)02178-4.

[24] Ajay Aggarwal et al. "The future of cancer care in the UK—time for a radical and sustainable National Cancer Plan". *The Lancet Oncology* 25.1 (2024), e6–e17. ISSN: 1470-2045. DOI: 10.1016/S1470-2045(23)00511-9.

[25] Jaspreet Kaur and Bidhu K Mohanti. "Transition from curative to palliative care in cancer". *Indian journal of palliative care* 17.1 (2011), p. 1. DOI: 10.4103/0973-1075.78442.

[26] Sophie Knipper et al. "Options for curative treatment of localized prostate cancer". *Deutsches Ärzteblatt International* 118.13 (2021), p. 228. DOI: 10.3238/arztebl.m2021.0026.

[27] Nazeer Hasan et al. "Skin cancer: understanding the journey of transformation from conventional to advanced treatment approaches". *Molecular cancer* 22.1 (2023), p. 168. DOI: 10.1186/s12943-023-01854-3.

[28] Carolyn Taylor et al. "Breast cancer mortality in 500 000 women with early invasive breast cancer in England, 1993-2015: population based observational cohort study". *Bmj* 381 (2023). DOI: 10.1136/bmj-2022-074684.

[29] Craig Gouldthorpe et al. *Specialist Palliative Care for Patients with Cancer: More Than End-of-Life Care*. 2023. DOI: 10.3390/cancers15143551.

[30] Rajiv Agarwal and Andrew S Epstein. "The role of palliative care in oncology". *Seminars in interventional radiology*. Vol. 34. 04. Thieme Medical Publishers. 2017, pp. 307–312. DOI: 10.1055/s-0037-1608702.

[31] Hyuna Sung et al. "Global Cancer Statistics 2020: GLOBOCAN Estimates of Incidence and Mortality Worldwide for 36 Cancers in 185 Countries". *CA: A Cancer Journal for Clinicians* 71.3 (2021), pp. 209–249. DOI: 10.3322/caac.21660.

[32] Joerg Haier and Juergen Schaefers. "Economic perspective of cancer care and its consequences for vulnerable groups". *Cancers* 14.13 (2022), p. 3158. DOI: 10.3390/cancers14133158.

[33] Simiao Chen et al. "Estimates and Projections of the Global Economic Cost of 29 Cancers in 204 Countries and Territories From 2020 to 2050". *JAMA Oncology* 9.4 (2023), pp. 465–472. ISSN: 2374-2437. DOI: 10.1001/jamaoncol.2022.7826.

[34] Bernardo Pereira Cabral, Maria da Graça Derengowski Fonseca, and Fabio Batista Mota. "The recent landscape of cancer research worldwide: a bibliometric and network analysis". *Oncotarget* 9.55 (2018), p. 30474. DOI: 10.18632/oncotarget.25730.

[35] Daniel A Goldstein et al. "A global comparison of the cost of patented cancer drugs in relation to global differences in wealth". *Oncotarget* 8.42 (2017), p. 71548. DOI: 10.18632/oncotarget.17742.

[36] Lorna Wills et al. "Estimating surgery, radiotherapy and systemic anti-cancer therapy treatment costs for cancer patients by stage at diagnosis". *The European Journal of Health Economics* (2023), pp. 1–12. DOI: 10.1007/s10198-023-01623-5.

[37] Dejene Tolossa Debela et al. "New approaches and procedures for cancer treatment: Current perspectives". *SAGE open medicine* 9 (2021), p. 20503121211034366. DOI: 10.1177/20503121211034366.

[38] Manuel Arruebo et al. "Assessment of the evolution of cancer treatment therapies". *Cancers* 3.3 (2011), pp. 3279–3330. DOI: 10.3390/cancers3033279.

[39] Uttpal Anand et al. "Cancer chemotherapy and beyond: Current status, drug candidates, associated risks and progress in targeted therapeutics". *Genes & Diseases* 10.4 (2023), pp. 1367–1401. ISSN: 2352-3042. DOI: 10.1016/j.gendis.2022.02.007.

[40] Muhammad T Amjad, Anusha Chidharla, and Anup Kasi. "Cancer chemotherapy" (2020). URL: https://www.ncbi.nlm.nih.gov/books/NBK564367/.

[41] Dipanjan Karati and Dileep Kumar. "A Comprehensive Review on Targeted Cancer Therapy: New Face of Treatment Approach". *Current Pharmaceutical Design* 29.41 (2023), pp. 3282–3294. DOI: 10.2174/0113816128272203231121034814.

[42] Kulmira Nurgali, R Thomas Jagoe, and Raquel Abalo. "Adverse effects of cancer chemotherapy: Anything new to improve tolerance and reduce sequelae?" *Frontiers in pharmacology* 9 (2018), p. 362658. DOI: 0.3389/fphar.2018.00245.

[43] Insaf Altun and Alper Sonkaya. "The most common side effects experienced by patients were receiving first cycle of chemotherapy". *Iranian journal of public health* 47.8 (2018), pp. 1218–1219. URL: https://www.ncbi.nlm.nih.gov/pmc/articles/PMC6123577/.

[44] Khalid O Alfarouk et al. "Resistance to cancer chemotherapy: failure in drug response from ADME to P-gp". *Cancer cell international* 15 (2015), pp. 1–13. DOI: 10.1186/s12935-015-0221-1.

[45] Lei Zhong et al. "Small molecules in targeted cancer therapy: advances, challenges, and future perspectives". *Signal transduction and targeted therapy* 6.1 (2021), pp. 1–48. DOI: 10.1038/s41392-021-00572-w.

[46] Alex D Waldman, Jill M Fritz, and Michael J Lenardo. "A guide to cancer immunotherapy: from T cell basic science to clinical practice". *Nature Reviews Immunology* 20.11 (2020), pp. 651–668. DOI: 10.1038/s41577-020-0306-5.

[47] Volker Schirrmacher. "From chemotherapy to biological therapy: A review of novel concepts to reduce the side effects of systemic cancer treatment". *International journal of oncology* 54.2 (2019), pp. 407–419. DOI: 10.3892/ijo.2018.4661.

[48] Rajamanickam Baskar et al. "Cancer and radiation therapy: current advances and future directions". *International journal of medical sciences* 9.3 (2012), p. 193. DOI: 10.7150/ijms.3635.

[49] Geoff Delaney et al. "The role of radiotherapy in cancer treatment". *Cancer* 104.6 (2005), pp. 1129–1137. DOI: 10.1002/cncr.21324.

[50] Fridtjof Nüsslin. "Wilhelm Conrad Röntgen: The scientist and his discovery". *Physica Medica* 79 (2020), pp. 65–68. DOI: 10.1016/j.ejmp.2020.10.010.

[51] Victor Despeignes. "Observation concernant un cas de cancer de l'estomac traite par les rayons Rontgen". *Lyon méd.* 82 (1896), pp. 428–430. URL: https://cir.nii.ac.jp/crid/1572543024963903232.

[52] Nicolas Foray. "Victor Despeignes, the Forgotten Pioneer of Radiation Oncology". *International Journal of Radiation Oncology*Biology*Physics* 96.4 (2016), pp. 717–721. ISSN: 0360-3016. DOI: https://doi.org/10.1016/j.ijrobp.2016.07.019.

[53] Manuel Lederman. "The early history of radiotherapy: 1895–1939". *International Journal of Radiation Oncology*Biology*Physics* 7.5 (1981), pp. 639–648. ISSN: 0360-3016. DOI: 10.1016/0360-3016(81)90379-5.

[54] Howard D. Thames. "On the origin of dose fractionation regimens in radiotherapy". *Seminars in Radiation Oncology* 2.1 (1992). Fractionation in Radiation Therapy, pp. 3–9. ISSN: 1053-4296. DOI: 10.1016/S1053-4296(05)80043-8.

[55] E. A. Owen and H. I. Jones. "Ionisation Chambers for X-Ray Dosage Measurement". *British Journal of Radiology* 4.43 (2014), pp. 309–338. ISSN: 0007-1285. DOI: 10.1259/0007-1285-4-43-309.

[56] Nicholas G Zaorsky et al. "The evolution of brachytherapy for prostate cancer". *Nature Reviews Urology* 14.7 (2017), pp. 415–439. DOI: 10.1038/nrurol.2017.76.

[57] Serena Gianfaldoni et al. "An overview on radiotherapy: from its history to its current applications in dermatology". *Open access Macedonian journal of medical sciences* 5.4 (2017), p. 521. DOI: 10.3889/oamjms.2017.122.

[58] HE Johns, LM Bates, and TA Watson. "I. The Saskatchewan Cobalt 60 Unit". *The British Journal of Radiology* 25.294 (1952), pp. 296–302. DOI: 10.1259/0007-1285-25-294-296.

[59] Jacob Van Dyk, Jerry J Battista, and Peter Richard Almond. "A RETROSPECTIVE OF COBALT-60 RADIATION THERAPY: "THE ATOM BOMB THAT SAVES LIVES"". 2020. URL: https://api.semanticscholar.org/CorpusID:221784247.

[60] BJ Healy et al. "Cobalt-60 machines and medical linear accelerators: competing technologies for external beam radiotherapy". *Clinical Oncology* 29.2 (2017), pp. 110–115. DOI: 10.1016/j.clon.2016.11.002.

[61] Benjamin H Kann et al. "The impact of cobalt-60 source age on biologically effective dose in high-dose functional Gamma Knife radiosurgery". *Journal of Neurosurgery* 125.Supplement_1 (2016), pp. 154–159. DOI: 10.3171/2016.6.GKS161497.

[62] W. W. Hansen. "A Type of Electrical Resonator". *Journal of Applied Physics* 9.10 (1938), pp. 654–663. ISSN: 0021-8979. DOI: 10.1063/1.1710371.

[63] Russell H. Varian and Sigurd F. Varian. "A high frequency oscillator and amplifier". *J. Appl. Phys.* 10 (1939), pp. 321–327. DOI: 10.1063/1.1707311.

[64] P. J. Bryant. "A Brief history and review of accelerators". *CERN Accelerator School: Course on General Accelerator Physics*. 1992, pp. 1–16. URL: https://inspirehep.net/literature/347557.

[65] M. Weissbluth et al. "The Stanford Medical Linear Accelerator". *Radiology* 72.2 (1959), pp. 242–265. DOI: 10.1148/72.2.242.

[66] M Weissbluth et al. "The Stanford medical linear accelerator: II. Installation and physical measurements". *Radiology* 72.2 (1959), pp. 242–265. DOI: 10.1148/72.2.242.

[67] Roger A Harvey, Lewis L Haas, and John S Laughlin. "Preliminary clinical experience with the betatron". *Radiology* 56.3 (1951), pp. 394–402. DOI: 10.1148/56.3.394.

[68] David I Thwaites and John B Tuohy. "Back to the future: the history and development of the clinical linear accelerator". *Physics in Medicine & Biology* 51.13 (2006), R343. DOI: 10.1088/0031-9155/51/13/R20.

[69] Giacomo Cuttone. "Applications of particle accelerators in medical physics". 2010, p. 057. DOI: 10.22323/1.103.0057.

[70] Xiufang Tian et al. "The evolution of proton beam therapy: Current and future status". *Molecular and clinical oncology* 8.1 (2018), pp. 15–21. DOI: 10.3892/mco.2017.1499.

[71] Shikha Goyal, Tejinder Kataria, et al. "Image guidance in radiation therapy: techniques and applications". *Radiology research and practice* 2014 (2014). DOI: 10.1155/2014/705604.

[72] Susan F Dunbar et al. "Stereotactic radiotherapy for pediatric and adult brain tumors: preliminary report". *International Journal of Radiation Oncology* Biology* Physics* 30.3 (1994), pp. 531–539. DOI: 10.1016/0360-3016(92)90938-e.

[73] A. S. Lichter et al. "Radiotherapy Treatment Planning: Past, Present, and Future". *New Directions in Cancer Treatment*. Ed. by Ian Magrath. Berlin, Heidelberg: Springer Berlin Heidelberg, 1989, pp. 53–84. DOI: 10.1007/978-3-642-83405-9_3.

[74] John V Pickstone. "Contested Cumulations: Configurations of Cancer Treatments through the Twentieth Century". *Bulletin of the History of Medicine* 81.1 (2007), p. 164. DOI: 10.1353/bhm.2007.0011.

[75] A Wambersie and R A Gahbauer. "Medical applications of electron linear accelerators" (1996). DOI: 10.5170/CERN-1996-002.229.

[76] J.I.M. Botman, T. Bates, and H.L. Hagedoorn. "A double focusing magnet system for a medical linear electron accelerator". *Nuclear Instruments and Methods in Physics Research Section B: Beam Interactions with Materials and Atoms* 10-11 (1985), pp. 796–798. ISSN: 0168-583X. DOI: 10.1016/0168-583X(85)90110-7.

[77] EB Podgorsak et al. “Design of X-ray targets for high energy linear accelerators in radiotherapy”. *American Journal of Roentgenology* 121.4 (1974), pp. 873–882. DOI: 10.2214/ajr.121.4.873.

[78] Yuhi Suda et al. “Direct energy spectrum measurement of X-ray from a clinical linac”. *Journal of Applied Clinical Medical Physics* 22.8 (2021), pp. 255–264. DOI: 10.1002/acm2.13354.

[79] Sunil Dutt Sharma. “Unflattened photon beams from the standard flattening filter free accelerators for radiotherapy: Advantages, limitations and challenges”. *Journal of medical physics* 36.3 (2011), pp. 123–125. DOI: 10.4103/0971-6203.83464.

[80] *Technical specifications of radiotherapy equipment for cancer treatment*. Tech. rep. World Health Organization, 2021, pp. 9–50. URL: http://www.jstor.org/stable/resrep30121.1 (visited on 03/06/2023).

[81] Thitiporn Jaruthien et al. “Flattening filter free stereotactic body radiation therapy for lung tumors: outcomes and predictive factors”. *Translational Cancer Research* 10 (2021), pp. 571–580. DOI: 10.21037/tcr-20-3174.

[82] Claudio Fiorino et al. “Skin-sparing reduction effects of thermoplastics used for patient immobilization in head and neck radiotherapy”. *Radiotherapy and Oncology* 30.3 (1994), pp. 267–270. ISSN: 0167-8140. DOI: https://doi.org/10.1016/0167-8140(94)90468-5.

[83] Radhe Mohan and David Grosshans. “Proton therapy–present and future”. *Advanced drug delivery reviews* 109 (2017), pp. 26–44. DOI: 10.1016/j.addr.2016.11.006.

[84] W Parker and H Patrocinio. *Clinical treatment planning in external photon beam radiotherapy*. 2005.

[85] Neil G Burnet et al. “Defining the tumour and target volumes for radiotherapy”. *Cancer Imaging* 4.2 (2004), p. 153. DOI: 10.1102/1470-7330.2004.0054.

[86] Christopher D. Willey and James A. Bonner. *Interaction of Chemotherapy and Radiation*. 2015. URL: https://clinicalgate.com/interaction-of-chemotherapy-and-radiation/.

[87] Guillaume Vogin et al. “Cranial organs at risk delineation: heterogenous practices in radiotherapy planning”. *Radiation Oncology* 16 (2021). DOI: 10.1186/s13014-021-01756-y.

[88] Osamu Tanaka et al. “Effect of stomach size on organs at risk in pancreatic stereotactic body radiotherapy”. *Radiation Oncology* 17.1 (2022), pp. 1–7. DOI: 10.1186/s13014-022-02107-1.

[89] Timothy Ritter et al. “Consideration of dose limits for organs at risk of thoracic radiotherapy: atlas for lung, proximal bronchial tree, esophagus, spinal cord, ribs, and brachial plexus”. *International Journal of Radiation Oncology* Biology* Physics* 81.5 (2011), pp. 1442–1457. DOI: 10.1016/j.ijrobp.2010.07.1977.

[90] Francois Eschwège Maurice Tubiana. “Conformal radiotherapy and intensity-modulated radiotherapy: clinical data”. *Acta Oncologica* 39.5 (2000), pp. 555–567. DOI: 10.1080/028418600750013249.

[91] T J Jordan and P C Williams. "The design and performance characteristics of a multileaf collimator". *Physics in Medicine & Biology* 39.2 (1994), p. 231. DOI: 10.1088/0031-9155/39/2/002.

[92] Byungchul Cho. "Intensity-modulated radiation therapy: a review with a physics perspective". *Radiation oncology journal* 36.1 (2018), p. 1. DOI: 10.3857/roj.2018.00122.

[93] J Staffurth et al. *Radiotherapy Board-Intensity Modulated Radiotherapy (IMRT) in the UK: Current access and predictions of future access rates*. 2015. URL: https://www.sor.org/learning-advice/professional-body-guidance-and-publications/documents-and-publications/archive-documents/radiotherapy-board-intensity-modulated-radiotherapy.

[94] A Taylor and MEB Powell. "Intensity-modulated radiotherapy—what is it?" *Cancer Imaging* 4.2 (2004), p. 68. DOI: 10.1102/1470-7330.2004.0003.

[95] Chen-Shou Chui and Spiridon V Spirou. "Inverse planning algorithms for external beam radiation therapy". *Medical Dosimetry* 26.2 (2001), pp. 189–197. DOI: 10.1016/s0958-3947(01)00069-3.

[96] May Teoh et al. "Volumetric modulated arc therapy: a review of current literature and clinical use in practice". *The British journal of radiology* 84.1007 (2011), pp. 967–996. DOI: 10.1259/bjr/22373346.

[97] Gerald B Fogarty et al. "Volumetric modulated arc therapy is superior to conventional intensity modulated radiotherapy-a comparison among prostate cancer patients treated in an Australian centre". *Radiation Oncology* 6 (2011), pp. 1–5. DOI: 10.1186/1748-717X-6-108.

[98] Sherisse Ornella Hunte et al. "Volumetric modulated arc therapy (VMAT): a review of clinical outcomes—what is the clinical evidence for the most effective implementation?" *British Journal of Radiology* 95.1136 (2022), p. 20201289. ISSN: 0007-1285. DOI: 10.1259/bjr.20201289. URL: 10.1259/bjr.20201289.

[99] Penelope Knapp et al. "The role of volumetric modulated arc therapy (VMAT) in gynaecological radiation therapy: A dosimetric comparison of intensity modulated radiation therapy versus VMAT". *Journal of Medical Radiation Sciences* 66.1 (2019), pp. 44–53. DOI: 10.1002/jmrs.311.

[100] "Geant4—a simulation toolkit". *Nuclear Instruments and Methods in Physics Research Section A: Accelerators, Spectrometers, Detectors and Associated Equipment* 506.3 (2003), pp. 250–303. ISSN: 0168-9002. DOI: 10.1016/S0168-9002(03)01368-8.

[101] Pedro Andreo. "Monte Carlo simulations in radiotherapy dosimetry". *Radiation Oncology* 13 (2018), pp. 1–15. DOI: 10.1186/s13014-018-1065-3.

[102] Chunhao Wang et al. "Artificial intelligence in radiotherapy treatment planning: present and future". *Technology in cancer research & treatment* 18 (2019), pp. 1–11. DOI: 10.1177/1533033819873922.

[103] Maria Grazia Ronga et al. "Back to the future: very high-energy electrons (VHEEs) and their potential application in radiation therapy". *Cancers* 13.19 (2021), p. 4942. DOI: 10.3390/cancers13194942.

[104] Kenneth R Hogstrom and Peter R Almond. "Review of electron beam therapy physics". *Physics in Medicine & Biology* 51.13 (2006), R455. DOI: 10.1088/0031-9155/51/13/R25.

[105] Vieri Grandi et al. "Short-term efficacy and safety of total skin electron beam therapy in mycosis fungoides: Systematic review and meta-analysis". *Dermatologic Therapy* 35.11 (2022), e15840. DOI: 10.1111/dth.15840.

[106] Faiz M. Khan. "Basic Physics of Electron Beam Therapy". *The Role of High Energy Electrons in the Treatment of Cancer: 25th Annual San Francisco Cancer Symposium, February 1990*. S.Karger AG, 1991. ISBN: 978-3-8055-5235-6. DOI: 10.1159/000429575.

[107] CA Tobias et al. "Pituitary irradiation with high-energy proton beams a preliminary report". *Cancer research* 18.2 (1958), pp. 121–134. URL: https://api.semanticscholar.org/CorpusID:35408876.

[108] Andrzej Kacperek. "Protontherapy of eye tumours in the UK: a review of treatment at Clatterbridge". *Applied Radiation and Isotopes* 67.3 (2009), pp. 378–386. DOI: 10.1016/j.apradiso.2008.06.012.

[109] G Coutrakon et al. "A performance study of the Loma Linda proton medical accelerator". *Medical physics* 21.11 (1994), pp. 1691–1701. DOI: 10.1118/1.597270.

[110] Susu Yan et al. "Global democratisation of proton radiotherapy". *The Lancet Oncology* 24.6 (2023), e245–e254. DOI: 10.1016/S1470-2045(23)00184-5.

[111] PTCOG. *Particle Therapy Facilities in Clinical Operation*. 2024. URL: https://www.ptcog.ch/index.php/facilities-in-operation.

[112] Baldev Patyal. "Dosimetry aspects of proton therapy". *Technology in cancer research & treatment* 6.4_suppl (2007), pp. 17–23. DOI: 10.1177/15330346070060S403.

[113] Wayne D Newhauser and Rui Zhang. "The physics of proton therapy". *Physics in Medicine & Biology* 60.8 (2015), R155. DOI: 10.1088/0031-9155/60/8/R155.

[114] David Jette and Weimin Chen. "Creating a spread-out Bragg peak in proton beams". *Physics in Medicine & Biology* 56.11 (2011), N131. DOI: 10.1088/0031-9155/56/11/N01.

[115] Arnold Pompos, Marco Durante, and Hak Choy. "Heavy ions in cancer therapy". *JAMA oncology* 2.12 (2016), pp. 1539–1540. DOI: 10.1001/jamaoncol.2016.2646.

[116] Chia-Lun Chang et al. "Comparing the oncologic outcomes of proton therapy and intensity-modulated radiation therapy for head and neck squamous cell carcinoma". *Radiotherapy and Oncology* 190 (2024), p. 109971. DOI: 10.1016/j.radonc.2023.109971.

[117] Noorazrul Yahya and Hanani Abdul Manan. "Quality of life and patient-reported outcomes following proton therapy for oropharyngeal carcinoma: a systematic review". *Cancers* 15.8 (2023), p. 2252. DOI: 10.3390/cancers15082252.

[118] Justin D. Anderson et al. “Outcomes of Proton Beam Therapy Compared With Intensity-Modulated Radiation Therapy for Uterine Cancer”. *International Journal of Particle Therapy* 9.3 (2022), pp. 10–17. ISSN: 2331-5180. DOI: 10.14338/IJPT-22-00020.1.

[119] Alberto Degiovanni and Ugo Amaldi. “Proton and Carbon Linacs for Hadron Therapy”. *27th International Linear Accelerator Conference*. 2014, FRIOB02. URL: http://cds.cern.ch/record/206262.

[120] E Sengbusch et al. “Maximum proton kinetic energy and patient-generated neutron fluence considerations in proton beam arc delivery radiation therapy”. *Medical physics* 36.2 (2009), pp. 364–372. DOI: 10.1118/1.3049787.

[121] Thomas R Bortfeld and Jay S Loeffler. “Three ways to make proton therapy affordable”. *Nature* 549.7673 (2017), pp. 451–453. DOI: 10.1038/549451a.

[122] Hywel Owen et al. “Technologies for delivery of proton and ion beams for radiotherapy”. *International Journal of Modern Physics A* 29.14 (2014), p. 1441002. DOI: 10.1142/S0217751X14410024.

[123] Alberto Degiovanni et al. “LIGHT: A linear accelerator for proton therapy”. *Proceedings of NAPAC2016, Chicago, USA* (2016), p. 32. DOI: 10.18429/JACoW-NAPAC2016-FRB1IO02.

[124] Th Haberer et al. “The Heidelberg ion therapy center”. *Radiotherapy and Oncology* 73 (2004), S186–S190. DOI: 10.1016/s0167-8140(04)80046-x.

[125] R Fuchs, U Weinrich, and E Sust. “Assembly of the carbon beam gantry at the Heidelberg Ion Therapy (HIT) accelerator”. *Proceedings of the EPAC-2008, Genoa, Italy* (2008), pp. 23–27. URL: https://cds.cern.ch/record/1182949.

[126] Y. Iwata et al. “Design of a superconducting rotating gantry for heavy-ion therapy”. *Phys. Rev. ST Accel. Beams* 15 (2012), p. 044701. DOI: 10.1103/PhysRevSTAB.15.044701.

[127] S. Takayama et al. “Design and Magnetic Field Measurement of the Superconducting Magnets for the Next-Generation Rotating Gantry”. *IEEE Transactions on Applied Superconductivity* 32.6 (2022), pp. 1–4. DOI: 10.1109/TASC.2022.3160973.

[128] Reed Teyber et al. “Thermoeconomic cost optimization of superconducting magnets for proton therapy gantries”. *Superconductor Science and Technology* 33.10 (2020), p. 105005. DOI: 10.1088/1361-6668/abaa53.

[129] Sandro Rossi. “Hadron Therapy Achievements and Challenges: The CNAO Experience”. *Physics* 4.1 (2022), pp. 229–257. ISSN: 2624-8174. DOI: 10.3390/physics4010017.

[130] Vincent Favaudon et al. “Ultrahigh dose-rate FLASH irradiation increases the differential response between normal and tumor tissue in mice”. *Science translational medicine* 6.245 (2014), 245ra93–245ra93. DOI: 10.1126/scitranslmed.3008973.

[131] Marie-Catherine Vozenin, Jean Bourhis, and Marco Durante. "Towards clinical translation of FLASH radiotherapy". *Nature Reviews Clinical Oncology* 19.12 (2022), pp. 791–803. DOI: 10.1038/s41571-022-00697-z.

[132] Marie-Catherine Vozenin et al. "The advantage of FLASH radiotherapy confirmed in mini-pig and cat-cancer patients". *Clinical Cancer Research* 25.1 (2019), pp. 35–42. DOI: 10.1158/1078-0432.CCR-17-3375.

[133] Jean Bourhis et al. "Treatment of a first patient with FLASH-radiotherapy". *Radiotherapy and oncology* 139 (2019), pp. 18–22. DOI: 10.1016/j.radonc.2019.06.019.

[134] Jake Atkinson et al. "The current status of FLASH particle therapy: a systematic review". *Physical and Engineering Sciences in Medicine* 46.2 (2023), pp. 529–560. DOI: 10.1007/s13246-023-01266-z.

[135] Anastasia Velalopoulou et al. "FLASH Proton Radiotherapy Spares Normal Epithelial and Mesenchymal Tissues While Preserving Sarcoma Response". *Cancer Research* 81 (2021), canres.1500.2021. DOI: 10.1158/0008-5472.CAN-21-1500.

[136] Feng Gao et al. "First demonstration of the FLASH effect with ultrahigh dose rate high-energy X-rays". *Radiotherapy and Oncology* 166 (2022), pp. 44–50. ISSN: 0167-8140. DOI: 10.1016/j.radonc.2021.11.004.

[137] Walter Tinganelli et al. "FLASH with carbon ions: Tumor control, normal tissue sparing, and distal metastasis in a mouse osteosarcoma model". *Radiotherapy and Oncology* 175 (2022), pp. 185–190. DOI: 10.1016/j.radonc.2022.05.003.

[138] Abdullah Muhammad Zakaria et al. "Ultra-high dose-rate, pulsed (FLASH) radiotherapy with carbon ions: generation of early, transient, highly oxygenated conditions in the tumor environment". *Radiation research* 194.6 (2020), pp. 587–593. DOI: 10.1667/RADE-19-00015.1.

[139] Daria Boscolo et al. "May oxygen depletion explain the FLASH effect? A chemical track structure analysis". *Radiotherapy and Oncology* 162 (2021), pp. 68–75. DOI: 10.1016/j.radonc.2021.06.031.

[140] J.Y. Jin et al. "FLASH Dose Rate Effect on Circulating Immune Cells: A Potential Mechanism for FLASH-RT?" *International Journal of Radiation Oncology*Biology*Physics* 108.3, Supplement (2020). Proceedings of the American Society for Radiation Oncology, S7. ISSN: 0360-3016. DOI: 10.1016/j.ijrobp.2020.07.2079.

[141] Reinhard Schulte et al. "Transformative Technology for FLASH Radiation Therapy". *Applied Sciences* 13.8 (2023). ISSN: 2076-3417. DOI: 10.3390/app13085021.

[142] Carla Rohrer Bley et al. "Dose-and volume-limiting late toxicity of FLASH radiotherapy in cats with squamous cell carcinoma of the nasal planum and in mini pigs". *Clinical Cancer Research* 28.17 (2022), pp. 3814–3823. DOI: 10.1158/1078-0432.CCR-22-0262.

[143] Till Tobias Böhlen et al. "Normal Tissue Sparing by FLASH as a Function of Single-Fraction Dose: A Quantitative Analysis". *International Journal of Radiation Oncology*Biology*Physics* 114.5 (2022). A Red Journal Special Issue: Oligometastasis, Part 2, pp. 1032–1044. ISSN: 0360-3016. DOI: 10.1016/j.ijrobp.2022.05.038.

[144] Sumin Zhou et al. "Minimum dose rate estimation for pulsed FLASH radiotherapy: A dimensional analysis". *Medical physics* 47.7 (2020), pp. 3243–3249. DOI: 10.1002/mp.14181.

[145] Pierre Montay-Gruel et al. "FLASH radiotherapy with photon beams". *Medical Physics* 49.3 (2022), pp. 2055–2067. DOI: 10.1002/mp.15222.

[146] Nolan Esplen et al. "Design optimization of an electron-to-photon conversion target for ultra-high dose rate x-ray (FLASH) experiments at TRIUMF". *Physics in Medicine & Biology* 67.10 (2022), p. 105003. DOI: 10.1088/1361-6560/ac5ed6.

[147] Magdalena Bazalova-Carter and Nolan Esplen. "On the capabilities of conventional x-ray tubes to deliver ultra-high (FLASH) dose rates". *Medical physics* 46.12 (2019), pp. 5690–5695. DOI: 10.1002/mp.13858.

[148] Simon Jolly et al. "Technical challenges for FLASH proton therapy". *Physica Medica* 78 (2020), pp. 71–82. DOI: 0.1016/j.ejmp.2020.08.005.

[149] JM Schippers et al. "The SC cyclotron and beam lines of PSI's new protontherapy facility PROSCAN". *Nuclear Instruments and Methods in Physics Research Section B: Beam Interactions with Materials and Atoms* 261.1-2 (2007), pp. 773–776. DOI: 10.1016/j.nimb.2007.04.052.

[150] M Engelsman et al. "Commissioning a passive-scattering proton therapy nozzle for accurate SOBP delivery". *Medical physics* 36.6Part1 (2009), pp. 2172–2180. DOI: 10.1118/1.3121489.

[151] Alexander Gerbershagen et al. "Measurements and simulations of boron carbide as degrader material for proton therapy". *Physics in Medicine & Biology* 61.14 (2016), N337. DOI: 10.1088/0031-9155/61/14/N337.

[152] Pablo A. Arrutia Sota et al. "Millisecond burst extractions from synchrotrons using RF phase displacement acceleration". *Nuclear Instruments and Methods in Physics Research Section A: Accelerators, Spectrometers, Detectors and Associated Equipment* 1039 (2022), p. 167007. ISSN: 0168-9002. DOI: 10.1016/j.nima.2022.167007.

[153] K Mizushima et al. "Experimental studies of systematic multiple-energy operation at HIMAC synchrotron". *Nuclear Instruments and Methods in Physics Research Section B: Beam Interactions with Materials and Atoms* 331 (2014), pp. 243–247. DOI: 10.1016/j.nimb.2013.12.033.

[154] Y Iwata et al. "Multiple-energy operation with extended flattops at HIMAC". *Nuclear Instruments and Methods in Physics Research Section A: Accelerators, Spectrometers, Detectors and Associated Equipment* 624.1 (2010), pp. 33–38. DOI: 10.1016/j.nima.2010.09.016.

[155] Michael Pennock et al. “Proton Bragg Peak FLASH Enables Organ Sparing and Ultra-High Dose-Rate Delivery: Proof of Principle in Recurrent Head and Neck Cancer”. *Cancers* 15.15 (2023), p. 3828. DOI: 10.3390/cancers15153828.

[156] Anthony E. Mascia et al. “Proton FLASH Radiotherapy for the Treatment of Symptomatic Bone Metastases: The FAST-01 Nonrandomized Trial”. *JAMA Oncology* 9.1 (2023), pp. 62–69. ISSN: 2374-2437. DOI: 10.1001/jamaoncol.2022.5843.

[157] Esther Kneepkens et al. “Shoot-through proton FLASH irradiation lowers linear energy transfer in organs at risk for neurological tumors and is robust against density variations”. *Physics in Medicine & Biology* 68.21 (2023), p. 215020. DOI: 10.1088/1361-6560/ad0280.

[158] C DesRosiers et al. “150-250 MeV electron beams in radiation therapy”. *Physics in Medicine & Biology* 45.7 (2000), p. 1781. DOI: 10.1088/0031-9155/45/7/306.

[159] Till Tobias Böhlen et al. “Characteristics of very high-energy electron beams for the irradiation of deep-seated targets”. *Medical Physics* 48.7 (2021), pp. 3958–3967. DOI: 10.1002/mp.14891.

[160] Agnese Lagzda et al. “Influence of heterogeneous media on Very High Energy Electron (VHEE) dose penetration and a Monte Carlo-based comparison with existing radiotherapy modalities”. *Nuclear Instruments and Methods in Physics Research Section B: Beam Interactions with Materials and Atoms* 482 (2020), pp. 70–81. ISSN: 0168-583X. DOI: https://doi.org/10.1016/j.nimb.2020.09.008.

[161] K Kokurewicz et al. “Focused very high-energy electron beams as a novel radiotherapy modality for producing high-dose volumetric elements”. *Scientific Reports* 9.1 (2019), p. 10837. DOI: 10.1038/s41598-019-46630-w.

[162] Lucy Whitmore et al. “Focused VHEE (Very High Energy Electron) beams and dose delivery for radiotherapy applications”. English. *Scientific Reports* (2021). ISSN: 2045-2322. DOI: 10.1038/s41598-021-93276-8.

[163] Karolina Kokurewicz et al. “An experimental study of focused very high energy electron beams for radiotherapy”. *Communications Physics* 4.1 (2021), p. 33. DOI: 10.1038/s42005-021-00536-0.

[164] Lucy Whitmore et al. “Cern-based experiments and monte carlo simulations on focused vhee (very high energy electron) beams for radiotherapy” (2024). DOI: 10.1038/s41598-024-60997-5.

[165] Magdalena Bazalova-Carter et al. “Treatment planning for radiotherapy with very high-energy electron beams and comparison of VHEE and VMAT plans”. *Medical Physics* 42 (2015), pp. 2615–2625. DOI: 10.1118/1.4918923.

[166] Emil Schüler et al. “Very high-energy electron (VHEE) beams in radiation therapy; Treatment plan comparison between VHEE, VMAT, and PPBS”. *Medical Physics* 44 (2017). DOI: 10.1002/mp.12233.

[167] Till Tobias Böhlen et al. "3D-conformal very-high energy electron therapy as candidate modality for FLASH-RT: A treatment planning study for glioblastoma and lung cancer". *Medical Physics* 50.9 (2023), pp. 5745–5756. DOI: 10.1002/mp.16586.

[168] Annalisa Muscato et al. "Treatment planning of intracranial lesions with {VHEE}: comparing conventional and {FLASH} irradiation potential with state-of-the-art photon and proton radiotherapy". *Frontiers in Physics* 11 (2023). DOI: 10.3389/fphy.2023.1185598.

[169] Guoliang Zhang et al. "Treatment planning consideration for very high-energy electron FLASH radiotherapy". *Physica Medica* 107 (2023), p. 102539. ISSN: 1120-1797. DOI: 10.1016/j.ejmp.2023.102539.

[170] M Aicheler et al. *A Multi-TeV Linear Collider Based on CLIC Technology: CLIC Conceptual Design Report*. CERN Yellow Reports: Monographs. Geneva: CERN, 2012. DOI: 10.5170/CERN-2012-007.

[171] Minglei Kang et al. "Quantitative assessment of 3D dose rate for proton pencil beam scanning FLASH radiotherapy and its application for lung hypofractionation treatment planning". *Cancers* 13.14 (2021), p. 3549. DOI: 10.3390/cancers13143549.

[172] Ana Lourenço et al. "Absolute dosimetry for FLASH proton pencil beam scanning radiotherapy". *Scientific Reports* 13.1 (2023), p. 2054. DOI: 10.1038/s41598-023-28192-0.

[173] Michael M. Folkerts et al. "A framework for defining FLASH dose rate for pencil beam scanning". *Medical Physics* 47.12 (2020), pp. 6396–6404. DOI: https://doi.org/10.1002/mp.14456.

[174] Joseph Bateman et al. "Development of a novel fibre optic beam profile and dose monitor for very high energy electron radiotherapy at ultrahigh dose rates". *Physics in Medicine & Biology* 69 (2024). DOI: 10.1088/1361-6560/ad33a0.

[175] Luke Aidan Dyks. "Studies for Upgrading and Optimising the CLEAR Beamline, and Generating Uniform Electron-Beam Profiles for Irradiation Experiments". Presented 19 Aug 2022. Oxford U., 2022. URL: https://cds.cern.ch/record/2863106.

[176] Andrea Latina. "Introduction to Transverse Beam Dynamics" (2014). Accessed 2024. URL: https://indico.cern.ch/event/1149120/contributions/4822271/.

[177] Andrzej Wolski. *Beam Dynamics in High Energy Particle Accelerators*. IMPERIAL COLLEGE PRESS, 2014. DOI: 10.1142/p899.

[178] Kevin Li. *Collective Effects – an introduction*. Tech. rep. 53 pages, 48 figures, Proceedings of the CERN Accelerator School. CERN, 2021. URL: https://cds.cern.ch/record/2775931.

[179] Stephanie Diana Rädel. "On space charge driven microbunching instability in bERLinPro". PhD thesis. Humboldt-Universität zu Berlin, Mathematisch-Naturwissenschaftliche Fakultät, 2017. DOI: 10.18452/17714.

[180] C Gohil et al. "Luminosity performance of the Compact Linear Collider at 380 GeV with static and dynamic imperfections". *Physical Review Accelerators and Beams* 23.10 (2020), p. 101001. DOI: 10.1103/PhysRevAccelBeams.23.101001.

[181] Rogelio Tomas. "Overview of the Compact Linear Collider". *Physical Review Special Topics-accelerators and Beams - PHYS REV SPEC TOP-AC* 13 (2010). DOI: 10.1103/PhysRevSTAB.13.014801.

[182] Hao Zha and Alexej Grudiev. "Design and optimization of Compact Linear Collider main linac accelerating structure". *Physical Review Accelerators and Beams* 19.11 (2016), p. 111003. DOI: 10.1103/PhysRevAccelBeams.19.111003.

[183] V. Soldatov et al. "Engineering Design and Fabrication of X-band Damped Detuned Structure for the CLIC Study". *Proc. IPAC'11* (San Sebastian, Spain). International Particle Accelerator Conference 2. JACoW Publishing, Geneva, Switzerland, 2011, pp. 154–156. ISBN: 978-9-29-083366-6. URL: https://jacow.org/IPAC2011/papers/MOPC037.pdf.

[184] Andrea Latina et al. "A Compact Inverse Compton Scattering Source Based on X-Band Technology and Cavity-Enhanced High-Average-Power Ultrafast Lasers". *JACoW* LINAC2022 (2022), pp. 44–46. DOI: 10.18429/JACoW-LINAC2022-MOPOJO09.

[185] "CERN, CHUV and THERYQ join forces for FLASH". *Cern Courier* (2023). URL: https://cerncourier.com/a/cern-chuv-and-theryq-join-forces-for-flash/.

[186] JE Clendenin. *RF photoinjectors*. Tech. rep. Accessed 2024. SLAC National Accelerator Lab., Menlo Park, CA (United States), 1996. URL: https://accelconf.web.cern.ch/l96/PAPERS/TU204.PDF.

[187] Luke Dyks et al. "Generation of Transversely Uniform Bunches from a Gaussian Laser Spot in a Photoinjector for Irradiation Experiments". *13th International Particle Accelerator Conference* 2022 (2022), pp. 2483–2486. DOI: 10.18429/JACoW-IPAC2022-THPOST019.

[188] Alexander Malyzhenkov et al. "Experimental generation of the transversely uniform electron bunches at the CLEAR facility at CERN". *JACoW* IPAC2023 (2023), TUPL119. DOI: 10.18429/JACoW-IPAC2023-TUPL119.

[189] Gert Moliere. "Theorie der streuung schneller geladener teilchen ii mehrfach-und vielfachstreuung". *Zeitschrift für Naturforschung A* 3.2 (1948), pp. 78–97. DOI: 10.1515/zna-1948-0203.

[190] H. A. Bethe. "Molière's Theory of Multiple Scattering". *Phys. Rev.* 89 (1953), pp. 1256–1266. DOI: 10.1103/PhysRev.89.1256.

[191] William T. Scott. "The Theory of Small-Angle Multiple Scattering of Fast Charged Particles". *Rev. Mod. Phys.* 35 (1963), pp. 231–313. DOI: 10.1103/RevModPhys.35.231. URL: https://link.aps.org/doi/10.1103/RevModPhys.35.231.

[192] J. J. Devaney. *Electron multiple, plural and single scattering*. 1985.

[193] Gerald R. Lynch and Orin I. Dahl. "Approximations to multiple Coulomb scattering". *Nuclear Instruments and Methods in Physics Research Section B: Beam Interactions with Materials and Atoms* 58.1 (1991), pp. 6–10. ISSN: 0168-583X. DOI: 10.1016/0168-583X(91)95671-Y.

[194] H. W. Koch and J. W. Motz. "Bremsstrahlung Cross-Section Formulas and Related Data". *Rev. Mod. Phys.* 31 (1959), pp. 920–955. DOI: 10.1103/RevModPhys.31.920.

[195] Donald E Groom and SR Klein. "Passage of particles through matter". *The European Physical Journal C-Particles and Fields* 15.1-4 (2000), pp. 163–173. DOI: 10.1007/BF02683419.

[196] GC Baldwin and GS Klaiber. "Photo-fission in heavy elements". *Physical Review* 71.1 (1947), p. 3. DOI: 10.1103/PhysRev.71.3.

[197] B. L. Berman and S. C. Fultz. "Measurements of the giant dipole resonance with monoenergetic photons". *Rev. Mod. Phys.* 47 (1975), pp. 713–761. DOI: 10.1103/RevModPhys.47.713.

[198] Umberto Deut et al. "Secondary radiation dose modeling in passive scattering and pencil beam scanning very high energy electron (VHEE) radiation therapy". *Medical Physics* 50.7 (2023), pp. 4491–4504. DOI: 10.1002/mp.16443.

[199] Kevin Balanda and H. Macgillivray. "Kurtosis: A Critical Review". *The Americal Statistician* 42 (1988), pp. 111–119. DOI: 10.1080/00031305.1988.10475539.

[200] L. Bottura et al. "GaToroid: A novel toroidal gantry for hadron therapy". *Nuclear Instruments and Methods in Physics Research Section A: Accelerators, Spectrometers, Detectors and Associated Equipment* 983 (2020), p. 164588. ISSN: 0168-9002. DOI: 10.1016/j.nima.2020.164588.

[201] E Felcini et al. "Particle tracking and beam optics analysis on a toroidal gantry for proton therapy". *Physics in Medicine & Biology* 66.10 (2021), p. 104002. DOI: 10.1088/1361-6560/abf760.

[202] Enrico Felcini et al. "Magnetic Design of a Superconducting Toroidal Gantry for Hadron Therapy". *IEEE Transactions on Applied Superconductivity* PP (2020), pp. 1–1. DOI: 10.1109/TASC.2020.2966174.

[203] Enrico Felcini et al. "Design of the first HTS single-coil demonstrator of GaToroid toroidal gantry for hadron therapy". *IEEE Transactions on Applied Superconductivity* 31.5 (2021), pp. 1–5. DOI: 10.1109/TASC.2021.3067808.

[204] E Felcini et al. "Feasibility Study of GaToroid Gantries for Carbon Ions". *IEEE Transactions on Applied Superconductivity* 32.6 (2022), pp. 1–5. DOI: 10.1109/TASC.2022.3160380.

[205] L. Bottura et al. "Magnetic Design of a Compact GaToroid for Very High Energy Electron and Pre-Clinical Hadron Beams". *IEEE Transactions on Applied Superconductivity* PP (2024), pp. 1–5. DOI: 10.1109/TASC.2024.3379970.

[206] Hywel Owen et al. "Technologies for Delivery of Proton and Ion Beams for Radiotherapy". *International Journal of Modern Physics A* 29 (2013), p. 14. DOI: 10.1142/S0217751X14410024.

[207] Laurent Deniau et al. *The MAD-X Program*. 2017. URL: http://madx.web.cern.ch/madx/.

[208] F Schmidt, E Forest, and E McIntosh. *Introduction to the polymorphic tracking code: Fibre bundles, polymorphic Taylor types and exact tracking*. Tech. rep. Geneva: CERN, 2002. URL: https://%20cds.cern.ch/record/573082.

[209] Andrea Latina. "Update of the Tracking Code RF-Track". *JACoW* IPAC 2021 (2021), pp. 4180–4182. DOI: 10.18429/JACoW-IPAC2021-THPAB203.

[210] F. Schmidt. "Mad-X PTC Integration". *Proceedings of the 2005 Particle Accelerator Conference*. 2005, pp. 1272–1274. DOI: 10.1109/PAC.2005.1590731.

[211] B. Stechauner et al. "Comparison of tracking codes for beam-matter interaction". *JACoW* IPAC2023 (2023), MOPL165. DOI: 10.18429/JACoW-IPAC2023-MOPL165.

[212] A Latina et al. "Update of the RF-Track particle tracking code". *JACoW IPAC* 2023 (2023), WEPL151. DOI: 10.18429/JACoW-IPAC2023-WEPL151.

[213] Erik Grusell et al. "A general solution to charged particle beam flattening using an optimized dual-scattering-foil technique, with application to proton therapy beams". *Physics in Medicine & Biology* 39.12 (1994), p. 2201. DOI: 10.1088/0031-9155/39/12/005.

[214] Hong Qi Tan et al. "Implementing dispersion measurement as part of scanning proton therapy commissioning and quality assurance". *Physics in Medicine & Biology* 68.22 (2023), p. 225001. DOI: 10.1088/1361-6560/ad0536.

[215] J. A. Nelder and R. Mead. "A Simplex Method for Function Minimization". *The Computer Journal* 7.4 (1965), pp. 308–313. ISSN: 0010-4620. DOI: 10.1093/comjnl/7.4.308.

[216] Gunilla C Bentel, Lawrence B Marks, and Mitchell S Anscher. "The effect of beam divergence on target coverage". *Medical Dosimetry* 24.2 (1999), pp. 99–113. DOI: 10.1016/s0958-3947(99)00009-6.

[217] J. Perl et al. "TOPAS: An innovative proton Monte Carlo platform for research and clinical applications". *Medical Physics* 39 (2012), p. 6818. DOI: 10.1118/1.4758060.

[218] B. Faddegon et al. "The TOPAS Tool for Particle Simulation, a Monte Carlo Simulation Tool for Physics, Biology and Clinical Research". *Physica Medica* (2020). DOI: 10.1016/j.ejmp.2020.03.019.

[219] VN Ivanchenko et al. "Geant4 models for simulation of multiple scattering". *Journal of Physics: Conference Series*. Vol. 219. 3. IOP Publishing. 2010, p. 032045. DOI: 0.1088/1742-6596/219/3/032045.

[220] Przemysław Adrich. "A new method for designing dual foil electron beam forming systems. I. Introduction, concept of the method". *Nuclear Instruments and Methods in Physics Research Section A: Accelerators, Spectrometers, Detectors and Associated Equipment* 817 (2016), pp. 93–99. ISSN: 0168-9002. DOI: 10.1016/j.nima.2016.01.043.

[221] Justin Deloy LeBlanc. *Design of electron dual foil scattering systems for Elekta Infinity radiotherapy accelerators*. Louisiana State University and Agricultural & Mechanical College, 2012. DOI: 10.31390/gradschool_theses.2440.

[222] K K Kainz et al. "Dual scattering foil design for poly-energetic electron beams*". *Physics in Medicine & Biology* 50.5 (2005), p. 755. DOI: 10.1088/0031-9155/50/5/002.

[223] Thongchai AM Masilela, Rachel Delorme, and Yolanda Prezado. "Dosimetry and radioprotection evaluations of very high energy electron beams". *Scientific Reports* 11.1 (2021), p. 20184. DOI: 10.1038/s41598-021-99645-7.

[224] C S Robertson et al. "Beam optics study for a potential VHEE beam delivery system". *Journal of Physics: Conference Series* 2420.1 (2023), p. 012102. DOI: 10.1088/1742-6596/2420/1/012102. URL: https://dx.doi.org/10.1088/1742-6596/2420/1/012102.

[225] Rainer Storn and Kenneth Price. "Differential evolution–a simple and efficient heuristic for global optimization over continuous spaces". *Journal of global optimization* 11 (1997), pp. 341–359. DOI: 10.1023/A:1008202821328.

[226] R. Assmann, M. Lamont, and S. Myers. "A brief history of the LEP collider". *Nucl. Phys. B Proc. Suppl.* 109 (2002). Ed. by F. L. Navarria, M. Paganoni, and P. G. Pelfer, pp. 17–31. DOI: 10.1016/S0920-5632(02)90005-8.

[227] Thomas Taylor and Daniel Treille. "The Large Electron Positron Collider (LEP): Probing the Standard Model". *Technology Meets Research*. Chap. Chapter 7, pp. 217–261. DOI: 10.1142/9789814749145_0007.

[228] DJ Warner. *First electron beams from the LEP Injector Linacs*. Tech. rep. 1986. URL: https://cds.cern.ch/record/2840034.

[229] G Bienvenu et al. *Accelerating structure developments for the LEP injector linac (LIL)*. Tech. rep. 1984. URL: https://accelconf.web.cern.ch/l84/papers/frq0003.pdf.

[230] Günther Geschonke and A Ghigo. *CTF3 Design Report*. Tech. rep. revised version number 1 submitted on 2002-06-19 12:11:29. Geneva: CERN, 2002. URL: https://cds.cern.ch/record/559331.

[231] R. Ruber et al. "The CTF3 Two-beam Test Stand". *Nuclear Instruments and Methods in Physics Research Section A: Accelerators, Spectrometers, Detectors and Associated Equipment* 729 (2013), pp. 546–553. ISSN: 0168-9002. DOI: 10.1016/j.nima.2013.07.055.

[232] Andrea Palaia et al. "Effects of rf breakdown on the beam in the Compact Linear Collider prototype accelerator structure". *Physical Review Special Topics-Accelerators and Beams* 16.8 (2013), p. 081004. DOI: 10.1103/PhysRevSTAB.16.081004.

[233] M. Olvegård et al. “Beam profile monitoring at the test beam line at the Compact Linear Collider test facility”. *Phys. Rev. ST Accel. Beams* 16 (2013), p. 082802. DOI: 10.1103/PhysRevSTAB.16.082802.

[234] D. Gamba et al. “The CLEAR user facility at CERN”. *Nuclear Instruments and Methods in Physics Research Section A: Accelerators, Spectrometers, Detectors and Associated Equipment* 909 (2018). 3rd European Advanced Accelerator Concepts workshop (EAAC2017), pp. 480–483. ISSN: 0168-9002. DOI: 10.1016/j.nima.2017.11.080.

[235] *CLEAR User Facility Website*. URL: https://clear.cern/.

[236] Alban Mosnier et al. “The probe beam linac in CTF3”. *Tenth European Particle Accelerator Conference" EPAC’06"*. 2006, pp. 679–681. URL: https://api.semanticscholar.org/CorpusID:111386228.

[237] Julien Brossard et al. “Construction of the probe beam photo-injector of CTF3”. *10th European Particle Accelerator Conference" EPAC’06"*. 2006, pp. 828–830. URL: https://cds.cern.ch/record/1078567.

[238] Agnese Lagzda et al. “Relative insensitivity to inhomogeneities on very high energy electron dose distributions”. *Proc. 8th Int. Particle Accelerator Conf.(IPAC’17)*. 2017. DOI: 10.18429/JACoW-IPAC2017-THPVA139.

[239] Maris Tali et al. “Mono-energetic electron induced single-event effects at the VESPER facility”. *2016 16th European Conference on Radiation and Its Effects on Components and Systems (RADECS)*. IEEE. 2016, pp. 1–5. DOI: 10.1109/RADECS.2016.8093166.

[240] Collette Pakuza. “Development of a beam position monitor based on Cherenkov diffraction radiation for the AWAKE experiment at CERN”. PhD thesis. Oxford U., 2023. DOI: 10.5287/ora-w4b4orge6.

[241] P Korysko et al. “The clear user facility: a review of the experimental methods and future plans”. *Proc. 14th Int. Particle Accelerator Conf., number 14 in IPAC’23-XIV Int. Particle Accelerator Conf. JACoW Publishing, Geneva, Switzerland*. 2023, pp. 876–879. DOI: 10.18429/JACoW-IPAC2023-MOPL141.

[242] KN Sjobak et al. “Status of the CLEAR electron beam user facility at CERN”. *Proc. IPAC’19* (2019), pp. 983–986. URL: 10.18429/JACoW-IPAC2019-MOPTS054.

[243] Vilde Rieker et al. “VHEE High Dose Rate Dosimetry Studies in CLEAR”. *JACoW IPAC* 2022 (2022), pp. 3026–3029. DOI: 10.18429/JACoW-IPAC2022-THPOMS031.

[244] Hideharu Miura et al. “Gafchromic EBT-XD film: dosimetry characterization in high-dose, volumetric-modulated arc therapy”. *Journal of applied clinical medical physics* 17.6 (2016), pp. 312–322. DOI: 10.1120/jacmp.v17i6.6281.

[245] Valeria Casanova Borca et al. “Dosimetric characterization and use of GAFCHROMIC EBT3 film for IMRT dose verification”. *Journal of applied clinical medical physics* 14.2 (2013), pp. 158–171. DOI: 10.1120/jacmp.v14i2.4111.

[246] Maud Jaccard et al. “High dose-per-pulse electron beam dosimetry: commissioning of the Oriatron eRT6 prototype linear accelerator for preclinical use”. *Medical physics* 45.2 (2018), pp. 863–874. DOI: 10.1002/mp.12713.

[247] Jose Fernando Pérez Azorín, Luis Isaac Ramos García, and Josep M. Martí-Climent. “A method for multichannel dosimetry with EBT3 radiochromic films”. *Medical Physics* 41.6Part1 (2014), p. 062101. DOI: 10.1118/1.4871622.

[248] Ivan Vladislavov Panayotov et al. “Polyetheretherketone (PEEK) for medical applications”. *Journal of Materials Science: Materials in Medicine* 27 (2016), pp. 1–11. DOI: 10.1007/s10856-016-5731-4.

[249] Valeria Borca et al. “Dosimetric characterization and use of GAFCHROMIC EBT3 film for IMRT dose verification”. *Journal of applied clinical medical physics / American College of Medical Physics* 14 (2013), p. 4111. DOI: 10.1120/jacmp.v14i2.4111.

[250] C. Robertson et al. “Dual-scattering foil installation at CLEAR”. English. *Proc. IPAC’23* (Venice, Italy). IPAC’23 - 14th International Particle Accelerator Conference 14. JACoW Publishing, Geneva, Switzerland, 2023, pp. 5059–5062. ISBN: 978-3-95450-231-8. DOI: 10.18429/JACoW-IPAC2023-THPM073.

[251] Luke Dyks et al. “The Design of a Second Beamline for the CLEAR User Facility at CERN”. *JACoW IPAC* 2022 (2022), pp. 2479–2482. DOI: 10.18429/JACoW-IPAC2022-THPOST018.

[252] E. W. Snedden et al. “Specification and design for full energy beam exploitation of the compact linear accelerator for research and applications”. *Phys. Rev. Accel. Beams* 27 (2024), p. 041602. DOI: 10.1103/PhysRevAccelBeams.27.041602. URL: https://link.aps.org/doi/10.1103/PhysRevAccelBeams.27.041602.

[253] Florian Burkart et al. “The ARES Linac at DESY”. *Proc. LINAC’22* 31 (2022), pp. 691–694. DOI: 10.18429/JACoW-LINAC2022-THPOJO01.

[254] L Faillace et al. “Perspectives in linear accelerator for FLASH VHEE: Study of a compact C-band system”. *Physica Medica* 104 (2022), pp. 149–159. DOI: 10.1016/j.ejmp.2022.10.018.

A Surplus PLA/Al Scattering Results

Tables A.1 and A.2 display surplus fitting results for the in-air experiments as described in Sections 5.4 and 5.5 respectively.

Table A.1: Super-Gaussian fitting parameters in experiment and simulations of PLA dual-scattering setup, for results with evidence for uniformity region of 1 cm radius. t_{S1} is the thickness of S1; z_{S2} is the distance from the upstream face of S1 to the downstream face of S2, as shown in Figure 5.12. Units of mm unless otherwise specified. Errors from fitting covariance output.

z_{S2}	t_{S1}	Sim x_{95}	Exp x_{95}	Sim y_{95}	Exp y_{95}	Exp k_x [a.u.]	Exp k_y [a.u.]
281	10	5.9±0.1	4.3±0.1	5.82±0.1	4.5±0.1	-1.5±0.1	-0.2±0.1
335	10	6.2±0.1	5.2±0.1	6.2±0.1	5.5±0.1	1.3±0.2	-0.1±0.1
381	10	7.2±0.1	5.5±0.1	6.9±0.1	5.7±0.1	1.4±0.1	-0.2±0.10
281	20	7.8±0.3	8.6±0.1	8.0±0.3	7.6±0.2	1.5±0.1	2.1±0.3
181	30	8.0±3.2	6.6±0.1	7.7±1.3	8.4±0.2	-0.2±0.1	2.4±0.3
231	30	8.5±0.5	8.3±0.1	8.3±0.6	10.8±0.2	1.3±0.1	1.9±0.1

Table A.2: Super-Gaussian fitting parameters from transverse experimental dose profiles and TOPAS simulated intensity profiles for aluminium dual-scattering setup. S2, Loc column refers to the choice of scatterer and positioning of transverse profile measurement, as shown in Figure 5.15. Errors from fitting covariance output.

S2, Loc	Sim x_{95} [mm]	Exp x_{95} [mm]	Sim y_{95} [mm]	Exp y_{95} [mm]	Exp k_x [a.u.]	Exp k_y [a.u.]
1,A	4.6±0.1	3.9±0.1	4.7±0.2	3.3±0.1	-1.0±0.3	0.5±0.7
1,A	4.6±0.1	4.4±0.2	4.7±0.2	3.5±0.1	0.1±0.3	0.5±0.7
Al 1,B (No S1)	1.7±0.3	1.5±0.1	1.70±0.3	1.4±0.1	0	0
Al 1,B (No S1)	1.7±0.3	1.4±0.1	1.70±0.3	1.3±0.1	0	0
Al 2,B (No S1)	2.10±0.3	2.1±0.1	2.1±0.3	2.0±0.1	0	0
Al 2,B (No S1)	2.10±0.3	2.0±0.1	2.1±0.3	1.9±0.1	0	0

B Availability of Data

The complete collection of simulated, YAG and film data is far too extensive to include even in an extended appendix section. A OneDrive folder comprising of all experimental data taken at CLEAR and used for the work of this thesis in some way, by date is available by request. Simulated comparisons can be generated through dedicated code available by request or in the same Github repository outlined previously - https://github.com/gilettejr/dosimetry.